

# Chiral Symmetry Restoration and Dileptons in Relativistic Heavy-Ion Collisions

R. Rapp<sup>1</sup> and J. Wambach<sup>2</sup>

1) Department of Physics and Astronomy, State University of New York,  
Stony Brook, NY 11794-3800, U.S.A.

2) Institut für Kernphysik, Technische Universität Darmstadt,  
Schloßgartenstr. 9, D-64289 Darmstadt, Germany

### **Abstract**

The current theoretical status in the analysis and interpretation of low-mass dilepton measurements in (ultra-) relativistic heavy-ion experiments is reviewed. Special emphasis is put on potential signals of (partial) restoration of dynamically broken chiral symmetry in a hot and dense hadronic medium. It follows from chiral symmetry alone that parity partners of hadronic correlation functions must become identical when the symmetry is restored. The assessment of medium effects in the vector channel, which governs the dilepton production, thus necessitates a simultaneous treatment of the vector and axialvector degrees of freedom. While significant progress in this respect has been made some open questions remain in establishing a rigorous link in the mass region below 1 GeV. From the present calculations a suggestive 'quark-hadron duality' emerges near the phase boundary. It implies substantial medium effects in the dilepton signal from the hadronic phase which smoothly matches a perturbative description within the plasma phase.

# Contents

<b>1</b>	<b>Introduction</b>	<b>3</b>
<b>2</b>	<b>'Strong QCD' and Vector Mesons</b>	<b>10</b>
2.1	Symmetries and Anomalies of QCD . . . . .	11
2.2	Vacuum Condensates . . . . .	14
2.3	In-Medium Condensates via Low-Density Expansions . . . . .	16
2.4	Lattice Results . . . . .	19
2.5	Dilepton Production and Vector Mesons . . . . .	25
2.6	Vector-Axialvector Mixing . . . . .	27
2.7	QCD Sum rules . . . . .	33
2.8	Chiral Reduction Formalism . . . . .	38
<b>3</b>	<b>Modeling Vector Mesons in the Medium</b>	<b>41</b>
3.1	Effective Meson Lagrangians: Impact of Finite Temperature . . . . .	41
3.1.1	Gauged Linear $\sigma$ -Model + VDM . . . . .	42
3.1.2	Massive Yang-Mills Approach . . . . .	44
3.1.3	Hidden Local Symmetry . . . . .	46
3.1.4	Phenomenological Meson Lagrangians . . . . .	51
3.2	Finite Baryon Density . . . . .	61
3.2.1	Mean-Field Approach: Brown-Rho Scaling . . . . .	61
3.2.2	Pion Cloud Modifications . . . . .	64
3.2.3	Direct $\rho$ -Nucleon Resonances . . . . .	73
3.2.4	Dispersive Approaches at High Energies . . . . .	76
3.2.5	Finite Temperature Effects in Baryonic Matter . . . . .	77
<b>4</b>	<b>Analysis of Dilepton Spectra: Constraints, Predictions and Implications</b>	<b>80</b>
4.1	Constraints on Hadronic Dilepton Production . . . . .	81
4.1.1	Decay Widths and Hadronic Scattering Data . . . . .	82
4.1.2	Photoabsorption Spectra . . . . .	85
4.2	Dilepton Rates in Hot and Dense Matter . . . . .	91
4.2.1	Comparison of Hadronic Approaches . . . . .	91
4.2.2	Beyond Conventional Scenarios for Dilepton Enhancement . . . . .	97

4.2.3	Quark-Hadron Duality . . . . .	102
4.3	Photon Production Rates . . . . .	106
4.4	Space-Time Evolution of Heavy-Ion Collisions . . . . .	107
4.4.1	Hydrodynamical Approach . . . . .	108
4.4.2	Transport Simulations . . . . .	110
4.4.3	Thermal Fireball Expansion . . . . .	114
4.5	Dilepton Spectra at BEVALAC/SIS Energies . . . . .	116
4.6	Dilepton Spectra at CERN-SpS Energies . . . . .	120
4.6.1	Decays after Freezeout: Hadronic Cocktail versus Experiment . . . . .	120
4.6.2	Free $\pi^+\pi^-$ Annihilation in the Hadronic Fireball . . . . .	124
4.6.3	Medium Effects I: Invariant Mass Spectra . . . . .	125
4.6.4	Medium Effects II: Transverse Momentum Dependencies . . . . .	133
4.6.5	Time Dependence of In-Medium Signals . . . . .	135
4.6.6	Intermediate-Mass Spectra . . . . .	138
4.7	Direct Photon Spectra . . . . .	141
4.8	Theoretical Implications . . . . .	144
<b>5</b>	<b>Conclusions</b>	<b>149</b>

# Chapter 1

## Introduction

In recent years substantial experimental and theoretical efforts have been undertaken to investigate the versatile physics issues involved in (ultra-) relativistic heavy-ion collisions, *i.e.*, collisions of atomic nuclei in which the center-of-mass (*cms*) energy per nucleon is (much) larger than the nucleon rest mass [1, 2]. The principal goal of this initiative is to explore the phase structure of the underlying theory of strong interactions – Quantum Chromodynamics (QCD) – by creating in the laboratory new states of matter. Through varying experimental conditions such as the collision energy or impact parameter, one aims at covering as broad a regime as possible in temperature and baryon density of the excited nuclear system. In nature such new states are believed to have existed and still may be encountered on large scales in at least two astrophysical contexts: in the evolution of the early universe where a few tens of microseconds after the 'big bang' a transient stage of strongly interacting matter prevailed at temperatures a few times  $10^{12}$  K ( $\sim 200$  MeV) with very small net baryon excess; in the interior of neutron stars where mass densities are likely to exceed  $10^{15}$  g/cm<sup>3</sup> – about four times the central density of nuclei – while surface temperatures are as low as  $10^5$  K or less. Experiments have been performed until recently at the Alternating Gradient Synchrotron (AGS) in Brookhaven (BNL) with *cms* energies around  $\sqrt{s} \sim 5$  AGeV and are currently underway at the CERN Super-proton-Synchrotron (SpS) at  $\sqrt{s} \sim 20$  AGeV. In the near future the Relativistic Heavy-Ion Collider (RHIC) at BNL will start data-taking at  $\sqrt{s} \sim 200$  AGeV, and eventually heavy ions will also be injected into the CERN Large Hadron Collider (LHC) reaching  $\sqrt{s} \sim 10$  ATeV.

As nuclear matter is heated and compressed hadrons occupy more and more of the available space. Eventually they start to overlap and the initially confined quarks and gluons begin to 'percolate' between the hadrons thus being 'liberated'. This simple picture has originally provided the basis for models of the quark-hadron transition and has been essentially confirmed by ab-initio numerical QCD lattice calculations at finite temperature. The latter demonstrate that strongly interacting matter exhibits a rapid change in energy- and entropy-density (possibly constituting a true phase transition) within a narrow temperature interval indicating a change-over from confined hadrons to a 'quark-gluon plasma' (QGP). At the same time the quarks – most notably up (*u*) and down (*d*) quarks, carrying an effective mass of a few hundred MeV in the confined phase – lose their 'constituent mass' leading to the restoration of 'chiral symmetry', an approximate symmetry

of QCD in the sector of 'light' quarks. Once massless, left- and right-handed quarks decouple leading to a degeneracy in (hadronic) states of opposite parity. The expected phase diagram of hadronic matter is shown in Fig. 1.1. The 'confined phase' consists of an interacting gas of

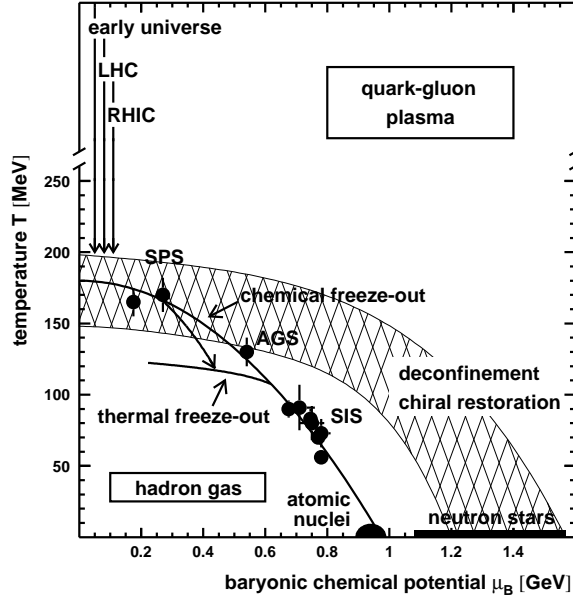


Figure 1.1: QCD phase diagram [3, 4] in the temperature and baryon chemical potential plane with freezeout points extracted from hadrochemical analyses at SIS, AGS and SpS energies.

hadrons (a 'resonance gas') while the 'deconfined phase' is comprised of a (non-ideal) gas of quarks and gluons. The hatched 'phase boundary' reflects the present uncertainties from lattice QCD extrapolated to finite baryochemical potential,  $\mu_B$ . Also shown are locations realized in heavy-ion systems for various laboratory bombarding energies at the point where *inelastic* collisions between the particles in the fireball cease – the so-called 'chemical freezeout' – characterizing the stage where the fireball acquires its final particle composition. The 'thermal freezeout' refers to the stage where *elastic* collisions are no longer supported as the mean-free paths of the hadrons exceed the size of the fireball. Their momentum distributions do no longer change and they stream freely to the detector. Based on the assumption of thermodynamic equilibrium the chemical freezeout is determined from a hadrochemical analysis of the measured abundances of particle species [5, 3] with the conclusion that at the highest presently available energies the produced systems must be close to the phase boundary. However, subsequent rescattering still maintains local thermal equilibrium for about 10 fm/c, cooling the system to appreciably lower temperatures until the thermal freezeout is reached. The latter is reconstructed from a combination of (comoving) thermal distributions and a collective transverse and longitudinal expansion of the fireball.

If the quark-hadron transition can indeed be induced in heavy-ion collisions the challenge is how to detect it in the laboratory and isolate observable signals (see, *e.g.*, Refs. [6, 7] for recent reviews). Because of their negligible final-state interactions with the hadronic environment, dileptons (correlated lepton pairs,  $l^+l^- = e^+e^-$  or  $\mu^+\mu^-$ ) as well as photons are considered ideal probes for the high-density/-temperature regions formed in the early stages of the collision [8, 9]. However, as they are emitted continuously, they sense in fact the entire space-time history of the reaction [10, 11]. Because of an additional variable, the invariant pair mass  $M_{ll}$ , dileptons have the experimental advantage of a superior signal to background ratio as compared to real photons [12]. Consequently, dileptons provide the most promising electromagnetic data up to date.

The finally measured dilepton spectra can be chronologically divided into several phases. Before the nuclear surfaces actually touch dileptons are produced through coherent Bremsstrahlung [13] in the decelerating Coulomb field of the approaching nuclei. Their contribution seems to be negligible as compared to subsequent sources [14]. Within the first 1 fm/c or so of the nuclear overlap, the excited hadronic system is far from thermal equilibrium and the corresponding 'pre-equilibrium' dilepton radiation mostly consists of hard processes such as Drell-Yan annihilation leaving its trace mainly at large invariant masses  $M_{ll} \gtrsim 3$  GeV. A rapid thermalization [15] is expected to subsequently establish the QGP phase, sometimes also called the 'partonic phase', where dilepton production proceeds predominantly via (perturbative) quark-antiquark annihilation. It should reflect a thermal spectrum even though, towards smaller masses, radiative corrections from gluons as well as thermal loop effects are likely to become important. At later stages when, upon expansion and cooling, the QGP has converted into a hot hadron gas, dileptons are preferentially radiated from pion and kaon annihilation processes as well as other collisions between various hadrons. The two-body annihilation processes are dynamically enhanced through the formation of (light) vector meson resonances, such as the  $\rho$ ,  $\omega$  and  $\phi$  mesons, which directly couple to  $l^+l^-$  pairs. Thus the invariant mass of the lepton pair directly reflects the mass distribution of the vector meson at the moment of decay! This explains the distinguished role that vector mesons – in conjunction with their in-medium modifications – play for dilepton measurements in heavy-ion reactions. The situation is somewhat different for the heavy quarkonium states such as the  $J/\Psi$  or  $\Upsilon$ : in contrast to the light vector mesons, their lifetime is substantially longer than the typical one of the hadronic fireball such that they will predominantly decay after freezeout. Therefore, as detailed further below, the importance of the corresponding dilepton signal largely resides in its magnitude and not so much in the spectral shape. Finally, when the freezeout stage is reached, the dominant sources are hadronic resonance as well as Dalitz decays, mostly from  $\pi^0$ ,  $\eta$  and  $\omega$  mesons, all feeding into the low-mass region,  $M_{ll} \lesssim 1$  GeV.

A schematic view of characteristic dilepton sources in ultrarelativistic heavy-ion collisions (URHIC's) is given in Fig. 1.2. With respect to invariant mass one can roughly distinguish three regions. Let us try to draw some qualitative connections with the basic properties of strong interactions that might be addressed in the respective regimes. The low-mass region below and around the  $\phi$  meson is governed by the light-quark sector of  $u$ ,  $d$  and  $s$  quarks. In fact, it is known that in the limit of vanishing (current) quark masses the order parameter of the QCD finite-temperature phase transition is associated with chiral symmetry restoration (*e.g.*, the quark condensate) and is most likely of first order for three flavors. Thus, in the low-mass region signals of chiral restoration should turn up, transmitted in terms of medium modifications of light hadrons. On the other hand, in the limit of very large current quark masses, the order parameter of the QCD finite- $T$

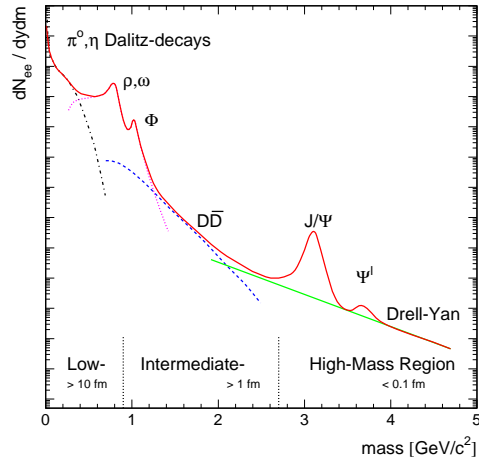


Figure 1.2: Expected sources for dilepton production as a function of invariant mass in ultrarelativistic heavy-ion collisions[16].

transition is associated with deconfinement (the so-called 'Wilson line'), again realized in a strong first-order transition. Thus, for heavy quarks one might hope to become sensitive to features of deconfinement. This seems indeed to be the case: the confining potential within heavy quarkonium states ( $J/\Psi$ ,  $\Upsilon$ ) will be Debye-screened due to freely moving color charges in a QGP leading to a dissolution of the bound states [17]. As a consequence the final abundance of, *e.g.*,  $J/\Psi$  mesons – and thus their contribution to the dilepton spectrum – is suppressed, signaling (the onset of) the deconfinement transition. This very important topic will not be covered in the present review, see Refs. [18] for the recent exciting developments. Finally, the intermediate-mass region (IMR) might allow insights into aspects of quark-hadron 'duality'. As is evident from the saturation of the vacuum annihilation cross section  $e^+e^- \rightarrow \text{hadrons}$  by perturbative QCD above  $\sim 1.5$  GeV, the essentially structureless thermal 'continuum' up to the  $J/\Psi$  can be equally well described by either hadronic or quark-gluon degrees of freedom. However, as a QGP can only be formed at higher temperatures than a hadronic gas, the intermediate mass region might be suitable to observe a thermal signal from plasma radiation [9, 19] in terms of absolute yield. The most severe 'background' in this regime is arising from decays of 'open-charm' mesons, *i.e.*, pairwise produced  $D\bar{D}$  mesons followed by individual semileptonic decays. Although an enhanced charm production is interesting in itself – probably related to the very early collision stages – it may easily mask a thermal plasma signal. To a somewhat lesser extent, this also holds true for the lower-mass tail of Drell-Yan production.

Until today, the measurement of dilepton spectra in URHIC's has mainly been carried out at the CERN-SpS by three collaborations: CERES/NA45 is dedicated to dielectron measurements in the low-mass region [20, 21, 22, 23], HELIOS-3 [24] has measured dimuon spectra from threshold



up to the  $J/\Psi$  region, and NA38/NA50 [25, 26, 27, 28] measures dimuon spectra from threshold to very high masses of about 8 GeV, with emphasis on  $J/\Psi$  suppression (for a summary of low- and intermediate-mass dilepton measurements see Refs. [29, 30, 31]). In the near future, with RHIC coming on line pushing the collision energies to new frontiers, high resolution dilepton spectra will be measured by the PHENIX collaboration [32]. At much lower bombarding energies dilepton data have also been taken by the DLS collaboration at the BEVALAC [33, 34] and will soon become available from the high-precision detector HADES at SIS (GSI) [35]. Here only the low-mass region up to the kinematical limit of around 1 GeV is accessible and the focus is on the role of high baryon density. Unfortunately, no dilepton measurements have been performed at the AGS where presumably the highest baryon densities were attained. However, the already commissioned low-energy run at the CERN-SpS at a projectile energy of 40 AGeV is believed to close this gap penetrating into the regime of extreme baryon density.

The objective of the present article is to review the theoretical efforts in understanding the experimental results in the low-mass region which – as discussed above – is intimately connected to the question of chiral symmetry restoration. A great deal of theoretical activity has been triggered by recent observations from the CERES [20, 23] and the HELIOS-3 [24] collaborations that central nucleus-nucleus ( $A$ - $A$ ) collisions exhibit a strong enhancement of low-mass dilepton production as compared to proton-nucleus reactions<sup>1</sup>. Whereas the  $p$ - $A$  data can be well reproduced by final-state hadron decays with known abundances – the so-called hadronic ‘cocktail’ – (Fig. 1.3), the

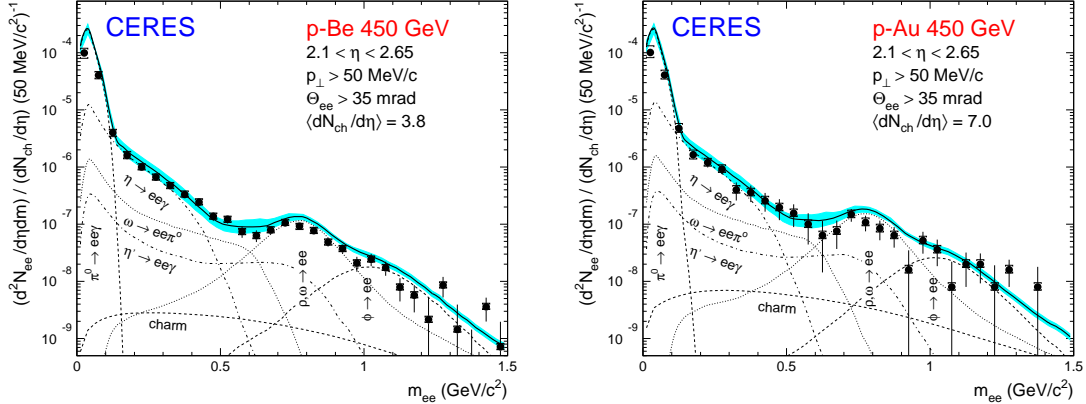


Figure 1.3: Invariant mass spectra of dileptons as measured by the CERES collaboration [20] in 450 GeV proton-induced collisions on Beryllium (left panel) and Gold targets (right panel). The data are compared to expectations from various hadron decay channels (labeled explicitly) based on measured hadron multiplicities. The bands indicate the systematic uncertainty in the cocktail.

<sup>1</sup>One should note that similar effects have *not* been found by NA38/50 [28], which, however, is most likely related to a rather large  $M_T$ -cut applied in their analysis. On the other hand, the DLS-data [34], taken at much lower incident energies, *do* show a very strong enhancement.

latter strongly underestimate the  $A$ - $A$  spectra. As several hundreds of pions are produced in  $A$ - $A$  collisions, the observed increase of dilepton pairs has been attributed to  $\pi^+\pi^- \rightarrow l^+l^-$  annihilation during the interacting phase of the hadronic fireball. Using vacuum meson properties many theoretical groups have included this process within different models for the space-time evolution of  $A$ - $A$  reactions. Their results are in reasonable agreement with each other, but in disagreement with the data: the experimental spectra in the mass region from 0.3–0.6 GeV are significantly underestimated as seen from Fig. 1.4 (see also Ref. [29]). This has led to the suggestion of various

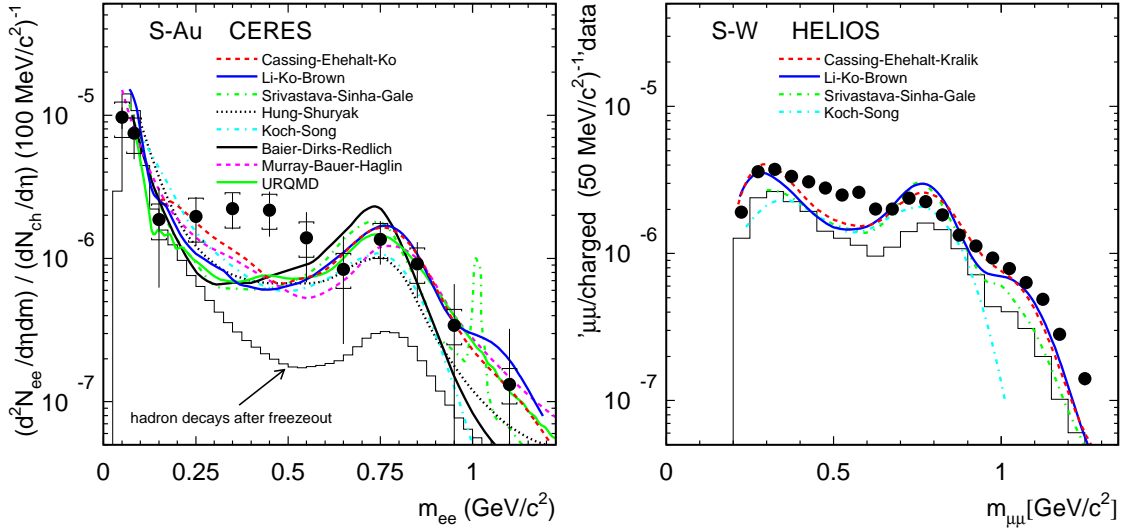


Figure 1.4: Dilepton invariant mass spectra as measured in central collisions of 200 AGeV sulfur nuclei with Au targets (left panel:  $e^+e^-$  spectra from CERES/NA45 [20]) and W targets (right panel:  $\mu^+\mu^-$  spectra from HELIOS-3 [24], no systematic errors included) as compared to a compilation [22] of theoretical calculations using free meson properties performed by Koch/Song [36], Li *et al.* [37], Cassing *et al.* [38, 39], Srivastava *et al.* [40], Baier *et al.* [41], the Frankfurt group [42], Hung/Shuryak [43] as well as Murray *et al.* [44]. The histograms indicate the hadron ‘cocktail’ of final state decays which gives a good description of the  $p$ - $A$  data as shown in Fig. 1.3.

medium effects that might be responsible for the observed enhancement. Among these, the ‘dropping’ vector meson mass scenario [37, 45, 46], as will be detailed below, provides an interesting possibility since it conjectures a direct link between hadron masses and the quark condensate and thus to the restoration of chiral symmetry towards the phase transition. When incorporated within a transport-theoretical treatment of the collision dynamics it is found to provide a unified description of both the CERES and HELIOS-3 data. Based on an interacting hadron gas many-body

approaches also seem to be able to describe the observed phenomena [47, 48, 49, 50]. Here the restoration of chiral symmetry manifests itself in more subtle ways which will be one of the key issues in our review.

More explicitly, the article is organized as follows: In Chapter 2 we will first recall some basic properties of strong interactions in the light-quark sector, with emphasis on the underlying symmetries of the QCD Lagrangian and their consequences in the nonperturbative regime, such as the emergence of quark and gluon condensates and the non-degeneracy of chiral partners in the hadronic spectrum. Special attention is paid to the vector and axialvector mesons as the former directly couple to dileptons. We then present model-independent methods to evaluate medium modifications of their spectral properties. Being based on virial expansions the results are in general restricted to low density and low temperature.

In Chapter 3 we move on to more specific model calculations that have been performed to assess medium modifications of vector and axialvector mesons. The presentation here concentrates on hadronic Lagrangians which can be classified into two categories, namely purely mesonic ones addressing temperature effects and those including the impact of finite baryon densities.

Chapter 4 starts out by discussing how hadronic models can be (and have been) subjected to empirical constraints that do *not* involve dilepton data in URHIC's. The philosophy here is to essentially fix the underlying model parameters to enable reliable predictions for thermal dilepton rates in hot and dense matter. In addition we will also discuss rate calculations within 'non-standard' (or non-hadronic) scenarios for highly excited strong-interaction matter that cannot be reliably founded on empirical information, such as Disoriented Chiral Condensates (DCC's) or thermal quark-antiquark annihilation. The main part of Chapter 4 is then devoted to a confrontation of the various model results within a detailed analysis of recent dilepton data taken in heavy-ion experiments at the BEVALAC and CERN-SpS. An additional crucial ingredient needed to do so is the description of the space-time collision dynamics, which thermal rates have to be convoluted over. We will briefly discuss three approaches, *i.e.*, relativistic hydrodynamics, transport simulations and more simplistic fireball expansions. Chapter 4 will end with a critical reassessment of the different mechanisms that have been invoked and outline possible theoretical implications for the nature of chiral symmetry restoration as indicative from the present status of the observed spectra.

Chapter 5 tries to summarize the major theoretical achievements in the field over the past five years or so. Based on these we will attempt to draw conclusions on our current understanding of the QCD phase transition in hot/dense matter as evidenced from the interplay of vigorous experimental and theoretical efforts in low-mass dilepton production.

## Chapter 2

# 'Strong QCD' and Vector Mesons

In the Standard Model (SM) of particle physics strong interactions are described by Quantum Chromodynamics (QCD), a local  $SU(3)$  gauge theory with quarks and gluons as elementary degrees of freedom [51]. The dynamics is governed by the QCD Lagrangian

$$\mathcal{L}_{\text{QCD}} = \bar{\psi}(i\gamma^\mu D_\mu - \mathcal{M}^\circ)\psi - \frac{1}{4}G_{\mu\nu}^a G_a^{\mu\nu} \quad (2.1)$$

with the non-abelian gluonic field-strength tensor given as

$$G_{\mu\nu}^a = \partial_\mu A_\nu^a - \partial_\nu A_\mu^a + igf^{abc}A_\mu^b A_\nu^c, \quad (2.2)$$

where  $A_\mu^a$  represents the spin-1 gauge field with color index  $a$  ( $a = 1, 8$ ). The gauge covariant derivative

$$D_\mu = \partial_\mu - ig(\lambda_a/2)A_\mu^a \quad (2.3)$$

induces a coupling between the spin-1/2, colored matter fields  $\psi$  of  $N_f$  flavors and the gauge fields  $A_\mu^a$  (with  $\lambda_a$  denoting the usual  $SU(3)$  Gell-Mann matrices).

In Eq. (2.1)  $\mathcal{M}^\circ$  represents the diagonal matrix of current quark masses,

$$\mathcal{M}^\circ = \begin{pmatrix} m_u & & & \\ & m_d & & \\ & & m_s & \\ & & & \ddots \end{pmatrix}, \quad (2.4)$$

which are parameters of the SM. With  $m_u, m_d, m_s \simeq 4, 7, 150$  MeV and  $m_c, m_b, m_t \simeq 1.5, 4.5, 175$  GeV there is an obvious separation into sectors of 'light' and 'heavy' quarks. For the discussion in the present article only the light-quark sector will be relevant.

To fully specify QCD we need to take account of the fact that – due to quantum-loop effects – the 'fine-structure constant'  $\alpha_s \equiv g^2/4\pi$  depends on the space-time distance or, equivalently, the four-momentum transfer  $Q$  of a given strong process,

$$\alpha_s(Q) = \frac{\alpha_s(\Lambda)}{1 + \alpha_s(\Lambda) \frac{33-2N_f}{12\pi} \ln\left(\frac{Q^2}{\Lambda^2}\right)}, \quad (2.5)$$

where  $\Lambda$  is a scale at which the coupling constant is to be fixed by experiment, *e.g.*,  $\alpha_s(M_Z) = 0.118$  at the  $Z$  boson mass  $M_Z = 91$  GeV (see Fig. 2.1). As  $Q$  increases  $\alpha_s$  decreases logarithmically

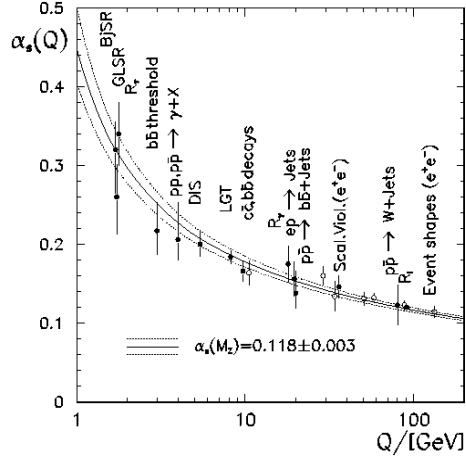


Figure 2.1: The 'running' of the strong coupling constant  $\alpha_s(Q)$  from various measurements compared to theory [52].

('asymptotic freedom') and perturbation theory can be applied. In this regime QCD is well tested. At momentum scales of  $Q \simeq 1$  GeV – a typical mass scale for 'light' hadrons – standard perturbation theory, however, breaks down due to a rapid increase of  $\alpha_s$ . This is the realm of 'strong QCD' where not only effective couplings but also the relevant degrees of freedom change with scale. It is this phenomenon that poses the most challenging intellectual problem in strong interaction theory and is subject to intense study via ab-initio lattice calculations and model building. At large distance scales the QCD degrees of freedom become encoded in colorless ('white') light mesons, low-mass baryons and glueballs rather than quarks and gluons. In dealing with their mutual interactions the underlying symmetries and anomalies of QCD are of utmost importance.

## 2.1 Symmetries and Anomalies of QCD

The structure of the lowest-mass hadrons – involving the light-quark sector comprised of  $u, d, s$  quarks – is largely determined by chiral symmetry [53] and its dynamical breaking in the physical vacuum with confinement presumably playing a much lesser role. This is evidenced from the dominant role of instantons – believed to be responsible for chiral symmetry breaking and other nonperturbative phenomena – in hadronic correlators [54]. Recent lattice QCD calculations with cooling algorithms corroborate such a picture [55].

Apart from invariance under local  $SU(3)_{\text{color}}$  transformations and a global  $U(1)$  symmetry, *i.e.*, multiplication of the matter fields  $\psi$  by a phase – entailing baryon number conservation – the QCD Lagrangian (2.1) has additional symmetries for vanishing quark masses. In this limit – well justified in the up- and down-quark sector and to a somewhat lesser extent in the strange-quark

sector – the theory is invariant under global vector and axialvector transformations in  $SU(3)$ -flavor space

$$\psi \rightarrow e^{-i\alpha_V^i \frac{\lambda_i}{2}} \psi, \quad \psi \rightarrow e^{-i\alpha_A^i \frac{\lambda_i}{2} \gamma_5} \psi \quad (2.6)$$

with conserved vector and axialvector Noether currents

$$j_{V,i}^\mu = \bar{\psi} \gamma^\mu \frac{\lambda_i}{2} \psi, \quad j_{A,i}^\mu = \bar{\psi} \gamma^\mu \gamma_5 \frac{\lambda_i}{2} \psi. \quad (2.7)$$

As a consequence, the corresponding charges

$$Q_i^V = \int d^3x \psi^\dagger \frac{\lambda_i}{2} \psi, \quad Q_i^A = \int d^3x \psi^\dagger \frac{\lambda_i}{2} \gamma_5 \psi \quad (2.8)$$

commute with the QCD Hamiltonian,  $[Q_i^{V,A}, H_{\text{QCD}}] = 0$ .

When decomposing the quark fields into left and right chirality components,  $\psi_{L,R} = \frac{1}{2}(1 \mp \gamma_5)\psi$ , the Lagrangian (2.1) takes the form

$$\mathcal{L}_{\text{QCD}} = \bar{\psi}_L i \gamma^\mu D_\mu \psi_L + \bar{\psi}_R i \gamma^\mu D_\mu \psi_R - \frac{1}{4} G_{\mu\nu}^a G_a^{\mu\nu} - (\bar{\psi}_L \mathcal{M}^\circ \psi_R + \bar{\psi}_R \mathcal{M}^\circ \psi_L) \quad (2.9)$$

and the transformations (2.6) translate to

$$\psi_L \rightarrow e^{-i\alpha_L^i \frac{\lambda_i}{2}} \psi_L, \quad \psi_R \rightarrow \psi_R \quad (2.10)$$

$$\psi_R \rightarrow e^{-i\alpha_R^i \frac{\lambda_i}{2}} \psi_R, \quad \psi_L \rightarrow \psi_L, \quad (2.11)$$

which – in the limit of vanishing quark masses – constitutes a global  $SU(3)_L \times SU(3)_R$  *chiral symmetry* in flavor space. Left- and right-handed quarks are not mixed dynamically and thus preserve their 'handedness' in strong interactions. The associated conserved charges

$$Q_i^L = \int d^3x \psi_L^\dagger \frac{\lambda_i}{2} \psi_L = \frac{1}{2}(Q_i^V - Q_i^A) \quad (2.12)$$

$$Q_i^R = \int d^3x \psi_R^\dagger \frac{\lambda_i}{2} \psi_R = \frac{1}{2}(Q_i^V + Q_i^A) \quad (2.13)$$

again commute with the QCD Hamiltonian.

For  $m_q = 0$ , the Lagrangian of QCD contains yet another symmetry. Under global  $U_A(1)$  (axial) transformations

$$\psi \rightarrow e^{-i\alpha \gamma_5} \psi \quad (2.14)$$

(2.1) is also invariant implying a conserved (singlet) Noether current of the form

$$j_{A,0}^\mu = \bar{\psi} \gamma^\mu \gamma_5 \psi. \quad (2.15)$$

However, in the full quantum theory the divergence of  $j_{A,0}^\mu$  has an anomaly

$$\partial_\mu j_{A,0}^\mu = \frac{3}{8} \alpha_s G_{\mu\nu}^a \tilde{G}_a^{\mu\nu}, \quad \tilde{G}_{\mu\nu}^a = \epsilon^{\mu\nu\alpha\beta} G_{\alpha\beta}^a, \quad (2.16)$$

– the  $U(1)_A$  axial anomaly – such that finally QCD is symmetric only under the group

$$SU(3)_L \times SU(3)_R \times U(1)_V . \quad (2.17)$$

This implies the conservation of the baryonic as well as the vector and axialvector currents.

Moreover, at the classical level, massless QCD is *scale invariant*. To see this consider a scale transformation in Minkowski space,

$$x^\mu \rightarrow x'^\mu = \lambda x^\mu . \quad (2.18)$$

Quantum fields scale as

$$\phi(x) \rightarrow \phi'(x) = \lambda^d \phi(\lambda x) , \quad (2.19)$$

where  $d = 3/2$  for fermions and  $d = 1$  for vector bosons. A field theory is called scale invariant if the action  $S$  remains invariant under scale transformations (2.18):

$$S' = \int d^4x \mathcal{L}'(x) = \int d^4x \lambda^4 \mathcal{L}(\lambda x) = S , \quad (2.20)$$

*i.e.*,  $\mathcal{L}$  scales as  $\lambda^4$ . Associated with scale invariance is another conserved current – the dilation (or scale) current –,

$$j_D^\mu = x_\nu T^{\mu\nu} , \quad \partial_\mu j_D^\mu = T_\mu^\mu = 0 , \quad (2.21)$$

where  $T^{\mu\nu}$  denotes the energy-momentum tensor of the theory. Considering classical quark and gluon fields and explicitly constructing  $T^{\mu\nu}$  it is easily verified that the dilation current of QCD is conserved.

As in the case of the axial anomaly, scale invariance is broken in the full quantum theory. Renormalization requires the introduction of a scale  $\Lambda$  resulting in a running coupling constant, Eq. (2.5). As a consequence the dilation current is no longer conserved. Including finite quark masses the full expression becomes

$$\partial_\mu j_D^\mu = \frac{\beta(\alpha_s)}{4\alpha_s} G_{\mu\nu}^a G_a^{\mu\nu} + (1 + \gamma) \bar{\psi} \mathcal{M}^\circ \psi , \quad (2.22)$$

where  $\beta(\alpha_s) = \Lambda d\alpha_s(\Lambda)/d\Lambda$  is the Gell-Mann-Low  $\beta$ -function of QCD and  $\gamma = d(\ln m_q(\Lambda))/d(\ln \Lambda)$  the anomalous dimension. Expanding the  $\beta$ -function in powers of  $\alpha_s$ ,

$$\beta(\alpha_s) = -(33 - 2N_f) \frac{\alpha_s^2}{6\pi} + O(\alpha_s^3) , \quad (2.23)$$

and keeping only the lowest term results in the operator identity [56]

$$T_\mu^\mu = -\frac{9}{8} G^2 + \bar{\psi} \mathcal{M}^\circ \psi , \quad (2.24)$$

where  $G^2 \equiv \frac{\alpha_s}{\pi} G_{\mu\nu}^a G_a^{\mu\nu}$  and the (small) anomalous dimension  $\gamma$  has been neglected.

## 2.2 Vacuum Condensates

In the physical vacuum quarks and gluons condense giving rise to nonvanishing vacuum expectation values  $\langle\bar{\psi}\psi\rangle$  [57, 58] and  $\langle G^2\rangle$  [59]. The physical mechanism is believed to be provided by instantons – semiclassical configurations of the gluon fields in 4-dimensional euclidean space [54]. The gluon condensate may be viewed as a strength parameter associated with nonperturbative scale breaking effects. A finite quark condensate implies that chiral symmetry is spontaneously broken. In mathematical terms the symmetry group (2.17) is broken down to

$$SU(3)_V \times U(1)_V . \quad (2.25)$$

The baryon and vector current remain conserved but the QCD vacuum is no longer symmetric under axialvector transformations (2.6). While the axial charges  $Q_k^A$  still commute with the QCD Hamiltonian the axial charge of the vacuum is nonvanishing:  $Q_k^A|0\rangle \neq 0$ . The situation is analogous to a ferromagnet which consists of separate domains of aligned spins. For a given domain rotational symmetry is partially broken in the ground state, although the Hamiltonian is rotationally invariant.

For the light meson spectrum spontaneous chiral symmetry breaking manifests itself in two ways:

- (i) the appearance of eight (nearly) massless Goldstone bosons (pions, kaons, eta) which interact weakly at low energies. The ferromagnetic analogy of Goldstone particles is the occurrence of a spin wave. For large wavelengths the spin configuration begins to resemble a uniform rotation of all the spins. In the limit of infinite wavelength this does not cost any energy, thus yielding a massless Goldstone mode.
- (ii) the absence of parity doublets, *i.e.*, the splitting of scalar and pseudoscalar, as well as vector and axialvector mesons. For massless fermions helicity eigenstates are also parity eigenstates. Were chiral symmetry unbroken one would expect degenerate hadronic isospin multiplets of opposite parity which is clearly not observed in nature as apparent from Fig. 2.2.

As a further consequence of chiral symmetry breaking the axial-current matrix element between the vacuum and a Goldstone boson is nonvanishing. For pions one has for instance:

$$\langle 0|j_{A,k}^\mu(x)|\pi_j(p)\rangle = -i\delta_{jk}f_\pi p^\mu e^{-ipx} , \quad (2.26)$$

and the pion decay constant  $f_\pi = 93$  MeV serves as an order parameter which measures the strength of the symmetry breaking. A second order parameter is the quark condensate

$$\langle\bar{\psi}\psi\rangle \equiv \langle 0|\bar{\psi}_L\psi_R + \bar{\psi}_R\psi_L|0\rangle , \quad (2.27)$$

which exhibits the explicit mixing of left- and right-handed quarks in the QCD vacuum. The order parameters  $f_\pi$  and  $\langle\bar{\psi}\psi\rangle$  are related. To see this one makes use of the operator identity

$$[Q_i^A, [Q_j^A, H_{QCD}]] = \delta_{ij} \int d^3x \bar{\psi}(x) \mathcal{M}^o \psi(x) . \quad (2.28)$$



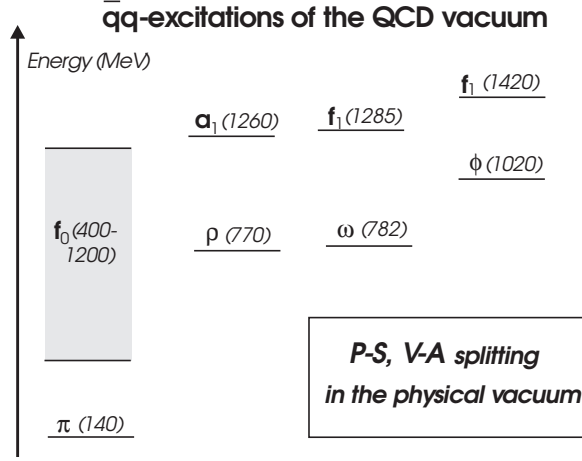


Figure 2.2: Experimentally observed spectrum of low-mass mesons.

Taking the vacuum matrix element and inserting a complete set of excited states  $|n\rangle$  one obtains the 'energy-weighted sum rule' [60]

$$\sum_n 2E_n |\langle n|Q_i^A|0\rangle|^2 = -\langle m_u \bar{u}u + m_d \bar{d}d \rangle = -2\bar{m} \langle \bar{q}q \rangle \quad (2.29)$$

where  $\bar{m}$  denotes the average of  $m_u$  and  $m_d$  and  $\langle \bar{q}q \rangle \equiv \langle \bar{u}u \rangle = \langle \bar{d}d \rangle$ . Upon saturating  $|n\rangle$  by single-pion states the Gell-Mann-Oakes-Renner relation (GOR) [58]

$$m_\pi^2 f_\pi^2 = -2\bar{m} \langle \bar{q}q \rangle \quad (2.30)$$

is obtained. Taking  $\bar{m} = 6$  MeV yields a value for the quark condensate,  $\langle \bar{q}q \rangle = -(240 \text{ MeV})^3 = -1.8 \text{ fm}^{-3}$ . Focusing on vector mesons a further order parameter can be specified as the difference between the vector and axialvector current correlators,  $\langle j_{V,k}^\mu(x) j_{V,k}^\mu(0) \rangle - \langle j_{A,k}^\mu(x) j_{A,k}^\mu(0) \rangle$ . It provides a direct link between chiral symmetry breaking and the spectral properties of vector and axialvector mesons and will be of most relevance in connection with dilepton production in heavy-ion experiments. Also this order parameter is related to  $f_\pi$  via 'Weinberg sum rules' as will be discussed later.

For the medium modification of the quark condensate it will be important to consider matrix elements of the operator identity (2.28) for a given hadron  $h$ . This defines the hadronic sigma commutator, or ' $\sigma$ -term'

$$\Sigma_h = \langle h|[Q_i^A, [Q_j^A, H_{\text{QCD}}]]h \rangle = \langle h|\bar{\psi} \mathcal{M}^\sigma \psi|h \rangle, \quad (2.31)$$

and the ratio  $\Sigma_h/\bar{m}$  has the physical interpretation of the scalar quark density inside the hadron  $h$ . By using the Feynman-Hellmann Theorem  $\Sigma_h$  can also be expressed in terms of the hadron mass as

$$\Sigma_h = m_q \frac{\partial m_h}{\partial m_q}. \quad (2.32)$$

From this relation and the GOR one immediately derives for the pion that  $\Sigma_\pi = m_\pi/2 = 69$  MeV, *i.e.*, the scalar quark density inside the pion is  $\Sigma_\pi/\bar{m} \simeq 12$ . This large value reflects the Goldstone nature of the pion in which quark-antiquark pairs are highly correlated. The sigma commutator for the nucleon can be inferred phenomenologically from low-energy pion-nucleon scattering [61] and has a value  $\Sigma_N \simeq 45 \pm 8$  MeV. In models such as the 'cloudy bag model' about 2/3 of this value originates from the virtual pion cloud around the nucleon [62, 63], again reflecting the collective nature of the pion.

## 2.3 In-Medium Condensates via Low-Density Expansions

It is to be expected that the quark and gluon condensates are modified at finite temperature,  $T$ , and quark chemical potential,  $\mu_q$ . To discuss these modifications we first recall some basic thermodynamics. The equilibrium properties of a given system of 3-volume  $V$  in contact with a reservoir are specified by the grand canonical partition function

$$\mathcal{Z}(V, T, \mu_q) = \text{Tr}\{e^{-(\hat{H}-\mu_q\hat{N})/T}\}, \quad (2.33)$$

where  $\hat{H}$  is the Hamiltonian and  $\hat{N}$  the quark number operator. The thermal average of any operator  $\mathcal{O}$  is then given as

$$\langle\langle\mathcal{O}\rangle\rangle = \mathcal{Z}^{-1} \sum_n \langle n|\mathcal{O}|n\rangle e^{-(E_n-\mu_q)/T}, \quad (2.34)$$

where the sum extends over a complete set of eigenstates of  $H$  and  $E_n$  are the corresponding eigenvalues. When applied to the QCD condensates one has

$$\langle\langle\bar{\psi}\psi\rangle\rangle = \mathcal{Z}^{-1} \sum_n \langle n|\bar{\psi}\psi|n\rangle e^{-(E_n-\mu_q)/T} \quad (2.35)$$

and

$$\langle\langle G^2\rangle\rangle = \mathcal{Z}^{-1} \sum_n \langle n|G^2|n\rangle e^{-(E_n-\mu_q)/T}, \quad (2.36)$$

where  $|n\rangle$  and  $E_n$  are now the exact QCD eigenstates and energies. The equation of state (EoS) can be directly obtained from the logarithm of  $\mathcal{Z}$ . The free energy density is given as

$$\Omega = -\frac{T}{V} \ln \mathcal{Z}, \quad (2.37)$$

while the energy density and pressure are derivatives of  $\ln \mathcal{Z}$  with respect to  $T$  and  $V$ ,

$$\epsilon = \frac{T^2}{V} \left( \frac{\partial \ln \mathcal{Z}}{\partial T} \right)_{V, N} + \mu_q \frac{N}{V} \quad (2.38)$$

$$p = T \left( \frac{\partial \ln \mathcal{Z}}{\partial V} \right)_{T, N}. \quad (2.39)$$

In the thermodynamic limit ( $V \rightarrow \infty$ ;  $N/V = \text{const}$ ) the pressure is directly given by the free energy density as

$$p = -\Omega . \quad (2.40)$$

In fact, the state variables of the EoS determine directly the condensates. The quark condensate is obtained as the derivative of the free energy density (or pressure) with respect to the current quark mass,

$$\langle \bar{\psi}\psi \rangle = \frac{\partial \Omega}{\partial m_q} = -\frac{\partial p}{\partial m_q} . \quad (2.41)$$

This is analogous to a spin system in an external magnetic field, where, in QCD, the role of the latter is played by the quark mass. To relate the gluon condensate to the thermodynamic variables one should notice that the thermal average of the trace of the energy-momentum tensor is given by

$$\langle\langle T_\mu^\mu \rangle\rangle = \epsilon - 3p . \quad (2.42)$$

From Eq. (2.24) we then have

$$\langle\langle G^2 \rangle\rangle = -\frac{8}{9} \left[ (\epsilon - 3p) + m_q \frac{\partial p}{\partial m_q} \right] . \quad (2.43)$$

Model-independent results for the changes of the quark and gluon condensate can be obtained at low temperatures and small baryon densities. In both cases one deals with a low-density gas of confined hadrons. It is therefore appropriate to evaluate the thermal averages (2.35) and (2.36) in a hadronic basis including the vacuum as well as the lowest-mass mesons and baryons. As the temperature increases pions are thermally excited first since they represent the lightest hadrons. Considering a dilute, non-interacting pion gas, the leading correction to the vacuum condensate  $\langle \bar{\psi}\psi \rangle$  is therefore given by the matrix element  $\langle \pi | \bar{\psi}\psi | \pi \rangle$ , and from (2.30) and (2.32) it is easily worked out that the condensate ratio becomes

$$\frac{\langle\langle \bar{\psi}\psi \rangle\rangle}{\langle \bar{\psi}\psi \rangle} \simeq 1 - \frac{\Sigma_\pi \varrho_\pi^s(T)}{f_\pi^2 m_\pi^2} , \quad (2.44)$$

where  $\Sigma_\pi$  denotes the pion  $\sigma$ -term and  $\varrho_\pi^s$  the pion scalar density at given temperature. This expression is consistent with Eq. (2.41) when using the free energy density of a non-interacting Bose gas and the  $\sigma$ -term as the quark-mass derivative (2.32). A similar argument holds for finite baryon density and vanishing temperature. In this case nucleons give the dominant correction to  $\langle \bar{\psi}\psi \rangle$  and

$$\frac{\langle\langle \bar{\psi}\psi \rangle\rangle}{\langle \bar{\psi}\psi \rangle} \simeq 1 - \frac{\Sigma_N \varrho_N^s(\mu_N)}{f_\pi^2 m_\pi^2} , \quad (2.45)$$

where  $\Sigma_N$  is the nucleon  $\sigma$ -term and  $\varrho_N^s$  the nucleon scalar density at given  $\mu_q$  (the nucleon chemical potential is related to the one of quarks by simply  $\mu_N = 3\mu_q$ ). Since nucleons are heavy the scalar density is nearly equal to the number density,  $\varrho_N$ . The underlying physical picture that emerges from the low-density expansion is very simple. Whenever a hadron is created in the vacuum, the condensate is changed locally since the  $\bar{\psi}\psi$ -expectation value inside a hadron is different from that of the vacuum.

Let us now turn to the low-density expansion of the gluon condensate. At finite temperature the leading correction to the vacuum condensate should again be given by non-interacting pions. Since  $G^2$  is a chiral singlet its one-pion matrix element vanishes and there is no contribution from the ideal pion gas. At finite baryon density the situation is different. First we note that the nucleon mass is determined by  $T_\mu^\mu$  as

$$\langle N|T_\mu^\mu|N\rangle = m_N\bar{\psi}_N\psi_N = \left[-\frac{9}{8}\langle N|G^2|N\rangle + \langle N|\bar{\psi}\mathcal{M}^o\psi|N\rangle\right]\bar{\psi}_N\psi_N, \quad (2.46)$$

where  $\psi_N$  represents the nucleon spinor and the operator identity (2.24) has been used. According to (2.32) the term proportional the quark mass,  $m_q$ , is nothing but the nucleon  $\sigma$ -term which is about 45 MeV. Thus the bulk of the nucleon mass is in fact generated by the gluon field. Putting things together the leading correction to the gluon condensate arises from finite baryon density such that

$$\langle\langle G^2\rangle\rangle - \langle G^2\rangle = -\frac{8}{9}m_N^{(0)}\varrho_N^s(\mu_N), \quad (2.47)$$

where  $m_N^{(0)}$  denotes the contribution of the nucleon mass from the  $G^2$  matrix element.

One important conclusion which can be drawn from the above arguments is that, in spite of changing condensates, the properties of the involved hadrons by definition remain unchanged to lowest order.

At vanishing baryon density interactions in the pion gas can be included via chiral perturbation theory leading to a rigorous low-temperature expansion of the condensates [64, 65, 66]. The starting point are the thermodynamic relations (2.41) and (2.43). For simplicity we restrict ourselves to the chiral limit,  $m_q \rightarrow 0$ . In this case the leading contribution to  $p$  or  $\epsilon$  is from the massless ideal Bose gas which is of order  $O(T^4)$ . The interactions among the Goldstone bosons only show up at order  $O(T^8)$  such that

$$p = \frac{\pi^2}{90}(N_f^2 - 1)T^4 \left[1 + N_f^2 \left(\frac{T^2}{12f_G^2}\right)^2 \ln\left(\frac{\Lambda_p}{T}\right)\right] + O(T^{10}), \quad (2.48)$$

where  $f_G$  denotes the weak-decay constant of the Goldstone boson in the chiral limit and  $\Lambda_p$  appearing in the chiral logarithm is the regularization scale. There is no  $T^6$ -term since – in the chiral limit – the forward scattering amplitude for two Goldstone bosons vanishes. The quark-mass derivative occurring in (2.41) can be rewritten in terms of a derivative *w.r.t.* the mass of the Goldstone boson,  $m_G$ , and by means of the Gell-Mann-Oakes-Renner relation,

$$\frac{\langle\langle\bar{\psi}\psi\rangle\rangle}{\langle\bar{\psi}\psi\rangle} = 1 + \frac{1}{f_G^2} \frac{\partial p}{\partial m_G^2}. \quad (2.49)$$

Injecting the expression (2.48) for the pressure one arrives at

$$\frac{\langle\langle\bar{\psi}\psi\rangle\rangle}{\langle\bar{\psi}\psi\rangle} = 1 - \frac{(N_f^2 - 1)}{N_f} \frac{T^2}{12f_G^2} + \frac{(N_f^2 - 1)}{2N_f} \left(\frac{T^2}{12f_G^2}\right)^2 - N_f(N_f^2 - 1) \left(\frac{T^2}{12f_G^2}\right)^3 \ln\left(\frac{\Lambda_q}{T}\right) + O(T^8). \quad (2.50)$$

While the  $T^2$ - and  $T^4$ -terms are model-independent, model dependence enters at order  $O(T^6)$  through the regularization scale  $\Lambda_q$  which is related to  $\Lambda_p$  as [66]

$$\ln\left(\frac{\Lambda_q}{\Lambda_p}\right) = \frac{N_f^2 + 1}{6N_f^4} + 0.491 . \quad (2.51)$$

The numerical value  $\Lambda_q \simeq 470$  MeV ( $N_f = 2$ ) is determined by the isoscalar  $D$ -wave  $\pi\pi$  scattering length. For two flavors the temperature scale is set by  $\sqrt{8}f_\pi \simeq 260$  MeV. To derive a low-temperature expansion for the gluon condensate from (2.43) one uses the fact that

$$\langle\langle T_\mu^\mu \rangle\rangle = \epsilon - 3p = T^5 \frac{d}{dT} \left( \frac{p}{T^4} \right) , \quad (2.52)$$

from which  $\langle\langle G^2 \rangle\rangle$  can be expressed in terms of the Bose gas pressure alone. The use of Eq. (2.48) leads to

$$\langle\langle G^2 \rangle\rangle - \langle G^2 \rangle = -\frac{\pi^2}{3240} N_f^2 (N_f^2 - 1) \frac{T^8}{f_G^4} \left[ \frac{\Lambda_p}{T} - \frac{1}{4} \right] + \dots . \quad (2.53)$$

The leading  $O(T^8)$ -behavior is easily understood from the observation that to order  $O(T^4)$  one has a massless ideal Bose gas for which  $\epsilon = 3p$  and hence  $\langle\langle T_\mu^\mu \rangle\rangle = 0$ . This is in agreement with the fact that a free gas of massless particles is scale invariant. The change in the gluon condensate arises solely on account of the interaction of Goldstone bosons which is not scale invariant. The high power of  $T$  implies that the gluon condensate 'melts' much more slowly than the quark condensate.

## 2.4 Lattice Results

Obviously the low-density expansion of  $\langle\langle \bar{\psi}\psi \rangle\rangle$  and  $\langle\langle G^2 \rangle\rangle$  discussed in the previous section is of limited validity and cannot address the nature of the QCD phase transition. The low-temperature expansion is restricted to below  $T \simeq 120$  MeV, mostly because at this point heavier mesons start to enter [65]. For finite  $\varrho_N$  and vanishing  $T$  the dilute gas expression (2.45) predicts a decrease of the chiral condensate ratio which is linear in the number density. At nuclear saturation density,  $\varrho_0 = 0.16 \text{ fm}^{-3}$ , this yields a  $\sim 30$  % drop and a naive extrapolation would indicate chiral restoration at  $\varrho_c \simeq 3\varrho_0$ . This clearly cannot be trusted, since the EoS of nuclear matter greatly differs from that of a free Fermi gas at such high densities. Going beyond the dilute gas limit by using a realistic EoS it has been found [67] that deviations from the dilute gas set in slightly above  $\varrho_0$ .

In the vicinity of the phase boundary nonperturbative methods are needed. Even though many-body approaches [68] and renormalization-group techniques [69] are quite promising the most stringent framework is lattice QCD. Here the aim is an ab-initio understanding of the quark-hadron transition by evaluating the partition function (2.33) of QCD numerically. Because of technical difficulties this has been achieved, so far, only at vanishing baryon density.

In a theory of interacting boson fields  $\phi$  and fermion fields  $\psi$  in contact with a heat bath the partition function  $\mathcal{Z}$  at vanishing  $\mu_q$  is given by the finite-temperature path integral

$$\mathcal{Z}(V, T) = \int \mathcal{D}\phi \mathcal{D}\psi \mathcal{D}\bar{\psi} e^{-S^E(\phi, \psi, \bar{\psi})} \quad (2.54)$$

involving the euclidean action

$$S^E(\phi, \psi, \bar{\psi}) = \int_0^{T^{-1}} d\tau \int_V d^3x \mathcal{L}^E(x) , \quad (2.55)$$

where  $x = (\vec{x}, \tau)$  with  $\tau = it$  and  $\mathcal{L}^E$  denotes the imaginary-time Lagrange density. The boson (fermion) fields obey periodic (antiperiodic) boundary conditions [70]. The thermal expectation value of a given operator  $\mathcal{O}$  is given as an ensemble average

$$\begin{aligned} \langle\langle \mathcal{O} \rangle\rangle &= \frac{1}{\mathcal{Z}} \text{tr}\{e^{-(\hat{H}-\mu_q \hat{N})/T} \mathcal{O}\} \\ &= \frac{1}{\mathcal{Z}} \int \mathcal{D}\phi \mathcal{D}\psi \mathcal{D}\bar{\psi} \mathcal{O}(\phi, \psi, \bar{\psi}) e^{-S^E(\phi, \psi, \bar{\psi})} , \end{aligned} \quad (2.56)$$

and the field theory has been turned into a statistical mechanics problem.

For QCD the euclidean Lagrange density is given by (cf. Eq. (2.1))

$$\mathcal{L}_{QCD}^E(x) = \bar{\psi}(x)(-i\gamma_\mu D_\mu - i\mathcal{M}^\circ)\psi(x) + \frac{1}{4}G_{\mu\nu}^a(x)G_{\mu\nu}^a(x) \quad (2.57)$$

with the euclidean Dirac matrices obeying  $\{\gamma_\mu, \gamma_\nu\} = 2\delta_{\mu\nu}$ . The corresponding euclidean action is obtained as

$$S_{QCD}^E(A_\mu, \psi, \bar{\psi}) = \int_0^{T^{-1}} d\tau \int_V d^3x \mathcal{L}_{QCD}^E(x) . \quad (2.58)$$

For a numerical evaluation of the partition function  $\mathcal{Z}_{QCD}$  via the path integral a hypercubical lattice of spacing  $a$  with  $N_s$  lattice points in each spatial direction and  $N_\tau$  points in the temporal direction is introduced. Temperature and volume are related to the lattice size,  $N_s^3 \times N_\tau$ , as

$$T^{-1} = N_\tau a , \quad V = (N_s a)^3 , \quad (2.59)$$

and the temperature and volume derivatives are replaced according to

$$\begin{aligned} \frac{\partial}{\partial T} &\rightarrow \frac{1}{N_\tau} \frac{\partial}{\partial a} \\ \frac{\partial}{\partial V} &\rightarrow \frac{1}{3a^2 N_s^3} \frac{\partial}{\partial a} . \end{aligned} \quad (2.60)$$

Because of the scale dependence of  $\alpha_s$ , Eq. (2.5), the lattice spacing becomes a function of the bare gauge coupling  $\beta \equiv 6/g^2$  which fixes the temperature and the physical volume at a given coupling. The next step is to discretize the euclidean QCD action (2.58). Two requirements have to be met. The first is the correct continuum form of the action in the limit  $a \rightarrow 0$ . The second is local gauge invariance. To proceed one considers the 'Schwinger line integral'

$$U^\mu(x) = e^{ig \int_x^{x+a\hat{\mu}} dy A_\mu(x+y)} \quad (2.61)$$

rather than the gauge field  $A_\mu$ . In terms of  $U^\mu$  the QCD partition function is expressed as

$$\mathcal{Z}_{QCD} = \int \mathcal{D}U \mathcal{D}\psi \mathcal{D}\bar{\psi} e^{-S_{QCD}^E(U, \psi, \bar{\psi})}. \quad (2.62)$$

The discretization of the field variables  $U^\mu(x) \rightarrow U_n^\mu$  and  $\psi(x) \rightarrow \psi_n$  turns the line integral into a 'link variable' which connects lattice site  $n$  to its neighbor  $n + \hat{\mu}$ . The quark fields are defined on the lattice sites  $n$ .

In the Wilson formulation [71] the gluonic part of the action,  $S_G = \int \frac{1}{4} (G_{\mu\nu}^a)^2$ , is expressed in terms of elementary plaquettes

$$U_\square \equiv U_n^\mu U_{n+\hat{\mu}}^\nu U_{n+\hat{\mu}}^{\mu\dagger} U_n^{\nu\dagger}, \quad (2.63)$$

which constitute the smallest closed path starting from lattice site  $n$ . In terms of these plaquettes one has

$$S_G^E = \beta \sum_\square (1 - \frac{1}{3} \text{ReTr} U_\square), \quad (2.64)$$

where the sum runs over all possible plaquettes. For small  $a$

$$S_G^E = \frac{\beta g^2}{12} \sum_n a^4 (\text{Tr} G_{\mu\nu}(n) G_{\mu\nu}(n) + \mathcal{O}(a^2)), \quad (2.65)$$

which extrapolates to the proper continuum limit with  $\beta = 6/g^2$  and hence satisfies both requirements of the lattice action.

To find an appropriate form for the fermionic part is more difficult. A naive discretization of the continuum Dirac action,

$$S_F^E = \int_0^{T^{-1}} d\tau \int_V d^3x \bar{\psi}(x) (\gamma_\mu D_\mu + \mathcal{M}^\circ) \psi(x), \quad (2.66)$$

leads to a lattice action

$$S_F^E = \sum_{n,m} a^4 \bar{\psi}_n K_{nm}[U] \psi_m, \quad (2.67)$$

where

$$\begin{aligned} K_{nm} &= \gamma_\mu D_{\mu,nm} + \mathcal{M}^\circ \delta_{nm} \\ D_{\mu,nm} &= \frac{1}{2a} \{ U_n^\mu \delta_{n+\hat{\mu},m} - U_{n-\hat{\mu}}^{\mu\dagger} \delta_{n-\hat{\mu},m} \}. \end{aligned} \quad (2.68)$$

In the continuum limit it describes  $2^4 = 16$  fermion species rather than one. This fermion doubling per field component has its origin in the first derivative occurring in the Dirac equation. To remove the spurious degeneracy two methods have been proposed: Wilson fermions [71] in which the naive lattice action is supplemented by an extra term which ensures that in the continuum limit the extra 15 species are removed. It has the disadvantage that the numerical realization of the chiral limit  $m_q \rightarrow 0$  is extremely time consuming. In studies which focus on the chiral phase transition the method of staggered fermions [72] is more suitable. Here the unwanted fermions are removed

by doubling the effective lattice spacing: two separate fermion fields are introduced for even and odd lattice sites, which in the continuum limit are associated with the upper-two and lower-two components of the 4-component Dirac spinor, *i.e.*, the quark fields  $\psi$  can be reconstructed by suitable linear combination on hypercubes of length  $2a$ . More recently, another promising method called 'domain wall fermions' has been developed to treat fermions in discretized vector gauge theories [73]. Here, a fifth dimension (in addition to 4-dimensional space-time) is introduced, and the low-lying (zero mode) fermion states are localized on 'domain walls' in this extra dimensions. This method has the attractive feature that – contrary to staggered or Wilson fermions – the full chiral symmetry of QCD is preserved to a high accuracy in its discretized version.

On a finite lattice the QCD partition function finally takes the form

$$\mathcal{Z}_{QCD} = \int \prod_{n,\mu} dU_n^\mu \prod_{n_1} d\bar{\psi}_{n_1} \prod_{n_2} d\psi_{n_2} e^{-S_{QCD}^E(U_n^\mu, \bar{\psi}_{n_1}, \psi_{n_2})}. \quad (2.69)$$

In contrast to the symbolic notation in Eq. (2.62) the measure  $\mathcal{D}U\mathcal{D}\bar{\psi}\mathcal{D}\psi \equiv \Pi dU \Pi d\bar{\psi} \Pi d\psi$  now has a well-defined meaning:  $dU_n^\mu$  refers to the measure on the  $SU(3)$  gauge group while  $d\psi$ ,  $d\bar{\psi}$  are the usual measures over Grassmann variables on site  $n$ .

The discretized fermion fields appear quadratic in the action and can therefore be integrated out to yield

$$\int \prod_{n_1} d\bar{\psi}_{n_1} \prod_{n_2} d\psi_{n_2} e^{S_F^E[U_n^\mu, \bar{\psi}_{n_1}, \psi_{n_2}]} = \det K[U]. \quad (2.70)$$

Thus the QCD partition function is given by a path integral solely over gauge fields  $U$

$$\mathcal{Z}_{QCD} = \int \prod_{n,\mu} dU_n^\mu e^{-S_G^E(U_n^\mu)} \det K[U]. \quad (2.71)$$

When factorizing out the quark mass dependence in the matrix  $K_{nm}$  (2.68) as

$$K_{nm} = m_q \left( \frac{1}{m_q} \gamma_\mu D_{nm}^\mu + 1 \delta_{n,m} \right), \quad (2.72)$$

one sees that in the limit of large quark masses ( $m_q \rightarrow \infty$ ) the term involving the covariant derivative gives a negligible contribution and the Grassmann integration (2.70) becomes a pure Gaussian integral. This results in a constant multiplicative factor in the partition function which cancels out in the expectation values of operators,  $\langle\langle \mathcal{O} \rangle\rangle$ . Thus the limit of large  $m_q$  reduces to a pure gauge theory and is referred to as the 'quenched approximation'. Physically it corresponds to the omission of vacuum polarization effects via quark loops.

Although in principle the condensates and the EoS can be derived from the free energy density as discussed in Sect. 2.3, in practice a direct computation of the partition function is rather difficult. Instead one calculates the expectation value of the action by taking the derivative of  $\ln \mathcal{Z}_{QCD}$  with respect to the bare gauge coupling  $\beta$  and the bare quark masses  $m_q$ . In this way the pressure, the energy density and the condensates are obtained by proper extrapolation to the continuum limit  $a \rightarrow 0$  via a renormalization group analysis on the lattice.

Recent two-flavor results for  $\epsilon$ ,  $p$  and the so-called 'interaction measure'  $\Delta \equiv (\epsilon - 3p)/T^4 = \langle\langle T_\mu^\mu \rangle\rangle/T^4$  are shown in Fig. 2.3. One observes a rapid rise in  $\epsilon$  (left panel) above a critical coupling



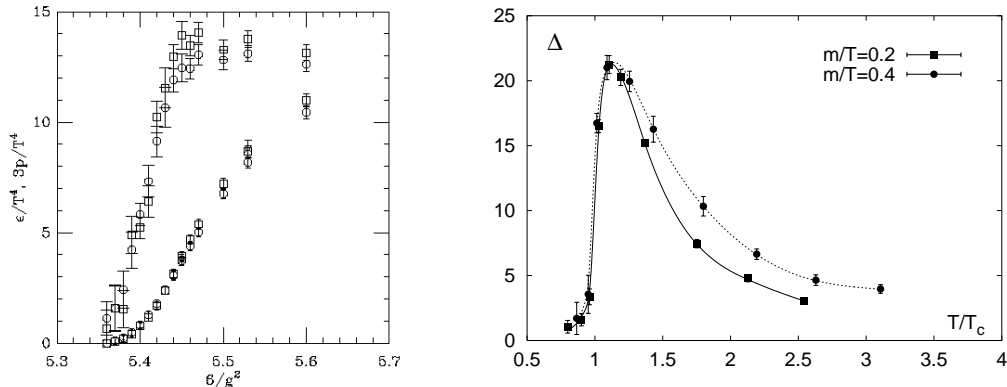


Figure 2.3: Left panel: the energy density  $\epsilon/T^4$  and  $3p/T^4$  as a function of  $\beta = 6/g^2$  [74]. The lattice data are for  $am_q = 0.0125$ . Right panel: the interaction measure  $\Delta$  as a function of  $T/T_c$  [75].

of  $\beta_c = 5.36$  roughly reaching the continuum Stephan-Boltzmann limit at the last data point. The critical coupling of  $\beta_c = 5.36$  translates to a transition temperature  $T_c = 140$  MeV. On the other hand, the pressure rises much more slowly such that  $\Delta$  remains large above the transition (right panel). This implies that above  $T_c$  the system is far from being ideal. However, the entropy density quickly approaches that of an ideal gas of quarks and gluons. A natural interpretation of this feature is that the dominant part of the nonperturbative pressure is provided by the remnant of the (vacuum) gluon condensate [76], which persists across the transition to a substantial extent (see below). Thus, above  $T_c$  one might indeed have a deconfined plasma of weakly interacting quarks and gluons in the background of a residual 'bag' pressure.

Lattice results for the condensates  $\langle\langle\bar{\psi}\psi\rangle\rangle$  and  $\langle\langle G^2\rangle\rangle$  are shown in Fig. 2.4. The condensate ratio stays basically flat up to about  $0.9 T_c$  after which it rapidly decreases. At first sight the relative constancy at small temperatures is at variance with the rigorous result from chiral perturbation theory which predicts a  $T^2$ -dependence of the condensate ratio. It should, however, be realized that the lattice results are not in the chiral limit. Instead the simulations implicitly contain a rather 'heavy pion' with a mass of roughly twice the physical mass. This explains the apparent differences with chiral perturbation theory. The temperature dependence of the gluon condensate can be inferred from the interaction measure  $\Delta$  and the quark condensate via the relations (2.43) and (2.41). The right panel of Fig. 2.4 displays results for two flavors (solid squares) and for four flavors (open squares) while the dashed line shows the condensate in the quenched approximation rescaled by the number of degrees of freedom. While the condensate remains essentially unchanged below  $T_c$  which is consistent with the  $T^8$ -dependence predicted from chiral perturbation theory, there is a rapid decrease slightly above  $T_c$  and the condensate eventually turns negative around  $T = 200$  MeV. Asymptotic freedom implies that the effects of nonperturbative scale breaking disappear at high temperature where perturbation theory should become reliable. Intuitively one

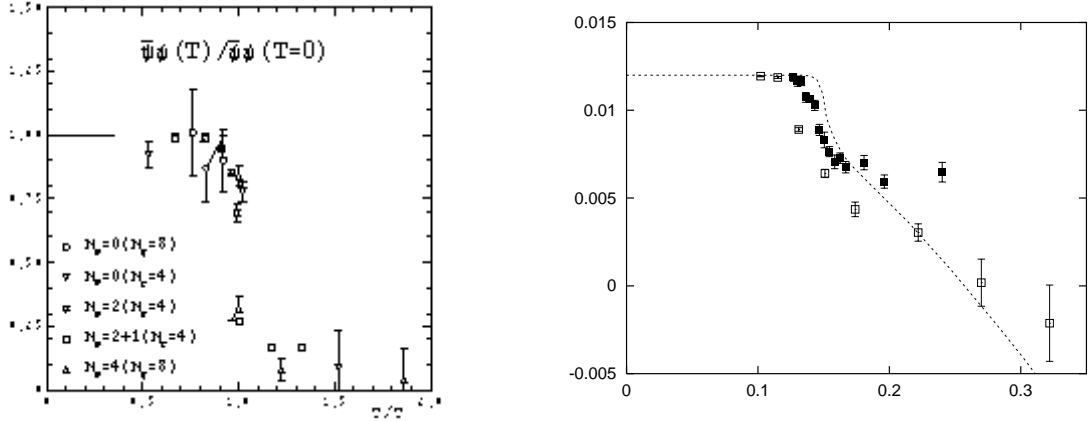


Figure 2.4: Left panel: the quark condensate ratio  $\langle\langle\bar{\psi}\psi\rangle\rangle/\langle\langle\bar{\psi}\psi\rangle\rangle(T=0)$  as a function of  $T/T_c$  [77]; right panel: the temperature dependence of the gluon condensate [75].

might therefore expect the gluon condensate to vanish at high temperature in accordance with the notion of an ideal quark-gluon plasma. As the lattice results (as well as chiral perturbation theory) show, this is however not the case. Scale invariance remains broken also in the high-temperature phase. This is related to the scale dependence of the running coupling constant (2.5). Identifying the scale with  $T$  introduces  $1/\ln(T)$  corrections to the pressure such that at high temperatures  $\langle\langle T_\mu^\mu\rangle\rangle$  is of order  $T^4/(\ln T)^2 \propto g^4 T^4$  [66]. While small compared to the energy density of the plasma,  $\langle\langle T_\mu^\mu\rangle\rangle$  itself grows without bounds as the temperature rises such that the gluon condensate does not disappear but becomes negative and large.

As a further result of lattice QCD we discuss the temperature dependence of 'screening masses' which will become relevant for the later discussion of axial-/vector correlation functions. In general screening masses are extracted from the ensemble averaged current-current correlation functions  $\langle\langle j_\mu(x)j_\mu(0)\rangle\rangle$  where the appropriate currents are denoted generically by  $j_\mu(x)$ . In practical calculations these correlation functions are evaluated for spatial separations  $r$ . For large  $r$  they show exponential behavior

$$\langle\langle j_\mu(x)j_\mu(0)\rangle\rangle \rightarrow e^{-m_h r}, \quad (2.73)$$

from which the (screening) masses of the lowest-energy hadron in the appropriate channel can be extracted numerically. Fig. 2.5 displays results for the screening masses of the  $\rho$  and  $a_1$  meson. As dictated by spontaneous chiral symmetry breaking they are different in the physical vacuum. At the chiral transition they are found to be degenerate. The point of degeneracy coincides with the transition temperature for the melting of the condensate. The screening masses need not necessarily correspond to the 'pole masses' in the propagators of the  $\rho$  and  $a_1$  meson but rather represent the 'centroids' of the in-medium vector and axialvector spectral functions. The spectral distributions themselves are likely to be quite complicated with significant reshaping, *e.g.*, a strong

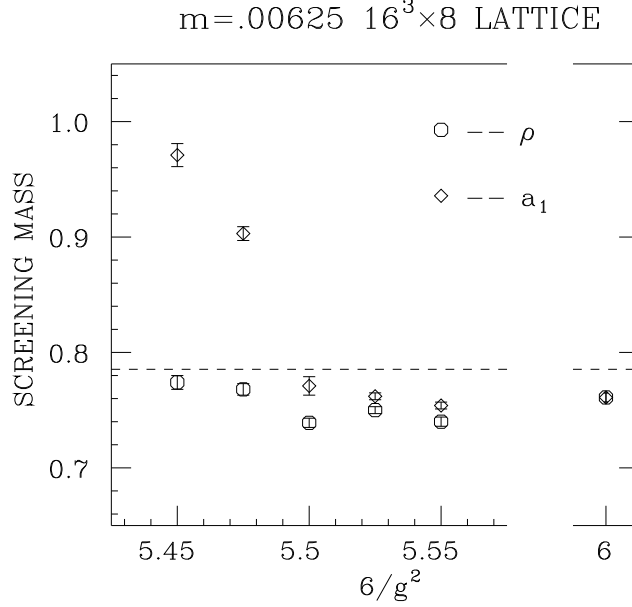


Figure 2.5: The temperature dependence of the  $\rho$  and  $a_1$  screening masses. The results are taken from Ref. [78].

broadening as emerging in models of an interacting hadron gas, to be discussed later.

## 2.5 Dilepton Production and Vector Mesons

As mentioned in the Introduction dileptons probe all stages in the course of a heavy-ion reaction. The most interesting hot and dense phase emits low-mass dileptons predominantly from thermal annihilation processes such as quark-antiquark or pion and kaon annihilation.

The thermal rate for the production of dileptons at four-momentum  $q$  from a heat bath at temperature  $T$  is given by [8, 19]

$$\frac{d^8 N_{l+l^-}}{d^4 x d^4 q} \equiv \frac{d^4 R}{d^4 q} = L^{\mu\nu}(q) W_{\mu\nu}(q), \quad (2.74)$$

where to lowest order in the electromagnetic coupling,  $\alpha=1/137$ , the lepton tensor is obtained as

$$\begin{aligned} L_{\mu\nu}(q) &= \frac{(4\pi\alpha)^2}{M^4} \int \frac{d^3 p_+}{(2\pi)^3 2p_{0,+}} \frac{d^3 p_-}{(2\pi)^3 2p_{0,-}} \text{tr}[(\not{p}_+ - m)\gamma_\mu(\not{p}_- + m)\gamma_\nu] \delta^{(4)}(q - p_+ - p_-) \\ &= -\frac{\alpha^2}{6\pi^3 M^2} \left( g_{\mu\nu} - \frac{q_\mu q_\nu}{M^2} \right) \end{aligned} \quad (2.75)$$

with  $p_{0,\pm} = (m_{l\pm}^2 + \vec{p}_{\pm}^2)^{1/2}$ . For simplicity we will focus on the  $e^+e^-$  case and thus neglect the rest mass of the leptons as compared to their individual 3-momenta  $|\vec{p}_+|, |\vec{p}_-|$ .  $M^2 = (p_+ + p_-)^2$  is the total four-momentum of the pair in the heat bath. The effect of the hadronic medium is encoded in the hadron tensor  $W_{\mu\nu}(q)$ . It is obtained from the thermal average of the electromagnetic current-current correlation function as [8, 19]

$$W_{\mu\nu}(q) = \int d^4x e^{-iqx} \langle\langle j_{\mu}^{\text{em}}(x) j_{\nu}^{\text{em}}(0) \rangle\rangle, \quad (2.76)$$

where the average is taken in the grand canonical ensemble. For invariant masses below the charm threshold ( $M < 2m_c \simeq 3 \text{ GeV}$ ) the current can be decomposed as

$$j_{\mu}^{\text{em}} = \frac{2}{3} \bar{u} \gamma_{\mu} u - \frac{1}{3} \bar{d} \gamma_{\mu} d - \frac{1}{3} \bar{s} \gamma_{\mu} s. \quad (2.77)$$

With the identification

$$j_{\mu}^{\text{em}} = j_{\mu}^{\rho} + j_{\mu}^{\omega} + j_{\mu}^{\phi} \quad (2.78)$$

$$j_{\mu}^{\rho} = \frac{1}{2} (\bar{u} \gamma_{\mu} u - \bar{d} \gamma_{\mu} d) \quad (2.79)$$

$$j_{\mu}^{\omega} = \frac{1}{6} (\bar{u} \gamma_{\mu} u + \bar{d} \gamma_{\mu} d) \quad (2.80)$$

$$j_{\mu}^{\phi} = -\frac{1}{3} (\bar{s} \gamma_{\mu} s), \quad (2.81)$$

its flavor content can be expressed in physical channels with the quantum numbers of the  $\rho$ ,  $\omega$  and  $\phi$  meson.

For an ideal plasma of quarks and gluons at finite temperature and vanishing chemical potential the rate (2.74) is readily evaluated. Applying lowest-order perturbation theory and integrating over the three-momentum of the dilepton pair one obtains the familiar expression

$$\frac{dR^q}{dM^2} = R^q \frac{\alpha^2}{6\pi^2} M T K_1(M/T) \quad (2.82)$$

where  $K_1(M/T)$  denotes a modified Bessel function and  $R^q$  involves the sum over squared quark charges and the number of colors,

$$R^q = N_c \sum_f e_f^2 = 3 \left( \frac{4}{9} + \frac{1}{9} + \frac{1}{9} \right). \quad (2.83)$$

A similar expression can be derived for an ideal resonance gas at finite temperature:

$$\frac{dR^h}{dM^2} = R^h(M) \frac{\alpha^2}{6\pi^2} M T K_1(M/T), \quad (2.84)$$

where

$$R^h = \frac{\sigma(e^+e^- \rightarrow \text{hadrons})}{\sigma(e^+e^- \rightarrow \mu^+\mu^-)} \quad (2.85)$$

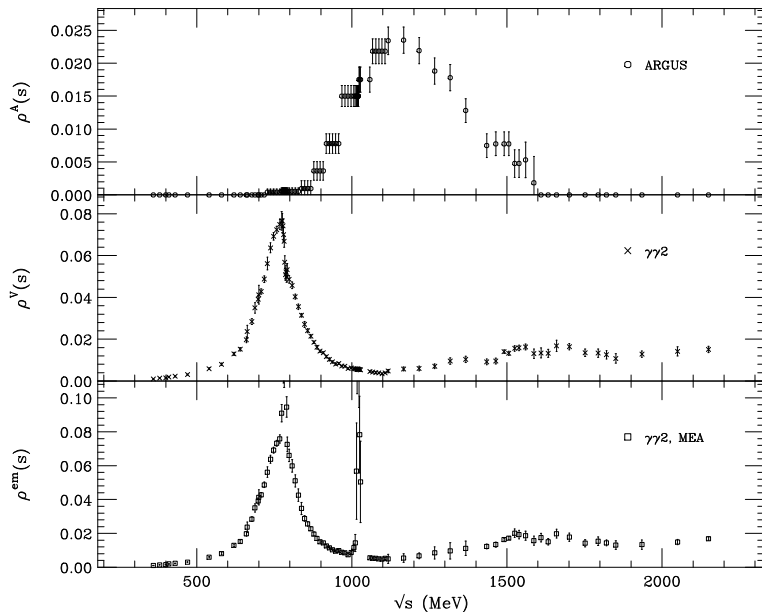


Figure 2.6: Lower panel: experimental cross section ratio  $R^h(s)/12\pi^2$  according to Eq. (2.85) from a recent data compilation [79] of various experiments on  $e^+e^-$  annihilation [80, 81, 82, 83, 84]. The middle and upper panel show the individual experimental information on vector and axialvector spectral densities, Eqs. (2.92) and (2.93), as extracted from  $e^+e^- \rightarrow 2n\pi$  and  $\tau$ -decay data, respectively.

is accessible from experiment as indicated in the lower panel of Fig. 2.6.

From the rates (2.82) and (2.84) a simple estimate can be made for the expected dilepton signal when the hadronic fireball is close to the phase boundary (Fig. 1.1). As displayed in Fig. 2.7 for  $T = 160$  MeV and  $\mu_B = 0$  the predicted rates coincide above  $\sim 1.5$  GeV but differ greatly below due to the  $\rho$ ,  $\omega$  and  $\phi$  resonance structures in the electromagnetic spectral function (lower panel of Fig. 2.6)

## 2.6 Vector-Axialvector Mixing

As has been discussed the quark-hadron phase transition is accompanied by the restoration of chiral symmetry, *i.e.*, a 'melting' of the quark condensate at the transition temperature,  $T_c \simeq 160$  MeV. The change of  $\langle\langle\bar{\psi}\psi\rangle\rangle$  is not an experimental observable, however. On the other hand it follows

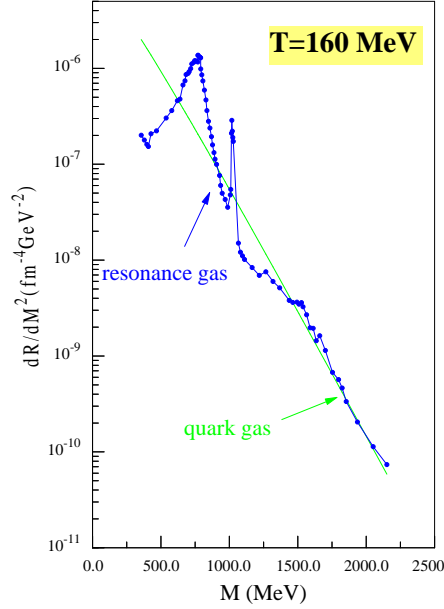


Figure 2.7: Three-momentum integrated dilepton production rate at a temperature  $T = 160$  MeV using either the resonance gas approximation, Eq. (2.84), or the perturbative  $q\bar{q}$  prediction, Eq. (2.82).

from chiral symmetry alone that, at the phase boundary, vector and axialvector correlators must become identical (in the chiral limit). This is evidenced by the temperature dependence of the lattice screening masses (Fig. 2.5) as will be discussed more generally in the following.

First we consider the isovector ( $I = 1$ ) vacuum vector and axialvector correlators for two flavors. The former clearly dominates the electromagnetic spectral function (Fig. 2.6) and hence the dilepton rate. One has

$$\begin{aligned}\Pi_V^{\circ\mu\nu}(q) &= -i \int d^4x e^{iq \cdot x} \langle 0 | \mathcal{T} j_V^\mu(x) j_V^\nu(0) | 0 \rangle \\ \Pi_A^{\circ\mu\nu}(q) &= -i \int d^4x e^{iq \cdot x} \langle 0 | \mathcal{T} j_A^\mu(x) j_A^\nu(0) | 0 \rangle ,\end{aligned}\tag{2.86}$$

where

$$j_V^\mu = \frac{1}{2}(\bar{u}\gamma_\mu u - \bar{d}\gamma_\mu d)\tag{2.87}$$

$$j_A^\mu = \frac{1}{2}(\bar{u}\gamma_\mu\gamma_5 u - \bar{d}\gamma_\mu\gamma_5 d)\tag{2.88}$$

carry the quantum numbers of the  $\rho$  and  $a_1$  meson, respectively. The imaginary parts of (2.86)

can be expressed in terms of the vector and axialvector spectral densities,  $\rho_V$  and  $\rho_A$ , as

$$\begin{aligned}\frac{1}{\pi}\text{Im}\Pi_V^{\circ\mu\nu}(q) &= (q^2 g^{\mu\nu} - q^\mu q^\nu)\rho_V^\circ(q^2) \\ \frac{1}{\pi}\text{Im}\Pi_A^{\circ\mu\nu}(q) &= (q^2 g^{\mu\nu} - q^\mu q^\nu)\rho_A^\circ(q^2) - q^\mu q^\nu f_\pi^2 \delta(q^2 - m_\pi^2).\end{aligned}\quad (2.89)$$

Due to spontaneous symmetry breaking in the physical vacuum and the resulting Goldstone nature of the pion the axialvector correlator contains an additional pion pole term. Chiral symmetry also dictates a relationship between the vector and axialvector sector which is encoded in two sum rules [85]:

$$\int ds \left( \rho_V^\circ(s) - \rho_A^\circ(s) \right) = f_\pi^2 \quad (2.90)$$

$$\int ds s \left( \rho_V^\circ(s) - \rho_A^\circ(s) \right) = 0. \quad (2.91)$$

The first one directly links the spectral functions to  $f_\pi$ , one of the order parameters of spontaneous symmetry breaking, while the second one is a well-known consequence of the conservation of vector and axialvector currents in the chiral limit.

The vacuum spectral functions  $\rho_V^\circ(s)$  and  $\rho_A^\circ(s)$  are related to physical processes. The vector spectral function can be obtained from the  $e^+e^-$ -annihilation into an even number of pions:

$$\rho_V^\circ(s) = -\frac{s}{16\pi^3\alpha^2} \sum_{n=1} \sigma(e^+e^- \rightarrow 2n\pi), \quad (2.92)$$

while  $\rho_A^\circ(s)$  can be extracted from data on  $\tau$ -decay into a  $\nu_\tau$ -neutrino and an odd number of pions:

$$\rho_A^\circ(s) = \frac{8\pi m_\tau^3}{G_F^2 \cos\theta_c (m_\tau^2 + 2s)(m_\tau^2 - s)^2} \sum_{n=1} \frac{d\Gamma(\tau \rightarrow \nu_\tau(2n+1)\pi)}{2s}. \quad (2.93)$$

An available data compilation [79] is displayed in the upper and middle panel of Fig. 2.6. The two spectral functions are clearly different which is one of the experimental signatures that chiral symmetry is spontaneously broken. Replacing the spectral functions by a simplifying pole ansatz

$$\rho_V^\circ(s) = \frac{m_\rho^4}{g_\rho^2} \frac{1}{s} \delta(s - m_\rho^2), \quad \rho_A^\circ(s) = \frac{m_{a_1}^4}{g_{a_1}^2} \frac{1}{s} \delta(s - m_{a_1}^2), \quad (2.94)$$

one immediately derives from the Weinberg sum rules (2.91) that

$$\frac{m_\rho^4}{g_\rho^2} = \frac{m_{a_1}^4}{g_{a_1}^2}, \quad m_\rho^2 = ag_\rho^2 f_\pi^2 \quad \text{with } a = \left(1 - \frac{m_\rho^2}{m_{a_1}^2}\right)^{-1}. \quad (2.95)$$

For  $m_{a_1} = \sqrt{2}m_\rho$  (*i.e.*,  $a = 2$ ), which is not too far from reality, the KSFR relation [86] is recovered.

Turning to the hot hadronic medium the current-current correlation functions – in analogy to Eq. (2.86) – are given as the thermal averages

$$\Pi_V^{\mu\nu}(q) = -i \int d^4x e^{iq \cdot x} \langle\langle j_V^\mu(x) j_V^\nu(0) \rangle\rangle \quad (2.96)$$

$$\Pi_A^{\mu\nu}(q) = -i \int d^4x e^{iq \cdot x} \langle\langle j_A^\mu(x) j_A^\nu(0) \rangle\rangle . \quad (2.97)$$

Since the thermal medium specifies a preferred frame and thus explicitly breaks Lorentz invariance the tensor structure is now more complicated giving rise to a separate dependence on energy  $q_0$  and three-momentum  $\vec{q}$  as well as a splitting into longitudinal and transverse components. One has

$$\Pi_{V,A}^{\mu\nu}(q_0, \vec{q}) = \Pi_{V,A}^L(q_0, \vec{q}) P_L^{\mu\nu} + \Pi_{V,A}^T(q_0, \vec{q}) P_T^{\mu\nu} \quad (2.98)$$

where  $P_L$  and  $P_T$  are the usual longitudinal and transverse projection operators:

$$\begin{aligned} P_L^{\mu\nu} &= \frac{q^\mu q^\nu}{M^2} - g^{\mu\nu} - P_T^{\mu\nu} \\ P_T^{\mu\nu} &= \begin{cases} 0 & , \mu = 0 \text{ or } \nu = 0 \\ \delta^{ij} - \frac{q^i q^j}{\vec{q}^2} & , \mu, \nu \in \{1, 2, 3\} \end{cases} \end{aligned} \quad (2.99)$$

(the space-like components of  $\mu$  and  $\nu$  are denoted by  $i$  and  $j$ , respectively), and  $\Pi_{V,A}^{L,T}(q_0, \vec{q})$  denote the longitudinal and transverse polarization functions. In general they are different and only coincide for vanishing three-momentum  $\vec{q} = 0$ , *i.e.*, excitations which are at rest relative to the medium. In-medium Weinberg sum rules have been derived in Ref. [87]. Introducing the in-medium spectral distributions for vanishing three-momentum as

$$\rho_{V,A}(q_0) = -\frac{1}{q_0^2 \pi} \Pi_{V,A}^L(q_0, 0) , \quad (2.100)$$

these sum rules are given by

$$\int dq_0^2 \left( \rho_V(q_0) - \rho_A(q_0) \right) = 0 \quad (2.101)$$

$$\int dq_0^2 q_0^2 \left( \rho_V(q_0) - \rho_A(q_0) \right) = 0 . \quad (2.102)$$

Due to the presence of pions in the thermal heat bath the vector and axialvector correlators mix (Fig. 2.8). At low temperature this mixing can be calculated in a virial expansion. To lowest order in temperature one obtains [88] the model-independent 'mixing theorem' of vacuum correlators:

$$\begin{aligned} \Pi_V^{\mu\nu}(q) &= (1 - \epsilon) \Pi_V^{\circ\mu\nu}(q) + \epsilon \Pi_A^{\circ\mu\nu}(q) \\ \Pi_A^{\mu\nu}(q) &= (1 - \epsilon) \Pi_A^{\circ\mu\nu}(q) + \epsilon \Pi_V^{\circ\mu\nu}(q) . \end{aligned} \quad (2.103)$$

The mixing coefficient  $\epsilon$  is given by the thermal pion loop

$$\epsilon = \frac{2}{f_\pi^2} \int \frac{d^3k}{(2\pi)^3} \frac{f_\pi(\omega_\pi(k))}{\omega_\pi(k)} \quad (2.104)$$



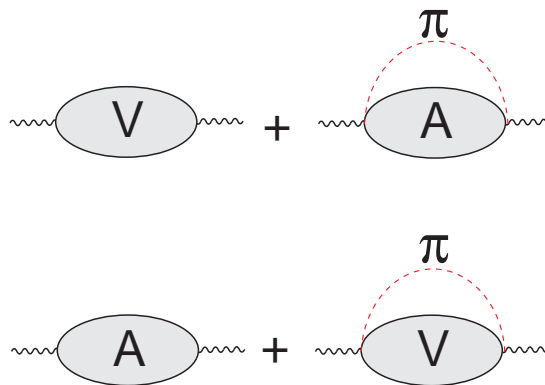


Figure 2.8: Diagrammatic representation of the mixing of vector and axialvector correlators in a heat bath of pions.

( $f^\pi(\omega) = 1/(\exp[\omega/T]-1)$ ): pion Bose distribution,  $\omega_\pi(k)^2 = m_\pi^2 + k^2$ ). In the chiral limit ( $m_\pi \rightarrow 0$ ) this reduces to

$$\epsilon = \frac{T^2}{6f_\pi^2}. \quad (2.105)$$

To lowest order there is no change in the spectral shapes themselves but rather a temperature-dependent coupling between the free vector and axialvector correlators. As is easily verified the mixing theorem fulfills the in-medium Weinberg sum rules and according to (2.103) chiral symmetry is restored for  $\epsilon = 1/2$ . Eq. (2.105) thus implies a transition temperature  $T_c = \sqrt{3}f_\pi \simeq 160$  MeV which coincides with the transition temperature  $T_c = 150 \pm 20$  MeV from lattice QCD. Clearly the low-temperature expansion cannot be trusted to such high temperature. Nonetheless it is instructive to see what the consequences for the dilepton spectrum are. This is displayed in Fig. 2.9. By comparing with the results from a quark-gluon plasma one observes that both are indistinguishable down to invariant masses of  $\sim 1$  GeV. This is significantly lower than without mixing in which case the two rates only coincide above  $\sim 1.5$  GeV (the latter is conceivable from the fact that chiral symmetry breaking is a long distance phenomenon which does not impact the short-distance behavior of the correlators). In other words: the vector-axialvector mixing at finite temperature entails that the 'duality threshold' – where hadronic and quark-gluon based descriptions start to agree – is reduced from its vacuum location at  $M \simeq 1.5$  GeV to about  $M \simeq 1$  GeV in the medium. At this level, the  $\phi$  and  $\rho/\omega$  resonance structures (which themselves are not affected by the simple mixing mechanism) inhibit a further penetration of the duality threshold into the low-mass region. However, let us note already at this point that it is precisely the broadening (or 'melting') of the resonances in the medium (as predicted in various hadronic

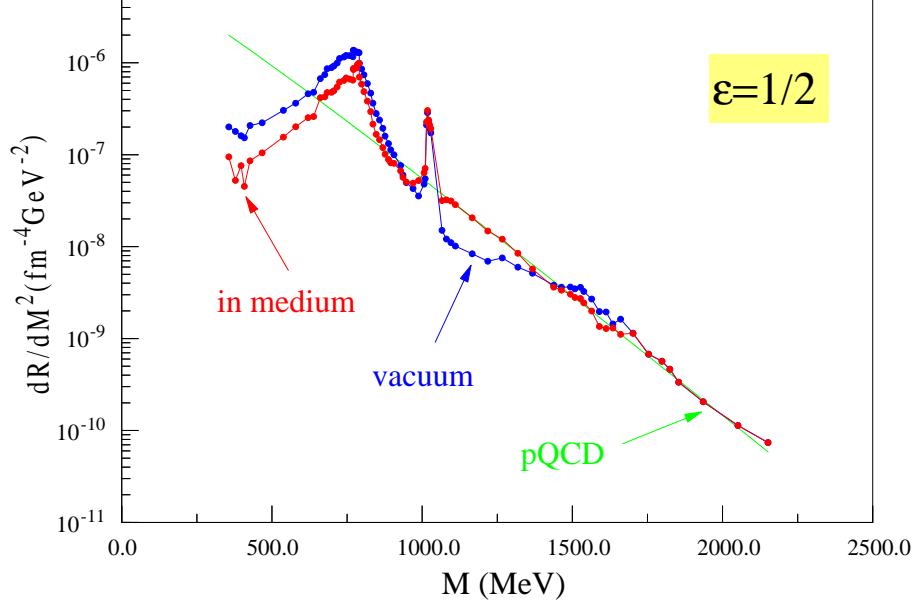


Figure 2.9: Three-momentum integrated dilepton production rates at fixed temperature  $T = 160$  MeV using the free electromagnetic correlator (labeled 'vacuum'), the fully mixed one from Eq. (2.103) ('in-medium') and the perturbative quark-gluon one according to Eq. (2.82) ('pQCD').

model calculations) that – at the same time – flattens the ( $\rho$ ) resonance structure and generates low-mass dilepton enhancement below the free  $\rho$  mass. These important issues will be reiterated in some detail throughout this article.

Further interesting conclusions about the in-medium correlators can be drawn by using a pole approximation [87] similar to (2.94):

$$\rho_V(q_0) = \frac{m_\rho^4}{g_\rho^2} Z_\rho \frac{1}{q_0^2} \delta(q_0^2 - m_\rho^{*2}), \quad \rho_A(q_0) = \frac{m_{a_1}^4}{g_{a_1}^2} Z_{a_1} \frac{1}{q_0^2} \delta(q_0^2 - m_{a_1}^{*2}) + f_\pi^{*2} \delta(q_0^2), \quad (2.106)$$

where  $m_\rho^*$ ,  $m_{a_1}^*$  and  $f_\pi^*$  denote the in-medium masses and pion decay constant while  $Z_\rho$  and  $Z_{a_1}$  are the residues at the quasiparticle pole. Inserting (2.106) into the Weinberg sum rules (2.101), (2.102) yields  $Z_\rho = Z_{a_1}$  from the second one, and thus from the first one

$$\frac{f_\pi^{*2}}{f_\pi^2} = a Z_\rho \left( \frac{m_\rho^2}{m_\rho^{*2}} - \frac{m_\rho^2}{m_{a_1}^{*2}} \right), \quad (2.107)$$

where  $a$  is given by (2.95). Since  $f_\pi^*$  is an order parameter of chiral symmetry the latter is

restored when  $m_\rho^* = m_{a_1}^*$ . Such an approach to mass degeneracy is indeed observed in lattice QCD calculations.

In close reminiscence to the finite temperature case, Krippa [89] derived an analogous mixing theorem for a zero-temperature gas of noninteracting nucleons using soft pion theorems and current algebra,

$$\begin{aligned}\Pi_V^{\mu\nu}(q) &= (1 - \xi) \Pi_V^{\circ\mu\nu}(q) + \xi \Pi_A^{\circ\mu\nu}(q) \\ \Pi_A^{\mu\nu}(q) &= (1 - \xi) \Pi_A^{\circ\mu\nu}(q) + \xi \Pi_V^{\circ\mu\nu}(q) .\end{aligned}\tag{2.108}$$

Here, the mixing parameter

$$\xi \equiv \frac{4\varrho_N \bar{\sigma}_{\pi N}}{3f_\pi^2 m_\pi^2}\tag{2.109}$$

appears in terms of the leading nonanalytic term in the current quark mass ( $\propto m_\pi^3$ ) in the chiral expansion of the nucleon  $\sigma$ -term, given by

$$\begin{aligned}\bar{\sigma}_{\pi N} &= 4\pi^3 m_\pi^2 \langle N | \pi^2 | N \rangle \\ &\simeq 20 \text{ MeV} .\end{aligned}\tag{2.110}$$

It is related to the pion mass contribution to the in-medium nucleon mass and arises from the long-distance physics encoded in the nuclear pion cloud being governed by chiral symmetry [90]. Naive extrapolation of the mixing to chiral restoration (*i.e.*,  $\xi = 1/2$ ) yields  $\rho_c \simeq 2.5\varrho_0$ , which again is not unreasonable.

## 2.7 QCD Sum rules

The QCD sum rule approach [59] aims at an understanding of physical current-current correlation functions in terms of QCD by relating the observed hadron spectrum to the nonperturbative QCD vacuum structure. This is achieved by a separation of short- and long-distance scales. The principal tool is the 'operator product expansion' (OPE) which evaluates the time-ordered product of the light-quark QCD currents at large space-like momenta  $Q^2 \equiv -q^2 > 0$ . In this case the current product can be related to a series of gauge invariant local operators  $\mathcal{O}_n$  as

$$-i \int d^4x e^{iq \cdot x} \mathcal{T} j^\mu(x) j^\nu(0) = -(g^{\mu\nu} - \frac{q^\mu q^\nu}{q^2}) \sum_n c_n(Q^2, \Lambda^2) \mathcal{O}_n(\Lambda^2) ,\tag{2.111}$$

where  $\Lambda$  is the renormalization scale and  $c_n$  denote c-number functions (the Wilson coefficients) which contain the short-distance physics and can be calculated reliably. The  $Q^2$ -independent operators  $\mathcal{O}_n$ , on the other hand, encompass the long-distance properties of QCD, manifest in the appearance of various condensates such as  $\langle \bar{\psi}\psi \rangle$  or  $\langle G^2 \rangle$ . These operators have various dimensions,  $d$ , such that at large  $Q^2$  (2.111) can be considered as an expansion in inverse powers of  $Q^2$  (corrected by logarithms due to renormalization). An increase in dimension implies extra inverse powers of  $Q^2$  such that operators of higher dimension are suppressed.

The general strategy is to take the vacuum matrix elements of (2.111) and to consider a dispersion relation (possibly subtracted) of the type

$$\Pi^\circ(Q^2 = -q^2) = \Pi^\circ(0) - \frac{Q^2}{\pi} \int_0^\infty \frac{ds}{s} \frac{\text{Im}\Pi^\circ(s)}{Q^2 + s} = \Pi^\circ(0) + Q^2 \int_0^\infty ds \frac{\rho^\circ(s)}{Q^2 + s}, \quad (2.112)$$

where  $\rho^\circ(s) = -(1/\pi s)\text{Im}\Pi^\circ(s)$  denotes the vacuum spectral function of the current-current correlator in question. For the electromagnetic current  $\Pi^\circ(0) = 0$ , since the photon is massless in the vacuum. The *l.h.s.* of Eq. (2.112) is evaluated in the OPE by determining the Wilson coefficients up to a certain dimension  $d$  while the *r.h.s.* is taken from measured cross sections (or simple parameterizations thereof) in the time-like region. For the *l.h.s.* one obtains

$$\frac{12\pi}{Q^2}\Pi^\circ(Q^2) = \frac{d}{\pi} \left[ -c_0 \ln(Q^2/\Lambda^2) + \frac{c_1}{Q^2} + \frac{c_2}{Q^4} + \frac{c_3}{Q^6} + \dots \right], \quad (2.113)$$

which exhibits the power series expansion in  $Q^2$ . In case of the  $\rho$  meson [91]

$$\begin{aligned} c_0^\rho &= 1 + \frac{\alpha_s}{\pi} \\ c_1^\rho &= -3(m_u^2 + m_d^2) \\ c_2^\rho &= \frac{\pi^2}{3} \langle G^2 \rangle + 4\pi^2 \langle m_u \bar{u}u + m_d \bar{d}d \rangle \\ c_3^\rho &\propto \alpha_s \langle (\bar{q}q)^2 \rangle, \end{aligned} \quad (2.114)$$

where  $\alpha_s(Q^2)$  is the running QCD coupling constant given in Eq. (2.5). Explicit expressions for the coefficients  $c_i$  of other mesons can be found in Ref. [91]. While for  $c_2$  the quark and gluon condensates enter, which are rather well known,  $c_3$  contains the four-quark condensate, *i.e.*,  $\langle (\bar{q}q)^2 \rangle$ , which is quite uncertain. Based on the assumption of vacuum saturation it is usually approximated in factorized form,  $\langle \bar{q}q \rangle^2$ , and higher meson states, especially pions, are incorporated by a phenomenological factor  $\kappa > 1$  such that

$$c_3 = \kappa \alpha_s \langle \bar{q}q \rangle^2 \quad (2.115)$$

The parameter  $\kappa$  typically varies between 1 and 6 [46, 92, 91].

Rather than working with (2.113) the convergence of the hadronic side can be improved by observing that the physical spectrum is dominated by low-lying resonances (Fig. 2.6). To enhance their weight one employs the fact that dispersion theory implies the following relation for derivatives of  $\Pi^\circ$ :

$$\frac{1}{n!} \left( -\frac{d}{dQ^2} \right)^n \Pi^\circ(Q^2) \Big|_{Q^2=Q_0^2} = \frac{1}{\pi} \int ds \frac{\text{Im}\Pi^\circ(s)}{(s + Q_0^2)^{n+1}}. \quad (2.116)$$

This leads to the introduction of the 'Borel transformation'

$$\hat{L}_M = \lim_{\substack{Q^2 \rightarrow \infty, n \rightarrow \infty \\ Q^2/n = M^2}} \frac{1}{(n-1)!} (Q^2)^n \left( -\frac{d}{dQ^2} \right)^n, \quad (2.117)$$

where  $M$  is the so-called Borel mass. When applied to both sides of Eq. (2.112) and by using general properties of  $\hat{L}_M$  the result of the transformation is

$$\frac{1}{\pi M^2} \int ds \rho_V^\circ(s) e^{-s/M^2} = \frac{d_V}{12\pi^2} \left[ c_0 + \frac{c_1}{M^2} + \frac{c_2}{M^4} + \frac{c_3}{2M^6} + \dots \right]. \quad (2.118)$$

Note the appearance of the exponential factor in the integrand of the *l.h.s.* which suppresses the contribution from higher resonances. The *r.h.s.* converges rapidly if  $M$  is sufficiently large such that the few lowest terms in the OPE suffice. Typically the minimum value of the Borel mass to achieve rapid convergence is around 1 GeV.

The QCD sum rule analysis in the vacuum can now be performed in two ways. Either the phenomenological side is experimentally accessible in which case values for the various condensates can be extracted, or, by using 'known' values for the condensates the properties of the physical spectrum, *i.e.*, masses and coupling constants, can be inferred. The latter procedure forms the basis of QCD sum rule applications in hadronic matter. The most simple ansatz for the vacuum spectral density consists of a 'delta function' parameterization of the resonance part supplemented by a 'continuum step function' (cf. Fig. 2.10):

$$\rho^\circ(s) = \frac{\mathcal{Z}_V}{12\pi^2} \delta(s - m_V^2) + \frac{d_V}{12\pi^2} \left(1 + \frac{\alpha_s}{\pi}\right) \Theta(s - s_V), \quad (2.119)$$

where  $\mathcal{Z}_V$  denotes the pole strength,  $m_V$  the vector meson mass and  $s_V$  the continuum threshold.

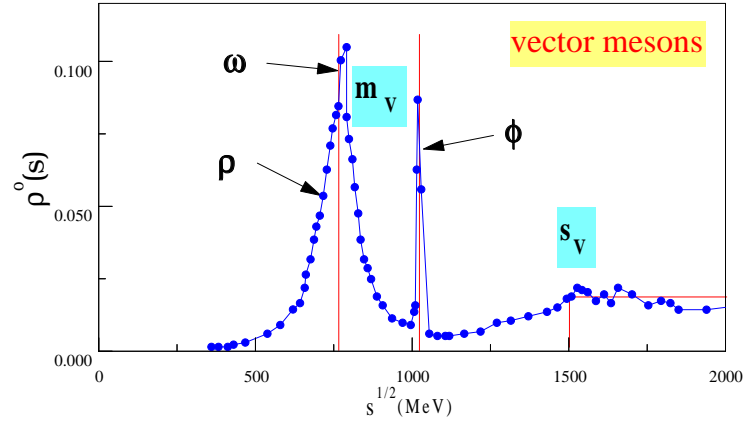


Figure 2.10: QCD sum rule parameterization of the strength function.

The continuum strength  $d_V$  is determined by perturbative QCD with  $d_\rho = 3/2$ ,  $d_\omega = 1/6$ ,  $d_\phi = 1/3$ . Applying this parameterization to (2.118) with  $\alpha_s = 0.36$ ,  $\langle \bar{u}u \rangle \simeq \langle \bar{d}d \rangle \simeq \langle \bar{s}s \rangle = (-250 \text{ MeV})^3$ ,  $\langle \frac{\alpha_s}{\pi} G_{\mu\nu}^a G_a^{\mu\nu} \rangle = (330 \text{ MeV})^4$  and  $\kappa = 2.36$  the *l.h.s.* and *r.h.s.* match for  $\mathcal{Z}_\rho = 9 \text{ GeV}^2$ ,  $\mathcal{Z}_\omega =$

2.4 GeV<sup>2</sup>,  $\mathcal{Z}_\phi = 0.79$  GeV<sup>2</sup>,  $m_{\rho,\omega} = 0.77$  GeV,  $m_\phi = 1.02$  GeV and  $s_{\rho,\omega} = 1.5$  GeV<sup>2</sup>,  $s_\phi = 2.2$  GeV<sup>2</sup> in a 'Borel window' of 0.8-1.5 GeV [91]. Inclusion of the vector-meson decay widths (especially for the  $\rho$  meson) does not affect these results appreciably.

The in-medium QCD sum rule analysis involves the vector current-current function in the interacting hadron gas (2.97). In the following it will be focused on the case of  $\vec{q} = 0$  for which  $\Pi_V^{L,T}(q_0)$  from Eq. (2.98) coincide. In analogy to the vacuum case (2.118) the in-medium sum rules at zero temperature are given by

$$\frac{1}{\pi M^2} \left[ \Pi_V(0) + \int dq_0^2 \rho_V(q_0) e^{-q_0^2/M^2} \right] = \frac{d_V}{12\pi^2} \left[ c_0 + \frac{c_1}{M^2} + \frac{c_2(\varrho)}{M^4} + \frac{c_3(\varrho)}{2M^6} + \dots \right], \quad (2.120)$$

where  $\rho_V(q_0)$  denotes the in-medium vector spectral function (2.100). Note that, in contrast to the vacuum,  $\Pi_V(0)$  no longer vanishes for the  $\rho$  and  $\omega$  meson. It is related to the  $\rho/\omega$ -nucleon forward-scattering amplitude [91]. On the *r.h.s.* of Eq. (2.120) the medium enters through the density-dependent Wilson coefficients  $c_2(\varrho)$  and  $c_3(\varrho)$ . These in turn are chiefly determined by the density-dependent quark and gluon condensates

$$\langle\langle \bar{q}q \rangle\rangle = \langle \bar{q}q \rangle - \frac{\Sigma_N}{2\bar{m}} \varrho, \quad \langle\langle G^2 \rangle\rangle = \langle G^2 \rangle - \frac{8}{9} m_N^{(0)} \varrho. \quad (2.121)$$

which follow from the dilute gas expressions (2.45) and (2.47) at zero temperature. As was pointed out in Ref. [46] additional contributions to the Wilson coefficients arise from new condensates which involve mixed quark and gluon fields, the latter entering through the gauge covariant derivative  $D_\mu$  (2.3). These matrix elements are proportional to moments of the quark and antiquark distribution functions

$$A_n^q = 2 \int_0^1 dx x^n [q(x) + \bar{q}(x)] \quad (2.122)$$

in the nucleon. Restricting oneself to the lowest moments and leading order in density one finally arrives for the  $\rho$  meson at [46]

$$c_2^{\rho}(\varrho) \simeq c_2^{\rho}(0) - \left( \frac{8\pi^2}{27} m_N^{(0)} - 2\pi^2 A_1^{u+d} m_N \right) \varrho \quad (2.123)$$

and

$$c_3(\varrho) \simeq c_3(0) + \left( \frac{896}{81} \kappa \pi^3 \alpha_s \frac{\Sigma_N}{\bar{m}} \langle \bar{q}q \rangle - \frac{10}{3} \pi^2 A_3^{u+d} m_N^3 \right) \varrho, \quad (2.124)$$

where  $m_N$  denotes the physical nucleon mass while  $m_N^{(0)}$  represents the nucleon mass in the chiral limit ( $m_N^{(0)} \simeq 750$  MeV [95]). Expressions for the density-dependent Wilson coefficient of other mesons can be found in Ref. [91].

In keeping the simple parameterization (2.119) for the in-medium spectral function,

$$\rho_V(q_0) = \frac{\mathcal{Z}_V^*}{12\pi^2} \delta(q_0^2 - m_V^{*2}) + \frac{d_V}{12\pi^2} \left( 1 + \frac{\alpha_s}{\pi} \right) \Theta(q_0^2 - s_V^*), \quad (2.125)$$

Hatsuda and Lee [46] extracted the medium dependence of the non-strange vector-meson masses as

$$\frac{m_{\rho,\omega}^*}{m_{\rho,\omega}} = 1 - (0.18 \pm 0.06) \frac{\varrho}{\varrho_0}. \quad (2.126)$$

The fact that these masses decrease as density increases has initially been taken as an indication of the 'dropping mass scenario' of Brown and Rho [45] to which we will return below. Rather than using the parameterization (2.125), it is, however, natural to take into account the fact that the strength distributions might broaden significantly in the hadronic medium, as will be discussed in detail later. A first step in this direction was taken in Ref. [93] by including effects of the  $\Delta$ -nucleonhole polarization in the pion cloud of the  $\rho$  meson. Its net impact on the in-medium QCD sum rule, however, turned out to be rather moderate, *i.e.*, a strong decrease of the in-medium  $\rho$  mass very similar to the Hatsuda-Lee results was still needed to satisfy the sum rule. A more

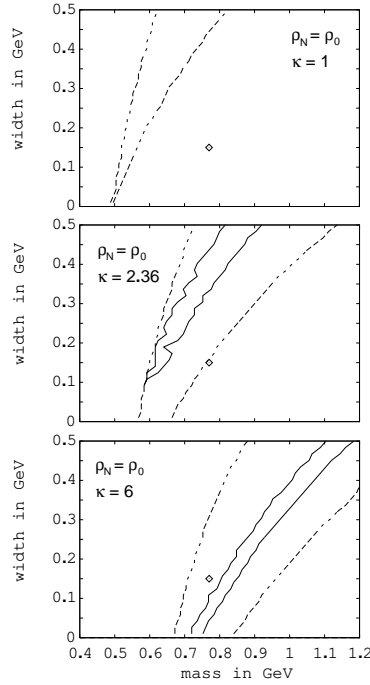


Figure 2.11: Constraints on allowed values for the in-medium width and mass of the  $\rho$  meson from the QCD sum rule analysis of Ref. [94]. The full and dashed lines border allowed regions at 0.2% and 1% accuracy level, respectively. The diamond marks the mass and width of the free  $\rho$  meson.

general investigation of broadening effects was performed in Ref. [94] by assuming a schematic Breit-Wigner spectral function

$$A_V(q_0) = \frac{1}{\pi} \frac{q_0 \Gamma_V(q_0)}{(q_0^2 - m_V^2)^2 + q_0^2 \Gamma_V(q_0)^2} \quad (2.127)$$

with

$$\Gamma_V(q_0) = \Gamma_0 \left( \frac{1 - (\omega_V^{\text{thr}}/q_0)^2}{(1 - (\omega_V^{\text{thr}}/m_V)^2)} \right)^{\frac{1}{2}} \Theta(q_0^2 - (\omega_V^{\text{thr}})^2), \quad (2.128)$$

$\omega^{\text{thr}}$  denoting the appropriate in-medium threshold (for the  $\rho$  meson  $\omega_\rho^{\text{thr}} = m_\pi$  was chosen which is correct to leading order in the density) and  $\Gamma_0$  being a constant width parameter. One concludes from Fig. 2.11 that QCD sum rules give no stringent prediction for a dropping of vector-meson masses. This result is corroborated by the findings of Ref. [91] where a microscopic spectral function for vector mesons was used.

## 2.8 Chiral Reduction Formalism

Another model-independent approach that has been put forward to assess medium modifications of the vector correlation function is the so-called chiral master formula framework developed in Ref. [96]. In the general case, it starts out from gauge covariant divergence equations (Veltmann-Bell equations [97]) including explicit chiral breaking in the presence of external sources,

$$\nabla_\mu j_{V,a}^\mu + \epsilon_{abc} a_{\mu,b} j_{A,c}^\mu = -f_\pi \epsilon_{abc} p_b \pi_c \quad (2.129)$$

$$\nabla_\mu j_{A,a}^\mu + \epsilon_{abc} a_{\mu,b} j_{V,c}^\mu = f_\pi (m_\pi^2 + s) \pi_a - f_\pi p_a \sigma, \quad (2.130)$$

where the (axial-) vector currents

$$j_{V,a}^\mu(x) = \frac{\delta S}{\delta v_\mu^a(x)}, \quad j_{A,a}^\mu(x) = \frac{\delta S}{\delta a_\mu^a(x)} \quad (2.131)$$

and (pseudo-) scalar densities

$$\sigma = -\frac{m_q}{f_\pi m_\pi^2} \bar{q} q, \quad \pi^a = \frac{m_q}{f_\pi m_\pi^2} \bar{q} i \gamma_5 \tau^a q \quad (2.132)$$

have been defined as functional derivatives of an action  $S$  *w.r.t.* a pertinent set of auxiliary fields  $\phi \equiv \{v_\mu^a, a_\mu^a, s, p^a\}$ , respectively (here,  $a, b, c=1-3$  are isospin indices and the short-hand notation for the covariant derivative is defined as  $\nabla_\mu j_a^\mu \equiv [\partial_\mu \delta_{ac} + \epsilon_{abc} v_{\mu,b}] j_c^\mu$ ). More specifically, the action can be thought of as the QCD action plus an external source part,

$$\begin{aligned} S &= \int d^4x \{ \mathcal{L}_{QCD} + \mathcal{L}_{ext} \} \\ \mathcal{L}_{ext} &= \bar{q} \left( \gamma^\mu [v_\mu^a + a_\mu^a \gamma_5] \frac{\tau^a}{2} - \frac{m_q}{m_\pi^2} [m_\pi^2 + s - i \gamma_5 \tau^a p^a] \right) q. \end{aligned} \quad (2.133)$$

With the help of the Peierls-Dyson formula [98] for the  $\mathcal{S}$ -matrix, the Veltmann-Bell equations can be rewritten as

$$\left( X_V^a + \epsilon^{abc} p^b \frac{\delta}{\delta p^c} \right) \mathcal{S} = 0 \quad (2.134)$$

$$\left( X_A^a - (m_\pi^2 + s) \frac{\delta}{\delta p^a} + p^a \frac{\delta}{\delta s} \right) \mathcal{S} = 0, \quad (2.135)$$



where  $X_{V,A}$  are functional differential operators involving the  $v_\mu^a$  and  $a_\mu^a$  fields. The feature of spontaneous chiral symmetry breaking is then imposed through appropriate boundary conditions, namely that asymptotic stable states are given in terms of (massive) pion fields, *i.e.*, for  $x^0 \rightarrow \pm\infty$  one requires

$$j_A^{\mu,a}(x) = -f_\pi \partial^\mu \pi_{in,out}^a(x) \quad (2.136)$$

$$\partial_\mu j_A^{\mu,a}(x) \rightarrow f_\pi m_\pi^2 \pi_{in,out}^a(x) . \quad (2.137)$$

With these boundary conditions the Veltmann-Bell equations (2.134), (2.135) can be integrated to give the so-called master formula for the  $SU(2)_L \times SU(2)_R$  symmetric  $\mathcal{S}$ -matrix for massive pions, which can be found in Ref. [96]. From the master formula one can derive expressions for pion Greens functions in terms of the (axial-) vector currents and (pseudo-) scalar densities, as well as corresponding Ward identities. Since the  $\mathcal{S}$ -matrix plays the role of a time evolution operator (within the Heisenberg picture), the Fourier transform of the master formula takes the form of a LSZ reduction formula, incorporating the proper chiral Ward identities, and thus has been coined 'chiral reduction formula'. It allows to express hadronic on-shell scattering reactions, determined by the *on-shell*  $\mathcal{S}$ -matrix (given by the limit of vanishing external fields  $\phi \rightarrow 0$ ), through well-defined correlation functions and form factors. The latter have to be either inferred from other experimental information (in which case the predictions for the processes under consideration are, in principle, exact, *i.e.*, compatible with unitarity, crossing symmetry and broken chiral symmetry) or evaluated in an appropriate expansion scheme.

Applications of this formalism to calculate medium modifications are readily performed using virial-type low-density approximations, as the processes have to be expressed in terms of stable final states within the hadronic matter, *i.e.*, pions and nucleons. For electromagnetic thermal production rates, this has been carried out in Refs. [99, 100]. Starting from the usual eightfold-differential rate expression,

$$\frac{d^8 N}{d^4 x d^4 q} = -\frac{\alpha^2}{6\pi^3 q^2} W(q) , \quad (2.138)$$

the thermal correlator  $W$  has been related to the time-ordered (Feynman) one by

$$\begin{aligned} W(q) &= \frac{2}{1 + e^{q_0/T}} \text{Im} W^F(q) \\ W^F(q) &= i \int d^4 x e^{iqx} \frac{1}{Z} \text{tr} \left[ e^{(\hat{H} - \mu_N \hat{N})/T} \mathcal{T} j^\mu(x) j_\mu(0) \right] . \end{aligned} \quad (2.139)$$

Up to first order in the density of either pions or nucleons the imaginary parts of the latter become

$$\begin{aligned} \text{Im} W^F(q) &= -3 \text{Im} \Pi_V^\circ(q) + \frac{1}{f_\pi^2} \int \frac{d^3 k}{(2\pi)^3 2\omega_\pi(k)} f^\pi(\omega_\pi(k); T) \text{Im} W_\pi^F(q, k) \\ &\quad + \int \frac{d^3 p}{(2\pi)^3 2E_N(p)} f^N(E_N(p); \mu_N, T) \text{Im} W_N^F(q, p) \end{aligned} \quad (2.140)$$

( $f^\pi$ : pion Bose distribution,  $f^N$ : nucleon Fermi distribution; note that our definition of the correlation functions  $\Pi(q)$  differs from the one in Refs. [99, 100] by a factor of  $q^2$ ). The first term on the

*r.h.s.* represents the vacuum part containing the free electromagnetic current correlator, whereas the second and third terms involve the forward scattering amplitudes of (real or time-like) photons on on-shell pions and nucleons from the medium,

$$\begin{aligned} W_\pi^F(q, k) &= i \int d^4x e^{iqx} \langle \pi(k) | \mathcal{T} j^\mu(x) j_\mu(0) | \pi(k) \rangle \\ W_N^F(q, p) &= i \int d^4x e^{iqx} \langle N(p) | \mathcal{T} j^\mu(x) j_\mu(0) | N(p) \rangle . \end{aligned} \quad (2.141)$$

The relevant expansion parameters for both cases have been quoted as  $\kappa_\pi = n_\pi/2m_\pi f_\pi^2$  and  $\kappa_N = \varrho_N g_A^2/2m_N f_\pi^2$ , which should provide reasonable lowest-order results for  $\kappa \lesssim 0.3$ , corresponding to temperatures  $T \lesssim 140$  MeV and nucleon densities  $\varrho_N \lesssim 2.5\varrho_0$ . However, especially for the nucleonic case, this counting scheme may be subject to large corrections if low-lying resonances or opening thresholds are present [100], see below.

Applying the chiral reduction formulae to the scattering tensors, the relevant terms of the pionic piece take the form [99]

$$\begin{aligned} \text{Im}W_\pi^F(q, k) &\simeq 12 \text{Im}\Pi_V^\circ(q) - 6 \text{Im}\Pi_A^\circ(k+q) + 6 \text{Im}\Pi_A^\circ(k-q) \\ &+ 8 \left[ \frac{(k \cdot q)^2}{q^2} - m_\pi^2 \right] \text{Im}\Pi_V^\circ(q) \text{Re}[D_\pi^R(k+q) + D_\pi^R(k-q)] \end{aligned} \quad (2.142)$$

with  $D_\pi^R$  denoting the retarded pion propagator and  $\Pi_A^\circ$  the free axialvector current correlator (extracted from  $\tau$ -decay data as indicated in the upper part of Fig. 2.6).

The nucleonic piece is more difficult to assess; at the photon point it can be inferred via the optical theorem from the total  $\gamma N$  cross section,

$$e^2 \text{Im}W_N^F(q, p) = -4(s - m_N) \sigma_{\gamma d}^{tot}(s) \quad (2.143)$$

(here, the deuteron cross section has been taken as representative for the isospin summed result). For time-like photons, an absorptive part starts to build up only from loop corrections for which a one-pion loop expansion was performed for non-resonant  $\pi N$  states (being related to on-shell  $\pi N$  scattering data). However, as is obvious from the experimental  $\gamma N$  cross section, the  $\Delta$  resonance has to be included. Its contribution has been evaluated as

$$\text{Im}W_\Delta^F(q, p) = \text{Im} \left[ \frac{4m_N m_\Delta}{s - m_\Delta^2 + im_\Delta \Gamma_\Delta^0} \right] \overline{|\mathcal{M}_{N\Delta}|^2} + (s \rightarrow u) \quad (2.144)$$

with  $\overline{|\mathcal{M}_{N\Delta}|^2}$  the spin-isospin summed modulus squared of the  $N\Delta$  transition amplitude. The latter has been constructed compatible with current conservation and crossing symmetry, and its parameters are constrained by electric and magnetic polarizabilities as well as the electromagnetic decay width  $\Gamma_{\Delta \rightarrow N\gamma} \simeq 0.7$  MeV. In subsequent work – after the importance of the  $N(1520)$  for dilepton production has been realized [101, 102, 48, 103, 49] – the  $N(1520)$  contribution has been included along similar lines as the  $\Delta$  in Ref. [104]. Higher order terms  $\propto \kappa_\pi \kappa_\pi, \kappa_\pi \kappa_N, \kappa_N \kappa_N$  have also been estimated and claimed to be rather small in the region of interest (*i.e.*, above invariant masses of about 200 MeV).

The discussion of the numerical results for the dilepton and photon production rates in the chiral reduction formalism is deferred to Sect. 4.2, where it will be put into context with other (model) approaches, most of which are elucidated in the following Chapter.

## Chapter 3

# Modeling Vector Mesons in the Medium

So far our assessment of medium effects in the current-current correlators was of a rather general nature focusing on the QCD aspects and model independence. We have repeatedly stressed the intimate relation between vector and axialvector channels, governed by chiral symmetry. The discussion now proceeds to various models that have been employed to investigate the properties of vector and axialvector mesons in hot and dense matter. On the one hand, this allows for much more specific predictions, but also implies at least a partial loss of generality. However, a careful comparison of the underlying assumptions and associated characteristic features of the results should provide valuable information on the relevant mechanisms for chiral symmetry restoration. Large efforts have been undertaken to investigate the in-medium vector meson properties, especially those of the  $\rho$  meson, due to its prominent role in heavy-ion dilepton measurements, as will be extensively addressed in Chapter 4. Much less has been done in the axialvector channel, dominated by the  $a_1(1260)$  meson. This is mainly due to the fact that experimental information, in particular concerning medium effects, is and will be scarce (the hope is, of course, that ultimately QCD lattice calculations will be able to overcome this unfortunate situation). Thus, in the following, the emphasis will inevitably be biased towards the vector channel, in particular the  $\rho$  meson.

The various approaches can be roughly divided into two categories, namely those which are based on purely mesonic Lagrangians, addressing the impact of finite temperature, and those including baryonic fields to account for finite density effects. For each model we will first briefly discuss its construction and vacuum properties, subsequently proceeding to the in-medium applications.

### 3.1 Effective Meson Lagrangians: Impact of Finite Temperature

### 3.1.1 Gauged Linear $\sigma$ -Model + VDM

Based on the presumption that for the properties of the lowest-lying meson multiplets near the phase boundary chiral symmetry restoration (rather than deconfinement) should be the prevailing feature of the QCD transition Pisarski proposed [105] to study the simplest version of an effective theory which incorporates the appropriate symmetry structure, *i.e.*, the linear  $\sigma$ -model. A low-lying genuine  $\sigma$  meson might not be the most realistic description of the zero temperature situation, as it strongly couples to two-pion states. As a result the width is of the order of the mass such that the  $\sigma$  meson does not represent a well-defined degree of freedom (or quasiparticle). He argued, however, that given the fact that at chiral restoration the pion and the sigma have to become degenerate there might well arise the situation in which the phase space for  $\sigma \rightarrow \pi\pi$  is locked and the  $\sigma$  field becomes a well-defined excitation [106].

In the linear  $\sigma$ -model the pion and sigma fields are grouped into the standard four-dimensional vector

$$\Phi = \sigma t^0 + i\vec{\pi} \cdot \vec{t}, \quad (3.1)$$

where  $\vec{t} = \vec{\tau}/2$  is defined via the standard Pauli matrices and  $t^0 = \mathbb{1}/2$  is proportional to the unit-matrix in isospin space. The (axial-) vector fields are introduced via left- and right-handed combinations as

$$\begin{aligned} A_L^\mu &= (\omega^\mu + f_1^\mu) t^0 + (\vec{\rho}^\mu + \vec{a}_1^\mu) \cdot \vec{t} \\ A_R^\mu &= (\omega^\mu - f_1^\mu) t^0 + (\vec{\rho}^\mu - \vec{a}_1^\mu) \cdot \vec{t} \end{aligned} \quad (3.2)$$

in obvious notation. The crucial step is now to assume that the  $SU(2)$  chiral transformations for vector fields are *local* ones, promoting it to a gauge symmetry. The basic motivation is a natural emergence of conventional vector dominance. Once the field-strength tensor and covariant derivative on the scalar fields are accordingly defined,

$$\begin{aligned} F_{L,R}^{\mu\nu} &= \partial^\mu A_{L,R}^\nu - \partial^\nu A_{L,R}^\mu - ig [A_{L,R}^\mu, A_{L,R}^\nu] \\ D^\mu &= \partial^\mu \Phi - ig (A_L^\mu \Phi - \Phi A_R^\mu), \end{aligned} \quad (3.3)$$

the gauged linear  $\sigma$ -model Lagrangian takes the form

$$\begin{aligned} \mathcal{L}_{\text{gl}\sigma} &= \text{tr} |D_\mu \Phi|^2 - 2h t^0 \text{tr}(\Phi) - \mu^2 \text{tr} |\Phi|^2 + \frac{1}{2} \lambda (\text{tr} |\Phi|^2)^2 \\ &\quad + \frac{1}{4} \text{tr} ((F_L^{\mu\nu})^2 + (F_R^{\mu\nu})^2) + \frac{1}{2} m_0^2 \text{tr} ((A_L^\mu)^2 + (A_R^\mu)^2). \end{aligned} \quad (3.4)$$

The corresponding vector (Noether) current is then solely determined by the mass term, resulting in

$$j_{L,R}^\mu = \frac{m_0^2}{g} A_{L,R}^\mu. \quad (3.5)$$

This is precisely the desired current-field identity of the vector dominance model [107] (VDM) where  $g$  is the universal (dimensionless) vector coupling and  $m_0$  the (bare) vector meson mass. Furthermore, in Eq. (3.4),  $\lambda$  denotes the (dimensionless) scalar coupling. The 'mass parameter'

$\mu^2$  is taken positive to generate the spontaneous breakdown of chiral symmetry in the physical vacuum. Explicit chiral symmetry breaking through a 'magnetic background field'  $h$  ensures that the resulting vacuum state is aligned in the  $\sigma$  direction implying a non-vanishing expectation value  $\langle \sigma \rangle \equiv \sigma_0 = \mu/\sqrt{\lambda}$  and a finite pion mass. However, after the standard shift  $\sigma \rightarrow \sigma_0 + \sigma$  a 'spurious' mixing term of the form  $g\vec{a}_1^\mu \cdot \partial_\mu \vec{\pi}$  between the pion and the  $a_1$  field emerges which has to be eliminated by a shift of the  $a_1$  field,

$$\vec{a}_1^\mu \rightarrow \vec{a}_1^\mu - \frac{g\sigma_0}{m_0^2 + (g\sigma_0)^2} \partial^\mu \vec{\pi} . \quad (3.6)$$

As a consequence the vector and axialvector meson masses, determined by the  $\text{tr}(A_{L,R})^2$  term, split according to

$$\begin{aligned} m_\rho^2 &= m_\omega^2 = m_0^2 \\ m_{a_1}^2 &= m_{f_1}^2 = m_0^2 + (g\sigma_0)^2 , \end{aligned} \quad (3.7)$$

and the standard relations of the linear  $\sigma$ -model are modified as

$$\begin{aligned} f_\pi &= \frac{m_\rho}{m_{a_1}} \sigma_0 \\ m_\pi^2 &= \left( \frac{m_\rho}{m_{a_1}} \right)^2 \frac{h}{\sigma_0} \\ m_\sigma^2 &= \frac{h}{\sigma_0} + 2\lambda\sigma_0^2 . \end{aligned} \quad (3.8)$$

At the mean-field level, the parameter values are fixed as  $\sigma_0 = 152$  MeV,  $g = 6.55$ ,  $h = (102\text{MeV})^3$  by imposing the experimental values for  $f_\pi = 93$  MeV,  $m_\pi = 138$  MeV,  $m_\rho = 770$  MeV and  $m_{a_1} = 1260$  MeV. Some latitude arises in the choice of  $\lambda$  and  $\mu$  due to the uncertainty in the  $\sigma$  mass; when identifying it as  $m_\sigma = 600$  MeV, one has  $\lambda = 7.6$  and  $\mu = 412$  MeV. As emphasized in Ref. [105], the virtue of complying with VDM through the requirement of locally gauge invariant couplings greatly restricts the number of possible interaction terms (*i.e.*, the mere requirement of a global chiral symmetry would allow many more terms).

When moving to the finite-temperature modifications, Pisarski evaluated selfenergy corrections in terms of a thermal loop expansion to lowest order in  $g$  for two limiting cases. At low temperatures and in the chiral limit, one can additionally expand in small pion momenta  $p \sim T \ll m_\rho, m_{a_1}$  to obtain for the on-shell thermal pole masses of the  $\rho$  and  $a_1$  meson [105]

$$\begin{aligned} m_\rho^2(T) &\simeq m_\rho^2 - \frac{g^2\pi^2 T^4}{45m_\rho^2} \left( \frac{4m_{a_1}^2(3m_\rho^2 + 4q^2)}{(m_{a_1}^2 - m_\rho^2)^2} - 3 \right) + \dots \\ m_{a_1}^2(T) &\simeq m_{a_1}^2 + \frac{g^2\pi^2 T^4}{45m_\rho^2} \left( \frac{4m_{a_1}^2(3m_\rho^2 + 4q^2)}{(m_{a_1}^2 - m_\rho^2)^2} + \frac{2m_\rho^4}{m_{a_1}^2(m_{a_1}^2 - m_\sigma^2)} - \frac{m_{a_1}^2}{m_\rho^2} \right) + \dots \end{aligned} \quad (3.9)$$

This result is consistent with the model-independent mixing theorem (2.103) of Dey et al. [88] stating that there are no mass corrections to order  $T^2$ . However, as stressed in Ref. [105], this only

holds strictly on the mass shell, *i.e.*, for  $q^2 = m_\rho^2$ , but not away from it. Moreover, for explicitly broken chiral symmetry, *i.e.*, for  $h \neq 0$ , the on-shell  $a_1$  pole mass does pick up a  $T^2$ -term

$$m_{a_1}^2(T) \simeq m_{a_1}^2 + \frac{g^2 m_\pi^2 T^2}{4m_\sigma^2} + \dots \quad (3.10)$$

One should also note that in Ref. [108], where the  $O(T^4)$  corrections have been assessed using the OPE in connection with deep-inelastic scattering amplitudes on the pion, *both* the  $\rho$  and  $a_1$  masses have been found to decrease.

As a second limit Pisarski considered the behavior of the masses at the critical temperature for chiral restoration. For the gauged linear  $\sigma$ -model the latter is given in terms of the zero temperature  $\sigma$  expectation value by  $T_c^X = \sqrt{2}\sigma_0 \simeq 215$  MeV (in the chiral limit). By definition,  $\sigma_0 \rightarrow 0$  for  $T \rightarrow T_c^X$ , such that in the immediate vicinity of the transition several of the trilinear vertices  $\propto \sigma_0$  encoded in the Lagrangian (3.4) vanish. Neglecting furthermore small terms of order  $T^2/m_\rho^2$ , the temperature corrections to both the  $\rho$  and  $a_1$  selfenergies turn out to be

$$\Sigma_{\rho, a_1}^{T_c^X} = \frac{1}{6} g^2 T^2 \quad (3.11)$$

resulting in  $m_\rho^2(T_c^X) = m_{a_1}^2(T_c^X) = (2m_\rho^2 + m_{a_1}^2)/3 = (962 \text{ MeV})^2$  (note that the  $(g\sigma_0)^2$ -term in Eq. (3.7) vanishes at  $T_c^X$ ). Since the rather large value of the coupling constant  $g$  implies that a lowest-order calculation cannot be quantitatively trusted the emphasis here is not on the exact mass values but rather on the qualitative feature that  $\rho$  and  $a_1$  masses become degenerate at a common value *in between* their vacuum masses. One should note the somewhat peculiar feature that in the low-temperature limit (3.9) the  $\rho$  and  $a_1$  masses start out by moving *apart*. As another striking result the  $\omega$  meson mass turns out not to be affected at all,  $m_\omega(T_c^X) = m_\omega$ , thus lifting the (theoretically not well-understood) zero temperature degeneracy with the  $\rho$  meson.

Pisarski also studied situations where vector meson dominance does not hold, *e.g.*, when replacing the local chiral symmetry-breaking vector mass term  $\propto m_0^2$  in Eq. (3.4) by

$$\mathcal{L}_\zeta = \zeta \text{tr}(|\Phi|^2) \text{tr}[(A_L^\mu)^2 + (A_R^\mu)^2] \quad (3.12)$$

In this case the vacuum  $\rho$  and  $a_1$  masses are still split by the spontaneous breaking term  $(g\sigma_0)^2$ , but an explicit finite-temperature calculation shows that close to the transition the masses uniformly decrease to  $m_\rho(T_c^X) = m_{a_1}(T_c^X) = m_\omega(T_c^X) = 629$  MeV. Other possible terms outside the VDM might induce different behavior. Thus, within the gauged linear  $\sigma$ -model, the fate of the (axial-) vector masses (especially for the  $\rho$ ) crucially depends on whether vector meson dominance, as represented by the field-current identity Eq. (3.5), continues to hold at finite temperature.

### 3.1.2 Massive Yang-Mills Approach

As a second variant of the chiral Lagrangian framework to study in-medium vector meson properties we discuss the massive Yang-Mills (MYM) approach. It is very similar in spirit to the gauged linear  $\sigma$ -model, only that the  $\sigma$  degrees of freedom have been eliminated using the non-linear realization of the  $SU(3)_L \times SU(3)_R$  chiral symmetry [109]. From a phenomenological point of view this might be

the more appropriate effective theory at zero and low temperatures. The Lagrangian is expressed through a matrix representation

$$U = \exp(i\sqrt{2}\phi/f_\pi) , \quad \phi \equiv \phi_a \frac{\tau_a}{\sqrt{2}} , \quad (3.13)$$

where, in the  $SU(2)$  case, the isospin index  $a$  of the pseudoscalar fields  $\phi_a$  runs from 1 to 3, contracted with the Pauli matrices  $\tau_a$ . The vector and axialvector fields are introduced in complete analogy to the linear  $\sigma$ -model of the previous Section, *i.e.*, as massive gauge fields. Defining them via

$$\begin{aligned} V^\mu &\equiv V_a^\mu \tau_a / \sqrt{2} & , & & A^\mu &\equiv A_a^\mu \tau_a / \sqrt{2} \\ A_L^\mu &\equiv \frac{1}{2}(V^\mu + A^\mu) & , & & A_R^\mu &\equiv \frac{1}{2}(V^\mu - A^\mu) \end{aligned} \quad (3.14)$$

leads to the Lagrangian

$$\begin{aligned} \mathcal{L}_{\text{mym}} &= \frac{1}{4} f_\pi^2 \text{tr} [D_\mu U D^\mu U^\dagger] - \frac{1}{2} \text{tr} [(F_L^{\mu\nu})^2 + (F_R^{\mu\nu})^2] + m_0^2 \text{tr} [(A_L^\mu)^2 + (A_R^\mu)^2] \\ &\quad - i\xi \text{tr} [D_\mu U D^\mu U^\dagger F_L^{\mu\nu} + D_\mu U D^\mu U^\dagger F_R^{\mu\nu}] + \sigma \text{tr} [F_L^{\mu\nu} U F_{R\mu\nu} U^\dagger] . \end{aligned} \quad (3.15)$$

Note that the normalization convention chosen in Eq. (3.14) (which differs from the previous Section by a factor of  $1/\sqrt{2}$ ), entails a factor of 2 in the terms bilinear in the (axial-) vector fields. Also, the  $\rho\pi\pi$  coupling constant picks up an additional factor in its relation to the gauge coupling constant  $g$ , *i.e.*,  $g = \sqrt{2}g_{\rho\pi\pi}$ . This is due to the definition of the covariant derivative which in (3.15) is taken as

$$D^\mu U = \partial^\mu - ig(A_L^\mu U - U A_R^\mu) . \quad (3.16)$$

The last two terms in the Lagrangian (3.15) are so-called non-minimal coupling terms (*i.e.*, of higher order in the derivatives than the other ones), which are necessary for a realistic description of the vector and axialvector meson sector in vacuum. The four free parameters ( $m_0, g, \sigma, \xi$ ) are readily adjusted to reproduce the phenomenological masses and decay widths of  $\rho, \omega, a_1$ , etc..

At finite temperature the calculation of the vector correlator – saturated by the  $\rho$  meson in VDM – has been shown [110] to obey the general low-energy theorem of Ref. [88]. To lowest order in the 'mixing parameter'  $\epsilon = T^2/6f_\pi^2$ , the finite-temperature  $\rho$  meson selfenergy receives two corrections from thermal one-pion loop diagrams. The relevant terms in the MYM Lagrangian (3.15),

$$\mathcal{L}_{\text{mym}} = \frac{1}{2} m_\rho^2 \vec{\rho}_\mu^2 + [m_\rho^2 + g^2 f_\pi^2] \vec{a}_{1\mu}^2 + g^2 f_\pi \vec{\pi} \times \vec{\rho}^\mu \cdot \vec{a}_{1\mu} + \frac{1}{2} g^2 [\vec{\rho}_\mu^2 \vec{\pi}^2 - \vec{\rho}^\mu \cdot \vec{\pi} \vec{\rho}_\mu \cdot \vec{\pi}] + \dots , \quad (3.17)$$

induce a  $\rho\rho\pi\pi$  'tadpole' diagram (last term) as well as a  $\pi a_1$  resonance loop (prelast term). The leading temperature dependence is driven by loops of pions from the heat bath. When evaluated in the chiral limit the resulting vector correlator takes the form

$$\begin{aligned} \Pi_V^{\mu\nu}(q) &= \left( g^{\mu\nu} - \frac{q^\mu q^\nu}{m_\rho^2} \right) g_\rho^2 \\ &\quad \times \left[ \frac{i}{m_\rho^2 - q^2} + \frac{i}{m_\rho^2 - q^2} i g^2 f_\pi^2 \epsilon \frac{i}{m_\rho^2 - q^2} + \frac{i}{m_\rho^2 - q^2} \frac{i^3 g^4 f_\pi^4 \epsilon}{m_{a_1}^2 - q^2} \frac{i}{m_\rho^2 - q^2} \right] , \end{aligned} \quad (3.18)$$

where the second and third terms arise from the interaction vertices in Eq. (3.17) and  $g_\rho = m_\rho^2/g$  is the VDM coupling constant. Making use of the Weinberg relation,  $m_{a_1}^2 = m_\rho^2 + g^2 f_\pi^2$ , one finally obtains

$$\Pi_V^{\mu\nu}(q) = \left( g^{\mu\nu} - \frac{q^\mu q^\nu}{m_\rho^2} \right) g_\rho^2 \left[ (1 - \epsilon) \frac{i}{m_\rho^2 - q^2} + \epsilon \frac{i}{m_{a_1}^2 - q^2} \right] \quad (3.19)$$

in accordance with the model-independent mixing theorem (2.103). Deviations occur, *e.g.*, through the finite pion mass or when including the non-minimal coupling term with  $\sigma \neq 0$  in the Lagrangian (3.15). As reported by Song [111] the  $\rho$  meson mass tends to increase whereas the  $a_1$  mass decreases. Quantitatively, however, the temperature dependencies seem to be very weak. The masses only change by a few percent even at temperatures as high as  $T = 200$  MeV which already is clearly beyond the range of applicability of the low-temperature expansion. Much before that chiral restoration is likely to be realized through the mixing effect.

### 3.1.3 Hidden Local Symmetry

The third chiral Lagrangian framework to incorporate vector mesons is the so-called 'Hidden Local Symmetry' (HLS) approach proposed by Bando *et al.* [112]. It originated from the observation that the conventional  $[SU(2)_L \times SU(2)_R]_{global}$ -symmetric non-linear  $\sigma$ -model Lagrangian,

$$\mathcal{L}_{nl\sigma} = \frac{1}{4} f_\pi^2 \text{tr} [\partial_\mu U \partial^\mu U^\dagger] \quad (3.20)$$

( $U$  as given in Eq. (3.13)), can be recast in a form that exhibits an additional  $[SU(2)_V]_{local}$  symmetry. This can be made explicit by rewriting the  $U$ -field as

$$U \equiv \xi_L^\dagger \xi_R \quad (3.21)$$

in terms of new SU(2)-valued variables  $\xi_L$  and  $\xi_R$  (notice that this implies the appearance of three additional, unphysical scalar degrees of freedom). Defining the usual covariant derivative

$$\mathcal{D}^\mu = \partial^\mu - igV^\mu \quad (3.22)$$

with an auxiliary gauge field  $V^\mu = V_a^\mu \tau_a / 2$  and associated gauge coupling  $g$  allows to construct two invariants under  $[SU(2)_L \otimes SU(2)_R]_{global} \times [SU(2)_V]_{local}$  transformations, namely

$$\begin{aligned} \mathcal{L}_A &= -\frac{1}{4} f_\pi^2 \text{tr} \left[ \mathcal{D}^\mu \xi_L \cdot \xi_L^\dagger + \mathcal{D}^\mu \xi_R \cdot \xi_R^\dagger \right] \\ \mathcal{L}_V &= -\frac{1}{4} f_\pi^2 \text{tr} \left[ \mathcal{D}^\mu \xi_L \cdot \xi_L^\dagger - \mathcal{D}^\mu \xi_R \cdot \xi_R^\dagger \right]. \end{aligned} \quad (3.23)$$

When imposing the so-called unitary gauge

$$\xi_L^\dagger = \xi_R = \exp(-\pi/f_\pi) \quad (3.24)$$

(which eliminates the unphysical scalar degrees of freedom) it can be verified that, with arbitrary constant  $a$ , the combination

$$\mathcal{L} = \mathcal{L}_A + a\mathcal{L}_V \quad (3.25)$$



is indeed equivalent to Eq. (3.20). In fact,  $\mathcal{L}_A$  is in one-to-one correspondence with the starting Lagrangian  $\mathcal{L}_{\text{nl}\sigma}$ , whereas  $\mathcal{L}_V$  identically vanishes by virtue of the equations of motion for the gauge field. It can be assigned a physical significance by assuming that it develops its own dynamics, generating a kinetic energy term in the Lagrangian (usually attributed to the underlying QCD-dynamics or quantum effects at the composite level [112]). The physical vector field is then identified with the (isovector)  $\rho$  meson, and the HLS Lagrangian becomes

$$\begin{aligned}\mathcal{L}_{\text{hls}} &= \mathcal{L}_A + a\mathcal{L}_V - \frac{1}{4}(\vec{\rho}^{\mu\nu})^2 \\ &= \frac{1}{4}f_\pi^2 \text{tr} [\partial_\mu U \partial^\mu U^\dagger] - \frac{1}{4}\vec{\rho}^{\mu\nu} \cdot \vec{\rho}_{\mu\nu} + \frac{a}{2}g^2 f_\pi^2 \vec{\rho}_\mu^2 + \frac{a}{2}g\vec{\rho}^\mu \cdot (\vec{\pi} \times \partial_\mu \vec{\pi}) + \mathcal{O}(\vec{\pi}^4)\end{aligned}\quad (3.26)$$

with the non-abelian field strength tensor

$$\vec{\rho}^{\mu\nu} = \partial^\mu \vec{\rho}^\nu - \partial^\nu \vec{\rho}^\mu + g \vec{\rho}^\mu \times \vec{\rho}^\nu . \quad (3.27)$$

The second line in Eq. (3.26) has been obtained using the weak-field expansion for the  $\xi$ -fields. One reads off that

$$g_{\rho\pi\pi} = \frac{1}{2}ag \quad (3.28)$$

$$m_\rho^2 = ag^2 f_\pi^2 , \quad (3.29)$$

*i.e.*, the gauge symmetry is spontaneously broken generating a mass for the vector field via the Higgs mechanism. This is accompanied by the disappearance of the scalar modes which have turned into the longitudinal components of now massive vectors. A particular advantage of the HLS framework is the unique way of introducing electromagnetic interactions. Since the photon couples to the charge  $Q = I_3^{(L)} + I_3^{(R)}$  corresponding to the global  $[SU(2)_L \otimes SU(2)_R]$  isospin symmetry, the electromagnetic field can be introduced as a global gauge symmetry. Thus the covariant derivative (3.22) can be simply extended to

$$\mathcal{D}^\mu \xi_{L,R} = (\partial^\mu - igV^\mu)\xi_{L,R} + e_0 \xi_{L,R} B^\mu \frac{\tau_3}{2} \quad (3.30)$$

with the  $U(1)_Q$  gauge field  $B^\mu$  and associated coupling  $e_0$ . In addition, the corresponding kinetic term  $-\frac{1}{4}B_{\mu\nu}^2$  ( $B_{\mu\nu} = \partial_\mu B_\nu - \partial_\nu B_\mu$ ) has to be added to the HLS Lagrangian in Eq. (3.26). After re-diagonalizing the fields one finds the following mass relations:

$$m_\gamma^2 = 0 , \quad m_{\rho^0}^2 = a(g^2 + e_0^2)f_\pi^2 , \quad m_{\rho^\pm}^2 = ag^2 f_\pi^2 . \quad (3.31)$$

For the special case of  $a = 2$ , Eqs. (3.28) and (3.29) give the universality of the  $\rho$  couplings as well as the KSFR relation [86]. Moreover, vector dominance emerges due to the vanishing of the direct  $\gamma\pi\pi$  coupling and the  $\rho$ - $\gamma$  coupling is given as  $g_{\rho\gamma} = m_\rho^2/g$ .

Let us now turn to the finite temperature calculations performed within the HLS framework. The minimal version of the HLS Lagrangian does not involve the  $a_1$  field. Nevertheless, the low-energy theorem, Eq. (2.103), ought to be satisfied for the vector correlator. This is indeed the case and is realized through temperature-dependent corrections to the VDM coupling constant  $g_{\rho\gamma}$ . As

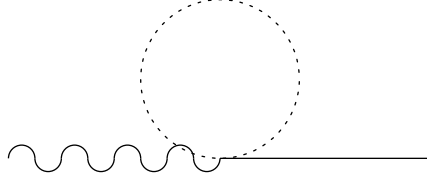


Figure 3.1: Finite temperature correction to the  $\gamma\rho$  vertex through a thermal pion tadpole loop in the HLS approach (wavy line: photon, solid line:  $\rho$  meson, dotted line: pion).

has been shown in Ref. [110], to lowest order in  $\epsilon$ , the thermal pion tadpole loop on the  $\rho - \gamma$  vertex, shown in Fig. 3.1, leads to correction factor  $(1 - \frac{1}{2}\epsilon)$ . Therefore

$$g_{\rho\gamma}^2(T) = (1 - \epsilon)g_{\rho\gamma}^2 + \mathcal{O}(\epsilon^2) . \quad (3.32)$$

Moreover, in the 'minimal' HLS there is no  $\rho\rho\pi\pi$  contact interaction. Thus, to lowest thermal pion-loop order, the in-medium  $\rho$  mass is only modified through temperature effects in the two-pion loop which do not pick up  $T^2$ -corrections due to the additional derivative in the  $\rho\pi\pi$  coupling.

For practical purposes the HLS approach has been mainly employed to study finite-temperature modifications of the pion electromagnetic form factor,  $F_\pi$ , and dilepton/photon production rates. The latter will be discussed in Chap. 4. In the thermal medium, the former can be defined through the total electromagnetic vertex for the  $\pi\pi \rightarrow \gamma$  transition,

$$\Gamma_\mu^{\gamma\pi\pi}(T) = q_\mu F_\pi(q_0, \vec{q}; T) . \quad (3.33)$$

For  $a = 2$  and in free space, it reduces to the well-known VDM expression,

$$F_\pi^\circ(M) = \frac{g_{\rho\pi\pi}g_{\rho\gamma}}{M^2 - (m_\rho^{(0)})^2 + \Sigma_{\rho\pi\pi}(M)} . \quad (3.34)$$

In Ref. [113],  $F_\pi(T)$  has been evaluated in terms of thermal one-pion loop corrections (using  $a = 2$ ). The total  $\gamma\pi\pi$  vertex function can then be written as

$$\Gamma_\mu(T) = \Gamma_\mu^{\text{mix}} + \Gamma_\mu^{\text{vert}} + \Gamma_\mu^{\text{rho}} + \Gamma_\mu^{\text{dir}} , \quad (3.35)$$

where  $\Gamma_\mu^{\text{mix}}$  encodes the pion-tadpole diagram (inducing  $V$ - $A$  mixing diagrammatically represented in Fig. 3.1),  $\Gamma_\mu^{\text{vert}}$  represents thermal-loop corrections of the  $\pi\pi\rho$  vertex (left panel of Fig. 3.2) and  $\Gamma_\mu^{\text{rho}}$  accounts for the temperature dependence in the  $\rho$  selfenergy  $\Sigma_{\rho\pi\pi}$  (*i.e.*, in the two-pion bubble). The appearance of a direct  $\gamma\pi\pi$  vertex  $\Gamma_\mu^{\text{dir}}$  is solely due to finite-temperature vertex modifications, induced by the diagrams shown in the right panel of Fig. 3.2. In the limit of vanishing three-momentum,  $\vec{q} = 0$ , the in-medium form factor can be characterized by a single scalar function (see Eq. (2.100)) depending on invariant mass  $M$  only, according to

$$F_\pi(T) = Z_\pi(T) \left[ \frac{g_{\rho\pi\pi}(T) g_{\rho\gamma}(T)}{M^2 - m_\rho^2 + im_\rho\Gamma_\rho^\circ - \Sigma_\rho(T)} + F_\pi'(T) \right] . \quad (3.36)$$

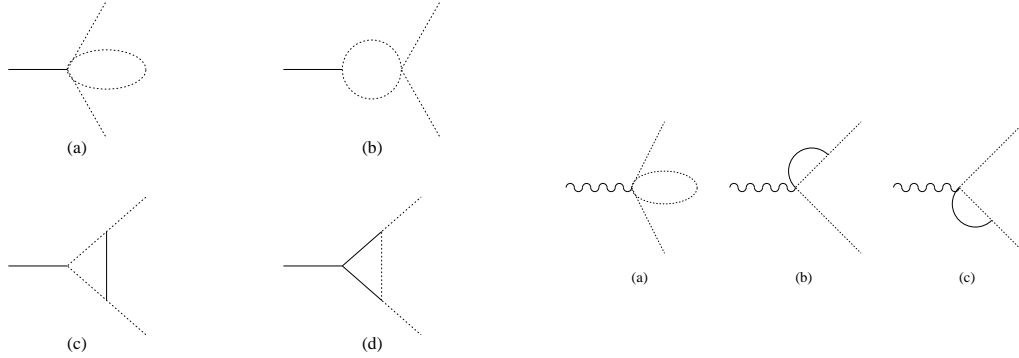


Figure 3.2: Thermal loop corrections to the  $\rho\pi\pi$  vertex (left panel) as well as the 'direct'  $\gamma\pi\pi$ ; the latter vanishes at zero temperature in the VDM (*i.e.* for  $a = 2$  in the HLS framework). The figures are taken from Ref. [113].

Here,  $Z_\pi(T)$  is the pion wave function renormalization constant. It can be inferred from the relevant Ward-Takahashi identity,

$$(p^\mu - p'^\mu)\Gamma_\mu(p, p') = \Sigma_\pi(p) - \Sigma_\pi(p') , \quad (3.37)$$

which ensures gauge invariance of the in-medium  $\gamma\pi\pi$  transition with  $\Sigma_\pi$  denoting the in-medium pion selfenergy to be evaluated to thermal one-loop order. For on-shell pions of vanishing three momentum, as considered in Ref. [113], the simple relation

$$Z_\pi(T) = \left[ 1 - \frac{\partial \Sigma_\pi}{\partial p_0^2}(p_0 = m_\pi, \vec{p} = 0) \right]^{-1} \quad (3.38)$$

is obtained. In Eq. (3.36), the temperature-dependent  $\rho\gamma$  and  $\rho\pi\pi$  couplings, the temperature part of the  $\rho$  selfenergy,  $\Sigma_{\rho\pi\pi}^T$ , as well as the direct  $\gamma\pi\pi$  piece,  $F_\pi'$ , arise from the various vertex terms in Eq. (3.35), respectively ( $\Gamma_{\rho\pi\pi}^\circ$  denotes the free  $\rho$  decay width, and the real part of the free  $\rho$  selfenergy has been absorbed into the physical  $\rho$  meson mass,  $m_\rho$ ). The resulting pion electromagnetic form factor is displayed in Fig. 3.3. One observes a strong suppression with increasing temperature over the entire invariant mass range which, to a large extent, is driven by the reduction of the vector dominance coupling  $g_{\rho\gamma}(T)$ , representing the vector-axialvector mixing effect. One should note, however, that the imaginary part of the vector correlator (which in VDM coincides with the imaginary part of the  $\rho$  meson propagator, *i.e.*, the spectral function), involves an additional factor from the imaginary part of the in-medium  $\rho$  selfenergy; *e.g.*, in VDM the isovector correlator is related to the pion electromagnetic form factor through

$$\text{Im}\Pi_V^{I=1} = \frac{\text{Im}\Sigma_{\rho\pi\pi}}{g_{\rho\pi\pi}^2} |F_\pi(T)|^2 . \quad (3.39)$$

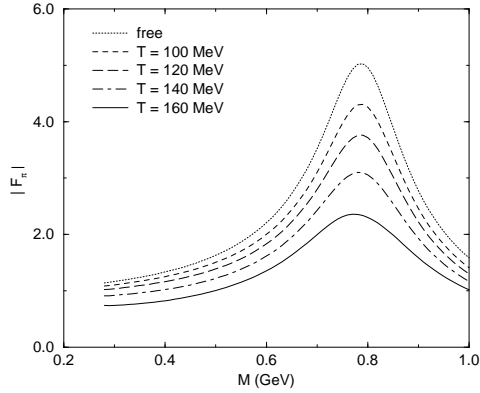


Figure 3.3: Pion electromagnetic form factor in a finite temperature pion gas as calculated within the hidden local symmetry approach in Ref. [113].

Within the quasiparticle approximation for pions, one obtains

$$\text{Im}\Sigma_{\rho\pi\pi}(q_0 = M, \vec{q} = 0) \propto \frac{k^4}{\omega_\pi(k)^2} \left| \frac{\partial\omega_\pi(k)}{\partial k} \right|^{-1} \quad (3.40)$$

with the in-medium pion dispersion relation  $\omega_\pi(k)$ . In a pion gas, the latter is softened at small momenta due to the attractive interaction with thermal pions in the  $\pi\pi \rightarrow \rho$  channel, causing a reduction of the group velocity  $v_k = |\partial\omega_\pi(k)/\partial k|^{-1}$ . This generates some enhancement in the vector correlator at low  $M$ , which is not captured by the electromagnetic form factor shown in Fig. 3.3 (the functional form of  $\Sigma_{\rho\pi\pi}$  as quoted in Eq. (3.40) should be taken with care. It only leads to a gauge invariant vector correlator in connection with the  $Z_\pi^2$  factor (3.38) which in Ref. [113] has been absorbed into the definition of  $|F_\pi|^2$ . In fact, one can show that  $Z_\pi^2 k^2 / \omega_\pi(k)^2 = v_k^2$ , which reduces the effect of the pion softening, see, *e.g.*, Ref. [114] for a nice discussion on this point).

Qualitatively similar features for the in-medium behavior of the pion electromagnetic form factor have been found earlier within a schematic treatment in Ref. [115]. Starting from the on-shell expression for the free  $\rho$  meson decay width (ignoring any pion mass),

$$\Gamma_\rho^o = \frac{g_{\rho\pi\pi}^2}{4\pi} \frac{m_\rho}{12}, \quad (3.41)$$

the finite temperature corrections have been estimated assuming the validity of the in-medium KSFR relation,  $2g_{\rho\pi\pi}^2 f_\pi^2 = m_\rho^2$ , as well as an unmodified  $\rho$  mass (later on it has been realized that  $m_\rho(T)$  does indeed not attain corrections to lowest order  $O(T^2)$  [116], as said before). Then, using the lowest-order chiral perturbation theory result for the pion decay constant (for three massless flavors),

$$f_\pi(T) = f_\pi(1 - T^2/8f_\pi^2) \quad (3.42)$$

(for  $N_f = 2$  the coefficient  $1/8$  is to be replaced by  $1/12$ ), the temperature dependence of the  $\rho$

decay width has been cast in the form

$$\Gamma_\rho(T) \simeq \frac{\Gamma_\rho^\circ}{1 - T^2/4f_\pi^2}, \quad (3.43)$$

indicating a broadening with increasing  $T$ . Vertex corrections of the  $\pi\pi\rho$  coupling as required by Ward identities to ensure the conservation of the vector current have not been included in this estimate. When naively extrapolating Eq. (3.43) to high temperatures one finds the  $\rho$  width to diverge at  $T = 2f_\pi \simeq 185$  MeV (230 MeV when using the two-flavor result for  $f_\pi(T)$ ). In Refs. [117, 115] this kind of resonance melting has been qualitatively associated with the approach towards color deconfinement.

### 3.1.4 Phenomenological Meson Lagrangians

The chiral Lagrangian frameworks discussed in the previous Sections allow a for systematic investigation of the low-temperature chiral dynamics of the vector meson properties. The inclusion of higher resonances, however, can become a quite formidable task due to the increasing number of interaction vertices. Furthermore, chiral symmetry does not always give unique prescriptions for the latter, as we have seen above. Since the impact of certain meson resonances, which have not been incorporated via chiral Lagrangians so far, may be non-negligible more phenomenologically oriented approaches have been pursued [118, 119, 120, 47, 121, 122, 123]. They aim at including the empirically important interactions in a tractable way that also respects the relevant symmetries, such as vector current conservation or chiral symmetry. In the following, we will elaborate on two variants that have been employed in this context, namely kinetic-theory and many-body type calculations.

At low and moderate temperatures the thermal meson gas is dominated by the light pseudoscalar Goldstone bosons  $P = \pi, K, \bar{K}$ . A rather extensive treatment of the possible scattering processes of on-shell vector mesons  $V$  in such a system has been undertaken by Haglin [120]. He specified the following interaction Lagrangians (isospin structure suppressed)

$$\begin{aligned} \mathcal{L}_{VPP} &= G_{VPP} V^\mu P \partial_\mu P \\ \mathcal{L}_{VVP} &= G_{VVP} \epsilon_{\mu\nu\alpha\beta} \partial^\mu V^\nu \partial^\alpha V^\beta P \\ \mathcal{L}_{AVP} &= G_{AVP} A_{\mu\nu} V^{\mu\nu} \end{aligned} \quad (3.44)$$

for the exchange of pseudoscalar, vector ( $V$ ) and axialvector ( $A$ ) mesons, respectively ( $V^{\mu\nu}$  and  $A^{\mu\nu}$  denote the usual field strength tensors). The average collision rate for the vector mesons in binary collisions with particles  $h$  from the heat bath,  $Vh \rightarrow 34$  was then obtained from the kinetic theory expression

$$\begin{aligned} \bar{\Gamma}_V^{\text{coll}}(T) &= \frac{g_V g_h}{n_V(T)} \int d^3\tilde{p}_V d^3\tilde{p}_h d^3\tilde{p}_3 d^3\tilde{p}_4 |\bar{\mathcal{M}}_{\rho h \rightarrow 34}|^2 (2\pi)^4 \delta^{(4)}(p_V + p_h - p_3 - p_4) \\ &\quad \times f^V(T) f^h(T) [1 + f^3(T)][1 + f^4(T)], \end{aligned} \quad (3.45)$$

where  $d^3\tilde{p}_i \equiv d^3p_i/2\omega_i(p_i)(2\pi)^3$ , etc.,  $g_i$  are the spin-isospin degeneracy factors,  $f^i(T)$  thermal Bose-Einstein distribution functions, and  $n_V(T)$  is the number density of the vector meson  $V$ . The

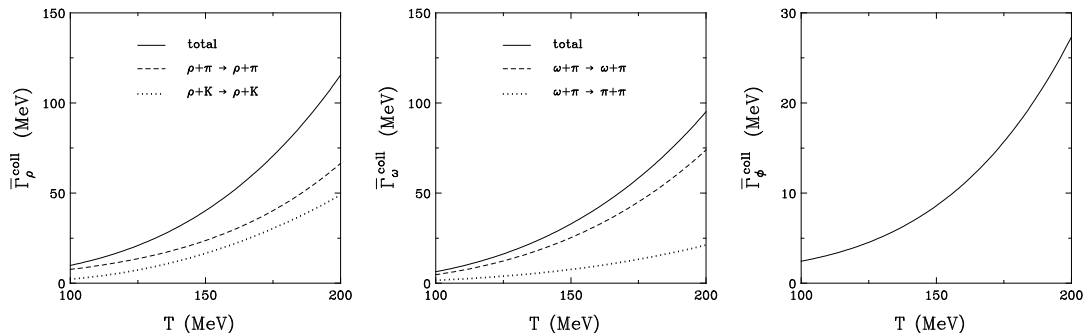


Figure 3.4: Temperature dependence of the collisional broadening of  $\rho$ ,  $\omega$  and  $\phi$  mesons (from left to right) as calculated in the kinetic theory approach of Ref. [120].

coherent sum of invariant amplitudes,

$$\mathcal{M}_{\rho P} = \sum_R \mathcal{M}_{\rho P R} , \quad (3.46)$$

has been computed for both  $s$ - and  $t$ -channel exchanges of mesons  $R$ . For elastic  $\rho\pi$  scattering,  $R = \{\pi, \omega, \phi, a_1(1260), \omega(1390)\}$ , for  $\rho K$  scattering,  $R = K_1(1270)$ , and for  $\omega\pi$  interactions,  $R = \{\rho, b_1(1235)\}$  were used. For the  $\phi$  meson the dominant processes involve kaon exchange (including inelastic channels such as  $\phi\pi \rightarrow K^*K$  or  $\phi K \rightarrow K^*\pi$ ). The final results, displayed in Fig. 3.4, reveal a moderate collisional broadening of about 40 MeV for the  $\rho$  meson at  $T = 150$  MeV. A similar value of  $\sim 30$  MeV has been found for the  $\omega$  meson in which case, however, it amounts to a factor of four times its natural width. The effects for the  $\phi$  meson are smaller.

Along similar lines, Gao *et al.* [122] extended Haglin's analysis for  $\rho\pi$  scattering by including isospin-exchange interactions such as  $\pi^+\rho^0 \rightarrow \pi^0\rho^+$  and by using a different regularization method for the singularity in the  $t$ -channel pion-exchange diagram. He also employed a somewhat modified  $\pi\rho a_1$  vertex which improves the phenomenology of the  $a_1 \rightarrow \pi\rho$  decay [124]. In addition, the in-medium broadening of the  $\rho\pi\pi$  decay width through Bose-Einstein enhancement factors of the pions (which will be discussed in more detail below) were accounted for. The resulting  $\rho$  meson spectral function,

$$A_\rho(M) = -\frac{2\text{Im}\Sigma_\rho(M;T)}{[M^2 - m_\rho^2 - \text{Re}\Sigma_\rho(M;T)]^2 + [\text{Im}\Sigma_\rho(M;T)]^2} , \quad (3.47)$$

has been obtained in terms of a total in-medium  $\rho$  selfenergy,

$$\Sigma_\rho(M;T) = \Sigma_{\rho\pi\pi}(M;T) + \Sigma_\rho^{\text{coll}}(T) , \quad (3.48)$$

consisting of a medium-modified  $\rho \rightarrow \pi\pi$  part (including the Bose enhancement) and a collisional contribution that has been approximated by its on-shell value (*i.e.*, for  $M = m_\rho$ ). Therefore

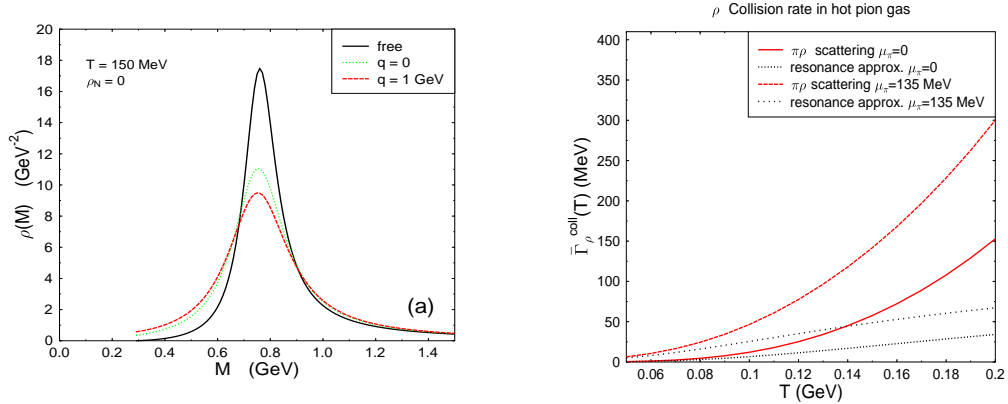


Figure 3.5:  $\rho$  meson spectral function at  $T = 150$  MeV (left panel) as evaluated in the kinetic theory calculations of Ref. [122] including the in-medium Bose-enhancement of the  $\rho \rightarrow \pi\pi$  width. The right panel shows the temperature dependence of the collisional part (using two values for the pion chemical potential) for the full result including  $t$ -channel processes (full curves, labeled ' $\pi\rho$  scattering') as well as for a calculation where only  $s$ -channel resonances have been accounted for (dotted curves, labeled 'resonance approx.').

it depends on temperature only. As apparent from Fig. 3.5, the  $\rho$  meson exhibits a thermal broadening which substantially exceeds the previous estimate by Haglin: at  $T = 150$  MeV, the scattering contribution from a pion gas turns out to be  $\bar{\Gamma}_\rho^{\text{coll}} = 58$  MeV (see also right panel of Fig. 3.5), whereas the in-medium Bose-enhancement of the  $\rho \rightarrow \pi\pi$  decay width amounts to 25 MeV. The three-momentum dependence of the spectral function is rather weak.

The evaluation of the in-medium vector meson properties in the kinetic theory treatments of Refs. [120, 122] was restricted to physical (on-shell) pole masses  $m_V$ . On the other hand, one might expect important effects from off-shell dynamics especially for the  $\rho$  meson as it is characterized by an appreciable width already in free space (this, in turn, marks its distinguished role for low-mass dilepton yields,  $M_{ll} < m_\rho$ , in heavy-ion reactions, to be discussed in Chap. 4). Off-shell dynamics are naturally accounted for within a many-body treatment of in-medium selfenergies, as we are going to discuss now.

The usual starting point is a microscopic model for the  $\rho$  meson with coupling to its 'pion cloud' via two-pion states. This not only renders the correct decay width but also quantitatively describes its energy dependence over a broad range of invariant mass as encoded, *e.g.*, in  $\pi\pi$   $P$ -wave scattering phase shifts or the pion electromagnetic form factor. Given the free  $\pi + \rho$  Lagrangian,

$$\mathcal{L}_{\pi+\rho}^{\text{free}} = \frac{1}{2} \text{tr} [(\partial^\mu \pi)^2 - \phi^2] - \frac{1}{2} \text{tr} [(\rho_{\mu\nu}^2) + (m_\rho^{(0)})^2 \text{tr} [\rho_\mu^2] , \quad (3.49)$$

Sakurai proposed to adopt the  $\rho$  meson as the gauge boson of the conserved isospin [125], which

can be realized by introducing the covariant derivative  $\partial^\mu \rightarrow (\partial^\mu + ig_{\rho\pi\pi}\rho^\mu)$ . This is rather close in spirit to the massive Yang-Mills approach discussed above. The resulting  $\pi\rho$  interaction vertices are then given by

$$\mathcal{L}_{\rho\pi}^{\text{int}} = g_{\rho\pi\pi}(\vec{\pi} \times \partial^\mu \vec{\pi}) \cdot \vec{\rho}_\mu - \frac{1}{2}g_{\rho\pi\pi}^2 \vec{\rho}^\mu \cdot \vec{\pi} \vec{\rho}^\mu \cdot \vec{\pi} . \quad (3.50)$$

To lowest order in  $g_{\rho\pi\pi}$  the corresponding selfenergy in vacuum reads

$$\begin{aligned} \Sigma_{\rho\pi\pi}^{\circ,\mu\nu}(M) &= ig_{\rho\pi\pi}^2 \int \frac{d^4p}{(2\pi)^4} \frac{(2p+q)_\mu(2p+q)_\nu}{((p+q)^2 - m_\pi^2 + i\eta)(p^2 - m_\pi^2 + i\eta)} \\ &\quad - i2g_{\rho\pi\pi}^2 g^{\mu\nu} \int \frac{d^4p}{(2\pi)^4} \frac{1}{p^2 - m_\pi^2 + i\eta} . \end{aligned} \quad (3.51)$$

The loop integrals have to be regularized. A symmetry conserving procedure is, *e.g.*, provided by the Pauli-Villars scheme which applies subtractions to the divergent integrals according to

$$\Sigma^{\mu\nu}(q; m_\pi) \rightarrow \Sigma^{\mu\nu}(q; m_\pi) + \sum_{i=1}^2 c_i \Sigma^{\mu\nu}(q; M_i) . \quad (3.52)$$

The required regulator masses  $M_i$  can be related to a single form factor cutoff  $\Lambda_\rho$  with [126]

$$\begin{aligned} c_1 = -2 , \quad M_1 &= \sqrt{m_\pi^2 + \Lambda_\rho^2} \\ c_2 = 1 , \quad M_2 &= \sqrt{m_\pi^2 + 2\Lambda_\rho^2} . \end{aligned} \quad (3.53)$$

Effectively, the same can also be achieved by writing the two-pion loop selfenergy in terms of a once-subtracted dispersion integral [114] as

$$\begin{aligned} \Sigma_{\rho\pi\pi}^\circ(M) &= \bar{\Sigma}_{\rho\pi\pi}^\circ(M) - \bar{\Sigma}_{\rho\pi\pi}^\circ(0) \\ \bar{\Sigma}_{\rho\pi\pi}^\circ(M) &= \int \frac{p^2 dp}{(2\pi)^2} v_{\rho\pi\pi}(p)^2 G_{\pi\pi}^0(M, p) \end{aligned} \quad (3.54)$$

with the vacuum two-pion propagator

$$G_{\pi\pi}^\circ(M, p) = \frac{1}{\omega_\pi(p)} \frac{1}{M^2 - (2\omega_\pi(p))^2 + i\eta} , \quad \omega_\pi(p) = \sqrt{m_\pi^2 + p^2} \quad (3.55)$$

and vertex functions

$$v_{\rho\pi\pi}(p) = \sqrt{\frac{2}{3}} g_{\rho\pi\pi} 2p F_{\rho\pi\pi}(p) \quad (3.56)$$

involving a hadronic form factor  $F_{\rho\pi\pi}$  [47]. From gauge invariance it follows that  $q_\mu \Sigma_{\rho\pi\pi}^{\circ,\mu\nu} = 0$  and the  $\rho$  meson selfenergy can be cast in the general form

$$\Sigma_{\rho\pi\pi}^{\circ,\mu\nu}(q) = \left( -g^{\mu\nu} + \frac{q^\mu q^\nu}{M^2} \right) \Sigma_{\rho\pi\pi}^\circ(M) . \quad (3.57)$$



Iterating it to all orders by solving the Dyson equation for the propagator, one arrives at

$$D_\rho^{\circ,\mu\nu}(q) = \left( -g^{\mu\nu} + \frac{q^\mu q^\nu}{M^2} \right) D_\rho^\circ(M) \quad (3.58)$$

with the scalar part

$$D_\rho^\circ(M) = \left[ M^2 - (m_\rho^{(0)})^2 - \Sigma_{\rho\pi\pi}^\circ(M) \right]^{-1} . \quad (3.59)$$

The three free parameters (coupling constant, bare mass and cutoff) can be readily adjusted to the  $P$ -wave  $\pi\pi$  phase shifts,

$$\tan(\delta_{\pi\pi}^{JI=11}(M)) = \frac{\text{Im}D_\rho^\circ(M)}{\text{Re}D_\rho^\circ(M)} , \quad (3.60)$$

and the pion electromagnetic form factor, which, imposing VDM, becomes

$$|F_\pi^\circ(M)|^2 = (m_\rho^{(0)})^4 |D_\rho^\circ(M)|^2 , \quad (3.61)$$

cf. Fig. 3.6. Typical values are  $g_{\rho\pi\pi}^2/4\pi = (2.7 - 2.9)$ ,  $m_\rho^{(0)} = (0.82 - 0.85)$  GeV and  $\Lambda_\rho =$

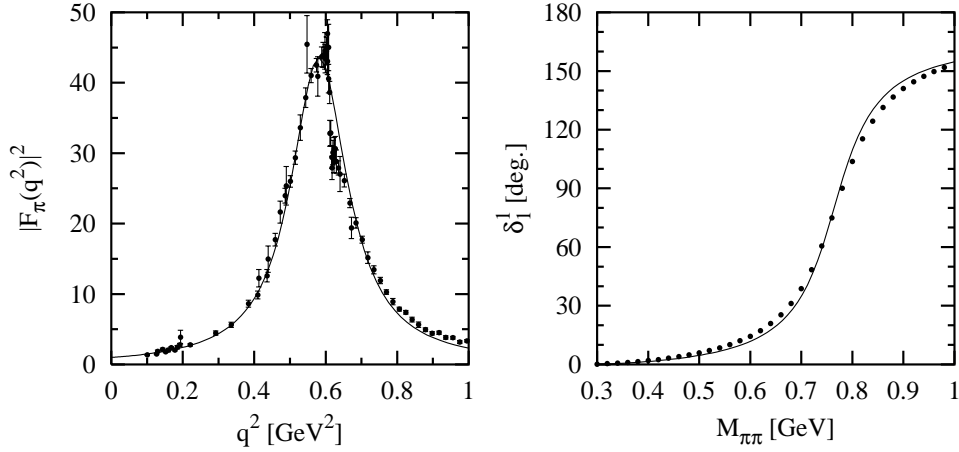


Figure 3.6: Pion electromagnetic form factor (left panel) and  $P$ -wave  $\pi\pi$  scattering phase shifts in free space as obtained in typical fits from phenomenological models for the  $\rho$  meson propagator.

(1 – 3) GeV, depending on the regularization procedure.

Based on this standard description of the free  $\rho$  meson one can distinguish two types of in-medium effects: (i) modifications of the pion cloud, leading to a temperature-dependent  $\rho\pi\pi$  selfenergy  $\Sigma_{\rho\pi\pi}$ , and (ii) scattering of the (bare)  $\rho$  meson on surrounding matter particles. Concerning (i) one needs to evaluate the in-medium properties of the pions. In a thermal pion gas they are only mildly affected chiefly because of their Goldstone nature. The corresponding pion

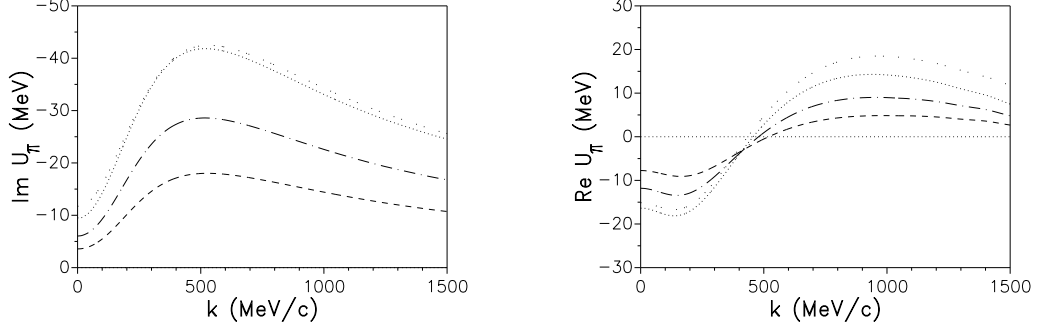


Figure 3.7: Pion 'optical' potentials (left panel: imaginary part, right panel: real part) in a hot pion gas as arising from a selfconsistent Brueckner calculation [128] of the pion selfenergy  $\Sigma_\pi$  and a chirally symmetric  $\pi\pi$  interaction ('Jülich model' [129, 130]) within the Matsubara formalism. The on-shell potentials shown are defined as  $U_\pi(k; T) = \Sigma_\pi(e_\pi(k), k; T)/2\omega_\pi(k)$ , where the quasiparticle energy  $e_\pi(k)$  is determined by the solution of  $e_\pi(k)^2 = \omega_\pi(k)^2 + \Sigma_\pi(e_\pi(k), k; T)$ . The dashed, dashed-dotted and dotted lines correspond to temperatures  $T = 150, 175$  and  $200$  MeV, respectively (the light-dotted line is obtained in first order of the selfconsistency iteration at  $T = 200$  MeV).

'optical' potentials amount to less than 10% corrections to the free pion dispersion relation even at temperatures as large as  $T = 200$  MeV [127, 128], cf. Fig. 3.7. In what follows, we shall therefore neglect the effects of a modified pion dispersion relation on the pion cloud of the  $\rho$  meson. A more important modification of  $\Sigma_{\rho\pi\pi}$  stems from the Bose-Einstein enhancement factors of the (on-shell) intermediate two-pion states, representing an enhancement of the in-medium  $\rho \rightarrow \pi\pi$  width by 'stimulated emission'. In the Matsubara formalism the (retarded) two-pion propagator (3.55) takes the form

$$G_{\pi\pi}(M, p; T) = \frac{1}{\omega_\pi(p)} \frac{[1 + 2f^\pi(\omega_\pi(p); T)]}{(M + i\eta)^2 - (2\omega_\pi(p))^2}, \quad (3.62)$$

which has been first quoted in Ref. [131]. Strictly speaking, the temperature factors are only exact for the imaginary part and the real part should be calculated from a dispersion integral. It has been shown [129], however, that the latter is well approximated by (3.62) as long as the in-medium pion dispersion relation is close to the free one. Furthermore, in Eq. (3.62) we have restricted ourselves to vanishing total three-momentum of the pion pair, the so-called 'back-to-back kinematics'. It has been verified in the model of Urban *et al.* [126] that the inclusion of finite three-momentum gives virtually identical results.

Next we turn to the contributions from direct  $\rho$  scattering off thermal mesons. In the many-body treatment of Refs. [47, 123] it has been assumed that the interactions in each spin-isospin channel are saturated by  $s$ -channel resonance formation ('leading resonance approximation'). A clue as to which meson resonances might be of importance is provided by their branching ratios

into  $\rho P$  states. This decay mode, however, is kinematically suppressed for resonance masses significantly below the naive kinematical threshold  $m_\rho + m_P$ . On the other hand, it should be emphasized that it is just these subthreshold states which potentially generate substantial strength for the in-medium  $\rho$  meson spectral function at low invariant masses (*e.g.*, in  $\rho\pi \rightarrow \omega(782)$  where, given a typical thermal pion energy of 300–400 MeV, the appropriate  $\rho$  meson mass would be  $M \simeq 400 - 500$  MeV). Using VDM the subthreshold states can be largely identified through their radiative decays  $R \rightarrow P\gamma$ . The various resonances  $R$  in  $\rho P$  collisions can be grouped into three major categories, namely vectors  $V$ , axialvectors  $A$  and pseudoscalars  $P'$ . Following Ref. [123] we restrict our discussion to states with masses  $m_R \leq 1.3$  GeV; higher ones are only relevant for invariant  $\rho$  masses beyond  $M \simeq 1$  GeV.

For  $\rho PA$  vertices a suitable interaction Lagrangian, compatible with chiral symmetry and electromagnetic current conservation, is given by

$$\mathcal{L}_{\rho PA} = G_{\rho PA} A_\mu (g^{\mu\nu} q_\alpha p^\alpha - q^\mu p^\nu) \rho_\nu P, \quad (3.63)$$

although other choices are possible [124]. The  $\rho P$  scattering via intermediate vector mesons  $V$  is determined by Wess-Zumino anomaly terms which are of unnatural parity and involve the four-dimensional antisymmetric Levi-Civita tensor  $\epsilon^{\mu\nu\sigma\tau}$ :

$$\mathcal{L}_{\rho PV} = G_{\rho PV} \epsilon_{\mu\nu\sigma\tau} k^\mu V^\nu q^\sigma \rho^\tau P. \quad (3.64)$$

In both Lagrangians (3.63) and (3.64),  $p^\mu$ ,  $q^\mu$  and  $k^\mu$  denote the four-momenta of the pseudoscalar,  $\rho$  and (axial-) vector mesons, respectively. As a third possibility  $\rho P$  scattering can proceed via a pseudoscalar resonance. Here an obvious candidate is  $\rho\pi \rightarrow \pi'(1300)$  which can be described by

$$\mathcal{L}_{\rho PP'} = G_{\rho PP'} P' (k \cdot q p_\mu - p \cdot q k_\mu) \rho^\mu P. \quad (3.65)$$

With increasing temperature the heat bath will consist of more and more heavier resonances, especially those with high spin-isospin degeneracy. After the light pseudoscalars the meson multiplet with the smallest masses are the vectors, most notably the  $\rho$  meson with nine-fold degeneracy. Motivated by the observation that the  $f_1(1285)$  resonance exhibits a large  $\rho\gamma$  decay width (together with a predominant  $4\pi$  decay), it has been interpreted as a 'resonance' in  $\rho\rho$  scattering [123]. The interaction vertex is also related to anomaly terms [132] and has been chosen in the following form,

$$\mathcal{L}_{\rho VA} = G_{\rho VA} \epsilon_{\mu\nu\sigma\tau} p^\mu V^\nu \rho^{\sigma\alpha} k_\alpha A^\tau - \frac{\lambda}{2} (k_\beta A^\beta)^2, \quad (3.66)$$

which again satisfies the appropriate conservation laws. Here, the kinetic-energy term of the axialvector field has been explicitly written to indicate a gauge freedom associated with the constant  $\lambda$  [133]. For practical purposes – following Ref. [123] –  $\lambda$  has been set to 1.

The free parameters involved, which are the coupling constants and the cutoffs for the hadronic vertex form factors, can be rather accurately determined from a simultaneous fit to both the hadronic  $R \rightarrow \rho P$  and radiative  $R \rightarrow \rho\gamma$  branching ratios as will be detailed in Sect. 4.1.1.

Within the imaginary time (Matsubara) formalism the  $\rho$  meson selfenergy tensor arising from binary collisions can now be calculated as

$$\Sigma_{\rho h}^{\mu\nu}(q) = \int \frac{d^3p}{(2\pi)^3} \frac{1}{2\omega_h(p)} [f^h(\omega_h(p)) - f^R(k_0)] \mathcal{M}_{\rho h}^{\mu\nu}(p, q) \quad (3.67)$$

with the thermal Bose-Einstein distribution function  $f^h(\omega_h(p)) = [\exp(\omega_h(p))/T - 1]^{-1}$  of the corresponding hadron species  $h$  with on-shell energy  $\omega_h(p) = \sqrt{m_h^2 + \vec{p}^2}$ .  $\mathcal{M}_{\rho h}^{\mu\nu}$  denotes the isospin-averaged forward scattering amplitude which, in the leading resonance approximation employed here, can be written as

$$\mathcal{M}_{\rho h R}^{\mu\nu}(p, q) = IF G_{\rho h R}^2 F_{\rho h R}(q_{cm})^2 D_R(s) v_R^{\mu\nu}(p, q) . \quad (3.68)$$

The explicit expressions for the vertex functions  $v_R^{\mu\nu}(p, q)$  can be derived from the above interaction Lagrangians as has been done in Ref. [123].  $IF$  denotes an isospin factor and the hadronic vertex form factor has been chosen of dipole type

$$F_{\rho h R}(q_{cm}) = \left( \frac{2\Lambda_{\rho h R}^2 + m_R^2}{2\Lambda_{\rho h R}^2 + [\omega_\rho(q_{cm}) + \omega_P(q_{cm})]^2} \right)^2 , \quad (3.69)$$

normalized to 1 at the resonance mass  $m_R$ . The scalar part of the intermediate resonance propagators is given by

$$D_R(s) = \frac{1}{s - m_R^2 + im_R \Gamma_R^{\text{tot}}(s)} \quad (3.70)$$

with  $s = k^2 = (p + q)^2$  and the total resonance width  $\Gamma_R^{\text{tot}}(s)$ . Using the standard projection operators of Eq. (2.99) the selfenergy tensors (3.67) can be conveniently decomposed into longitudinal and transverse components,

$$\Sigma_\rho^{\mu\nu}(q) = \Sigma_\rho^L(q_0, \vec{q}) P_L^{\mu\nu} + \Sigma_\rho^T(q_0, \vec{q}) P_T^{\mu\nu} , \quad (3.71)$$

which build up two independent modes of the in-medium  $\rho$  propagator according to

$$D_\rho^{\mu\nu}(q) = \frac{P_L^{\mu\nu}}{M^2 - (m_\rho^{(0)})^2 - \Sigma_\rho^L(q_0, \vec{q})} + \frac{P_T^{\mu\nu}}{M^2 - (m_\rho^{(0)})^2 - \Sigma_\rho^T(q_0, \vec{q})} + \frac{q^\mu q^\nu}{(m_\rho^{(0)})^2 M^2} . \quad (3.72)$$

Fig. 3.8 shows the individual contributions to the spin-averaged selfenergy,

$$\Sigma_{\rho h R}(M, \vec{q}) = \frac{1}{3} [\Sigma_{\rho h R}^L(M, \vec{q}) + 2\Sigma_{\rho h R}^T(M, \vec{q})] , \quad (3.73)$$

at fixed three-momentum modulus  $|\vec{q}| = 0.3$  GeV and temperature  $T = 150$  MeV. Around and above the free  $\rho$  meson mass the strongest absorption is caused by  $a_1(1260)$  resonance formation, which is about as large as the sum of all other channels, shared to roughly equal parts among  $K_1(1270)$ ,  $h_1(1170)$  and  $\pi'(1300)$ . The  $K_1(1270)$  contribution acquires its maximum at lower  $M$  than the pion-resonances due to the higher thermal energies of the kaons (including their rest mass). In the low-mass region,  $M \leq 0.6$  GeV, the prevailing contribution is due to the  $\omega$  meson which, however, leaves little trace in the resonance region. It is also seen that the effect of the  $f_1$  meson is very small. In the real part of the total selfenergy one observes appreciable cancellations until eventually all contributions turn repulsive (the latter feature is likely to be modified when accounting for further higher resonances). Such cancellations are typical for this kind of many-body calculations. They are the reason that one usually encounters only moderate modifications of the in-medium

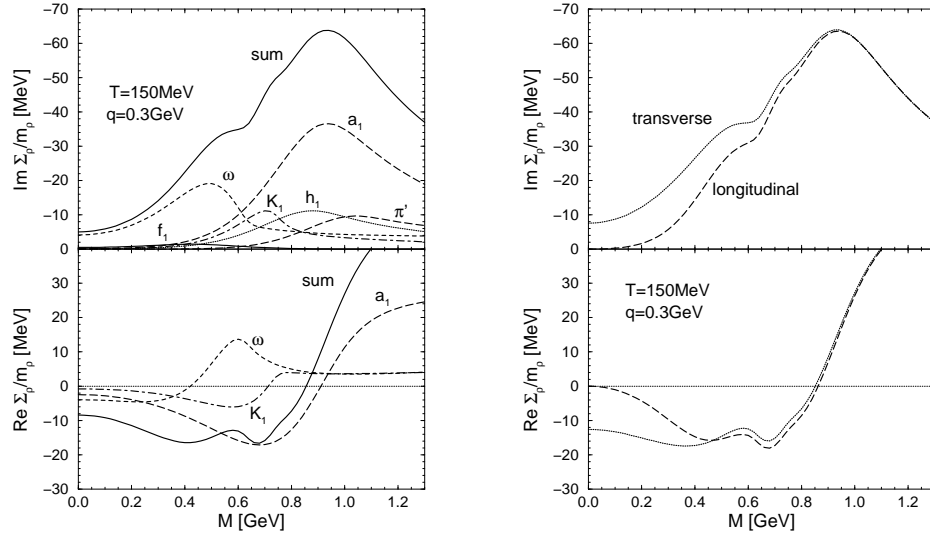


Figure 3.8: The real and imaginary parts (lower and upper panels, respectively) of the polarization-averaged  $\rho$  selfenergy (left panel) from resonant scattering off thermal  $\pi, K, \bar{K}$  and  $\rho$  mesons in a heat bath at  $T = 150$  MeV and  $\mu_\pi = 0$ ; the different channels are labeled by their intermediate resonances; right panel: polarization decomposition of the combined selfenergy contributions.

pole masses. On the other hand, the imaginary parts of  $\Sigma_\rho$  strictly add up, generating significant broadening. Not shown here is the in-medium Bose enhancement of the  $\rho \rightarrow \pi\pi$  selfenergy. It has a very smooth behavior with a broad maximum of  $\text{Im}(\Sigma_{\rho\pi\pi}(M; T) - \Sigma_{\rho\pi\pi}^0(M))/m_\rho \simeq 25$  MeV at about  $M \simeq 0.6$  GeV. We also note that the three-momentum dependence of the selfenergies is rather weak, being most pronounced at low  $M$  where the transverse part is responsible for the build-up of finite values. This can be seen more explicitly from the right panel of Fig. 3.8 where the summed selfenergy contributions have been separated into the two polarization states.

In Fig. 3.9 the full spin-averaged imaginary part of the  $\rho$  meson propagator,

$$\text{Im}D_\rho(M, \vec{q}; T) = \frac{1}{3} [\text{Im}D_\rho^L(M, \vec{q}; T) + 2\text{Im}D_\rho^T(M, \vec{q}; T)] , \quad (3.74)$$

in a thermal meson gas of temperatures  $T = 120, 150$  and  $180$  MeV (left panel) as appropriate for the hadronic phase in ultrarelativistic heavy-ion collisions is shown. More explicitly, one has

$$\text{Im}D_\rho^{L,T}(M, \vec{q}) = \frac{\text{Im}\Sigma_\rho^{L,T}(M, \vec{q})}{|M^2 - (m_\rho^{(0)})^2 - \Sigma_\rho^{L,T}(M, \vec{q})|^2} \quad (3.75)$$

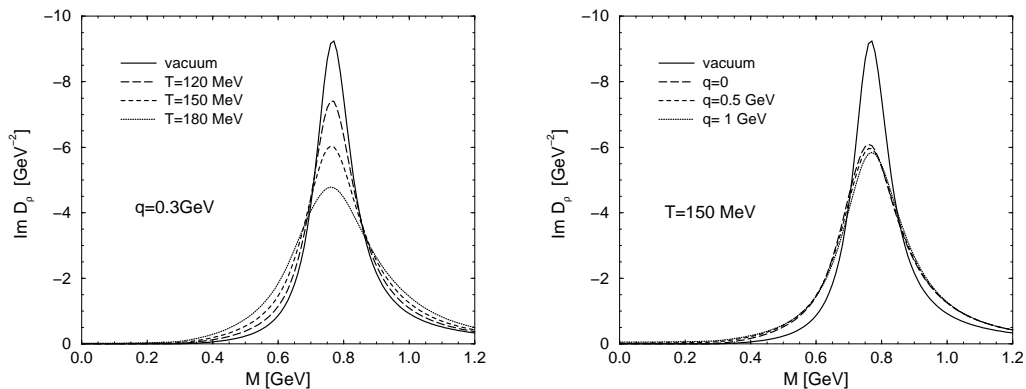


Figure 3.9: Imaginary part of the  $\rho$  propagator (which, up to a factor of  $(-2)$ , coincides with the spectral function) in the vacuum (full curve) and in a thermal  $\pi K \bar{K} \rho$  gas as calculated in the many-body framework of Ref. [47, 123]; left panel: for fixed three-momentum  $q = 0.3$  GeV at temperatures  $T = 120$  MeV (long-dashed curve),  $T = 150$  MeV (dashed curve) and  $T = 180$  MeV (dotted curve); right panel: for fixed temperature  $T = 150$  MeV at three-momenta  $q = 0$  (long-dashed curve),  $q = 0.5$  GeV (dashed curve) and  $q = 1$  GeV (dotted curve).

with the longitudinal and transverse selfenergy parts

$$\Sigma_{\rho}^{L,T} = \Sigma_{\rho\pi\pi} + \sum_{\alpha} \Sigma_{\rho\alpha}^{L,T}, \quad (3.76)$$

where the summation is over the mesonic excitation channels  $\alpha = \pi\omega, \pi h_1, \pi a_1, \pi\pi', KK_1, \bar{K}\bar{K}_1, \rho f_1$ , as discussed, and  $\Sigma_{\rho\pi\pi}$  now contains the Bose-Einstein factors through Eq. (3.62). The thermal  $\rho$  meson spectral function exhibits an additional broadening (defined as the full width at half maximum) of about 80 MeV at  $T = 150$  MeV which almost doubles to  $\sim 155$  MeV at  $T = 180$  MeV. On the other hand, the three-momentum dependence of the spectral function at fixed temperature is rather weak, cf. right panel of Fig. 3.9.

The results of the many-body approach are quite close to those obtained recently using kinetic theory [122] (see Fig. 3.5). The latter, however, attribute some portion of the collisional broadening to  $t$ -channel meson exchanges. Those have not been included in the many-body calculations, where the net medium effect is entirely driven by large imaginary parts from resonant  $s$ -channel interactions (including subthreshold states). At tree level, the neglected  $t$ -channel exchanges do not generate an imaginary part. They would do so once iterated in a Lippmann-Schwinger-type equation to construct a scattering amplitude beyond tree level. In this case, however, care has to be taken in avoiding double counting when performing a combined treatment of  $s$ - and  $t$ -channel graphs (in fact, the 'leading resonance approximation' implies that non-resonant interactions are, at least partially, subsumed in the resonance parameters). For the  $\rho$  meson selfenergy in a hot pion

gas an unambiguous way to disentangle  $s$ - and  $t$ -channel interactions would require experimental information on  $\pi\rho$  scattering phase shifts which, owing to the short lifetime of the  $\rho$  meson, can only be inferred by very indirect means.

## 3.2 Finite Baryon Density

The investigation of vector meson modifications in an environment of finite nucleon density via effective hadronic models has mainly been pursued within more phenomenologically oriented approaches. This is partly due to the fact that the impact of chiral symmetry on  $\rho$ -nucleon interactions is much less obvious than in the purely mesonic case (such as  $\pi\rho a_1$  dynamics). Also, the extension of VDM to the baryonic sector is less accurate such that electromagnetic observables provide less direct access to vector meson interactions involving baryons. Pionic interactions with nucleons and nuclei, on the other hand, are much better known: a wealth of pion-nucleus scattering data has provided a detailed understanding of the underlying physical mechanisms for their modification in cold nuclear matter [134] which are substantial. Since especially  $\rho$  mesons (and, to a lesser extent, also  $\omega$  mesons) exhibit a strong coupling to two- (three-) pion states, early analyses have focused on medium effects in the virtual pion cloud. These developments will be reviewed in the second part of this Section. Subsequently it has been realized that also direct  $\rho$ - $N$  interactions can induce substantial modifications of the  $\rho$  meson spectral function which we will discuss in the third part of this Section. The first part, however, will be devoted to recall the mean-field based analysis of effective chiral Lagrangians by Brown and Rho [45] which culminated in the famous conjecture of 'Brown-Rho Scaling'. It is not exaggerated to say that, although (or just because) this conjecture is controversial, the associated hypothesis for a 'dropping' of vector meson masses has been one of the main triggers for an ensuing intense theoretical (and experimental) activity.

### 3.2.1 Mean-Field Approach: Brown-Rho Scaling

As we have already eluded to in Sect. 2.1, in the massless limit the QCD action is scale invariant on the classical level implying that the QCD Lagrangian has scale dimension 4. Chiral meson Lagrangians, being constructed as effective low-energy theories of QCD, should in principle exhibit the same property. In the non-linear realization they are formulated in terms of the chiral field  $U \equiv e^{i\pi/f_\pi}$  ( $\pi = \vec{\pi} \cdot \vec{\tau}$ ) which, when including up to fourth-order derivatives (involving the quartic 'Skyrme term'), read

$$\mathcal{L} = \frac{f_\pi^2}{4} \text{tr}(\partial_\mu U \partial^\mu U) + \frac{\eta^2}{4} \text{tr} [U^\dagger \partial_\mu U, U^\dagger \partial_\nu U]^2 + c \text{tr}(\mathcal{M}^\circ U + \text{h.c.}) . \quad (3.77)$$

Here, also the explicit symmetry breaking term being proportional to the current quark mass  $m_q$  in the quark mass matrix  $\mathcal{M}^\circ$  has been incorporated. As has been argued in Ref. [135] the  $U$  field carries scale dimension zero which means that the three terms on the *r.h.s.* have scale dimensions 2,4 and 0, respectively.

Following Ref. [45] the first step in the derivation of Brown-Rho scaling consists of modifying the effective Lagrangian (3.77) to reflect the appropriate scaling behavior of the QCD Lagrangian.

The simplest way to restore it has been proposed by Ellis *et al.* [135] and is realized by introducing an effective 'glueball' field  $\chi$  with scale dimension 1 according to

$$\begin{aligned} \mathcal{L}_\chi = & \frac{f_\pi^2}{4} \left( \frac{\chi}{\chi_0} \right)^2 \text{tr}(\partial_\mu U \partial^\mu U) + \frac{\eta^2}{4} \text{tr} [U^\dagger \partial_\mu U, U^\dagger \partial_\nu U]^2 + \frac{1}{2} \partial_\mu \chi \partial^\mu \chi \\ & + c \left( \frac{\chi}{\chi_0} \right)^3 \text{tr}(\mathcal{M}^\circ U + \text{h.c.}) + V(\chi) . \end{aligned} \quad (3.78)$$

Besides a scale invariant (*i.e.*, dimension-4) kinetic energy term for the glueball field a potential-energy term of the form

$$V(\chi) = B \left[ \frac{1}{4} \chi_0^4 + \chi^4 \ln(\chi/e^4 \chi_0) \right] \quad (3.79)$$

has also been added. Minimizing  $V$  in  $\chi$  yields a nonzero ground state expectation value  $\chi_0 \equiv \langle 0|\chi|0\rangle$  signaling the spontaneous breakdown of scale invariance which mimics the (quantum part of the) QCD scale anomaly on the effective Lagrangian level. The divergence of the corresponding dilation current (2.21) becomes [135]

$$\partial_\mu j_D^\mu = -B\chi^4 . \quad (3.80)$$

Thus, comparing to the trace anomaly of QCD (2.22)  $\chi_0$  can be related to the gluon condensate  $\langle G^2 \rangle$ . In addition, the QCD trace anomaly receives a contribution from explicit scale breaking through the quark mass term  $(\bar{\psi} \mathcal{M}^\circ \psi)$  which has scale dimension 3 requiring the  $\chi^3$  factor in the corresponding term in Eq. (3.78).

As has been emphasized by Brown and Rho in subsequent work [136], the introduced  $\chi$ -field is to be understood as consisting of a 'soft' (mean-field) and a 'hard' (fluctuation) component according to

$$\chi = \chi^* + \chi' . \quad (3.81)$$

It is the soft mean-field component  $\chi^*$  that will govern the medium modifications in the chiral effective Lagrangian, whereas the hard component  $\chi'$  is to be associated with the glueball mass scale of  $> 1$  GeV, well beyond the applicability range of low-energy effective theory. Indeed, as discussed in Sect. 2.4, lattice calculations show that in the chiral transition with light quarks only about half of the gluon condensate is 'melted', corresponding to the  $\chi^*$  field (an analogous feature emerges within the instanton model [54] where it has been identified as a rearrangement of the chirally broken 'random' instanton liquid into a chirally restored phase with  $I$ - $A$  molecules, the latter characterizing the 'hard' component of the gluon fields that survive the transition).

In their second main step Brown and Rho postulate that, as the (quark and gluon) condensates change in dense matter, the symmetries of the Lagrangian remain intact such that the variation in the condensates can be absorbed in a density-dependent change in masses and coupling constants of the effective theory. In line with the above arguments, the change in the quark condensate at a given density can be expressed as

$$\frac{\langle\langle \bar{\psi} \psi \rangle\rangle}{\langle \bar{\psi} \psi \rangle} = \left( \frac{\chi^*}{\chi_0} \right)^3 , \quad (3.82)$$



where  $\tilde{\chi}_0$  denotes the vacuum expectation value of the  $\chi^*$  field. This suggests to define an in-medium pion decay constant as

$$f_\pi^* = f_\pi \frac{\chi^*}{\tilde{\chi}_0} \quad (3.83)$$

leading to the effective Lagrangian of the form

$$\mathcal{L}^* = \frac{f_\pi^{*2}}{4} \text{tr}(\partial_\mu U \partial^\mu U) + \frac{\eta^2}{4} \text{tr} [U^\dagger \partial_\mu U, U^\dagger \partial_\nu U]^2 + c \left( \frac{f_\pi^*}{f_\pi} \right)^3 \text{tr}(\mathcal{M}^\circ U + \text{h.c.}) + \dots, \quad (3.84)$$

where the fields are now defined as ensemble averages in cold nuclear matter, *i.e.*,  $\chi^* \equiv \langle\langle \chi \rangle\rangle$  etc.. In particular, with

$$U = \exp(i\pi^*/f_\pi^*), \quad (3.85)$$

the pion field  $\pi^* \equiv \pi \chi^*/\tilde{\chi}_0$  has picked up a scale dimension of one. Furthermore, it was argued that the fluctuating part of the glueball field strongly mixes with an effective low-lying  $\sigma$  meson (the quark-antiquark component of the scalar), and therefore the effective mass of the latter is inferred from

$$f_\pi^*/f_\pi \approx \chi^*/\tilde{\chi}_0 \approx m_\sigma^*/m_\sigma. \quad (3.86)$$

Moreover, when using the Goldberger-Treiman relation one has

$$m_N^*/m_N \approx (g_A^*/g_A)^{1/2} f_\pi^*/f_\pi. \quad (3.87)$$

Since in the Skyrme model, the (scale invariant) coefficient  $\eta^2$  of the quartic Skyrme term is directly related to the axialvector coupling constant  $g_A$ , the latter is not affected at the mean-field level. (The 'quenching' of  $g_A$  from 1.26 to 1, observed in Gamow-Teller and magnetic transitions in nuclei, has been argued to be due to loop effects, indicating an additional, lower scale induced in nuclei). Finally, making use of the KSFR relation [86],

$$m_V^2 = 2g^2 f_\pi^2, \quad (3.88)$$

and the fact that within the Skyrme model the hidden-gauge coupling  $g^2 = \frac{1}{8}\eta^2$  is scale invariant, the vector meson masses are conjectured to complete the (approximate) Brown-Rho (BR) scaling relation:

$$\Phi(\varrho) \equiv \frac{f_\pi^*}{f_\pi} = \frac{m_\sigma^*}{m_\sigma} = \frac{m_N^*}{m_N} = \frac{m_\rho^*}{m_\rho} = \frac{m_\omega^*}{m_\omega}. \quad (3.89)$$

In fact, early QCD sum rules calculations of Hatsuda and Lee [46] have given support to this relation, as discussed in Sect. 2.7, with typical values for  $\Phi(\varrho_0) = 0.82 \pm 0.06$  at normal nuclear matter density.

There might be, however, some problems with the BR scaling hypothesis, mainly in the finite temperature sector. On very general grounds the chiral condensate is locally altered whenever a hadron is present as discussed in Sect. 2.3. This leads to the dilute gas expressions (2.44) and (2.45) which are rigorously valid at low temperature and low density. Even though the quark condensate is decreased, by definition, nothing happens to the masses, the pion and the nucleon in this case. Secondly, when applied at low temperatures, the scaling relation (3.89) is at variance

with the low-temperature expansion of the in-medium vector and axialvector correlators (2.103) and the chiral condensate ratio (2.50). While the latter is reduced already at order  $O(T^2)$ , the  $T^2$ -dependence of the correlators is governed by mixing and corrections to the mass are of order  $O(T^4)$  (in the chiral limit). This is implied by chiral symmetry [88] and manifest in various effective models that we have discussed in the previous Section.

### 3.2.2 Pion Cloud Modifications

Let us first recall some basic features of the single-pion properties in nuclear matter (for a review see, *e.g.*, Ref. [137]). The most prominent effect on (on-shell) pions propagating through the nuclear environment is generated through resonant  $P$ -wave interactions exciting isobar-hole ( $\Delta N^{-1}$ ) states. As is well-known from pion nuclear physics another important pionic excitation channel is represented by  $P$ -wave nucleon-hole ( $NN^{-1}$ ) states. On the other hand,  $S$ -wave  $\pi N$  interactions are suppressed by about an order of magnitude in symmetric nuclear matter owing to an almost exact cancellation between the isospin 1/2 and 3/2 partial waves [134]. The standard Lagrangians for the  $\pi NN$  and  $\pi N\Delta$   $P$ -wave interactions are given (in non-relativistic form) by

$$\begin{aligned}\mathcal{L}_{\pi NN} &= \frac{f_{\pi NN}}{m_\pi} \Psi_N^\dagger \vec{\sigma} \cdot \vec{k} \vec{\tau} \cdot \vec{\pi} \Psi_N \\ \mathcal{L}_{\pi N\Delta} &= \frac{f_{\pi N\Delta}}{m_\pi} \Psi_\Delta^\dagger \vec{S} \cdot \vec{k} \vec{T} \cdot \vec{\pi} \Psi_N + \text{h.c.} ,\end{aligned}\quad (3.90)$$

which leads to corresponding pion selfenergies in nuclear matter of the type

$$\Sigma_{\pi\alpha}^{(0)}(k) = -\vec{k}^2 \chi_{\pi\alpha}^{(0)}(k) \quad (3.91)$$

( $k = (k_0, \vec{k})$ ,  $\alpha = NN^{-1}, \Delta N^{-1}$ ). The so-called (pionic) susceptibilities are given by

$$\chi_{\pi\alpha}^{(0)}(k) = \left( \frac{f_{\pi\alpha} F_{\pi\alpha}(k)}{m_\pi} \right)^2 SI(\pi\alpha) \phi_\alpha(k) \quad (3.92)$$

in terms of spin-isospin factors  $SI(\pi\alpha)$ , coupling constants  $f_{\pi\alpha}$  (cf. Table 3.1) and a hadronic vertex form factor usually chosen of monopole type,

$$F_{\pi\alpha}(k) = \left( \frac{\Lambda_\pi^2 - m_\pi^2}{\Lambda_\pi^2 + \vec{k}^2} \right). \quad (3.93)$$

In Eq. (3.92),  $\phi_\alpha$  denote the Lindhard functions which, for the more general case of a  $\alpha = ab^{-1}$  particle-hole excitation, read

$$\phi_\alpha(k) = - \int \frac{p^2 dp}{(2\pi)^2} f^b[E_b(p)] \int_{-1}^{+1} dx \sum_{\pm} \frac{1 - f^a[E_a(\vec{p} + \vec{k})]}{\pm k_0 + E_b(p) - E_a(\vec{p} + \vec{k}) \pm \frac{1}{2}(\Gamma_a + \Gamma_b)} \quad (3.94)$$

including direct (sign '+') and exchange (sign '-') diagrams with

$$\begin{aligned}E_a(p) &= (m_a^2 + p^2)^{1/2} , \\ E_b(\vec{p} + \vec{k}) &= (m_b^2 + p^2 + k^2 + 2pkx)^{1/2}\end{aligned}\quad (3.95)$$

$\pi\alpha$	$\pi NN^{-1}$	$\pi\Delta N^{-1}$	$\pi N\Delta^{-1}$	$\pi\Delta\Delta^{-1}$
$SI(\pi\alpha)$	4	16/9	16/9	400
$f_{\pi\alpha}^2/4\pi$	0.08	0.32	0.32	0.0032

Table 3.1: *Spin-isospin transition factors and coupling constants for pion induced (longitudinal) P-wave particle-hole excitations in a hot  $N\Delta$  gas [138].*

and Fermi-Dirac distribution functions  $f^a, f^b$ .  $\Gamma_a$  and  $\Gamma_b$  are the (energy- and density-dependent) total decay widths of particle  $a$  and hole  $b^{-1}$ , respectively (notice that the holes carry the imaginary part with opposite sign). For a realistic description of the pion selfenergy short-range correlations between particle and hole have to be accounted for. These are conveniently parameterized in terms of 'Migdal parameters'  $g'_{\alpha\beta}$ , which also induce a mixing between the channels. The resulting system of coupled equations,

$$\chi_\alpha = \chi_\alpha^{(0)} - \sum_\beta \chi_\beta^{(0)} g'_{\alpha\beta} \chi_\beta, \quad (3.96)$$

is solved by an elementary matrix inversion yielding

$$\Sigma_\pi(k_0, \vec{k}) = -\vec{k}^2 \sum_\alpha \chi_\alpha(k_0, \vec{k}). \quad (3.97)$$

As an illustrative example we show in Fig. 3.10 the off-shell two-pion propagator (restricted to zero total momentum) in nuclear matter,

$$\begin{aligned} G_{\pi\pi}(E, \vec{k}) &= \int \frac{idk_0}{\pi} D_\pi(k_0, \vec{k}) D_\pi(E - k_0, -\vec{k}) \\ D_\pi(k_0, \vec{k}) &= \left[ k_0^2 - \vec{k}^2 - m_\pi^2 - \Sigma_\pi(k_0, \vec{k}) \right]^{-1}, \end{aligned} \quad (3.98)$$

which directly enters into the two-pion selfenergy of the  $\rho$  meson, cf. Eq. (3.54). Clearly, the combination of  $\Delta N^{-1}$  and  $NN^{-1}$  excitations entails a rather rich structure with substantial shifts of strength towards low energies (*i.e.*, invariant  $\rho$  masses).

Besides the modification of the intermediate pion propagators in the in-medium  $\rho$  meson selfenergy, the  $\Delta N^{-1}$ - and  $NN^{-1}$ -bubbles induce a number of corresponding vertex corrections for the  $\rho\pi\pi$  and  $\rho\rho\pi\pi$  couplings that have to be incorporated to ensure transversality (*i.e.*, gauge invariance) of the resulting vector propagator. They can be systematically inferred from the appropriate Ward-Takahashi identities [139], as will be detailed below. The first investigations along these lines were performed by Herrmann *et al.* [140], Chanfray and Schuck [114] as well as Asakawa *et al.* [141]. Their calculations were restricted to the effects from the  $\Delta N^{-1}$  excitation and to vanishing total 3-momentum  $\vec{q} = 0$  of the  $\rho$  meson. Nevertheless, appreciable modifications of the spectral function were found, in particular an in-medium broadening as well as a rather pronounced peak structure at invariant masses  $M \simeq 3m_\pi$  stemming from transverse  $\Delta N^{-1}$  excitations (corresponding to the vertex correction represented by the left diagram in the middle panel of Fig. 3.12). In a next

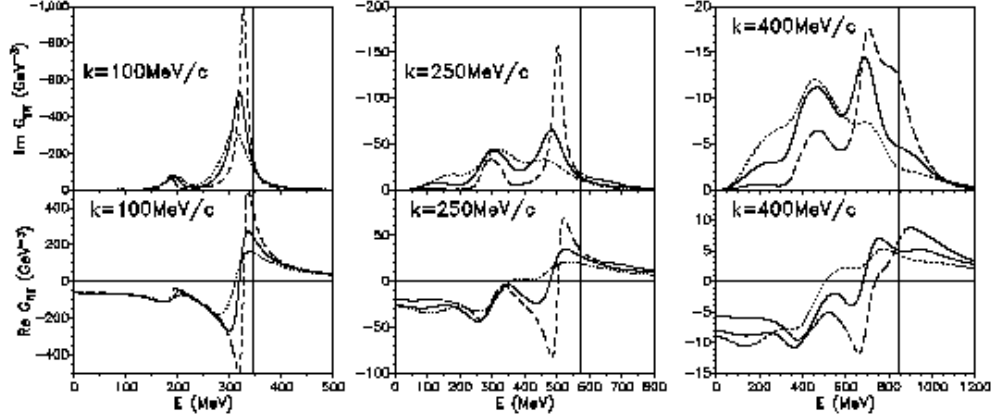


Figure 3.10: Two-pion propagator (upper panels: imaginary part, lower panels: real part) in cold nuclear matter at densities  $\varrho_N/\varrho_0 = 0.5, 1,$  and  $1.5$  represented by the long-dashed, full and dotted lines, respectively (the pion selfenergies have been evaluated using the  $\pi\alpha$  form factor cutoff from the Bonn potential,  $\Lambda_{\pi NN} = \Lambda_{\pi N\Delta} = 1.2$  GeV, together with correspondingly large values for the Migdal parameters of  $g'_{NN} = 0.8, g'_{N\Delta} = 0.5$ ). The vertical lines indicate the on-shell two-pion energy  $E_{on} = 2\omega_\pi(k)$  in free space.

step, the additional effects from  $P$ -wave  $NN^{-1}$  excitations were incorporated in Refs. [142, 47]. Although the  $NN^{-1}$  channel predominantly populates the space-like momenta in the in-medium pion spectral function, it is nevertheless of significance for the  $\rho$  selfenergy, since the off-shell integration over intermediate pion states does involve space-like pion kinematics, generating additional low-mass strength in the spectral function, as we have seen above. At the same time, additional broadening at the  $\rho$  meson resonance peak emerges.

In subsequent work, Urban *et al.* [126] could overcome the restriction to back-to-back kinematics of the previous analyses. One starts from the Ward-Takahashi identities, which for the  $\rho\pi\pi$  and  $\rho\rho\pi\pi$  interaction vertices from Eq. (3.50) read

$$q^\mu \Gamma_{\mu ab}^{(3)}(k, q) = g_{\rho\pi\pi} \epsilon_{3ab} \left( D_\pi^{-1}(k+q) - D_\pi^{-1}(k) \right) \quad (3.99)$$

$$q^\mu \Gamma_{\mu\nu ab}^{(4)}(k, k, q) = ig_{\rho\pi\pi} \left( \epsilon_{3ca} \Gamma_{\nu bc}^{(3)}(k, -q) - \epsilon_{3bc} \Gamma_{\nu ca}^{(3)}(k+q, -q) \right), \quad (3.100)$$

respectively. The spin, isospin and momentum assignments are indicated in Fig. 3.11 (for simplicity, we only consider neutral  $\rho$  mesons characterized by the third isospin component of the isovector  $\vec{\rho}$  field). In free space, where

$$\begin{aligned} \Gamma_{\mu ab}^{(3),0}(k, q) &= g_{\rho\pi\pi} \epsilon_{3ab} (2k+q)_\mu \\ \Gamma_{\mu\nu ab}^{(4),0}(k_1, k_2, q) &= 2ig_{\rho\pi\pi}^2 (\delta_{ab} - \delta_{3a}\delta_{3b}) g_{\mu\nu}, \end{aligned} \quad (3.101)$$

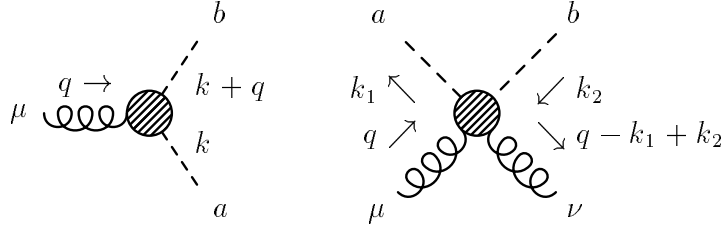


Figure 3.11:  $\rho\pi\pi$  (left) and  $\rho\pi\pi$  (right) vertices involving neutral  $\rho$  mesons (curly lines);  $\mu, \nu$  correspond to the  $\rho$  meson polarizations, whereas  $a, b$  are isospin indices of the pions (dashed lines); all other labels refer to the in-/outgoing four momenta.

Eqs. (3.99) and (3.100) are trivially satisfied. In nuclear matter, when including  $NN^{-1}$  and  $\Delta N^{-1}$  loops in the pion propagation, the required in-medium vertex corrections can be constructed by coupling the  $\rho$  meson to the lines and vertices of the pion selfenergy insertions in all possible ways, leading to the diagrams displayed in Fig. 3.12. The final result for the  $\rho$  meson selfenergy tensor in cold nuclear matter can then be written as

$$\begin{aligned} \Sigma_{\rho\pi\pi}^{\mu\nu}(q) &= i\frac{1}{2} \int \frac{d^4k}{(2\pi)^4} iD_\pi(k) \Gamma_{ab}^{(3)\mu}(k, q) iD_\pi(k+q) \Gamma_{ba}^{(3)\nu}(k+q, -q) \\ &+ i\frac{1}{2} \int \frac{d^4k}{(2\pi)^4} iD_\pi(k) \Gamma_{aa}^{(4)\mu\nu}(k, k, q) . \end{aligned} \quad (3.102)$$

The tensor can be decomposed into longitudinal and transverse components in the usual way, see Eq. (3.71). In Fig. 3.13 the spin-averaged  $\rho$  spectral function is shown for various densities (left panel) and 3-momenta (right panel). As opposed to Fig. 3.10 the underlying  $\pi NN$  and  $\pi N\Delta$  form factor cutoffs (cf. Eq.(3.93)), which essentially determine the magnitude of the medium effects, have been fixed at  $\Lambda_{\pi NN} = \Lambda_{\pi N\Delta} = 300$  MeV (together with rather small Migdal parameters of  $g'_{NN} = 0.6$ ,  $g'_{N\Delta} = 0.2$ ). These choices emerge as a consequence of model constraints imposed through the analysis of  $\pi N \rightarrow \rho N$  scattering data (this will be discussed in detail in Sect. 4.1.1 where we also elaborate on the appearance of such 'unnaturally' soft form factors). In spite of the soft form factors, the  $\rho$  meson spectral function still exhibits a significant broadening due to the pion cloud modifications, being about 55 MeV at nuclear saturation density. However, this is substantially smaller as compared to earlier calculations [140, 114, 141, 47, 126] where the  $\pi\alpha$  form factors were used with the 'Bonn value' (1.2 GeV) [143] for the cutoff. On the other hand, the common feature shared by all previous calculations, *i.e.*, an upward shift of the resonance peak persists. Furthermore, the relative smallness of the medium effects does not allow for a strongly developed momentum dependence: the most significant feature of finite momenta is an enhancement of the spectral function for low invariant masses  $M \leq 0.4$  GeV (see right panel of Fig. 3.13; for the chosen momentum of  $q = 0.5$  GeV the effects are largest).

On more general grounds it is important to note that the models for the in-medium  $\rho$  propagator

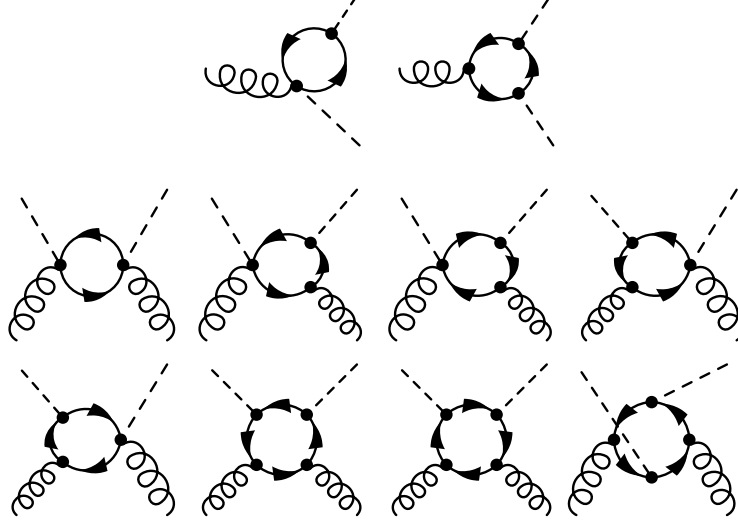


Figure 3.12: In-medium corrections to the  $\rho\pi\pi$  (upper panel) and  $\rho\rho\pi\pi$  vertex (middle and lower panel) when including  $NN^{-1}$  and  $\Delta N^{-1}$  excitations in the intermediate pion propagators of the  $\rho$  selfenergy; curly lines:  $\rho^0$ 's, dashed lines:  $\pi$ 's, solid lines: nucleons or deltas (when forward-going) and nucleon holes (backward-going).

discussed above contain a mixing of vector and axialvector correlators much in the same way as for the purely thermal case discussed in Sect. 2.6 and displayed in Fig. 2.8. This has been shown explicitly by Chanfray and collaborators [144] for the case in which the  $\rho$  meson couples to the pion-nucleon system (the conclusions remain valid when the  $\Delta$ -isobar is included in addition). To make the argument, consider the longitudinal and transverse selfenergies of the  $\rho$  meson. According to (3.71) these can be written as

$$\begin{aligned}\Sigma_\rho^L(q_0, \vec{q}) &= \frac{q^2}{q_0^2} \frac{q_i q_j}{\vec{q}^2} \Sigma_\rho^{ij}(q) \equiv g_{\rho\pi\pi}^2 \frac{q^2}{q_0^2} \frac{q_i q_j}{\vec{q}^2} V^{ij}(q) \\ \Sigma_\rho^T(q_0, \vec{q}) &= \frac{1}{2} \left( \delta_{ij} - \frac{q_i q_j}{\vec{q}^2} \right) \Sigma_\rho^{ij}(q) \equiv g_{\rho\pi\pi}^2 \frac{1}{2} \left( \delta_{ij} - \frac{q_i q_j}{\vec{q}^2} \right) V^{ij}(q)\end{aligned}\quad (3.103)$$

and (up to vertex form factors) define the spatial components of the vector correlator  $V^{ij}$  ( $i, j = 1, 2, 3$ ). When evaluated by including nucleons and pions one obtains [114]

$$\begin{aligned}V_{ij}(q) &= i \int \frac{d^4 k_1}{(2\pi)^4} [(1 + \Pi^0(k_1))k_{1i} - (1 + \Pi^0(k_2))k_{2i}] \\ &\quad \times D_\pi(k_1) D_\pi(k_2) [(1 + \Pi^0(k_1))k_{1j} - (1 + \Pi^0(k_2))k_{2j}]\end{aligned}$$

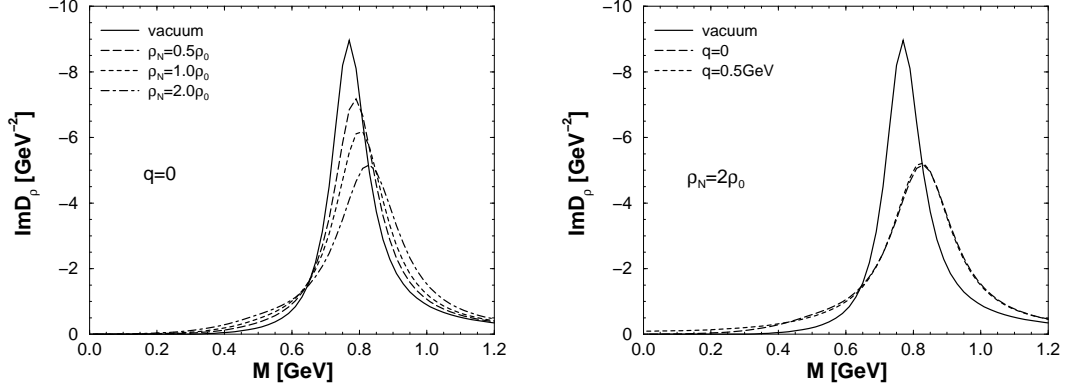


Figure 3.13: Spin-averaged in-medium  $\rho$  propagator when accounting for  $P$ -wave  $NN^{-1}$  and  $\Delta N^{-1}$  excitations in its pion cloud; left panel: density dependence at fixed three momentum  $q = 0$ ; right panel: three-momentum dependence at fixed nucleon density  $\rho_N = 2\rho_0$ .

$$\begin{aligned}
& +i \int \frac{d^4 k_1}{(2\pi)^4} \left\{ \left[ \hat{k}_{1i} \hat{k}_{1j} \Pi^0(k_1) + (\delta_{ij} - \hat{k}_{1i} \hat{k}_{1j}) \Pi^T(k_1) \right] D_\pi(k_2) \right. \\
& \left. + \left[ \hat{k}_{2i} \hat{k}_{2j} \Pi^0(k_2) + (\delta_{ij} - \hat{k}_{2i} \hat{k}_{2j}) \Pi^T(k_2) \right] D_\pi(k_1) \right\}, \quad (3.104)
\end{aligned}$$

where  $k_1$  and  $k_2$  are the single-pion four-momenta (their sum is the incident momentum  $q = k_1 + k_2$ ). In the above expression the dimensionless irreducible response function  $\Pi^0$  is related to the pion selfenergy (including effects of short-range correlations via Migdal parameters) as  $\Pi^0 = \Sigma_\pi / \vec{k}^2$  (see Eq. (3.97)), while  $D_\pi(k) = 1/[k_0^2 - \vec{k}^2 - m_\pi^2 - \vec{k}^2 \Pi^0(k)]$  denotes the fully dressed pion propagator with  $NN^{-1}$  insertions, cf. Eq. (3.98). Finally  $\Pi^T$  denotes the fully iterated spin-transverse response function, where the nucleon bubble is iterated to all orders. Expression (3.104) coincides with Eq. (3.102). The corresponding axial correlator  $A_{ij}$  can be defined in analogy to (3.103) and takes the form [144]

$$\begin{aligned}
\frac{1}{f_\pi^2} A_{ij}(k) &= k_i k_j D_\pi(k) + 2k_i k_j \Pi^0(k) D_\pi(k) + \hat{k}_i \hat{k}_j \Pi^L(k) + (\delta_{ij} - \hat{k}_i \hat{k}_j) \Pi^T(k) \\
&= k_i k_j (1 + \Pi^0(k))^2 D_\pi(k) + \hat{k}_i \hat{k}_j \Pi^0(k) + (\delta_{ij} - \hat{k}_i \hat{k}_j) \Pi^T(k), \quad (3.105)
\end{aligned}$$

where also the fully iterated spin-longitudinal response function  $\Pi^L$  has been introduced. The pertinent diagrams are depicted in Fig. 3.14. The crucial observation of Chanfray *et al.* is now that  $V_{ij}(q)$  can be expressed in terms of the axial correlator in a form

$$V_{ij}(q) = i \int \frac{d^4 k_1}{(2\pi)^4} \left[ \frac{1}{f_\pi^2} (A_{ij}(k_1) D_\pi(k_2) + A_{ij}(k_2) D_\pi(k_1)) \right]$$

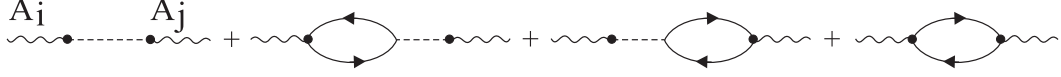


Figure 3.14: The axial correlator in nuclear matter.

$$-(1 + \Pi^0(k_1))(1 + \Pi^0(k_2))(k_{1i}k_{2j} + k_{2i}k_{1j})D_\pi(k_1)D_\pi(k_2) \ , \quad (3.106)$$

which displays the mixing effect through the first term. This term arises from the vertex corrections displayed in Fig. 3.11. Indeed, removing a (dressed) pion one is left with the axial correlator taken at the momentum of the other pion. In contrast to the thermal case the extra pion is, however, not provided by the heat bath but rather by a nucleon from the medium. The second term in Eq. (3.106) does not reduce to the product of the axial correlator with the pion propagator. Its existence is due to the interaction of the photon with the pion via the derivative term  $\vec{\pi} \times \partial^\mu \vec{\pi}$  in the interaction term of the VDM Lagrangian (3.50). The extra term does not invalidate the basic mixing concept. In fact, removing a pion the remainder is still of axial nature.

It is very pleasing to see that partial restoration of chiral symmetry through mixing of vector and axialvector correlators is also manifest in cold nuclear matter. As pointed out in Ref. [114, 126] the dominant mechanism for shifting strength to lower energies in the  $\rho$  spectral function is provided by coupling to  $\pi\Delta N^{-1}$ -states through vertex corrections. These are precisely of the type  $A_{ij}D_\pi$  arising from the last term of the axial correlator (3.105) with a transverse  $\Delta N^{-1}$ -bubble. Thus the manifestation of partial restoration of chiral symmetry is in the broadening of the spectral function! Due to the lack of the  $a_1$  meson as an explicit degree of freedom it is not clear at present whether the in-medium Weinberg sum rules (2.101), (2.102) are fulfilled.

A somewhat different approach for evaluating vector meson spectral distributions in cold nuclear matter has been pursued by Klingl *et al.* [91]. They start from an the  $SU(3)$  chiral Lagrangian for pseudoscalar mesons and baryons [145], based on pseudovector coupling as

$$\mathcal{L}_{\Phi B} = F \text{tr} (\bar{B} \gamma_\mu \gamma_5 [u^\mu, B]) + D \text{tr} (\bar{B} \gamma_\mu \gamma_5 \{u^\mu, B\}_+) \ , \quad (3.107)$$

where  $\{.,.\}_+$  and  $[.,.]$  denote anti-/commutators, respectively, and the  $SU(3)$  field matrices are given by

$$B = \begin{pmatrix} \frac{\Lambda}{\sqrt{6}} + \frac{\Sigma^0}{\sqrt{2}} & \Sigma^+ & p \\ \Sigma^- & \frac{\Lambda}{\sqrt{6}} - \frac{\Sigma^0}{\sqrt{2}} & n \\ \Xi^- & \Xi^0 & \frac{-2\Lambda}{\sqrt{6}} \end{pmatrix} \ , \quad \Phi = \begin{pmatrix} \frac{\pi^0}{\sqrt{2}} + \frac{\eta}{\sqrt{6}} & \pi^+ & K^+ \\ \pi^- & \frac{-\pi^0}{\sqrt{2}} + \frac{\eta}{\sqrt{6}} & K^0 \\ K^- & \bar{K}^0 & \frac{-2\eta}{\sqrt{6}} \end{pmatrix} \ . \quad (3.108)$$

The parameters  $F \simeq 0.51$  and  $D \simeq 0.75$  are chosen to comply with axial coupling constant  $g_A = F + D = 1.26$ . The four vector

$$u^\mu = -\frac{1}{2f_\pi} (\partial^\mu \Phi - ie[\mathcal{Q}, \Phi]A^\mu) \quad (3.109)$$



contains the axialvector current of the pseudoscalar fields as well as the minimal coupling term for the electromagnetic field  $A^\mu$ ,  $\mathcal{Q} = \text{diag}(2/3, -1/3, -1/3)$  being the  $SU(3)$  charge matrix. The vector meson-baryon interactions are then obtained from the minimal coupling scheme, *i.e.*, replacing  $e\mathcal{Q}A^\mu$  by  $gV^\mu/2$  with

$$V^\mu = \text{diag}(\rho^\mu + \omega^\mu, -\rho^\mu + \omega^\mu, \sqrt{2}\phi^\mu) , \quad (3.110)$$

and the relevant terms for  $V$ - $B$  interactions become

$$\begin{aligned} \mathcal{L}_{V\Phi B} &= \frac{ig}{4f_\pi} \{ F \text{tr} (\bar{B}\gamma_\mu\gamma_5 [[V^\mu, \Phi], B]) + D \text{tr} (\bar{B}\gamma_\mu\gamma_5 \{ [V^\mu, \Phi], B \}_+) \} \\ \mathcal{L}_{VB}^{(1)} &= \frac{g}{2} \{ \text{tr} (\bar{B}\gamma_\mu [V^\mu, B]) - \text{tr} (\bar{B}\gamma_\mu B) \text{tr} (V^\mu) \} \\ \mathcal{L}_{VN}^{(2)} &= \frac{g\kappa_\rho}{4M_N} \bar{N} \vec{\tau} \sigma_{\mu\nu} N \partial^\mu \vec{\rho}^\nu + \frac{g\kappa_\omega}{4M_N} \bar{N} \sigma_{\mu\nu} N \partial^\mu \omega^\nu . \end{aligned} \quad (3.111)$$

The last part,  $\mathcal{L}_{VN}^{(2)}$ , has been added to include corrections due to anomalous  $VN$  tensor couplings (using  $\kappa_\rho = 6$ ,  $\kappa_\omega = 0.1$ ,  $\kappa_\phi = 0$ ). Finally, the  $VB$  and (axial)  $\Phi B$  vertices are supplemented by phenomenological monopole form factors

$$F_{VB}(k^2) = \frac{\Lambda_V^2 - m_V^2}{\Lambda_V^2 - k^2} , \quad F_A(k^2) = \frac{\Lambda_A^2}{\Lambda_A^2 - k^2} , \quad (3.112)$$

respectively, with rather large cutoff parameters,  $\Lambda_V = 1.6$  GeV and  $\Lambda_A = 1$  GeV.

The in-medium vector meson selfenergies are then constructed from a low-density expansion as

$$\Sigma_V(q_0, \vec{q} = 0) \simeq \Sigma_V^\circ(q_0) - \varrho_N T_{VN}(q_0) , \quad (3.113)$$

which has been restricted to the case of vanishing three momentum  $\vec{q} = 0$  where the longitudinal and transverse parts coincide. The  $V$ - $N$  scattering amplitudes  $T_{VN}$  are constructed from the interaction vertices, Eqs. (3.111). The imaginary parts are evaluated from standard Cutkosky rules, and the real part is then obtained from a subtracted dispersion relation,

$$\text{Re } T_{VN}(q_0) = l_V + \int_0^\infty \frac{d\omega^2}{\pi} \frac{\text{Im} T_{VN}(\omega)}{(\omega^2 - q_0^2)} \frac{q_0^2}{\omega^2} , \quad (3.114)$$

the subtraction constants being fixed by the Thompson limit ( $q_0 \rightarrow 0$ ) for Compton scattering of real photons. The set of diagrams contributing to the  $\rho N$  amplitude is depicted in Fig. 3.15. Except for the last two 'box' diagrams involving  $\omega$  mesons, they are equivalent to the  $\rho$  selfenergy contributions obtained by Urban *et al.* [126] as encoded in the various vertex corrections displayed in Fig. 3.12.

Fig. 3.16 shows the resulting vector current correlators (divided by the energy squared) in the  $\rho$ ,  $\omega$  and  $\phi$  meson channel for  $\vec{q} = 0$ . In the improved vector dominance scheme of Ref. [91], they are related to the vector meson selfenergies via

$$\Pi_V(q_0, \vec{q} = 0) = \frac{1}{g_V^2} (\Sigma_V(q_0, 0) + [a_V q_0^4 - \Sigma_V(q_0, 0) q_0^2] D_V(q_0, 0)) \quad (3.115)$$

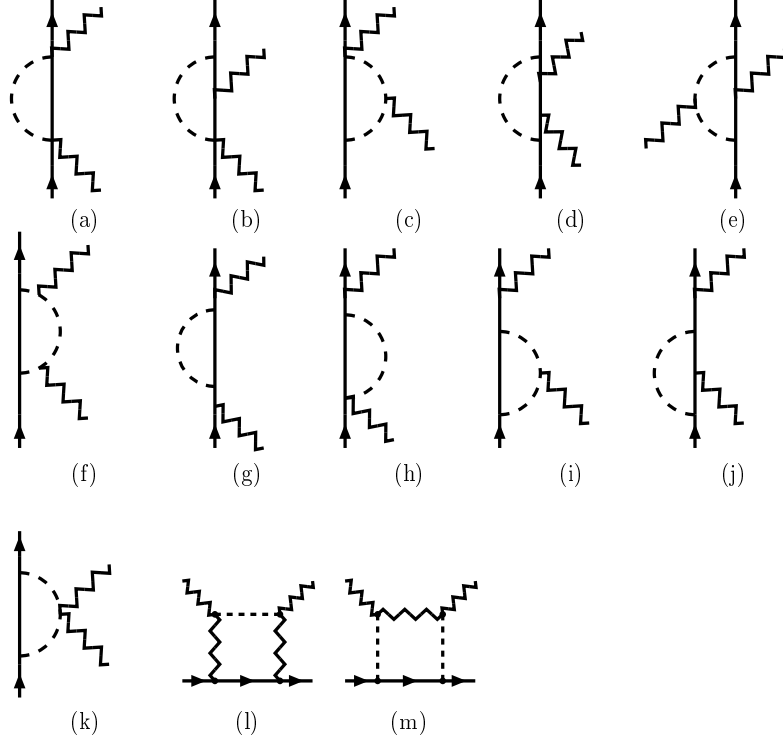


Figure 3.15: Diagrams contributing to the  $\rho$ - $N$  scattering amplitude in the approach of Klingl *et al.* [91]; dashed lines: pions, wavy lines:  $\rho$  mesons (in graphs (l) and (m) the internal wavy lines represent  $\omega$  mesons), solid lines: nucleons or deltas (the latter only for internal lines).

with constants  $a_\rho = 1.1$ ,  $a_\omega = a_\phi = 1$  (which give a good fit to the free  $e^+e^- \rightarrow \text{hadrons}$  cross sections). As in the other approaches discussed above, the  $\rho$  (as well as the  $\omega$ ) spectrum exhibit a strong broadening with increasing nuclear density (note, however, that it is quantitatively overestimated, as the hard form factors employed in this calculation, Eqs. (3.112), entail a large overprediction of  $\pi N \rightarrow \rho N$  and  $\pi N \rightarrow \omega N$  scattering data). In addition, the in-medium  $\omega$  meson mass is reduced, the  $\rho$  meson mass being practically unchanged (as is revealed by inspection of the real part of the correlator (not shown); the apparent peak shift in the left panel of Fig. 3.16 is due to an additional division by  $\omega^2$  in the plot). The modifications in the  $\phi$  channel, which are due to modifications in the kaon cloud, are rather moderate.

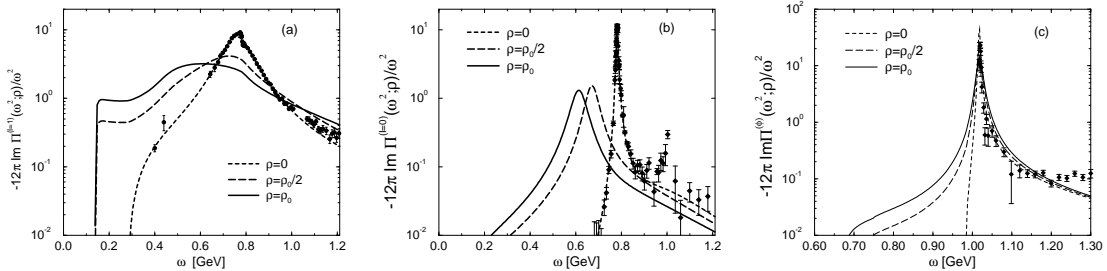


Figure 3.16: Medium Modifications of the vector correlators in nuclear matter within the approach of Klingl *et al.* [91]; panels (a), (b) and (c) correspond to the  $\rho$ ,  $\omega$  and  $\phi$  meson, respectively.

### 3.2.3 Direct $\rho$ -Nucleon Resonances

Besides modifications of the pion cloud the (bare)  $\rho$  meson may couple directly to the surrounding nucleons. From meson-exchange models such as the Bonn potential [143] one knows that, *e.g.*, the  $\rho NN$  (or  $\rho N\Delta$ ) coupling constant can be quite large, even though the corresponding  $s$ -channel process  $\rho N \rightarrow N \rightarrow \rho N$  is kinematically strongly disfavored. Such a kinematic suppression will be much less pronounced with increasing energy of the resonance in the intermediate state. There are indeed several baryonic resonances listed in the particle data table [146] which exhibit a significant branching fraction into the  $\rho N$  channel.

Friman and Pirner [147] first suggested to calculate a  $\rho$  meson selfenergy from direct  $\rho$ - $N$  interactions in terms of  $N(1720)$  and  $\Delta(1905)$  resonances. The latter two have large branching ratios of well above 50% to  $P$ -wave  $\rho$ - $N$  states. Later on it was realized [101, 102] that some lower-mass resonances – well below the naive  $\rho N$ -threshold of  $m_N + m_\rho$  – can have a strong coupling to predominantly  $S$ -wave  $\rho$ -nucleon states, most notably the  $N(1520)$ . Its decay into  $\rho N$  is only possible due to the finite width of the  $\rho$  going into  $\pi\pi$ . However, the kinematically accessible fraction of the  $\rho$  spectral function in  $N(1520) \rightarrow \rho N$  decays,

$$F = \int_{2m_\pi}^{M_{max}} \frac{M dM}{\pi} A_\rho(M), \quad (3.116)$$

amounts to only about  $F \simeq 2\%$  (with  $M_{max} = m_{N(1520)} - m_N \simeq 580$  MeV). Yet the experimental branching ratio for this decay is  $\sim 20\%$  out of the total width of  $\Gamma_{N(1520)}^{tot} = 120$  MeV. Another indication for the importance of the  $N(1520)$  in its coupling to vector meson-nucleon states is found in  $\gamma N$  cross sections, where, next to the  $\Delta(1232)$ , the  $N(1520)$  represents the most prominent resonance structure. Besides the (not always well-known) hadronic branching ratios, the photoabsorption cross sections are an important source of information to constrain the various  $\rho NB$  couplings, as will be discussed in Sect. 4.1.2.

Appropriate  $\rho NB$  interaction Lagrangians can be classified according to the parity of the resonance  $B$ : negative/positive parity states are associated with  $S$ -/ $P$ -waves in  $\rho$ - $N$ , respectively,

B	$l_{\rho N}$	$SI(\rho BN^{-1})$	$\Gamma_{\rho N}^0$ [MeV]	$\Gamma_{\rho N}^{0,fit}$ [MeV]	$\left(\frac{f_{\rho BN}^2}{4\pi}\right)$	$\Lambda_{\rho BN}$	$\Gamma^{med}$ [MeV]
N(939)	$P$	4	–	–	6.0	1500	0
$\Delta(1232)$	$P$	16/9	–	–	16.2	700	25
N(1440)	$P$	4	<28	0.5	1.1	600	200
N(1520)	$S$	8/3	24	23.5	6.8	600	300
$\Delta(1620)$	$S$	8/3	24	36	1.5	700	200
$\Delta(1700)$	$S$	16/9	128	111	2.5	1000	200
N(1720)	$P$	8/3	115	100	8.5	600	100
$\Delta(1905)$	$P$	4/5	>210	315	14.5	1200	50
N(2000)	$P$	6/5	$\sim 300$	75	1.0	1500	50

Table 3.2: Parameters of the  $\rho BN$  vertices as obtained from the interaction Lagrangians, Eqs. (3.117) and (3.118), when adjusted to photoabsorption spectra and  $\pi N \rightarrow \rho N$  scattering [102, 49]; table columns from left to right: baryon resonance  $B$ , relative angular momentum in the  $\rho N$  decay as implicit in the interaction Lagrangians, spin-isospin factor (note that in its definition we have absorbed an additional factor of  $\frac{1}{2}$  as compared to table 2 in Ref. [47]), average value for the partial decay width into  $\rho N$  as extracted from Ref. [146] (including all possible partial waves), partial decay width resulting from the fit using the parameter values in the subsequent two columns, and in-medium correction to the total decay width.

which are the dominant partial waves for moderate three-momenta. In the non-relativistic limit, gauge invariant interaction vertices can be written down as

$$\mathcal{L}_{\rho BN}^{S-wave} = \frac{f_{\rho BN}}{m_\rho} \Psi_B^\dagger (q_0 \vec{s} \cdot \vec{\rho}_a - \rho_a^0 \vec{s} \cdot \vec{q}) t_a \Psi_N + \text{h.c.} \quad (3.117)$$

$$\mathcal{L}_{\rho BN}^{P-wave} = \frac{f_{\rho BN}}{m_\rho} \Psi_B^\dagger (\vec{s} \times \vec{q}) \cdot \vec{\rho}_a t_a \Psi_N + \text{h.c.} \quad (3.118)$$

The summation over  $a$  is in isospin space with isospin matrices  $\vec{t} = \vec{\tau}, \vec{T}$  depending on whether the resonance  $B$  carries  $I=1/2$  or  $3/2$ , respectively. Analogously, the various vector/scalar products act in spin-momentum space with spin operators  $\vec{s} = \vec{\sigma}, \vec{S}$  corresponding to  $J=1/2$ - or  $J=3/2$ -resonances (spin-5/2 resonances such as  $B = \Delta(1905)$  considered in Ref. [147] require a tensor coupling of type  $[R_{ij} q_i \rho_{j,a} T_a]$ ). From these interaction vertices one can derive in-medium selfenergy tensors for  $\rho$ -induced  $BN^{-1}$  excitations, which proceeds in close analogy to the pionic case discussed above. Due to the spin-1 character of the  $\rho$  meson one encounters both transverse and longitudinal components as

$$\Sigma_{\rho\alpha}^{(0),T}(q_0, q) = - \left( \frac{f_{\rho\alpha} F_{\rho\alpha}(q)}{m_\rho} \right)^2 SI(\rho\alpha) Q^2 \phi_{\rho\alpha}(q_0, q) \quad (3.119)$$

$$\Sigma_{\rho\alpha}^{(0),L}(q_0, q) = - \left( \frac{f_{\rho\alpha} F_{\rho\alpha}(q)}{m_\rho} \right)^2 SI(\rho\alpha) M^2 \phi_{\rho\alpha}(q_0, q) \quad (3.120)$$

with  $Q^2 = q^2, q_0^2$  for the transverse  $P$ - and  $S$ -wave contributions, respectively, whereas the longitudinal part appears only for the  $S$ -wave interactions. The spin-isospin factors  $SI$  for various resonances can be found in Table 3.2, where also a typical set of coupling constants and cutoff parameters (entering the hadronic vertex form factor, taken to be of monopole form, cf. Eq. (3.93)) is quoted. The Lindhard functions  $\phi$  coincide with the pionic case, Eq. (3.94).

An important feature when calculating the corresponding  $\rho$  meson selfenergy and spectral function has been pointed out in Ref. [101]: as a result of low-energy strength appearing in the in-medium  $\rho$  spectral function (due to broadening), the phase space for the in-medium  $N(1520) \rightarrow \rho N$  decay increases substantially, *i.e.*, the fraction  $F$  defined in Eq. (3.116) becomes much larger than the 2% in case of a free  $\rho$  meson. This induces a strong density-dependent increase of the in-medium  $N(1520)$  decay width, which has to be reinserted into the expression for the  $N(1520)$  width entering into the Lindhard function. This selfconsistency problem has been solved by numerical iteration in Ref. [101], where besides the  $N(1520)$  eight further  $\rho N$  resonances have been included (essentially coinciding with the set given in Table 3.2, although using a somewhat different parameter set: most notably, the cutoffs have been uniformly set to  $\Lambda_{\rho BN} = 1500$  MeV with associated coupling constants to reproduce the  $\rho N$  branching ratios). The converged results for the transverse and longitudinal parts of the  $\rho$  spectral function,  $A_\rho^T$  and  $A_\rho^L$ , at normal nuclear matter density are shown in Fig. 3.17. One observes a strong broadening of 200–300 MeV (on

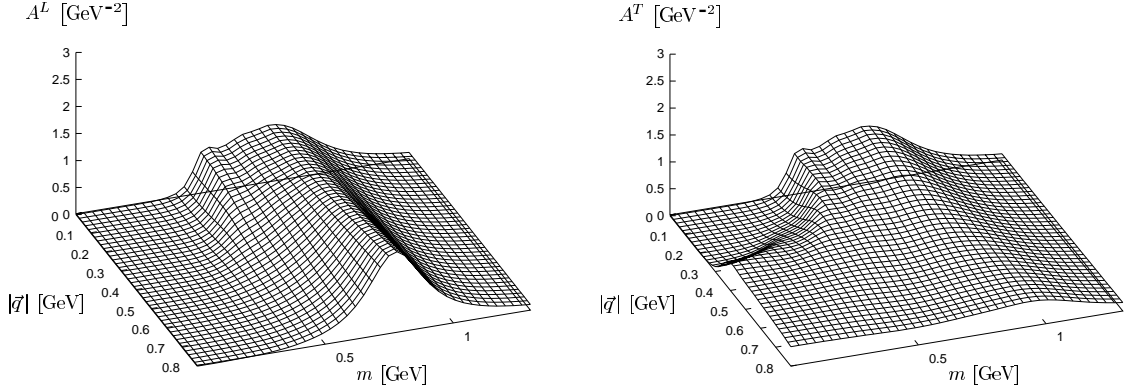


Figure 3.17: Transverse and longitudinal parts of the  $\rho$  spectral function in cold nuclear matter when including direct  $\rho$ -induced  $BN^{-1}$  excitations according to Ref. [101] (note that in this figure the spectral function has been defined as  $A^{L,T} = \frac{-1}{\pi} \text{Im} D_\rho^{L,T}$ , which differs, *e.g.*, from Fig. 3.13 by a factor of  $\frac{-1}{\pi}$ ).

top of the free width) with the only visible structure being a shoulder at  $M \simeq 0.5$  GeV (at zero three-momentum) originating from the  $N(1520)N^{-1}$  channel, which, however, is strongly washed out by a simultaneously emerging in-medium width of  $\Gamma_{N(1520)}^{tot} \simeq 350$  MeV. Similar results arise in the calculations of Ref. [102].

In Ref. [148] a  $\pi N/\rho N/\omega N$  coupled channel approach has been pursued to assess the  $\rho N$  scattering amplitude. Using the standard  $T$ - $\rho$  approximation to calculate in-medium selfenergies again

reveals a strong coupling of both  $\rho$  and  $\omega$  to collective  $N(1520)N^{-1}$  states with roughly equal strength. In-medium corrections to the widths have not yet been accounted for. In Ref. [103] they have been shown to somewhat reduce the strength in the low-lying  $N(1520)N^{-1}$  excitation in the  $\rho$  spectral function (in addition to a strong smearing).

### 3.2.4 Dispersive Approaches at High Energies

For  $\rho$  mesons of large energies,  $q_0 \gg 1$  GeV, the resonance descriptions discussed in the previous Sections should become less reliable. On the one hand, the couplings to resonances with masses beyond 2 GeV are not very well known. On the other hand, on general grounds, one should expect that a hadronic description ceases to be the appropriate one. An alternative way to extract in-medium  $\rho$  meson properties at large energies has been suggested in Ref. [149] using high-energy  $\gamma N$  cross sections in connection with vector dominance. Via the optical theorem the imaginary part of the  $\gamma N$  forward scattering amplitude can be related to the total cross section as

$$\sigma_{\gamma N}^{tot}(q_0) = -\frac{4\pi}{q} \text{Im}T_{\gamma N}(q_0) , \quad (3.121)$$

where  $q_0 = q$  denotes the incoming photon energy or laboratory momentum. A dispersion relation is applied to extract the real part as

$$\text{Re}T_{\gamma N}(q_0) = \int_0^\infty \frac{d\omega^2}{\pi} \frac{\text{Im}T_{\gamma N}(\omega)}{(\omega^2 - q_0^2)} \frac{q_0^2}{\omega^2} , \quad (3.122)$$

the subtraction point at zero energy being determined by the Thompson limit (cf. also eq. (3.114)). VDM then provides the link to the vector meson-nucleon scattering amplitude as

$$T_{\gamma N} = 4\pi\alpha \left( \frac{1}{g_\rho^2} f_{\rho N} + \frac{1}{g_\omega^2} f_{\omega N} + \frac{1}{g_\phi^2} f_{\phi N} \right) . \quad (3.123)$$

Both naive quark model arguments (where  $T_{\rho N} \simeq T_{\omega N}$ , while  $g_\omega^2/g_\rho^2 \simeq 8$ ) and empirical information inferred from photoproduction data of  $\rho$ ,  $\omega$  and  $\phi$  mesons (see, *e.g.*, Ref. [150]) suggest that the second and third term in eq. (3.123) are comparatively small. This allows the direct extraction of mass and width modifications for (on-shell)  $\rho$  mesons in the low-density limit (neglecting Fermi motion) according to the expressions

$$\begin{aligned} \Delta m_\rho(q_0) &\simeq -2\pi \frac{q_0}{m_\rho} \text{Re}T_{\rho N}(q_0) \\ \Delta \Gamma_\rho(q_0) &\simeq -4\pi \frac{q_0}{m_\rho} \text{Im}T_{\rho N}(q_0) , \end{aligned} \quad (3.124)$$

which reflect a simple version of the well-known in-medium optical potentials. In the applicable energy regime of  $q_0 \geq 2$  GeV, Eletsky and Ioffe obtained  $\Delta m_\rho \simeq (60-80)$  MeV and  $\Delta \Gamma_\rho \simeq 300$  MeV for transversely polarized  $\rho$  mesons at nuclear saturation density. However, the thus obtained  $\Delta \Gamma$

does not directly have the meaning of a resonance broadening as at high energies it includes contributions from both elastic and diffractive scattering processes.

A similar analysis has been performed by Kondratyuk *et al.* [151] based on photoproduction (rather than Compton scattering) data to extract  $T_{\gamma N \rightarrow \rho N}$ , and then using  $T_{\rho N} = (e/g_\rho)T_{\gamma N \rightarrow \rho N}$  to obtain the  $\rho N$  scattering amplitude. The results agree within  $\sim 30\%$  with those of Ref. [149]. Moreover, using a resonance model for the low-energy regime (based on similar  $\rho N$  resonances as discussed in the previous Section), they demonstrated that the  $T-\rho$  approximation does not lead to reliable predictions for mass shifts due to the importance of higher-order-in-density corrections as, *e.g.*, induced through the  $N^*$  broadening in matter. On the other hand, given the large broadening of the  $\rho$  spectral function as found in previous Sections, the quasiparticle nature of the in-medium  $\rho$  meson is lost and its in-medium mass ceases to be a well-defined quantity (note that, in general, the calculation of an in-medium spectral function does not rely on the quasiparticle concept).

### 3.2.5 Finite Temperature Effects in Baryonic Matter

When applying hadronic models to calculate dilepton production in (ultra-) relativistic heavy-ion collisions at present lab-energies, ranging from 1-200 AGeV, sizable temperatures and baryon densities are encountered simultaneously. Whereas (in thermal equilibrium) the meson densities are exclusively determined by a given temperature  $T$  (with an additional possibility of meson chemical potentials), the composition of baryon matter at fixed density  $\varrho_B$  changes appreciably with temperature. Apart from the appearance of finite thermal meson abundances, the heating of a cold nuclear system induces two additional features:

- (i) the nucleon Fermi-distribution functions experience a substantial smearing. Given a (kinetic) Fermi energy of  $\epsilon_N^F \simeq 40$  MeV at nuclear saturation density, it is clear that even at BEVALAC/SIS energies of 1-2 AGeV, where the typical temperatures are in the 50-100 MeV range, thermal motion is quite significant as seen from the left panel in Fig. 3.18.
- (ii) a certain fraction of the nucleons is thermally excited into baryonic resonances; *e.g.*, at a temperature of  $T = 170$  MeV and in chemical equilibrium the nucleon and  $\Delta$  number densities are equal owing to the larger spin-isospin degeneracy factor of the  $\Delta$  ( $g_\Delta = 16$ ) as compared to nucleons ( $g_N = 4$ ) (right panel of Fig. 3.18).

Realistic calculations of spectral functions in a hot and dense meson/baryon mixture should include these effects. The first one is readily incorporated by using finite-temperature Fermi distribution functions in connection with thermal propagators; *e.g.*, in the imaginary time (Matsubara) formalism, the finite- $T$  Lindhard functions for an excitation of a baryon resonance  $B$  on a nucleon  $N$  takes the form

$$\phi_\alpha(q_0, q; \mu_B, T) = - \int \frac{p^2 dp}{(2\pi)^2} \int_{-1}^{+1} dx \sum_{\pm} \frac{f^N[E_N(p)] - f^B[E_B(\vec{p} + \vec{k})]}{\pm q_0 + E_N(p) - E_B(\vec{p} + \vec{k}) \pm \frac{i}{2}(\Gamma_B + \Gamma_N)} \quad (3.125)$$

which, in fact, not only includes the direct  $BN^{-1}$  bubble and its exchange term, but also the corresponding  $NB^{-1}$  excitation (and exchange term) occurring on the finite (thermal) abundance

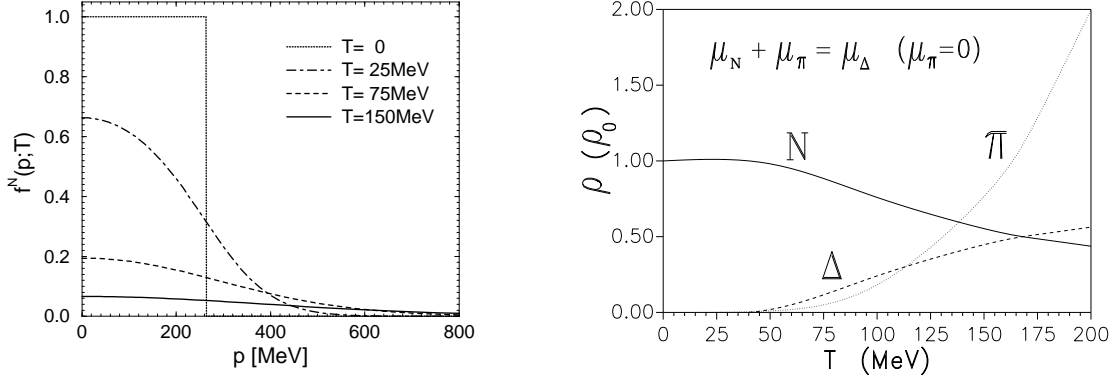


Figure 3.18: Finite-temperature effects in baryonic matter. Left panel: Fermi-distribution functions for nucleons at normal nuclear matter density  $\rho_0 = 0.16 \text{ fm}^{-3}$  at temperatures  $T=0$  (dotted curve),  $T=25 \text{ MeV}$  (dashed-dotted curve),  $T=75 \text{ MeV}$  (dashed curve) and  $T=150 \text{ MeV}$  (full curve). The corresponding (relativistic) nucleon chemical potentials are  $\mu_N = 975, 956, 832$  and  $542 \text{ MeV}$ , respectively. Note that the nuclear (kinetic) Fermi energy at zero temperature is about  $\epsilon_N^F(p_F) \simeq 37 \text{ MeV}$ . Right panel: composition of a hot  $\pi N \Delta$  gas as a function of temperature at a fixed baryon density of  $\rho_B = \rho_N + \rho_\Delta = 0.16 \text{ fm}^{-3}$ . For comparison, the thermal pion number density is also shown. Note that the nucleon density will be further depleted when including other baryonic resonances.

of the resonance species  $B$ . Apparently,  $\phi_\alpha$  has the correct analytic (retarded) properties, *i.e.*,  $\phi_\alpha(q_0) = \phi_\alpha^*(-q_0)$ .

Eq. (3.125) can be directly generalized to obtain baryonic resonance excitations on thermally excited baryons. Of course, the corresponding coupling constants (and form-factor cutoff parameters) for  $\rho B_1 B_2$  vertices ( $B_1, B_2 \neq N$ ) are mostly unknown. In Ref. [103] it has been argued, however, that (in analogy to the 'Brink-Axel' hypothesis for nuclear giant dipole resonances on excited states) the most important nucleonic excitation pattern, *i.e.*, the  $N(1520)N^{-1}$  should also be present on other baryonic resonances. From the particle data table one can indeed find some evidence for this conjecture: *e.g.*, the  $\Sigma(1670)$  (which is a well-established four-star resonance with spin-isospin  $IJ^P = 1\frac{3}{2}^-$ ), when interpreted as a  $\rho\Sigma$  (or  $\rho\Lambda$ ) 'resonance', very much resembles the quantum numbers and excitation energy ( $\Delta E \simeq 500 - 700 \text{ MeV}$ ) of the  $\rho N \rightarrow N(1520)$  transition. In addition, the branching ratio of  $\Sigma(1670)$  decays into 'simple' final states such as  $N\bar{K}, \Sigma\pi$  or  $\Lambda\pi$  is substantially less than 100%. Similar excitations on non-strange baryonic resonances are even more difficult to identify as the latter themselves decay strongly via pion emission (*i.e.*, the  $B_1 \rightarrow B_2\rho$  decay is immediately followed by further  $B_2 \rightarrow N\pi$  and  $\rho \rightarrow \pi\pi$  decays). Nevertheless, from pure quantum numbers it is tempting to associate, *e.g.*,  $\Delta(1930)\Delta^{-1}$  or  $N(2080)N(1440)^{-1}$  excitations with  $S$ -wave 'Rhosobar' states.



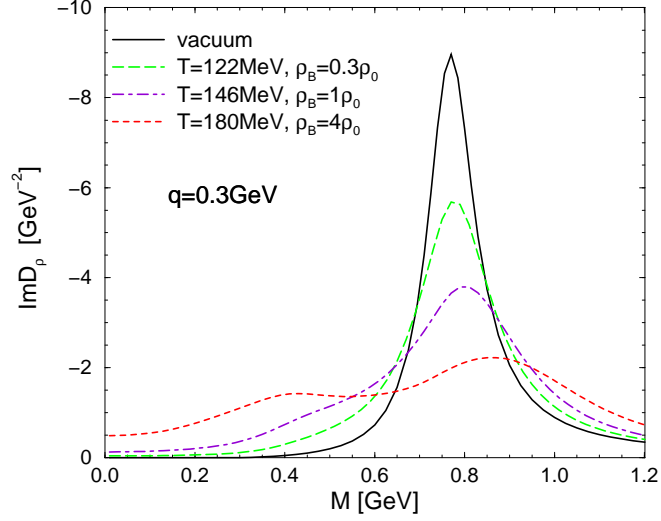


Figure 3.19: Spin-averaged  $\rho$  meson spectral function (at fixed 3-momentum  $q = 0.3$  GeV) in hot and dense hadronic matter in the many-body approach of Refs. [50] at various temperatures and total baryon densities corresponding to a fixed baryon chemical potential of  $\mu_B = 0.408$  GeV and vanishing meson chemical potentials.

To end this Chapter we show in Fig. 3.19 the final result of a many-body calculation [47, 49, 123, 50] for the  $\rho$  meson spectral function at finite temperatures and density including both thermal mesonic (Sect. 3.1.4) and baryonic resonances (Sects. 3.2.3 and 3.2.5) as well as pion cloud modifications (Sect. 3.2.2), also at both finite  $T$  and  $\mu_B$ . One finds a very strong broadening of the  $\rho$  in hot/dense matter, resulting in an almost entire 'melting' of the resonance structure at the highest temperatures and densities. Possible consequences for experimentally measured dilepton spectra in heavy-ion collisions and theoretical interpretations will be discussed in detail in the following Chapter.

## Chapter 4

# Analysis of Dilepton Spectra: Constraints, Predictions and Implications

As already mentioned in the Introduction, recent experimental analyses of dilepton production in fixed target heavy-ion collisions at both relativistic (1-2 AGeV, BEVALAC) and ultrarelativistic (158-200 AGeV, CERN-SpS) projectile energies have exhibited a strong enhancement of low-mass pairs as compared to expectations based on free decay processes of the various hadrons in the final state ('freezeout'). Once the hadronic composition of the freezeout state is known, this so-called 'hadronic cocktail' contribution to the observed spectra dilepton spectra can be quite reliably assessed without further assumptions, and has been shown to be in excellent agreement with the measurements performed under equivalent conditions in proton-induced collisions on various nuclei. This corroborated the naive expectation that the projectile protons essentially traverse the target nuclei with the hadronization of the produced secondaries mostly taking place outside the nucleus, thus leaving no traces of significant in-medium effects in the observed dilepton decays.

As a first step further from the theoretical side, various authors have calculated the contributions from  $\pi^+\pi^-$ -annihilation occurring during the lifetime of the interacting hot fireball formed in the heavy-ion induced reactions. Even without invoking any in-medium modifications, this already requires some knowledge about the dynamics within the fireball, in particular its pion abundance and momentum distributions. However, many different models for the URHIC-dynamics arrive at the same conclusion, namely that the experimentally observed enhancement at invariant masses  $M_{ll} \simeq (0.2 - 0.6)$  GeV cannot be explained when using free  $\pi\pi$  annihilation (see also Fig. 1.4).

To learn about the type of medium modifications which eventually can account for the spectacular experimental results, it is most desirable to perform as 'parameter-free' calculations as possible. Although at the present stage, modeling of the collision dynamics unavoidably involves some uncertainty, the underlying microscopic processes for dilepton production can and should be determined imposing as much independent experimental information as possible. This is particularly true for hadronic models involving medium effects, where the predictive power resides in the

reliability of the density dependence. Such models typically comprise a large number of different processes, some of which can be subjected to consistency checks.

The outline of this Chapter is as follows: in Sect. 4.1 we discuss various constraints that the existing hadronic models have been (partially) exposed to. In Sect. 4.2 the predictions for the dilepton production rates within different hadronic approaches and more exotic ones will be confronted. Photon rates are discussed in short in Sect. 4.3. Sect. 4.4 gives a brief (by no means complete) survey of the different ways to model heavy-ion collision dynamics with focus on those that have been employed to calculate dilepton spectra. We then proceed to the analysis of low-mass dilepton spectra, starting in Sect. 4.5 from intermediate bombarding energies (1–2 AGeV) as performed at the BEVALAC (DLS collaboration) and to be remeasured in future precision measurements at SIS (HADES collaboration). The main part, presented in Sect. 4.6, reviews the extensive theoretical efforts that have been made to date in studying the experimental data on low-mass dilepton production at the full CERN-SpS energies (158–200 AGeV), where most of our current understanding on the possible mechanisms involved is based on. Sect. 4.7 contains a much less comprehensive view at direct photon measurements, mainly to illustrate their potential for providing consistency checks on existing models for dilepton enhancement. Finally, in Sect. 4.8, we attempt to give a critical assessment of the theoretical implications that have emerged so far.

## 4.1 Constraints on Hadronic Dilepton Production

As with most problems in nonperturbative QCD, the calculation of low-mass dilepton radiation from interacting hot and dense hadronic matter has invariably to rely on effective approaches for the underlying production processes. To aim at quantitative predictions it is thus of essential importance to minimize the corresponding uncertainties in the calculations. In principle, two guidelines are at our disposal: (i) explicit implementation of (dynamical) symmetries shared with QCD, (ii) model constraints imposed by independent experimental information. Constraints of type (i) typically govern the interaction dynamics, (approximate) chiral symmetry in our context, whereas (ii) usually serves to narrow the range of the parameters within effective models on a quantitative level. Ideally, both aspects should be satisfied; in practice, however, the complexity of the problem enforces compromises in one or the other way.

In the previous two Chapters we have already elaborated on the chiral symmetry aspects of the various approaches in some detail, and how models for the vector-vector correlator in free space can be constructed in accordance with empirical data. Here we will address the issue of imposing constraints of type (ii) on the in-medium behavior of the vector mesons and their coupling to photons. Depending on the type of data, substantially different kinematical regimes may be probed, thus not only narrowing parameter choices but also sensing dynamical (off-shell) properties of the model under consideration. The simplest constraints on coupling constants of the interaction vertices one is interested in are provided by the partial decay widths of the corresponding resonances. These are usually not very precise and, more importantly, do not contain information on energy-momentum dependencies or combined effects of several processes. More stringent constraints are thus obtained from scattering data. We will discuss both purely hadronic reactions and photoabsorption spectra – which are more directly related to the dilepton regime – where a wealth of high-precision data on both the nucleon and various nuclei exists. The focus will again be on the  $\rho$  meson which,

as repeatedly mentioned, is the most important player in the game of low-mass dileptons from URHIC's.

#### 4.1.1 Decay Widths and Hadronic Scattering Data

A standard approach to calculate modifications of a particle  $a$  embedded in the medium is based on the two-body scattering amplitude  $T_{ab}$ , integrated over the momentum distributions of the matter particles  $b$ . In the simplest version this represents the standard  $T$ - $\rho$  approximation and thus captures the linear-in-density effects. However, for the  $\rho$  meson, which is a short-lived resonance (on strong interaction scales), the following complications arise: firstly, elastic  $\rho$ -hadron scattering amplitudes are not directly accessible from experiment. Secondly, the large (vacuum) width implies that in realistic calculations one cannot just use the physical pole mass, but has to account for its spectral mass distribution,  $A_\rho(M)$ . This, in turn, allows one to consistently incorporate processes involving off-shell  $\rho$  mesons, in particular for masses  $M \leq m_\rho$  which are most relevant for low-mass dilepton spectra.

As mentioned in Chap. 3, a straightforward estimate of coupling constants for  $\rho$ -meson scattering on surrounding matter-hadrons,  $h$ , into a resonance  $R$  can be obtained from the reverse process, *i.e.*, the decay  $R \rightarrow \rho h$ , cf. Tab.4.1. Based on the interaction Lagrangians given in Chap. 3, one

$R$	$I^G J^P$	$\Gamma_{tot}$ [MeV]	$\rho h$ Decay	$\Gamma_{\rho h}^0$ [MeV]	$\Gamma_{\gamma h}^0$ [MeV]
$\omega(782)$	$0^- 1^-$	8.43	$\rho\pi$	$\sim 5$	0.72
$h_1(1170)$	$0^- 1^+$	$\sim 360$	$\rho\pi$	seen	?
$a_1(1260)$	$1^- 1^+$	$\sim 400$	$\rho\pi$	dominant	0.64
$K_1(1270)$	$\frac{1}{2} 1^+$	$\sim 90$	$\rho K$	$\sim 60$	?
$f_1(1285)$	$0^+ 1^+$	25	$\rho\rho$	$\leq 8$	1.65
$\pi(1300)$	$1^- 0^-$	$\sim 400$	$\rho\pi$	seen	not seen
$a_2(1320)$	$1^- 2^+$	110	$\rho\pi$	78	0.31

Table 4.1: *Mesonic Resonances  $R$  with masses  $m_R \leq 1300$  MeV and substantial branching ratios into final states involving either direct  $\rho$ 's (hadronic) or  $\rho$ -like photons (radiative).*

can derive the expression for the decay width  $\Gamma_{R \rightarrow \rho h}$  and then adjust the coupling constant to reproduce the experimentally measured value.

Let us first discuss purely mesonic interactions relevant for the finite-temperature modifications of the  $\rho$  meson [123]. For the axialvector meson resonances in  $P\rho$  scattering the vertex (3.63) leads to

$$\begin{aligned}
\Gamma_{A \rightarrow \rho P}(s) &= \frac{G_{\rho PA}^2}{8\pi s} \frac{IF(2I_\rho + 1)}{(2I_A + 1)(2J_A + 1)} \int_{2m_\pi}^{M_{max}} \frac{MdM}{\pi} A_\rho^0(M) q_{cm} \\
&\times \left[ \frac{1}{2}(s - M^2 - m_\pi^2)^2 + M^2 \omega_P(q_{cm})^2 \right] F_{\rho PA}(q_{cm})^2. \quad (4.1)
\end{aligned}$$

From Eq. (3.64) one obtains for vector mesons

$$\Gamma_{V \rightarrow \rho P}(s) = \frac{G_{\rho PV}^2}{8\pi} \frac{IF(2I_\rho + 1)}{(2I_V + 1)(2J_V + 1)} \int_{2m_\pi}^{M_{max}} \frac{MdM}{\pi} A_\rho^\circ(M) \times 2q_{cm}^3 F_{\rho PV}(q_{cm})^2. \quad (4.2)$$

Besides the coupling constant,  $G$ , the cutoff parameter  $\Lambda$  entering the hadronic vertex form factors is a priori unknown. From principle reasoning it should be in a sensible range for hadronic processes, *i.e.*,  $\Lambda \leq 1\text{-}2$  GeV. The hadronic widths are not very sensitive to the precise value of  $\Lambda$ , *e.g.*, variations in the above mentioned range entail variations in  $G^2$  of typically 10% or less. However, as has been stressed in Ref. [123], one can do better by simultaneously adjusting the radiative decay widths of the resonances. Within the vector dominance model the radiative decay widths follow from the hadronic ones by (i) taking the  $M^2 \rightarrow 0$  limit, *i.e.*, substituting  $A_\rho^\circ(M) = 2\pi\delta(M^2)$  for real photons, (ii) supplying the VDM coupling constant  $(e/g)^2 \simeq 0.052^2$  and (iii) omitting the  $(2I_\rho + 1)$  isospin degeneracy factor for the final state. This yields for both axialvector and vector resonances ( $R = A, V$ )

$$\Gamma_{R \rightarrow \gamma P} = \frac{G_{\rho PR}^2}{8\pi} \left(\frac{e}{g}\right)^2 \frac{IF}{(2I_R + 1)(2J_R + 1)} 2q_{cm}^3 F_{\rho PR}(q_{cm})^2. \quad (4.3)$$

Since the decay momentum,  $q_{cm}$ , acquires its maximum value at the photon point it is clear that the latter is more sensitive to the form-factor cutoff. With the dipole form factors of Eq. (3.69) a universal  $\Lambda_{\rho PR} = 1$  GeV yields quite satisfactory results for the decay widths of most resonances (cf. Tabs. 4.1, 4.2). If suitable data are available, an additional consistency check can be performed

$R$	$IF(\rho h R)$	$G_{\rho h R}$ [GeV $^{-1}$ ]	$\Lambda_{\rho h R}$ [MeV]	$\Gamma_{\rho h}^0$ [MeV]	$\Gamma_{\gamma h}^0$ [MeV]
$\omega(782)$	1	25.8	1000	3.5	0.72
$h_1(1170)$	1	11.37	1000	300	0.60
$a_1(1260)$	2	13.27	1000	400	0.66
$K_1(1270)$	2	9.42	1000	60	0.32
$f_1(1285)$	1	35.7	800	3	1.67
$\pi(1300)$	2	9.67	1000	300	0
$a_2(1320)$	2	5.16	2000	80	0.24

Table 4.2: Results of a fit [123] to the decay properties of  $\rho$ - $h$  induced mesonic resonances  $R$  with masses  $m_R \leq 1300$  MeV (the  $f_1(1285)$ ,  $\pi(1300)$  and  $a_2(1320)$  coupling constants are in units of GeV $^{-2}$ ).

by comparing to the dilepton Dalitz decay spectra for  $R \rightarrow Pl^+l^-$  as, *e.g.*, done in Ref. [152] for the case of the  $\omega$  meson.

A similar procedure can be applied for baryonic resonances. With the commonly employed

non-relativistic  $\rho NB$  Lagrangians given in Sect. 3.2.3, the decay width into  $\rho N$  states becomes

$$\Gamma_{B \rightarrow \rho N}(\sqrt{s}) = \frac{f_{\rho NB}^2}{4\pi m_\rho^2} \frac{2m_N}{\sqrt{s}} \frac{(2I_\rho + 1)}{(2J_B + 1)(2I_B + 1)} SI(\rho NB) \int_{2m_\pi}^{\sqrt{s}-m_N} \frac{M dM}{\pi} A_\rho^\circ(M) q_{cm} F_{\rho NB}(q_{cm})^2 v_{\rho NB}(M) \quad (4.4)$$

with the vertex function  $v_{\rho NB}(M) = (0.5M^2 + q_0^2)$  or  $q_{cm}^2$  for  $S$ - or  $P$ -wave resonances, respectively. However, the experimental values for  $\Gamma_{B \rightarrow \rho N}$  are often beset with substantial uncertainties, especially for resonance masses below the free  $\rho N$  threshold. Moreover, the simple version of VDM seems to be less accurate in the baryonic sector. As a consequence radiative decay widths,  $\Gamma_{B \rightarrow \gamma N}$ , can easily be overestimated [147]. But unlike the case for the mesonic resonances, much more quantitative constraints for the radiative couplings of baryonic excitations can be drawn from the analysis of photoabsorption spectra on single nucleons as well as nuclei, to be discussed in the following Section in detail. Before we come to that let us elaborate here on some further purely hadronic reactions which can provide valuable, comprehensive information on low-density nuclear effects in the vector correlator.

As first pointed out by Friman [153] the analysis of  $\pi N \rightarrow \rho N$  scattering data is closely related to the modifications of the  $\rho$ -propagator in nuclear matter. Diagrammatically, any cut through the in-medium  $\rho$ -selfenergy insertions represents a pertinent scattering process. In particular, all single cuts going through  $NN^{-1}$  lines in the diagrams of Fig. 3.12 or in the dressed single-pion propagator constitute a contribution to the  $\pi N \rightarrow \rho N$  reaction. Formally, this amounts to taking the imaginary part of the relevant contributions to the in-medium  $\rho$ -meson selfenergy. By using the optical theorem and detailed balance one finds for the isospin-averaged cross section

$$\sigma_{\pi N \rightarrow \rho N}(s, M) = \frac{-3q_{cm}m_N}{k_{cm}^2 \sqrt{s}} \lim_{\varrho_N \rightarrow 0} \frac{\text{Im}\Sigma_\rho^\circ(M) - \text{Im}\hat{\Sigma}_{\rho\pi N}(M)}{\varrho_N}, \quad (4.5)$$

where  $\hat{\Sigma}_{\rho\pi N}$  denotes the in-medium selfenergy containing only the diagrams with  $\pi NN^{-1}$  cuts. The center-of-mass 3-momenta  $k_{cm}$  and  $q_{cm}(M)$  belong to the incoming pion and outgoing  $\rho$  meson with fixed mass  $M$ , respectively. For comparison with experimental data,  $\sigma_{\pi N \rightarrow \rho N}(s, M)$  has to be integrated over the free  $\rho$ -meson spectral mass distribution, *i.e.*,

$$\sigma_{\pi N \rightarrow \rho N}(s) = \int_{2m_\pi}^{\sqrt{s}-m_N} \frac{M dM}{\pi} A_\rho^\circ(M) \sigma_{\pi N \rightarrow \rho N}(s, M). \quad (4.6)$$

Two types of contributions to  $\hat{\Sigma}_{\rho\pi N}$  arise: (i) from the medium modifications in the pion cloud of the  $\rho$  meson, namely pion-induced  $NN^{-1}$  excitations corresponding to  $t$ -channel pion exchange in the  $\pi N \rightarrow \rho N$  reaction, and (ii) from Rhosobar-type excitations through the  $B \rightarrow \pi N$  partial decay widths corresponding to the  $s$ -channel processes  $\pi N \rightarrow B \rightarrow \rho N$ . The surprising result [153] is that the total cross section (4.6) is very sensitive to the cutoff parameter  $\Lambda_{\pi NN}$  in the  $\pi NN$  form factor appearing in the pion cloud. Using the standard monopole form,  $\Lambda_{\pi NN}$ -values of slightly below 400 MeV already saturate the experimentally measured cross sections above the free  $\rho N$  threshold.

When additionally allowing for the type (ii)  $s$ -channel baryon resonance contributions which are essential for the description of the photoabsorption spectra (see next Section), this number has to be further reduced to about  $\Lambda_{\pi NN} \simeq 300$  MeV. Such on typical hadronic scales 'unnaturally' small values are presumably related to the lack of unitarity in the resulting Born-type scattering graphs for the  $\pi N \rightarrow \rho N$  process, as implicit in most models for the in-medium  $\rho$ -meson selfenergy. In fact, rather soft  $\pi NN/\Delta$  form factors (with 300-500 MeV cutoffs) have been encountered in the literature, *e.g.*, in separable models of  $\pi N$  scattering [154] (which resembles our model for the pion selfenergy) or pion photoproduction [155].

Other ways to extract information on the  $\rho$ -meson properties in nuclear matter which actually go beyond the low-density limit might be provided by two-pion production experiments on nuclei. Pion-induced experiments of the type  $\pi + A \rightarrow A + \pi\pi$  have been performed at TRIUMF for  $\pi\pi$  invariant masses of up to 400 MeV. This mass regime is, however, dominated by  $S$ -wave states [156]. Alternatively, one could use proton-induced reactions as had been proposed for 2.5-2.9 GeV energy beams at SATURNE [157]. At low scattering angle one might be able to probe the in-medium  $\rho$ -meson spectral function close to the  $q_0 = q$  line around  $q_0=1$  GeV, where  $P$ -wave Rho-sobars are expected to be important. Very interesting results have also been reported by the TAGX collaboration [158] for the reaction  ${}^3\text{He}(\gamma, \pi^+\pi^-)ppn$  where, based on a partial wave analysis of the outgoing pions, the data have been interpreted in terms of a large downward shift of the in-medium  $\rho$ -meson mass, although no calculations using medium-modified  $\rho$ -meson spectral functions are available yet. Another possibility might be provided by extracting phase information on electro-produced  $\rho$ -mesons in  $A(e, e')$  reactions at TJNAF [159].

For the  $\omega$  meson a similar analysis has been performed in the  $\pi N \rightarrow \omega N$  reaction [153] which also hints at a soft  $\pi NN$  form factor. In Refs. [153, 148] the effects of direct  $\omega N$  scattering have been assessed. It seems that the  $\omega$ - $N(1520)N^{-1}$  excitation (the 'Omeegasobar') plays an equally important role as in the  $\rho N$  interaction, leading to strong effects for the  $\omega$ -meson spectral function in nuclear matter.

A promising experiment to assess the in-medium  $\omega$  properties is planned at GSI [160]. In pion-induced reactions (via the elementary process  $\pi N \rightarrow \omega N$ ),  $\omega$  mesons can be produced in nuclei almost recoil free, thus allowing sufficient time for decay in the nuclear environment. The invariant mass spectrum will then be measured through the dilepton channel. Another option is the proposed transfer reaction  $d + A \rightarrow {}^3\text{He} + \omega(A - 1)$  [161].

### 4.1.2 Photoabsorption Spectra

A very important consistency check for any model of dilepton production can be inferred from photoabsorption spectra on both proton and nuclei [100, 162, 102, 104]. They represent the  $M^2 = 0$  limit of the (time-like) dilepton kinematics and are most relevant for heavy-ion energy regimes with sizable baryon densities (on the order of normal nuclear matter density and above). These are clearly realized at BEVALAC/SIS energies but apparently also at the CERN-SpS where, as seen from rapidity spectra, significant baryonic stopping is exhibited. Whereas the absorption spectra on the proton provide low-density constraints, the various nucleus data constitute a true finite-density test ground with the additional advantage over hadronic probes that the incoming photon suffers little absorption thus probing the inner, most dense regions of nuclei. The proton photoabsorption cross sections have been used by several groups to check their models for dilepton

production.

In the microscopic BUU transport model of Effenberger *et al.* [163] the elementary  $\gamma N$  cross sections have been calculated in terms of resonance contributions from  $\Delta(1232)$ ,  $N(1520)$ ,  $N(1535)$  and  $N(1680)$  as well as smooth background parameterizations of one- and two-pion photoproduction amplitudes to reproduce the nucleon data. When moving to finite nuclei, medium effects have been accounted for through modifications in the resonance widths (explicitly treated in terms of collisional broadening and Pauli-blocking), collective potentials in  $\Delta$  and nucleon propagation as well as Fermi motion. Reasonable agreement with the experimental data is obtained. However, applications for dilepton production in nucleus-nucleus collisions are not available yet.

In the 'master formula approach' for the vector correlator [99, 100] (cf. Sect. 2.8),  $\gamma$  absorption spectra have been calculated in Refs. [100, 104]. Fig. 4.1 shows the results for the nucleon (left panel) and nuclei (right panel). The dashed curve in the left panel represents a parameter-free

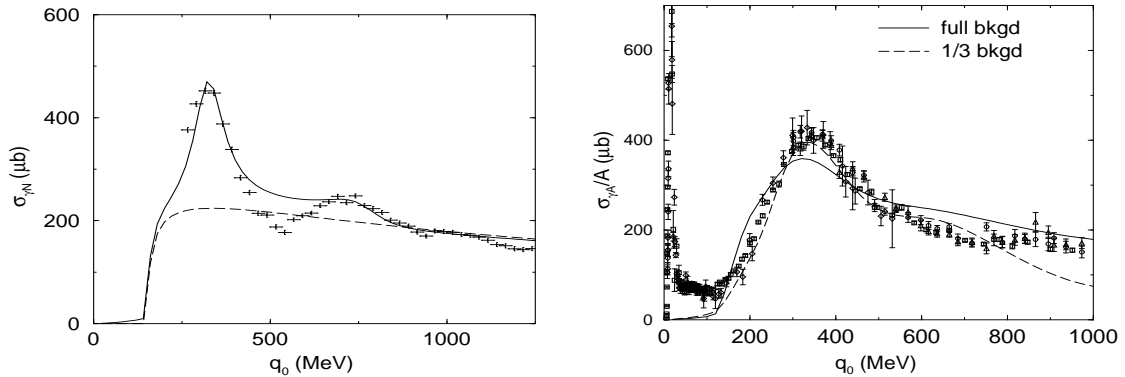


Figure 4.1: Total photoabsorption cross section on the nucleon (left panel) and on nuclei (right panel) within the chiral reduction approach taken from Ref. [104]; the nucleon and nuclei data are from Ref. [164] and Refs. [165, 166, 167, 168], respectively.

prediction of the contribution from non-resonant  $\pi N$  states (opening at the threshold energy of about  $q_0 = 140$  MeV) as extracted from  $\pi N$  scattering data. It corresponds to non-resonant one-pion photoproduction and essentially saturates the data beyond the  $\Delta$  resonance region. This is at variance with both the BUU calculations mentioned above [163] as well as experimental phase analyses [169, 164, 170] which show that for incoming photon energies  $q_0 \geq 0.6$  GeV two-pion production processes start to prevail [171]. The photoabsorption cross sections on nuclei are calculated by averaging the nucleon cross section over Fermi motion,

$$\frac{\sigma_{\gamma A}}{A} = \int \frac{d^3 p}{4\pi p_F^3/3} \Theta(p_F - |\vec{p}|) \sigma_{\gamma N}(s), \quad (4.7)$$

yielding a reasonable fit to the experimental data. The dashed curve in the right panel of Fig. 4.1 was obtained with the  $\pi N$  background being artificially reduced by a factor of three (compensated



by larger  $\Delta(1232)$  and  $N(1520)$  contributions to still reproduce the nucleon data) which seems to improve the fit. Note here that a simple averaging over Fermi motion seems to give a sufficient smearing of the  $N(1520)$  resonance, in contrast to previous findings in the literature [172, 173, 163, 102] where a strong in-medium resonance broadening was required.

In the effective Lagrangian approaches where the in-medium vector meson properties are calculated in terms of explicit interactions with surrounding matter particles, the resulting spectral functions can be related to total photoabsorption cross sections. In Refs. [162, 91] the electromagnetic current-current correlation function has been expressed to lowest order in density in terms of the Compton tensor for forward  $\gamma N$  scattering,  $T_{\gamma N}^{\mu\nu}$ , as

$$\Pi_{\text{em}}^{\mu\nu}(q) = \Pi_{\text{em}}^{\circ\mu\nu}(q) + g_N \int \frac{d^3p}{(2\pi)^3} \frac{M_N}{E_p^N} T_{\gamma N}^{\mu\nu}(q; p) \Theta(p_F - |\vec{p}|) . \quad (4.8)$$

For real photons, only the transverse part of  $T_{\gamma N}$  survives. Taking the low-density limit,  $p_F \rightarrow 0$ , and using the optical theorem,

$$\sigma_{\gamma N}(q_0) = -\frac{4\pi\alpha}{q_0} \text{Im} T_{\gamma N}^T(q_0, |\vec{q}| = q_0) , \quad (4.9)$$

as well as VDM,

$$\text{Im}\Pi_{\text{em}}^T(q_0, \vec{q}) = \sum_{V=\rho,\omega,\phi} \frac{1}{g_V^2} \text{Im}\Sigma_V^T(q_0, \vec{q}) , \quad (4.10)$$

one obtains the desired relation between the isospin-averaged  $\gamma$ -nucleon cross section and the vector meson selfenergies:

$$\sigma_{\gamma N}(q_0) = -\frac{4\pi\alpha}{q_0} \lim_{\varrho_N \rightarrow 0} \frac{1}{\varrho_N} \sum_{V=\rho,\omega,\phi} \frac{1}{g_V^2} \text{Im}\Sigma_V^T(q_0, |\vec{q}| = q_0) \quad (4.11)$$

(note that  $\text{Im}\Pi^\circ(M^2)$  vanishes below the two-pion threshold  $M = 2m_\pi$ ). Unfortunately, no explicit results for photoabsorption spectra are available in the approach of Refs. [162, 91].

A slightly different way of deriving analogous relations has been pursued in Ref. [102]. Here, the starting point is the total cross section of a photon per unit volume element  $d^3x$  of cold nuclear matter, averaged over the incoming polarizations,

$$\begin{aligned} \frac{d\sigma}{d^3x} &= \frac{1}{2} \sum_\lambda \sum_f \frac{1}{v_{in}} \frac{1}{2q_0} |\mathcal{M}_{fi}|^2 (2\pi)^4 \delta^{(4)}(p_f - q) \\ &= -\frac{4\pi\alpha}{q_0} \frac{1}{2} \sum_\lambda \varepsilon_\mu(q, \lambda) \varepsilon_\nu(q, \lambda) \text{Im}\Pi_{\text{em}}^{\mu\nu}(q) , \end{aligned} \quad (4.12)$$

where  $\mathcal{M}_{fi} = e \langle f | j_\mu^{\text{em}}(0) | 0 \rangle \varepsilon^\mu(q, \lambda)$  is the transition matrix element of the electromagnetic current, taken between the initial nuclear ground state  $|i\rangle = |0\rangle$  and final states  $|f\rangle$  with  $\varepsilon_\mu(q, \lambda)$  being the photon polarization vector. Neglecting small contributions from isoscalar vector mesons within the VDM, the electromagnetic correlator can be saturated by the neutral  $\rho$  meson using the field-current identity

$$j_{\text{em}}^\mu = (m_\rho^{(0)})^2 / g_\rho \rho_3^\mu . \quad (4.13)$$

Using the completeness relation for photon polarization vectors,

$$\sum_{\lambda} \varepsilon_{\mu}(q, \lambda) \varepsilon_{\nu}(q, \lambda) = -g_{\mu\nu} , \quad (4.14)$$

the total photoabsorption cross section, normalized to the number of nucleons  $A$ , takes the form

$$\begin{aligned} \frac{\sigma_{\gamma A}^{\text{abs}}}{A} &= \frac{1}{\varrho_N} \frac{d\sigma}{d^3x} \\ &= -\frac{4\pi\alpha}{q_0} \frac{(m_{\rho}^{(0)})^4}{g_{\rho}^2} \frac{1}{\varrho_N} \text{Im}D_{\rho}^T(q_0, |\vec{q}| = q_0) \end{aligned} \quad (4.15)$$

with the transverse in-medium  $\rho$ -meson propagator

$$\text{Im}D_{\rho}^T = \frac{\text{Im}\Sigma_{\rho}^T}{|M^2 - (m_{\rho}^{(0)})^2 - \Sigma_{\rho}^T|^2} \quad (4.16)$$

(for  $M^2 = 0$  the longitudinal part vanishes identically). Note that Eq. (4.15) does not involve any low-density approximations. However, for  $\varrho_N \rightarrow 0$  and  $A = 1$  (corresponding to the absorption process on a single nucleon), one has

$$\lim_{\varrho_N \rightarrow 0} \text{Im}D_{\rho}^T(q_0, \vec{q}) = \lim_{\varrho_N \rightarrow 0} \text{Im}\Sigma_{\rho}^T(q_0, \vec{q}) / (m_{\rho}^{(0)})^4 , \quad (4.17)$$

thus readily recovering Eq. (4.11). In the model of Ref. [102] the  $\rho$ -meson selfenergy in nuclear matter receives two contributions,

$$\Sigma_{\rho}^T = \Sigma_{\rho\pi\pi}^T + \Sigma_{\rho N}^T , \quad (4.18)$$

representing the renormalization of the pion cloud through  $\pi NN^{-1}$  and  $\pi\Delta N^{-1}$  excitations as well as direct  $\rho BN^{-1}$  interactions, respectively. However, as has been noted long ago, the most simple version of the VDM (4.13) typically results in an overestimation of the  $B \rightarrow N\gamma$  branching fractions when using the hadronic coupling constants deduced from the  $B \rightarrow N\rho$  partial widths. One can correct for this by employing an improved version of the VDM [174], which allows to adjust the  $BN\gamma$  coupling  $\mu_B$  (the transition magnetic moment) at the photon point independently [147]. It amounts to replacing the combination  $(m_{\rho}^{(0)})^4 \text{Im}D_{\rho}^T(q_0, \vec{q})$  entering Eq. (4.15) by the following 'transition form factor':

$$\begin{aligned} \mathcal{F}^T(q_0, \vec{q}) &= -\text{Im}\Sigma_{\rho\pi\pi}^T |d_{\rho} - 1|^2 - \text{Im}\Sigma_{\rho N}^T |d_{\rho} - r_B|^2 \\ d_{\rho}(q_0, \vec{q}) &= \frac{M^2 - \Sigma_{\rho\pi\pi}^T - r_B \Sigma_{\rho N}^T}{M^2 - (m_{\rho}^{(0)})^2 - \Sigma_{\rho\pi\pi}^T - \Sigma_{\rho N}^T} , \end{aligned} \quad (4.19)$$

where

$$r_B = \frac{\mu_B}{\frac{f_{\rho BN}}{m_{\rho}} \frac{e}{g}} \quad (4.20)$$

denotes the ratio of the photon coupling to its value in the naive VDM. In principle, each resonance state  $B$  can be assigned a separate value for  $r_B$  but, as will be seen below, reasonable fits to

the photoabsorption spectra can be achieved with a single value making use of some latitude in the hadronic couplings  $f_{\rho BN}$  and form-factor cutoff parameters  $\Lambda_\rho$  within the experimental uncertainties of the partial widths (4.4). The final expression to be used for the photoabsorption calculations then reads

$$\frac{\sigma_{\gamma A}^{\text{abs}}}{A} = \frac{4\pi\alpha}{g^2 q_0} \frac{1}{\varrho_N} \mathcal{F}^T(q_0, |\vec{q}| = q_0) . \quad (4.21)$$

Let us first discuss the  $\gamma N$  spectra, in particular the role of background contributions (which in this context can be regarded as 'meson exchange' processes), encoded in the low-density limit of  $\Sigma_{\rho\pi\pi}$ . With the coupling constants of the  $\pi NN$ - and  $\pi\Delta N$ -vertices fixed at their standard values (cf. Tab. 3.1), the strength of the background is controlled by the cutoff  $\Lambda_{\pi NN}$  in the phenomenological (hadronic) vertex form factors. In early applications to dilepton spectra [140, 114, 141, 142, 47, 91] the values were chosen around (1–1.2) GeV in reminiscence to the Bonn potential [143]. However, with the analysis of photoabsorption spectra [102] it became clear that much lower values are required, at most of around 600 MeV. Shortly thereafter, Friman pointed out [153] that this is still too large to be compatible with available  $\pi N \rightarrow \rho N$  scattering data as discussed in the previous Section, enforcing even smaller values [49], thereby further suppressing the 'background' contribution in the photoabsorption spectra. Using the value of  $\Lambda_\pi \simeq 300$  MeV deduced in Sect. 4.1.1 actually improves the description of the  $\gamma N$  spectra in the 'dip region' between the  $\Delta(1232)$  and the  $N(1520)$  resonances [49] as compared to the results obtained with  $\Lambda_{\pi NN} = 550$  MeV in Ref. [102], see left panel of Fig. 4.2. Moreover, the non-resonant contribution in the  $\Delta$  region now amounts to about  $70 \mu b$ , which coincides with what has been extracted from experimental phase analyses [169, 164, 170]. On the other hand, the parameter-free assessment of this background component in the 'master formula approach' [100] differs by approximately a factor of 3 across the entire photon energy range under consideration (a very similar result is found when using the Bonn-value of 1.2 GeV deduced from  $\pi N$  data in the framework of Ref. [126]). Given the magnitude of the background, the resonance contributions encoded in  $\Sigma_{\rho B}$  are readily adjusted to obtain a good fit to the  $\gamma N$  data. The employed resonances and vertex parameters are summarized in Tab. 3.2. One should note that an unambiguous determination of coupling constants and form-factor cutoffs parameters is not possible from the total absorption cross section alone. To further disentangle them more exclusive reaction channels (*e.g.*, one- and two-pion photoproduction) need to be analyzed. Nevertheless, for the purpose of predicting reliable dilepton production rates the constraints from the total absorption cross sections give reasonable confidence.

For absorption spectra on nuclei, one experimentally observes an almost independent scaling with the mass number  $A$  of different nuclei (cf. right panel of Fig. 4.2). This suggests that both surface and nuclear structure effects play a minor role as might be expected since the incoming photon predominantly probes the interior of the nuclei. Therefore it appears justified to perform the calculations for the idealized situation of infinite nuclear matter at an average density, which has been taken as  $\bar{\varrho}_N = 0.8\varrho_0$  (in fact, the results for the normalized cross section, Eq. (4.21), depend only weakly on density within reasonable limits of  $0.6 \leq \varrho/\varrho_0 \leq 1$ ). As compared to the free nucleon two additional features appear in the nuclear medium: short-range correlation effects in the resummation of the particle-hole bubbles and in-medium corrections to the resonance widths. Due to the rather soft form factors involved, the  $P$ -wave pion-induced excitations turn out to favor rather small Landau-Migdal parameters of  $g'_{NN} = 0.6$  and  $g'_{\alpha\beta} = 0.2$  for all other transitions including

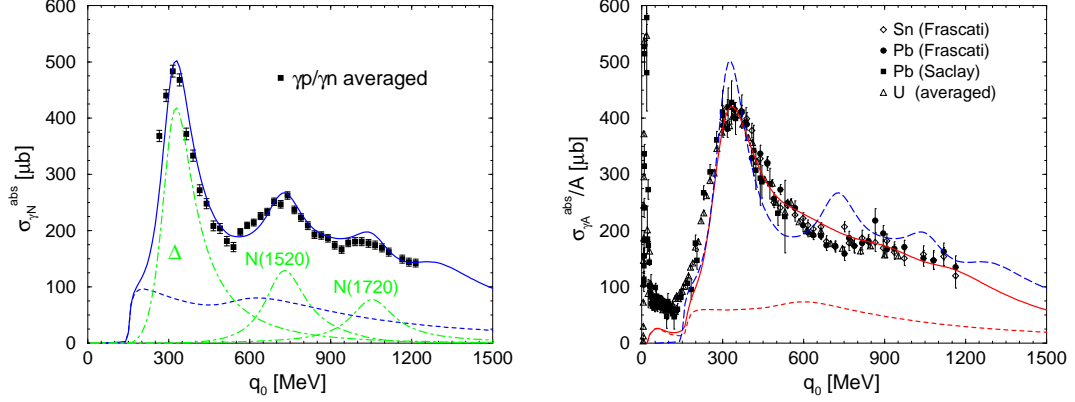


Figure 4.2: Total photoabsorption cross section on the nucleon (left panel) and on nuclei (right panel) as obtained in the  $\rho$  spectral function approach [102, 50]. Left panel: full result of the fit using the parameters of Tab. 3.2 (solid line),  $\pi\pi$  'background' (dashed line) as well as the three dominant  $\rho N$  resonances  $\Delta(1232)$ ,  $N(1520)$  and  $N(1720)$  (dashed-dotted lines); the data are averaged over proton [175] and neutron [176] measurements. Right panel: full result (solid line) and non-resonant background contributions (short-dashed line) for  $\varrho_N = 0.8\varrho_0$ , as well as the lowest-order-density result from the nucleon fit (long-dashed line); the data are taken from Refs. [165, 166, 167, 168].

*P*-wave Rhosobars. The *S*-wave  $\rho BN^{-1}$  bubbles show only marginal evidence for short-range correlations with a slight tendency towards larger values (the results in the left panel of Fig. 4.2 have been obtained with  $g'_{S-wave} = 0.6$ ). However, as already mentioned above, the observed disappearance of the  $N(1520)$  resonance in the nuclear medium requires a large in-medium increase of its width. Such a behavior has indeed been found in a selfconsistent microscopic treatment of the  $\rho$ -meson spectral function and the  $N(1520)$  width in nuclear matter [101], which is based on a very similar framework as employed here. The actual value used for  $\Gamma_{N(1520)}^{med}$  in Fig.4.2 is in accordance with Ref. [101]. On the other hand, the net in-medium correction to the  $\Delta(1232)$  width is quite small. This reflects the fact that a moderate in-medium broadening is largely compensated by Pauli blocking effects on the decay nucleon. The sensitivity of the results with respect to the in-medium widths of the higher lying resonances is comparatively small. It is also noteworthy that below the pion threshold some strength appears. This is nothing but the well-known 'quasi deuteron' tail above the giant dipole resonance, arising from pion-exchange currents. These are naturally included in the spectral function framework through higher orders in density in the pion cloud modifications. Also note that a linear-density approximation to Eq. (4.19), which is equivalent to the  $\gamma N$  result, does not properly reproduce the  $\gamma A$  data.

## 4.2 Dilepton Rates in Hot and Dense Matter

Having discussed the approaches that have been constructed to compute the vector correlator in hot and dense matter as well as the corresponding efforts and philosophies to constrain the underlying assumptions, we now turn our attention to the results for the dilepton production rates. To be able to draw any conclusions from the eventual analysis of dilepton spectra in heavy-ion collisions it is essential to assess the differences and similarities in the model predictions on an equal footing, *i.e.*, without the complications arising from modeling the space-time history of the collisions or experimental acceptance cuts. In practically all microscopic approaches one calculates an eight-fold differential rate per unit four momentum and four volume. To facilitate the comparison, it has become common to focus on the 3-momentum integrated rates

$$\frac{dR_{l+l^-}}{dM^2}(M) = \int \frac{d^3q}{2q_0} \frac{dR_{l+l^-}}{d^4q}(q_0, \vec{q}) \quad (4.22)$$

at fixed temperature  $T$  and baryon density  $\varrho_B$  (or, equivalently, baryon chemical potential  $\mu_B$ ). In the following we will first address the class of more 'conventional', hadronic calculations based on essentially known interactions, and then put these into context with results from scenarios associated with 'new' physics such as QGP or DCC formation.

### 4.2.1 Comparison of Hadronic Approaches

As elaborated in Sect. 2.5 the general expression for the dilepton production rate in a hadronic medium of given temperature  $T$  and baryon chemical potential  $\mu_B$  can be written as

$$\frac{dR_{l+l^-}}{d^4q} = L_{\mu\nu}(q)W^{\mu\nu}(q) , \quad (4.23)$$

where  $L_{\mu\nu}$  and  $W_{\mu\nu}$  denote the leptonic and hadronic tensor, respectively, cf. Eqs. (2.75) and (2.76). The latter can also be written as

$$W^{\mu\nu}(q; T) = \sum_i \frac{e^{E_i/T}}{\mathcal{Z}} \sum_f \langle i | j^\mu(0) | f \rangle \langle f | j^\nu(0) | i \rangle (2\pi)^4 \delta^{(4)}(q + p_f - p_i) , \quad (4.24)$$

which is straightforwardly related to the retarded current-current correlation function according to

$$-2 \operatorname{Im}\Pi_{\text{em}}^{\mu\nu}(q) = (e^{q_0/T} - 1) W^{\mu\nu}(q) . \quad (4.25)$$

Inserting Eqs. (2.75) and (4.25) into (4.23), and exploiting gauge invariance,  $q_\mu \Pi_{\text{em}}^{\mu\nu} = 0$ , one obtains the general result

$$\frac{dR_{l+l^-}}{d^4q} = -\frac{\alpha^2}{\pi^3 M^2} f^B(q_0; T) \operatorname{Im}\Pi_{\text{em}}(q_0, \vec{q}) \quad (4.26)$$

with the thermal Bose occupation factor  $f^B(q_0; T) = (e^{q_0/T} - 1)^{-1}$  and the spin-averaged correlator

$$\operatorname{Im}\Pi_{\text{em}}(q_0, \vec{q}) = \frac{1}{3} [\operatorname{Im}\Pi_{\text{em}}^L(q_0, \vec{q}) + 2\operatorname{Im}\Pi_{\text{em}}^T(q_0, \vec{q})] , \quad (4.27)$$

given in terms of its standard decomposition into longitudinal and transverse projections.

## Effects of a Hot Meson Gas

Let us start by considering a hot meson gas without any baryons. The most obvious source of dilepton radiation from such a system is the free  $\pi^+\pi^- \rightarrow l^+l^-$  annihilation process with no further medium effects included. This process is reliably described within the simple VDM framework, so that very little model uncertainty is involved once the experimental data for the pion electromagnetic form factor in the time-like region are properly accounted for. Therefore we will use this process as a standard baseline for comparing medium effects within various approaches. In VDM (*i.e.*, invoking the field-current identity (4.13))  $\pi\pi$  annihilation proceeds via the formation of an intermediate  $\rho$  meson. The corresponding hadronic tensor is then saturated by the  $\rho$ -meson propagator,

$$W^{\mu\nu}(q) = -2 f^\rho(q_0; T) \frac{(m_\rho^{(0)})^4}{g_{\rho\pi\pi}^2} \text{Im}D_\rho^{\mu\nu}(q) . \quad (4.28)$$

Thus the dilepton production rate for  $\pi^+\pi^- \rightarrow \rho \rightarrow \gamma^* \rightarrow e^+e^-$  becomes

$$\begin{aligned} \frac{dR_{\pi\pi \rightarrow ee}}{d^4q}(q_0, \vec{q}) &= -\frac{\alpha^2(m_\rho^{(0)})^4}{\pi^3 g_{\rho\pi\pi}^2} \frac{f^\rho(q_0; T)}{M^2} \text{Im}D_\rho(q_0, \vec{q}) \\ &= -\frac{\alpha^2}{\pi^3 g_{\rho\pi\pi}^2} \frac{f^\rho(q_0; T)}{M^2} \text{Im}\Sigma_{\rho\pi\pi}^\circ(M) |F_\pi^\circ(M)|^2 , \end{aligned} \quad (4.29)$$

where the second equality implies the use of the free  $\rho$ -meson propagator. As is well-known a thermodynamically equivalent way to describe the *same* contribution is to consider the decay of thermal  $\rho$  mesons in the system. Accounting for both  $\pi\pi$  annihilation and  $\rho$  decays clearly constitutes double counting.

In-medium modifications to the free  $\pi\pi$  annihilation process in a hot meson gas have been studied by several groups, as we have already discussed in some detail in Sect. 3.1. At a fixed temperature of  $T = 150$  MeV the three-momentum integrated rates (as given by Eq. (4.22)) are confronted in Fig. 4.3 for some of the different approaches available in the literature. One of the selected examples is of model-independent nature [99] putting the emphasis on chiral symmetry aspects of the interactions, whereas the other two [119, 123] represent the more phenomenological approaches based on effective Lagrangians.

The chiral reduction formalism employed by Steele *et al.* (which combines chiral Ward identities with experimental data on spectral functions in the vector and axialvector channels, dominated by the  $\rho$  and  $a_1(1260)$  mesons, respectively, cf. Sect. 2.8) is shown as the short-dashed line in Fig. 4.3. The appearance of the  $a_1$  (predominantly formed in resonant  $\rho\pi$  scattering) in the electromagnetic rates represents the mixing effect of the vector and axialvector correlators as dictated by chiral symmetry. Most of the enhancement over the free  $\pi\pi$  rate for invariant masses below  $M_{ee} \simeq 0.6$  GeV can indeed be assigned to the (Dalitz-decay) tails of the  $a_1(1260)$ . On the other hand, note that there is practically no depletion of the  $\rho$ -meson peak around  $M_{ee} \simeq m_\rho$ . This is a consequence of the density expansion inherent in this virial-type expansion which evades any kind of diagrammatic resummations. Such resummations naturally occur in the propagator formalism: even if the (in-medium) selfenergy correction is evaluated to lowest order, the solution of the corresponding Dyson equation automatically generates iterations to all orders which typically leads to a downward shift of strength as we will see below.

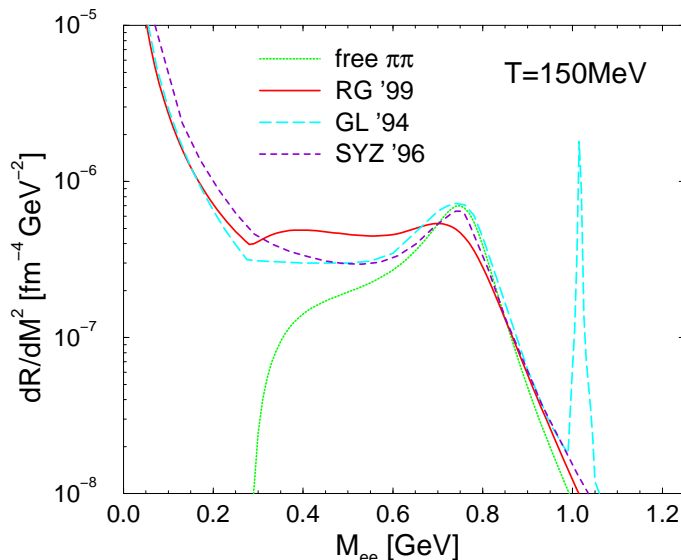


Figure 4.3: Three-momentum integrated dilepton rates in a hot meson gas at  $T = 150$  MeV in the hadron-based approaches of Gale/Lichard [119] (long-dashed line), Steele *et al.* [99] (short-dashed line) and Rapp *et al.* [47, 123] (full line). The dotted line represents free  $\pi\pi$  annihilation.

In Ref. [119] a large number of mesonic tree level scattering amplitudes involving  $e^+e^-$  final states has been computed within the VDM, employing phenomenological Lagrangians compatible with gauge invariance and inspired by the chiral properties of low-energy QCD [109]. The corresponding coupling constants have been determined along the lines discussed in Sect. 4.1.1 using the experimental branching ratios for radiative decays, etc.. Within standard relativistic kinetic theory the dilepton production rate has then been obtained by suitable momentum integrations over the squared matrix elements including appropriate thermal occupation factors (for a given process, the kinetic theory expressions can be shown to be equivalent to standard finite-temperature field theoretic results to leading order in temperature). The long-dashed curve in Fig. 4.3 represents the final result of this analysis, also exhibiting substantial excess over the free  $\pi\pi$  rate for low masses  $M_{ee} \leq 0.6$  GeV, which is predominantly generated by the radiative decay of the omega,  $\omega \rightarrow \pi^0 e^+ e^-$ . Contributions from  $a_1(1260)$  mesons have not been included. The incoherent summation of the various processes does again not induce any depletion of the peak, leading to a close overall resemblance with the rate from the chiral reduction formalism [99] (short-dashed curve).

In Ref. [47] the imaginary time (Matsubara) formalism has been employed to calculate the  $\rho$  propagator in hot hadronic matter accounting for the full off-shell dynamics of the considered interactions. As far as meson gas effects are concerned, only resonant  $\rho\pi \rightarrow a_1(1260)$  and  $\rho K/\bar{K} \rightarrow$

$K_1(1270)/\bar{K}_1(1270)$  contributions were included at the time, yielding very similar results as have been obtained before in an (on-shell) kinetic theory framework [120] (which is mainly due to the fact that both the  $a_1$  and  $K_1$  resonances are situated above the free  $\rho\pi$  and  $\rho K$  thresholds, respectively, resulting in little off-shell sensitivity). A more comprehensive analysis of the finite temperature  $\rho$ -meson selfenergy was performed in Ref. [123] along the same lines as in Ref. [47]. The most notable of the additionally included mesonic resonances turned out to be the  $\omega(782)$  meson accessible through interactions of off-shell  $\rho$  mesons (with mass  $M \simeq 500$  MeV, cf. Fig. 3.8) with thermal pions. The corresponding dilepton production process is  $\rho\pi \rightarrow \omega \rightarrow \pi e e$ , *i.e.*, the radiative Dalitz decay of thermal  $\omega$  mesons. It indeed quantitatively coincides with the equivalent contribution calculated in Ref. [119]. In addition, the most simple temperature effect in the pion cloud of the  $\rho$  meson has been included, consisting of a Bose-Einstein enhancement in the in-medium  $\rho \rightarrow \pi\pi$  decay width. Schematically written it modifies the imaginary part of the  $\rho\pi\pi$  selfenergy as

$$\text{Im}\Sigma_{\rho\pi\pi}^{\circ}(M) \rightarrow \text{Im}\Sigma_{\rho\pi\pi}(M; T) = \text{Im}\Sigma_{\rho\pi\pi}^{\circ}(M) [1 + 2f^{\pi}(M/2)] , \quad (4.30)$$

cf. also Eq. (3.62). The full result of Ref. [123] is shown by the solid line in Fig. 4.3: in the low-mass region it exceeds the results of both the chiral reduction approach [99] and of the incoherent summation of decay/scattering processes [119]. The discrepancy to the latter can be traced back to the  $a_1$ -meson contribution and, more importantly, to the Bose enhancement in the  $\rho \rightarrow \pi\pi$  decay width [123]. Also note that the  $\rho$ -meson spectral function calculation induces a  $\sim 40\%$  suppression of the signal in the vicinity of the free  $\rho$  mass. This is a characteristic feature of many-body type approaches and is not present in density-expansion schemes as implicit in the calculations of Gale/Lichard and Steele *et al.*. It can be easily understood as follows [123]: the  $\rho$  spectral function (which governs the dilepton rate in the many-body framework) can be schematically written in terms of the selfenergy as

$$\text{Im}D_{\rho} = \frac{\text{Im}\Sigma_{\rho}}{|M^2 - m_{\rho}^2|^2 + |\text{Im}\Sigma_{\rho}|^2} , \quad (4.31)$$

where we have absorbed the real part of the selfenergy in the (physical)  $\rho$  mass  $m_{\rho}$ . In the low-mass region, where  $m_{\rho} \gg M$  and  $m_{\rho}^2 \gg |\text{Im}\Sigma_{\rho}|$ , the denominator is dominated by  $m_{\rho}$  so that

$$\text{Im}D_{\rho}(M \ll m_{\rho}) \propto \frac{\text{Im}\Sigma_{\rho}}{m_{\rho}^4} . \quad (4.32)$$

Since  $\text{Im}\Sigma_{\rho}$  basically encodes a summation of scattering amplitudes times (pion-) density, one immediately recognizes the close analogy to kinetic theory or low-density expansions. On the other hand, in the vicinity of the  $\rho$ -peak, where  $M \simeq m_{\rho}$ , the denominator in Eq. (4.31) is dominated by  $\text{Im}\Sigma_{\rho}$  so that

$$\text{Im}D_{\rho}(M \simeq m_{\rho}) \propto \frac{1}{\text{Im}\Sigma_{\rho}} , \quad (4.33)$$

demonstrating that the consequence of an increase in density is a suppression of the maximum, which cannot be straightforwardly casted in a low-density expansion.



## Effects of Finite Baryon Density

The situation becomes more involved when comparing dilepton production rates in the presence of baryons. Most of the investigations so far have been restricted to the case of nucleons at zero temperature, which is particularly obvious for model constraints inferred from  $\rho N$  or  $\gamma N/\gamma A$  scattering data as discussed in Sect. 4.1. The first complication arises from the fact that in any finite temperature system with a net baryon density, some fraction of the nucleons will be thermally excited into baryonic resonances and therefore, in principle, should not be included in medium modifications generated by nucleons. For instance, at a temperature of  $T = 150$  MeV and total baryon density  $\varrho_B = \varrho_0$  (which, when accounting for all baryonic resonances with masses  $m_B \leq 1.7$  GeV as well as the lowest-lying  $\Lambda$  and  $\Sigma$  hyperons, translates into a common baryon chemical potential of  $\mu_B \simeq 385$  MeV) only about one third of the baryons are actually nucleons. On the other hand, also excited resonances will have nonzero cross sections with pions or  $\rho$  mesons which are, however, usually somewhat smaller in magnitude. The second subtlety consists of a substantial smearing of the zero temperature nucleon distribution functions (Fig. 3.18) which might further suppress any nucleon-driven medium effects in high-energy heavy-ion collisions. Nevertheless, meson-nucleon interactions are typically much stronger than meson-meson ones, such that even at full CERN-SpS energies (158–200 AGeV), where the final pion-to-nucleon ratio is about 5:1, baryons have a substantial impact on pion and  $\rho$ -meson properties as has been demonstrated by several authors.

In one class of models, medium effects in dilepton production rates are again studied by focusing on the role of the  $\rho$ -meson spectral function [140, 114, 47, 147]. As a representative we choose the most recent version of Refs. [102, 49, 123, 50], where both effects of finite temperature and finite density have been incorporated. In the baryonic sector the naive VDM, which works well for the description of purely mesonic processes (see previous Section), is improved by the Kroll-Lee-Zumino coupling [174] in the transverse part to optimally reproduce photoabsorption data (cf. Sect. 4.1.2). The dilepton rate is then given by

$$\frac{dR_{\pi\pi\rightarrow ee}}{d^4q}(q_0, \vec{q}) = \frac{\alpha^2}{\pi^3 g_{\rho\pi\pi}^2} \frac{f^\rho(q_0; T)}{M^2} \frac{1}{3} [\mathcal{F}^L(q_0, \vec{q}) + 2\mathcal{F}^T(q_0, \vec{q})] \quad (4.34)$$

with the transverse transition form factor  $\mathcal{F}^T$  from Eq. (4.19), whereas the longitudinal part, not being constrained by photon data, is obtained in the naive VDM,

$$\mathcal{F}^L(q_0, \vec{q}) = -(m_\rho^{(0)})^4 \text{Im}D_\rho^L(q_0, \vec{q}) . \quad (4.35)$$

Within model-independent approaches, a simultaneous assessment of finite temperature and finite density effects has been performed by Steele *et al.* [100, 104] using the chiral reduction formalism. Here the in-medium dilepton rates are based on the in-medium vector correlator as outlined in Sect. 2.8.

The thermal rate results employing the in-medium  $\rho$  spectral function and the chiral reduction formalism are confronted in Fig. 4.4. We should stress again that both approaches have been thoroughly constrained in both their finite density and finite temperature behavior (cf. Sects. 4.1.1 and 4.1.2). However, some differences emerge in the dilepton regime. At low invariant masses  $M_{ee} \leq 0.6$  GeV the rates qualitatively agree in that a strong additional enhancement due to the

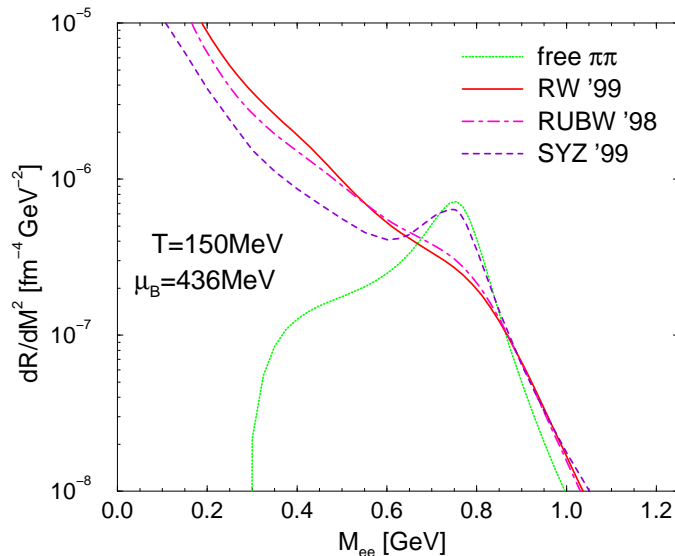


Figure 4.4: Three-momentum integrated dilepton rates in a hot meson-nucleon gas at  $T = 150$  MeV and a nucleon density  $\rho_N = 0.5\rho_0$  (corresponding to a nucleon chemical potential  $\mu_N = 436$  MeV) in the hadronic approaches of Steele *et al.* [100] (dashed line) and Rapp *et al.* [102, 123] (dashed-dotted line); the solid line corresponds to the full results of Ref. [50], *i.e.*, when additionally including scattering contributions off thermally excited baryonic resonances at a common baryon chemical potential  $\mu_B = \mu_N$  as described in Sect. 3.2.5.

presence of nucleons is observed. Quantitatively, the spectral function results give up to a factor of  $\sim 2$  more  $e^+e^-$  yield around  $M_{ee} \simeq 0.4$  GeV – exactly the region where the  $N(1520)$  contribution figures in most importantly. This discrepancy indeed originates from the different assignment of ‘background’ and resonance contributions in the photoabsorption spectra: in the chiral reduction formalism, the  $\gamma N$  cross sections are dominated by the non-resonant ‘background’ (see left panel of Fig. 4.1), whereas the most recent  $\rho$  spectral function calculations attribute the major strength to direct  $\rho N$  resonances, most relevant the  $N(1520)$  (see left panel of Fig. 4.2). The important point is now that when moving from the photon point to the time-like dilepton regime (at small three-momentum), the resonance contributions are much more enhanced than the more or less structureless background, which is essentially a kinematic effect<sup>1</sup>. As we have pointed out in

<sup>1</sup>Similar conclusions have been reached in Ref. [104]; it has been shown there that when ‘artificially’ reducing the  $\pi N$  background obtained from the chiral reduction formalism in the photoabsorption spectra by a factor of 3 and assigning the missing strength to the  $N(1520)$ , the resulting prediction for the dilepton rate in the  $M = 0.4$  GeV region increases by a factor of 2–3.

Sect. 4.1.2, these deviations can be resolved by analyzing more exclusive channels in the photoabsorption data. A more severe, *qualitative* difference in the rate predictions of Fig. 4.4 again shows up around the free  $\rho/\omega$  mass. Whereas the virial-type density expansion of the chiral reduction formalism leaves the dilepton yield essentially unchanged, the spectral function result exhibits a strong reduction of the resonance peak due to a large in-medium broadening of the  $\rho$  meson (see the discussion at the end of the previous Section). Thus, contrary to collective effects, which are typically driven by strong resummation effects in the *real* part of the selfenergy, higher order effects in the *imaginary* part of the vector meson propagators seem to play an important role. Finally we remark that the additional inclusion of excitations on thermally excited resonances of type  $B_1 B_2^{-1}$  (cf. Sect. 3.2.5) [50] further reinforces the broadening and low-mass enhancement by up to 20%, see solid curve in Fig. 4.4.

To summarize this Section about the various hadronic dilepton rate calculations one may conclude that quite different approaches pursued in the literature so far have reached a reasonable consensus in the pure mesonic sector. The corresponding enhancement over the 'standard candle' of free  $\pi\pi$  annihilation below the free  $\rho/\omega$  masses amounts to a factor of  $\sim 3 - 5$  at typical temperatures around  $T = 150$  MeV. At finite baryon density, due to the stronger nature of meson-baryon interactions, a substantially stronger impact on in-medium dilepton rates has been found, entailing more pronounced discrepancies between various models, differing *quantitatively* in the low-mass region (by factors of 2–3), and, more importantly, *qualitatively* as far as the fate of the vector meson resonance peaks is concerned.

## 4.2.2 Beyond Conventional Scenarios for Dilepton Enhancement

In this Section we will present some more speculative mechanisms for dilepton production which conceptually deviate from the rather well established hadronic reactions discussed in the previous Section. In particular, we will address radiation from quark-antiquark annihilation, disoriented chiral condensates and a dropping  $\rho$ -meson mass as implied by BR scaling.

### Quark-Gluon Plasma

At sufficiently high invariant masses as well as temperatures and densities asymptotic freedom of the quark interactions implies that the rate can be described by perturbation theory. In lowest order of the strong coupling constant,  $O(\alpha_S^0)$ , it is determined by the free  $q\bar{q} \rightarrow \gamma^* \rightarrow e^+e^-$  annihilation process through a convolution over anti-/quark three-momenta  $p_{\bar{q}}, p_q$  according to

$$\frac{dR_{q\bar{q} \rightarrow ee}}{d^4q} = \int \frac{d^3p_q}{(2\pi)^3} \frac{d^3p_{\bar{q}}}{(2\pi)^3} \sum_q v_{q\bar{q}} \sigma_{q\bar{q} \rightarrow ee}(M) f^q(p_q^0) f^{\bar{q}}(p_{\bar{q}}^0) \delta^{(4)}(q - p_q - p_{\bar{q}}), \quad (4.36)$$

where the total color-averaged  $q\bar{q} \rightarrow ee$  cross section for each flavor  $q = u, d, s, \dots$  is given by

$$\sigma_{q\bar{q} \rightarrow ee}(M) = e_q^2 \frac{4\pi\alpha^2}{9M^2} \left(1 - \frac{4m_q^2}{M^2}\right)^{-\frac{1}{2}} \left(1 + \frac{2m_q^2}{M^2}\right) \quad (4.37)$$

with current quark masses  $m_q$  and fractional quark charges  $e_q = -\frac{1}{3}, +\frac{2}{3}$ . In Eq. (4.36)

$$v_{q\bar{q}} = \frac{M\sqrt{M^2 - 4m_q^2}}{2\omega_{p_q}\omega_{p_{\bar{q}}}} \quad (4.38)$$

denotes the relative velocity between quark and antiquark, and

$$\begin{aligned} f^q(p_q) &= \frac{N_s N_c}{\exp[u \cdot p_q - \mu_q] + 1} \\ f^{\bar{q}}(p_{\bar{q}}) &= \frac{N_s N_c}{\exp[u \cdot p_{\bar{q}} + \mu_q] + 1} \end{aligned} \quad (4.39)$$

their Fermi distribution functions including spin-color degeneracy factors as well as the quark chemical potential  $\mu_q$ . The fluid velocity of the plasma relative to the thermal frame is denoted by  $u^\mu$ . For a plasma at rest  $u^\mu = (1, 0, 0, 0)$  and in the limit of vanishing quark masses the momentum integrations can be performed analytically yielding [177, 178]

$$\frac{dR_{q\bar{q} \rightarrow ee}}{d^4q} = \frac{\alpha^2 T}{4\pi^4 q} f^B(q_0; T) \sum_q e_q^2 \ln \frac{(x_- + \exp[-(q_0 + \mu_q)/T])(x_+ + \exp[-\mu_q/T])}{(x_+ + \exp[-(q_0 + \mu_q)/T])(x_- + \exp[-\mu_q/T])} \quad (4.40)$$

with  $x_\pm = \exp[-(q_0 \pm q)/2T]$ . For  $\mu_q = 0$  Eq. (4.40) simplifies to

$$\frac{dR_{q\bar{q} \rightarrow ee}}{d^4q} = \frac{\alpha^2}{4\pi^4} f^B(q_0; T) \left( \sum_q e_q^2 \right) \left( 1 + \frac{2T}{q} \ln \left[ \frac{1 + x_+}{1 + x_-} \right] \right). \quad (4.41)$$

Note that, apart from the overall Bose factor  $f^B$ , this result carries a temperature-dependent correction factor as compared to the widely used  $O(T^0)$  approximation. The additional  $\ln$ -term gives in fact a negative contribution which becomes significant for invariant masses below  $M_{ee} \simeq 1$  GeV, cf. Fig. 4.5. Another noteworthy feature is that with increasing net quark density ( $\mu_q > 0$ ) the perturbative emission rate from a QGP decreases slightly at low masses due to the mismatch between the quark and antiquark Fermi spheres.

Perturbative QCD corrections to the  $q\bar{q}$  rate have been studied, *e.g.*, in Refs. [179, 180, 181] and turned out to be appreciable, especially when extrapolated to invariant masses well below 1 GeV where the results cease to be reliable. Furthermore, since in the plasma phase at moderate temperatures,  $T \simeq (1-2)T_c$ , the strong coupling constant is still of order 1, nonperturbative effects might not be small either in this regime. In particular, the gluon condensate is non-vanishing as discussed in Sect. 2.4. In Ref. [182], *e.g.*, the somewhat speculative existence of an (euclidean)  $A_4$  condensate of type  $\langle \frac{\alpha_s}{\pi} A_4^2 \rangle$  has been shown to generate a strong enhancement in the rate at low invariant masses. More conservative approaches include instanton-induced interactions [54] (known to be of prime importance for the nonperturbative QCD vacuum structure and the low-lying hadronic spectrum) which, in somewhat modified appearance at finite temperature/density (*i.e.*, as so-called instanton-antiinstanton ( $I$ - $A$ ) molecules) might still prevail at moderate plasma conditions [183, 184, 185]; in fact,  $I$ - $A$  molecule induced  $q\bar{q}$  interactions, as opposed to single

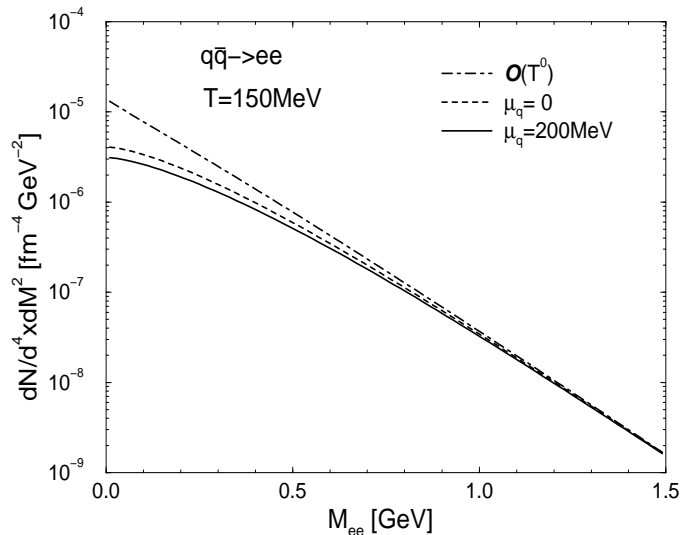


Figure 4.5: Three-momentum integrated perturbative  $q\bar{q} \rightarrow e^+e^-$  annihilation rates at temperature  $T=150$  MeV: for  $\mu_q = 0$  (dashed line) and  $\mu_q = 200$  MeV (solid line) using Eq. (4.40), and at  $\mu_q = 0$  using Eq. (4.41) to order  $O(T^0)$  (dashed-dotted line); all curves have been obtained for three massless quark flavors.

instantons, lead to nonzero contributions in the vector channel, which, however, seem to be quite small [184].

A generic feature of dilepton production rates from the plasma phase are the so-called van-Hove singularities [179, 186, 187], *i.e.*, (possibly) sharp structures as a function of the dilepton energy. They originate from a softening of the quark dispersion relation in the medium (the so-called 'plasmino' branch [179]) and are typically located at rather small energies below  $\sim 0.5$  GeV. On the other hand, finite imaginary parts in the quark selfenergy as well as smearing effects when accounting for finite three-momenta of the virtual photon [188] will damp these peaks. Also, soft Bremsstrahlung-type processes involving gluons such as  $q\bar{q} \rightarrow g\gamma^*$  or  $qg \rightarrow \gamma^*q$  may easily overshadow the van-Hove structures at low  $M$  [179], even after including Landau-Pomeranchuk type effects [189], *i.e.*, destructive interferences in the coherent emission.

### Disoriented Chiral Condensate

Another possibility of increased (soft) dilepton radiation related to the chiral phase transition has been associated with so-called Disoriented Chiral Condensates (DCC's), which have been suggested to develop in the cooling process of high-energy heavy-ion collisions [190, 191]. Assuming the

formation of a chirally restored plasma phase in the early stages of the collision, a sufficiently rapid transition into the chirally broken phase might not select the standard ground state characterized by a single scalar (sigma) condensate  $\langle\sigma\rangle = \langle\bar{q}q\rangle \neq 0$ , but rather 'jump' into a chirally rotated (metastable) state carrying a nonvanishing pseudoscalar (*i.e.*, pion-) condensate  $\langle\vec{\pi}\rangle = \langle\bar{q}\gamma_5\vec{\tau}q\rangle \neq \vec{0}$ . In particular, this state carries nonzero net isospin, which provides the basis for detecting it in event-by-event analyses of heavy-ion collisions through anomalous fluctuations in, *e.g.*, the number of  $\pi^0$ 's. Since the pion condensates inherent in the DCC constitute an enhanced source of predominantly soft pions, it has soon been realized that within this coherent state a copious annihilation into soft dilepton pairs might occur, similar to the standard  $\pi\pi$  annihilation, only at much lower invariant masses. In fact, the dominant yield from such coherent radiation will be concentrated well below the two-pion threshold [192]. Therefore, such a signal will be very difficult to discriminate in a heavy-ion collision due to the notoriously large background from  $\pi^0 \rightarrow \gamma e^+ e^-$  Dalitz decays after freezeout. However, as suggested in Ref. [193], non-coherent pions from the surrounding heat bath may annihilate on the coherent state, forming dilepton pairs of typical invariant masses in a rather narrow window around  $M \simeq 2m_\pi$ , thus avoiding the  $\pi^0$  Dalitz-decay region. Starting from the standard linear  $\sigma$ -model Lagrangian,

$$\mathcal{L}_{lsm} = \frac{1}{2}\partial_\mu\phi\partial^\mu\phi - \frac{1}{4}\lambda(\phi^2 - v^2)^2 + H\sigma, \quad (4.42)$$

the coupling to the electromagnetic current is realized through the third component of the isovector current as

$$\begin{aligned} j_\mu^{\text{em}}(x) &= [\vec{\pi} \times \partial_\mu \vec{\pi}]_3 \\ &= \frac{i}{2} \left[ \pi^\dagger(x) \overleftrightarrow{\partial}_\mu \pi(x) \pi(x) \overleftrightarrow{\partial}_\mu \pi^\dagger(x) \right], \end{aligned} \quad (4.43)$$

where the pion fields in charge basis are related to the isospin fields as

$$\begin{aligned} \pi(x) &= \frac{1}{\sqrt{2}} [\pi_1(x) - i\pi_2(x)] \\ \pi^\dagger(x) &= \frac{1}{\sqrt{2}} [\pi_1(x) + i\pi_2(x)]. \end{aligned} \quad (4.44)$$

The electromagnetic current-current correlator entering the dilepton rate can then, employing a mean-field treatment, be expressed by pion two-point functions as

$$\begin{aligned} W_{\mu\nu}(x, y) &= \langle\pi^\dagger(x)\pi(x)\rangle \langle\partial_\mu\pi(x)\partial_\nu\pi^\dagger(y)\rangle + \langle\partial_\mu\pi^\dagger(x)\partial_\nu\pi(x)\rangle \langle\pi(x)\pi^\dagger(y)\rangle \\ &\quad - \langle\partial_\mu\pi(x)\pi^\dagger(x)\rangle \langle\pi^\dagger(x)\partial_\nu\pi(y)\rangle - \langle\partial\pi^\dagger(x)\pi(x)\rangle \langle\pi(x)\partial_\nu\pi^\dagger(y)\rangle. \end{aligned} \quad (4.45)$$

Further following Ref. [193], the charged pion fields are expanded in creation and annihilation operators ( $a_k^\dagger, a_k$  for positive and  $b_k^\dagger, b_k$  for negative pions) with accompanying mode functions  $f_k$  as

$$\pi(\vec{x}, t) = \int \frac{d^3k}{(2\pi)^3} e^{i\vec{k}\cdot\vec{x}} \left[ f_k(t)a_k + f_k^*(t)b_{-k}^\dagger \right]. \quad (4.46)$$

The time evolution of the pion fields, and thus of the dilepton production rate, is then determined by specifying the mode functions together with appropriate initial conditions for the  $\sigma$  mean-field. Results have been obtained for both a purely thermal scenario (pion gas) and a DCC ('quench') scenario at equivalent initial energy density. A strong enhancement (factors of  $\sim 10$ – $50$ ) of the DCC based rates over the thermal ones, Eq. (4.29), was found at invariant masses around  $2m_\pi$ , but restricted to rather low total three-momenta  $|\vec{q}| \leq 300 - 500$  MeV. The quoted ranges roughly reflect the uncertainty in the underlying approximations as estimated from a second calculation using classical equation-of-motion techniques to describe the time evolution of pion and  $\sigma$  fields.

### 'Dropping' Rho-Meson Mass

The most prominent approach that has been successfully applied to explain the low-mass dilepton enhancement in the CERN-SpS experiments in connection with the chiral restoration transition is based on the BR scaling conjecture [45] for effective chiral Lagrangians. In the dilepton context, the most relevant feature is the decrease of the  $\rho$ -meson mass at finite temperature and density which, reinforced through enhanced thermal occupation factors at lower masses, leads to a strong excess of  $e^+e^-$  pairs below the free  $\rho$  mass through the  $\pi\pi$ -annihilation channel. As long as no collisional broadening in the  $\rho$  width is included, the  $e^+e^-$  yield is sharply centered around the corresponding in-medium mass  $m_\rho^*$ . Unlike in the DCC scenario, where the enhancement is localized at invariant masses around  $2m_\pi$ ,  $m_\rho^*$  will 'sweep' over the entire low-mass region in the course of a heavy-ion collision due to the continuous cooling and dilution of the system from the chiral restoration point towards freezeout. More realistically, also in the dropping mass scenario the  $\rho$ -meson spectral function will undergo a substantial broadening in the hot and dense hadronic medium. In particular, if the decrease in the  $\rho$  mass is (partially) identified with resonant  $S$ -wave  $\rho$ - $N(1520)N^{-1}$  interactions (as discussed in detail in Ref. [103]), then large in-medium widths of the  $N(1520)$  resonance (as inferred from nuclear photoabsorption data) inevitably induce a large width of the low-lying  $N(1520)N^{-1}$  state. Since such an increase in width affects both the denominator *and* the numerator of  $\text{Im}D_\rho$ , entering the dilepton rate (4.29), the broadening does in essence not reduce the total number of produced pairs.

### Off Equilibrium Pion Gas

Another class of non-conventional scenarios with potential impact on dilepton radiation is associated with off-equilibrium situations. Deviations from thermal equilibrium are usually addressed within kinetic theory or transport-type approaches, and the preferred method to assess dilepton yields under these conditions should be numerical simulations. Fortunately, in the case of heavy-ion collisions, thermalization of the hadronic system seems to require only a few rescatterings, so that local thermal equilibrium (in the comoving frame of collective expansion) is established on time scales which are much shorter than the typical lifetime of the hadronic fireball [194, 195]. A fast approach to thermal equilibrium is further corroborated in scenarios with initially deconfined matter as demonstrated, *e.g.*, in QCD inspired event generators such as HIJING [196] or parton cascades [15]. Complete chemical equilibration, however, is by far less certain; in an expanding pion gas, *e.g.*, the empirical absence of pion number changing processes in low-energy  $\pi\pi$  interactions (*i.e.*, for invariant masses below  $M_{\pi\pi} \simeq 1$  GeV) together with the assumption of isentropic

expansion entails the build-up of a finite pion chemical potential  $\mu_\pi > 0$  towards lower temperatures [197]. Another possibility is that early hadron formation processes do not transform into a chemically equilibrated initial hadron gas but rather follow, *e.g.*, string dynamics [198].

The field-theoretical implementation of a finite  $\mu_\pi$  into the thermal dilepton production rate from  $\pi\pi$  annihilation has been studied by Baier *et al.* [41, 199] in the real-time formalism of finite temperature field theory. For practical purposes they worked in an approximation which amounts to introducing the chemical potential through Bose distribution functions as

$$\tilde{f}^B(k_0; \mu_\pi, T) = \begin{cases} f^B(|k_0|; \mu_\pi, T) & , k_0 > 0 \\ -[1 + f^B(|k_0|; \mu_\pi, T)] & , k_0 < 0 \end{cases} \quad (4.47)$$

with the standard finite- $\mu_\pi$  Bose factor  $f^B(|k_0|; \mu_\pi, T) = [e^{(|k_0| - \mu_\pi)/T} - 1]^{-1}$ . In the Boltzmann approximation and for situations not too far off equilibrium it was shown that the production rate in the standard one loop approximation (*i.e.*, Eq. (4.29) with  $\Sigma_{\rho\pi\pi}$  given by the free  $\pi\pi$  bubble) simply picks up an overall enhancement factor according to

$$\frac{dR_{\pi\pi \rightarrow ee}}{d^4q}(q_0, \vec{q}; \mu_\pi) = (1 + 2\delta\lambda) \frac{dR_{\pi\pi \rightarrow ee}}{d^4q}(q_0, \vec{q}; \mu_\pi = 0) \quad (4.48)$$

with  $\delta\lambda = \lambda - 1$  and the 'fugacity'  $\lambda = e^{\mu_\pi/T}$  (to lowest order in  $\mu_\pi/T$  one recognizes  $(1 + 2\delta\lambda) \simeq e^{2\mu_\pi/T}$ ).

The situation becomes more complicated if one includes higher thermal loop corrections in the pion propagators of the intermediate two-pion states. Without going into further details, we mention that the use of off-equilibrium distribution functions then implies the appearance of terms involving products of retarded and advanced propagators, schematically given as

$$\begin{aligned} D_\pi^R(k) D_\pi^A(k) &= \frac{1}{k^2 - m_\pi^2 + i \text{sgn}(k_0)\epsilon} \frac{1}{k^2 - m_\pi^2 - i \text{sgn}(k_0)\epsilon} \\ &= \frac{1}{(k^2 - m_\pi^2)^2 - \epsilon^2} , \end{aligned} \quad (4.49)$$

which apparently exhibit ill-defined poles, the so-called 'pinch-singularities'. They have to be regularized, *e.g.*, by accounting for thermal pion selfenergies  $\Sigma_\pi$  with finite imaginary parts  $\text{Im}\Sigma_\pi \neq 0$ , as was done in Refs. [41, 199]. As a somewhat surprising result, to leading order in  $1/\text{Im}\Sigma_\pi$  the pinch term actually generates an overall reduction (enhancement) of the dilepton production rate for positive (negative)  $\mu_\pi$ .

### 4.2.3 Quark-Hadron Duality

A key question that is at the heart of the entire heavy-ion physics program concerns discriminating signatures for the possible occurrence of a chiral restoration phase transition. In our context of low-mass dilepton observables we have already qualitatively eluded to some of them in the preceding Section, most notably DCC formation (characterized by a strong enhancement in the two-pion threshold region at low three-momenta) and the dropping  $\rho$ -meson mass (characterized by a complete extinction of the yield around the  $\rho$  peak, accompanied by a strong enhancement for lower



invariant masses). However, there is also the possibility that in the vicinity of the phase transition the dilepton radiation from the hot and dense fireball does *not* depend on whether it is in the chirally broken confined phase or the chirally restored QGP phase. In other words, in a certain temperature and density window around the transition region the dilepton rate calculations using either hadronic or quark-gluon degrees of freedom merge together, *i.e.*, the two descriptions become *dual*. Although this would imply that there is no unique dilepton signature which could distinguish the two phases, it is a highly non-trivial scenario. In the low-mass region, say for invariant masses  $M_{ll} \leq 1.5$  GeV, it requires that the hadronic side, which at low densities/temperatures is dominated by rather narrow resonances  $\rho, \omega, \phi, \rho'$ , etc., develops into a supposedly more or less structureless quark-gluon world (although the latter might still involve nonperturbative interactions). To illustrate that there are indeed indications for such a scenario [50, 200], we compare in Fig. 4.6 the lowest-order perturbative QCD  $q\bar{q}$  annihilation rates with the (most recent) full hadronic in-medium spectral function calculations at identical temperatures and equivalent baryon-/quark-chemical potential. Already at moderate temperature ( $T = 140$  MeV) and density ( $\rho_B = 0.75\rho_0$ ) they are not very

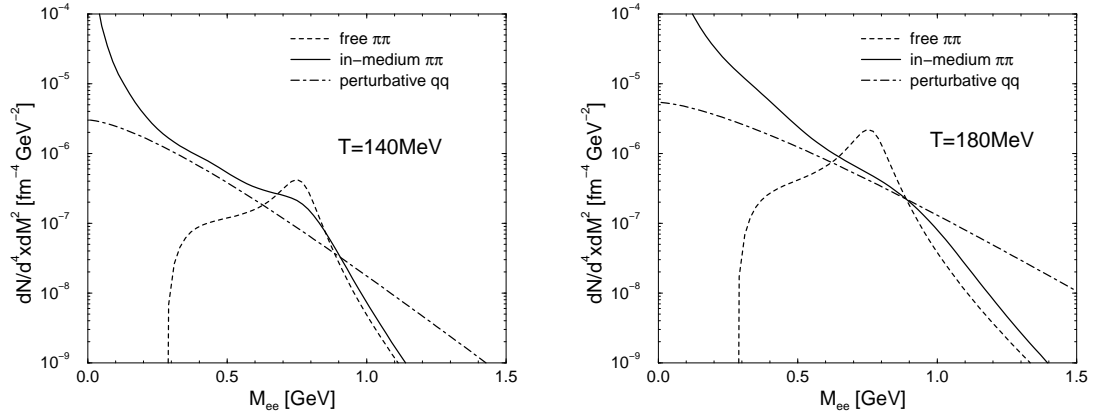


Figure 4.6: Three-momentum integrated dilepton production rates at a baryon chemical potential  $\mu_B = 408$  MeV and temperatures  $T = 140$  MeV (left panel) and  $T = 180$  MeV from free  $\pi\pi$  annihilation (dashed curves), in-medium  $\pi\pi$  annihilation within the most recent hadronic many-body approach of Refs. [47, 102, 123, 50], and from lowest order QCD  $q\bar{q}$  annihilation (dashed-dotted curves); the latter two are calculated at equivalent baryon/quark chemical potentials of  $\mu_q = \mu_B/3 = 136$  MeV.

different from each other (left panel), especially when contrasted with the result for free  $\pi\pi$  annihilation. Nevertheless, the in-medium  $\pi\pi$  curve still exhibits a clear trace of the  $\rho$  peak. The latter is completely 'melted' at  $T = 180$  MeV,  $\rho_B = 4\rho_0$  leading to remarkably close agreement with the  $q\bar{q}$  result in the invariant mass range of  $M_{ee} \simeq (0.5 - 1.0)$  GeV (one should note that the deviations between the partonic and the in-medium hadronic results towards low  $M_{ee}$  might be reduced once soft 'Bremsstrahlung'-type graphs are accounted for in the QGP environment.

On the other hand, as discussed in Sect. 4.2.2, plasmino modes can lead to additional nontrivial structures in the dilepton production rate [179, 186, 187] below  $M_{ee} \simeq 0.5$  GeV. The disagreement beyond 1 GeV is mainly caused by missing states involving more than two pions (such as the  $\rho'(1450)$ ) in the hadronic description of the free vector correlator, most notably four-pion type  $\pi a_1$  annihilation graphs, see also below). From an experimental point of view this means that, even if no *distinct* signatures for the appearance of new phases are extractable from low-mass dilepton production, the absolute yields and spectral shape are very different from free  $\pi\pi$  annihilation and contain rather specific information on properties of strongly interacting matter in the vicinity of the phase boundary. We will reiterate this point within a detailed analysis of low-mass dilepton observables below.

The duality arguments can be made more rigorous starting from the intermediate-mass region,  $1.5 \text{ GeV} \lesssim M_{ll} \lesssim 3 \text{ GeV}$ . Conceptually the situation there is more transparent: firstly, one might expect that at these energies the  $q\bar{q}$  annihilation process is already rather well described by a perturbative treatment. In fact, there is strong empirical support for this expectation from the well-known  $e^+e^- \rightarrow \text{hadrons}$  cross section, which can be accounted for by the perturbative result for  $e^+e^- \rightarrow q\bar{q}$  within a 30% accuracy in the above mentioned range, *i.e.*,

$$\sigma(e^+e^- \rightarrow \text{hadrons}) \simeq \frac{4\pi\alpha^2}{3M^2} R^{\text{pert}} \quad (4.50)$$

with the famous  $\sigma(e^+e^- \rightarrow \text{hadrons})/\sigma(e^+e^- \rightarrow \mu^+\mu^-)$ -ratio

$$R^{\text{pert}} = N_c \sum_q (e_q)^2 . \quad (4.51)$$

Secondly, since at  $\sim 2$  GeV one is probing space-time distances of the order of 0.1 fm, possible corrections from the surrounding heat bath should also be small. This gives some confidence that the perturbative expression for the dilepton emission rate from a quark-gluon plasma (4.36) is a reasonable approximation at intermediate masses. The challenge then is to match this result to a hadron-based calculation at temperatures in the vicinity of  $T_c$ .

In Ref. [201] this type of duality has been *enforced* in the spirit of a Hagedorn-type hadronic mass spectrum, where the complicated structure of overlapping, interacting hadronic resonances is encoded in some simple spectral density  $\xi_h(M)$ . Using VDM for the dilepton decays of the vector mesons,

$$\Gamma_{V \rightarrow ll}(M) = \frac{1}{g^2(M)} \frac{4\alpha^2 M}{3} , \quad (4.52)$$

the corresponding three-momentum integrated dilepton production rate at temperature  $T$  in Boltzmann approximation,

$$\frac{dR_{V \rightarrow ll}}{dM^2} = \xi_V(M) \frac{\alpha^2 M^2 T}{6\pi g^2(M)} K_1(M/T) \quad (4.53)$$

( $K_1$ : modified Bessel function), is then determined by the subspectrum of vector mesons,  $\xi_V(M)$ , and the corresponding VDM coupling  $1/g(M)$ . Further assuming that the  $e^+e^- \rightarrow \text{hadrons}$  cross section is saturated by vector mesons,

$$\sigma(e^+e^- \rightarrow V) = \frac{(2\pi)^3 \alpha^2}{g^2(M) M} \xi_V(M)$$

$$\simeq \sigma(e^+e^- \rightarrow h) \quad (4.54)$$

one can trade the dependence on  $g(M), \xi_V(M)$  for the experimental cross section ratio as [201]

$$\frac{dR_{V \rightarrow ll}}{dM^2} = \frac{\alpha^2 MT}{6\pi^3} K_1(M/T) R^{\text{exp}}(M), \quad (4.55)$$

where  $R^{\text{exp}}(M)$  now also accounts for (moderate) deviations from the lowest-order QCD result, Eq. (4.51). A similar procedure has been pursued by Huang [79] who additionally included lowest-order temperature effects through the vector-axialvector mixing phenomenon induced by soft pion contributions from the heat bath (cf. Sect. 2.6), leading to

$$\frac{dR_{ll}}{dM^2} = \frac{4\alpha^2 MT}{2\pi} K_1(M/T) \left( \rho_{\text{em}}^\circ(M) - \left( \epsilon - \frac{\epsilon^2}{2} \right) [\rho_V^\circ(M) - \rho_A^\circ(M)] \right) \quad (4.56)$$

with  $\epsilon = T^2/6f_\pi^2$  (in the chiral limit and for two flavors). The first term involving the full vacuum electromagnetic correlator coincides with (4.55), whereas the free vector and axialvector correlators are responsible for the soft pion corrections. Huang also extracted them from data, as delineated in Sect. 2.6, see Eqs. (2.92) and (2.93). It turns out that the finite-temperature corrections are marginal for dilepton invariant masses  $1.5 \text{ GeV} \leq M_{ee} \leq 2.5 \text{ GeV}$  and, moreover, that the 'empirical' results using Eq. (4.55) closely follow the perturbative results (4.51), cf. the open circles and the dotted line in Fig. 4.7. This is not surprising recalling that the 'duality threshold' in vacuum is situated at  $M \simeq 1.5 \text{ GeV}$ . On the other hand, it was pointed out in Ref. [201] that, when comparing the 'empirically' inferred rate (4.55) to the phenomenological hadronic rate calculations in terms of binary collisions of Ref. [119], the latter fall short by a factor of 2–3. However, in the hadronic treatment of Ref. [119] contributions from  $a_1(1260)$  mesons (in particular  $\pi a_1 \rightarrow ll$ ), which are most relevant for the intermediate-mass region, had not been included at the time. This has been improved later on [202, 203, 204] and shown to resolve the afore mentioned discrepancy (Fig. 4.7). The yield from  $\pi a_1$  processes was indeed found to dominate other sources such as  $\pi\omega, \pi\rho, \pi\pi$  or  $K\bar{K}$  channels for invariant masses  $1.2 \text{ GeV} \leq M_{ll} \leq 2.2 \text{ GeV}$ . In particular, it results in good agreement with both the perturbative  $q\bar{q}$  and the 'empirical' calculations including the lowest order  $V$ - $A$  mixing effect [79], Eq. (4.56), down to invariant masses of about 1 GeV, cf. solid line, dotted line and open points, respectively, in Fig. 4.7. In fact, the  $\pi a_1 \rightarrow \rho' \rightarrow e^+e^-$  contributions exactly correspond to the mixing effect since thermal pions colliding with an  $a_1$  meson 'move' strength from the axialvector to the vector channel! Also shown in Fig. 4.7 are the results obtained within the chiral reduction formalism [205]; here the free correlators have been determined from a set of 12  $\rho, \omega, \phi, a_1$  and  $K_1$  resonances below  $M = 2 \text{ GeV}$ , and by a parameterization of  $R^{\text{exp}}(M)$  above. Single-meson final-state corrections have then been inferred via chiral Ward identities. Again, the agreement with the other approaches is quite satisfactory.

As we will see in Sect. 4.6.6, the intermediate-mass emission rates as deduced above provide a good description of experimental  $\mu^+\mu^-$  spectra measured by the HELIOS-3 collaboration [24] at full CERN-SpS energies (200 AGeV), which show an excess of a factor of 2–3 in S+W as compared to p+W collisions. Similar observations have been made by the NA50/NA38 collaboration [25, 27], and the most natural explanation seems to be thermal radiation. This further supports the theoretical arguments for quark-hadron 'duality' in intermediate-mass dilepton production. Since

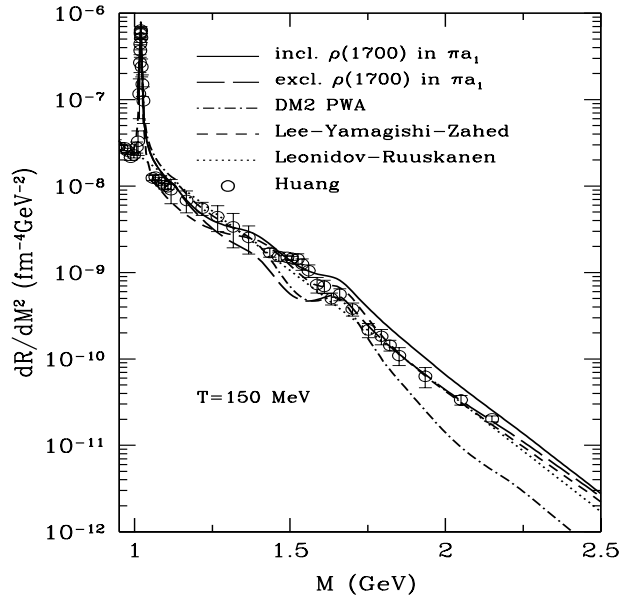


Figure 4.7: Three-momentum integrated dilepton production rates in the intermediate-mass region at a temperature  $T = 150$  MeV, as obtained in various approaches; solid, long-dashed and dashed-dotted curve: hadronic calculations of Ref. [204] with different ways of estimating the  $\pi a_1$  contribution; short-dashed curve: chiral reduction approach [205]; dotted curve: using the perturbative value  $R^{pert} = 2$  in Eq. (4.55) [201]; open circles: using empirical spectral densities including lowest order temperature corrections according to Eq. (4.56) [79]. The plot is taken from Ref. [204].

the intrinsic energy scales in this region are already suggestive for a perturbative treatment within the partonic picture, the agreement with the phenomenological hadronic calculations above 1.5 GeV may be considered as the more intriguing part (it will still be worthwhile to understand the origin of the 30–40% deviations of  $R_{exp}(M)$  from the lowest-order perturbative  $q\bar{q}$  results). As we have argued already in Sect. 2.6, medium effects start to become visible below 1.5 GeV, where the lowest-order in temperature  $V$ - $A$  mixing establishes a three-fold degeneracy between vector and axialvector correlators on the one hand (dictated by chiral symmetry), and the perturbatively calculated  $q\bar{q}$  rates on the other hand, reaching down to about 1 GeV.

### 4.3 Photon Production Rates

In our analysis of electromagnetic observables in heavy-ion reactions we will also address spectra of single (real) photons. This is motivated by the observation that every process capable of creating a dilepton pair can, in principle, lead to the radiation of a (real) photon: the latter simply constitutes the  $M^2 \rightarrow 0$  limit of the virtual (time-like) photon which occurs as an intermediate state in each dilepton-producing reaction. This intimate relation has already been extensively exploited for

imposing model constraints on in-medium effects through photoabsorption data on the nucleon and nuclei, cf. Sect. 4.1.2. In Sect. 4.7 the reverse process, *i.e.*, photon production in heavy-ion reactions, will be used as an additional consistency check.

Theoretical calculations for photon production rates have been performed for both the hadronic and the plasma phases. In the latter, one has mainly focused on lowest-order QCD calculations for two-body reactions of the annihilation type,  $q\bar{q} \rightarrow g\gamma$ , as well as the Compton type,  $q(\bar{q})g \rightarrow q(\bar{q})\gamma$ . The first analysis of hadronic photon rates has been performed in Ref. [206] for a heat bath of the lightest, non-strange pseudoscalar ( $\pi, \eta$ ) and vector mesons ( $\rho, \omega$ ). The most important reactions have been attributed to the analogues of the QGP processes,  $\pi\pi \rightarrow \rho\gamma$  and  $\pi\rho \rightarrow \pi\gamma$ , as well as the vector meson decay channels  $\omega \rightarrow \pi\gamma$  and  $\rho \rightarrow \pi\pi\gamma$ . The conclusion of Ref. [206] was summarized as 'the hadron gas shines as brightly as the quark-gluon plasma', *i.e.*, the photon production rates of both phases closely coincided over a large range of photon energies  $E_\gamma \geq 0.5$  GeV. Later on the importance of the  $a_1(1260)$  meson – not included in Ref. [206] – as an intermediate state in  $\pi\rho \rightarrow a_1 \rightarrow \pi\gamma$  has been realized, especially for photon energies above 0.5 GeV. The impact of nucleons on photon production has been explicitly discussed, *e.g.*, in Ref. [100]. In fact, analogous information can be readily extracted from any dilepton rate calculation involving baryonic processes [47, 147, 91] by extrapolating it to the photon point. To be specific, the differential photon production rate can be obtained from the dilepton expression (4.23) by simply replacing the lepton tensor by the photon tensor

$$P_{\mu\nu} = 4\pi\alpha \int \frac{d^3p}{(2\pi)^3 2p_0} \sum_\lambda \varepsilon_\mu^*(\lambda, p) \varepsilon_\nu(\lambda, p) \delta^{(4)}(p - q) \quad (4.57)$$

such that

$$\frac{dR_\gamma}{d^4q} = P_{\mu\nu} W^{\mu\nu}, \quad (4.58)$$

which can be simplified to

$$q_0 \frac{dR_\gamma}{d^3q} = \frac{\alpha}{4\pi^2} W(q) \quad (4.59)$$

with  $q_0 = |\vec{q}|$  and  $W(q) \equiv g_{\mu\nu} W^{\mu\nu}$ . In the (improved) VDM, *e.g.*, the photon rate becomes

$$q_0 \frac{dR_\gamma}{d^3q} = \frac{\alpha}{\pi^2 g_\rho^2} f^\rho(q_0) \mathcal{F}^T(q_0, |\vec{q}| = q_0) \quad (4.60)$$

with the transverse transition form factor from Eq. (4.19).

## 4.4 Space-Time Evolution of Heavy-Ion Collisions

Dilepton spectra as measured in (ultra-) relativistic heavy-ion collision experiments might be, at least conceptually, split up into two components: the first one arises from the phase where the system is characterized by strong interactions among its constituents, as a result of which a certain amount of photons (real and virtual) is radiated. Once the hadronic system has reached a degree of diluteness where the short-range strong interactions are no longer effective (the so-called hadronic freezeout stage), all unstable resonances decay according to their vacuum lifetimes, with some

probability into radiative channels. Therefore, this second component (which has become known as the 'hadronic cocktail' contribution to the dilepton spectra) does not contain any information on in-medium properties of the parent particles. However, it can be reasonably well reconstructed once the hadronic abundances at freezeout are known (this may not be that evident and we will come back to this issue in Sect. 4.6.1). On the other hand, given one's favorite dilepton production rate in hot and dense matter, the calculation of the first component requires the knowledge of the space-time history of the colliding and expanding nuclear system. This is one of the major objectives in relativistic heavy-ion physics by itself. In the following we will discuss three different approaches to simulate the reaction dynamics in their application to evaluate dilepton spectra.

#### 4.4.1 Hydrodynamical Approach

The hydrodynamic description of heavy-ion collisions is based on the assumption that the strong interactions in the matter are able to maintain local thermal equilibrium throughout the expansion of the nuclear system until some breakup stage (the freezeout). Thus, each fluid cell in its rest frame is characterized by standard thermodynamic variables such as pressure, temperature and (energy-) density. For this reason the hydrodynamic framework is the most natural one for the implementation of equilibrium dilepton rates, as the latter are formulated in exactly the same variables. It has a long tradition in its application to high-energy reactions involving high-multiplicity hadronic final states, starting from hadron-hadron [207, 208] (or even  $e^+e^-$  [209]) collisions to the more modern field of relativistic nucleus-nucleus reactions [210, 211, 212, 213, 214]. The basic equations are the conservation of energy and momentum, which can be expressed in a Lorentz-covariant form as

$$\partial_\mu T^{\mu\nu}(x) = 0 \quad (4.61)$$

through the energy-momentum tensor  $T^{\mu\nu}(x)$ . For an ideal fluid, *i.e.*, neglecting any viscosity, the latter is given by

$$T^{\mu\nu}(x) = [\epsilon(x) + p(x)] u^\mu(x) u^\nu(x) - p(x) g^{\mu\nu} \quad (4.62)$$

with local energy-density  $\epsilon(x)$ , pressure  $p(x)$  and fluid 4-velocity  $u^\mu(x)$ . Additionally conserved currents, such as the baryon number current,  $j_B^\mu = \varrho_B u^\mu$ , or the strangeness current are enforced by pertinent continuity equations,

$$\partial_\mu j_B^\mu = 0, \quad \text{etc.} \quad (4.63)$$

Let us also mention here that in the later stages of heavy-ion collisions the pion number might be effectively conserved due to the empirical absence of pion-number changing processes at small  $cm$  energies (see also Sect. 4.2.2). In this case, one has a further continuity equation,

$$\partial_\mu j_\pi^\mu = 0, \quad (4.64)$$

which induces a nonzero pion chemical potential.

The basic ingredient governing the hydrodynamic evolution of the system is the equation of state (EoS), *i.e.*, the dependence of the pressure on energy- and baryon-density,  $p = p(\epsilon, \varrho_B)$ . For heavy-ion collisions at (ultra-) relativistic energies, the early stages can be barely considered as proceeding under any kind of equilibrium conditions. In the hydrodynamic description, one therefore has to assume a so-called formation time  $\tau_0$  (typically around 1-2 fm/c) together with

some initial conditions for the energy density. Given a specific EoS, these have to be determined by requiring a reasonable fit to the finally observed hadronic spectra, with some additional freedom of how and at which temperature the freezeout occurs. The differential equations for the evolution are usually solved numerically on a space-time grid using finite-differencing methods.

Many interesting issues can be addressed within the hydrodynamic framework, as, *e.g.*, the interrelation between collective flow and freezeout temperature [211] or properties of the EoS in connection with potential phase transitions in strongly interacting matter [215, 213, 216]. Here, we restrict ourselves to the evaluation of dilepton spectra. Given a thermal production rate,  $dR/d^4q$ , the total spectrum from in-medium radiation is straightforwardly obtained as a sum over all timesteps in the evolution and over all fluid cells of the grid of individual temperature and density above the freezeout value. The contribution of a single cell is given by

$$\left(\frac{dN_{ll}}{d^4q}\right)_{cell} = \left(\frac{dN_{ll}}{d^4qd^4x}(q_0, \vec{q}; T_{cell}, \mu_{B,cell})\right) V_{cell} \Delta t, \quad (4.65)$$

where the time-step width  $\Delta t$  and cell 3-volume  $V_{cell}$  are to be taken in the local rest frame of the cell. As there is no preferred direction in this frame, the virtual photon of invariant mass  $M = (q_0^2 - \vec{q}^2)^{1/2}$  and three-momentum  $\vec{q}$  can be assumed to decay isotropically into dileptons. The resulting two lepton tracks then have to be boosted to the lab-system according to the local fluid velocity  $u^\mu$ , where possible experimental acceptance cuts can be readily applied. However, in some practical applications, this procedure might be too time consuming. An approximate but more efficient way is to first integrate over the (possibly complicated) three-momentum dependencies to obtain  $dR/dM^2$  and then regenerate rapidity and transverse momentum distributions according to [217]

$$\frac{dR}{dM^2 dy q_t dq_t} = \frac{1}{2MT K_1(M/T)} e^{-E/T} \frac{dR}{dM^2}(M, T) \quad (4.66)$$

with  $E = q_\mu u^\mu$ . This procedure has been employed, *e.g.*, in the hydrodynamic models of Refs. [214, 43], where dilepton spectra at the full CERN-SpS energies have been analyzed. In both works the hydrodynamic equations have been solved locally in (2+1) dimensions assuming cylindrical symmetry of the collision system (which implies a restriction to central collisions).

A further simplification can be made in the limit of ultrarelativistic collision energies, as suggested by Bjorken [218]. In this case the longitudinal expansion is dominant and boost invariance can be assumed so that the longitudinal velocity scales with the distance from the central region as  $v_L = z/t$ . Neglecting transverse expansion, the 4-volume element simply becomes

$$d^4x = d^2r_t dz dt = \pi R_t^2 dy \tau d\tau \quad (4.67)$$

with the proper time  $\tau = (t^2 - z^2)^{1/2}$  and *cms* rapidity

$$y = \frac{1}{2} \ln \frac{t+z}{t-z}. \quad (4.68)$$

The transverse extension  $R_t$  is typically taken close to the overlap radius of the colliding nuclei. From local entropy conservation,

$$\frac{\partial(su_\mu)}{\partial x_\mu} = 0, \quad (4.69)$$

one finds the entropy-density to behave as  $s(\tau) = s(\tau_0)\tau_0/\tau$ . Moreover, for isentropic expansion one can relate the final-state hadron multiplicity to the formation time  $\tau_0$ , initial entropy-density and transverse size as [219]

$$\frac{dN_h}{dy} \simeq \pi R_t^2 \tau_0 s(\tau_0) . \quad (4.70)$$

If one further assumes an ideal gas EoS, the temperature scales as

$$T(\tau) = T_0 \left( \frac{\tau}{\tau_0} \right)^{-1/3} . \quad (4.71)$$

The dilepton rates are then easily integrated over the time history of the hot nuclear system, as has been done, *e.g.*, in Refs. [10, 177, 115, 220] or, specifically for CERN-SpS conditions at 158–200 AGeV in Refs. [40, 221, 41, 178].

The contribution to the dilepton spectrum from hadron decays after freezeout proceeds along similar lines as in transport calculations (see the following Section).

The discussion of the actual results for the final dilepton spectra is deferred to Sect. 4.6 where it will be put into perspective in comparison with other dynamical approaches for the heavy-ion reaction dynamics.

#### 4.4.2 Transport Simulations

The transport-theoretical approach has been extensively used in the past in various facets to describe heavy-ion reaction dynamics over a broad range of collision energies. Among these are the Boltzmann-Uehling-Uhlenbeck (BUU) approach [222] and its relativistic extensions (RBUU) [223, 224], Quantum Molecular Dynamics [225] and its relativistic versions RQMD [226], UrQMD [227], or the Hadron-String Dynamics (HSD) [195].

In the relativistic treatments the evolution dynamics of the two colliding nuclei are governed by a coupled set of (covariant) transport equations for the phase-space distributions  $f_h(x, p)$  of hadron  $h$ ,

$$\begin{aligned} & \left\{ (\Pi_\mu - \Pi_\nu \partial_\mu^p U_h^\nu - M_h^* \partial_\mu^p U_h^S) \partial_x^\mu + (\Pi_\nu \partial_\mu^x U_h^\nu + M_h^* \partial_\mu^x U_h^S) \partial_p^\mu \right\} f_h(x, p) \\ &= \sum_{h_2 h_3 h_4 \dots} \int d^2 d^3 d^4 \dots [G^\dagger G]_{12 \rightarrow 34 \dots} \delta^{(4)}(\Pi + \Pi_2 - \Pi_3 - \Pi_4 \dots) \\ & \times \left\{ f_{h_3}(x, p_3) f_{h_4}(x, p_4) \bar{f}_h(x, p) \bar{f}_h(x, p_2) - f_h(x, p) f_{h_2}(x, p_2) \bar{f}_{h_3}(x, p_3) \bar{f}_{h_4}(x, p_4) \right\} \dots \end{aligned} \quad (4.72)$$

The *lhs* describes the motion of particle 1 under consideration in momentum-dependent relativistic mean fields  $U_h^S(x, p)$  and  $U_h^\mu(x, p)$ , which correspond to the real part of the scalar and vector hadron selfenergies, respectively. The *rhs* represents the collision term for the process  $1 + 2 \rightarrow 3 + 4 + \dots$  involving momentum integrations for incoming particle 2 as well as all outgoing particles 3, 4,  $\dots$ . The associated ‘transition rate’  $W \equiv [G^\dagger G]_{12 \rightarrow 34 \dots} \delta^{(4)}(\Pi + \Pi_2 - \Pi_3 - \Pi_4 \dots)$  is given in terms of the relativistic G-matrix (*i.e.*, the in-medium scattering amplitude). For on-shell two-body scattering



the transition rate can be expressed through the differential cross section as

$$W = s \frac{d\sigma}{d\Omega}(s, \theta) \delta^{(4)}(\Pi + \Pi_2 - \Pi_3 - \Pi_4) \quad (4.73)$$

with *cms* energy  $s = (\Pi + \Pi_2)^2$  and scattering angle  $\theta$ . The hadron quasiparticle properties in Eq. (4.72) are defined via the mass-shell constraint [228], characterized by  $\delta(\Pi_\mu \Pi^\mu - M_h^{*2})$ , with effective masses and momenta given by

$$\begin{aligned} M_h^*(x, p) &= M_h + U_h^S(x, p) \\ \Pi^\mu(x, p) &= p^\mu - U_h^\mu(x, p) \quad , \end{aligned} \quad (4.74)$$

while the phase-space factors

$$\bar{f}_h(x, p) = 1 \pm f_h(x, p) \quad (4.75)$$

account for Pauli blocking or Bose enhancement, depending on the type of hadron in the final and initial state. The ellipsis in Eq. (4.72) indicate further contributions to the collision term with more than two hadrons in the final/initial channels. The transport approach (4.72) is fully specified by in-medium potentials  $U_h^S(x, p)$  and  $U_h^\mu(x, p)$  ( $\mu = 0, 1, 2, 3$ ), which determine the mean-field propagation of the hadrons, and by the transition rates  $G^\dagger G \delta^{(4)}(\dots)$  in the collision term that describe the scattering and hadron production/absorption rates. Clearly, these quantities should be in accordance with empirical information as much as possible. Therefore, a frequently used model for the underlying microscopic mean-field potentials is the  $\sigma - \omega$  (Walecka) model [229] (also known as 'Quantum Hadrodynamics' or QHD) which accounts for the ground-state properties of nuclear matter as well as proton-nucleus scattering, once momentum-dependent corrections are properly included. To make a more direct link to the underlying quark structure, which should become relevant at full CERN-SpS energies, the ideas of the Walecka model have been extended to couple the mean fields to the constituent quarks within the hadrons [37], without distorting the nuclear matter properties. In the HSD approach, where the (soft) hadronic dynamics are also based on (chiral) quark dynamics along the lines of NJL-models, extra care has been taken to correctly handle the 'hard' processes (relevant in the collision term). This has been achieved by employing the LUND string fragmentation model [198], which correctly describes inelastic hadronic reactions over a wide energy regime. The HSD model has been successfully applied to heavy-ion reactions ranging from SIS (1 AGeV) to CERN-SpS (200 AGeV) energies, see Ref. [195] for a comprehensive presentation.

In the transport framework, dilepton observables can be calculated with relative ease by incorporating the relevant process in the collision term using the corresponding cross sections. In the case of  $\pi\pi$  annihilation, which in VDM proceeds through  $\rho$ -meson formation, one has

$$\begin{aligned} \sigma_{\pi^+\pi^-\rightarrow e^+e^-}(M) &= \sigma_{\pi^+\pi^-\rightarrow\rho^0}(M) \Gamma_{\rho^0\rightarrow e^+e^-}(M)/\Gamma_{\rho^0}^{tot} \\ &= \frac{4\pi\alpha^2}{3} \frac{p_\pi}{M^3} |F_\pi(M)|^2 \end{aligned} \quad (4.76)$$

with the electromagnetic form factor  $F_\pi$  and the pion decay momentum  $p_\pi = (M^2/4 - m_\pi^2)^{1/2}$ . Since electromagnetic processes are suppressed by a factor  $\alpha = 1/137$  (for dilepton production

by even a factor of  $\alpha^2$ , *i.e.*, four orders of magnitude), the feedback on the heavy-ion reaction dynamics can be neglected. To account for decays of  $\rho$  mesons which are not produced in the  $\pi\pi$  channel but, *e.g.*, in  $\pi N$  or  $NN$  collisions, one integrates their (time-dependent) abundance in the fireball over its lifetime  $t_{fo}$  according to [37, 230]

$$\frac{dN_{\rho \rightarrow ee}}{dM} = \int_0^{t_{fo}} dt \frac{dN_{\rho^0}(t)}{dM} \Gamma_{\rho^0 \rightarrow ee}(M), \quad (4.77)$$

where  $dN_{\rho^0}(t)/dM$  is the number of  $\rho$  mesons per invariant mass bin  $dM$  at time  $t$ . In fact, the same treatment can be applied to  $\rho$  mesons produced in the  $\pi\pi$  channel, but then the latter should no longer be accounted for through Eq. (4.76) to avoid double counting. Without any further medium modifications both variants have been shown to be equivalent [231]. For  $\omega$  and  $\phi$  mesons relations analogous to Eq. (4.77) hold. Note, however, that apart from the absolute abundances of the vector mesons (which should be similar for  $\rho^0$  and  $\omega$  and somewhat suppressed for the  $\phi$  due to its higher mass) the key quantity which determines the dilepton yield in Eq. (4.77) are the *absolute* values of the dilepton decay widths. The (on-shell) numbers are

$$\begin{aligned} \Gamma(\rho^0 \rightarrow ee) &= 6.77 \pm 0.32 \text{ keV} \\ \Gamma(\omega \rightarrow ee) &= 0.60 \pm 0.02 \text{ keV} \\ \Gamma(\phi \rightarrow ee) &= 1.37 \pm 0.05 \text{ keV}, \end{aligned} \quad (4.78)$$

clearly indicating the prevailing character of the  $\rho$  meson for radiation originating from the interacting hadronic system. Three-body decays into dilepton channels are evaluated in a similar fashion, *e.g.*, for  $a_1(1260) \rightarrow \pi ee$ :

$$\frac{dN_{a_1 \rightarrow \pi ee}}{dM} = \int_0^{t_{fo}} dt N_{a_1}(t) \frac{d\Gamma_{a_1 \rightarrow \pi ee}}{dM} \quad (4.79)$$

with  $N_{a_1}(t)$  being the number of  $a_1$  mesons present at time  $t$ . The differential Dalitz-decay width is given via the radiative decay width  $\Gamma_{a_1 \rightarrow \pi\gamma} = 0.64 \text{ MeV}$  as [230]

$$\frac{d\Gamma_{a_1 \rightarrow \pi ee}}{dM} = \frac{2\alpha}{3\pi} \frac{\Gamma_{a_1 \rightarrow \pi\gamma}}{M} \frac{[(m_{a_1}^2 + M^2 - m_\pi^2)^2 - 4m_{a_1}^2 M^2]^{3/2}}{(M_{a_1}^2 - m_\pi^2)^3} \quad (4.80)$$

(this expression is reminiscent of Eq. (4.1) after stripping off the hadronic and VDM form factors from the latter).

Due to the above argument, also transport analyses have primarily investigated in-medium effects in dilepton production by focusing on modifications of the  $\rho$  meson (or  $\pi\pi$  annihilation). The most straightforward effect to incorporate is to simply change the in-medium  $\rho$  mass (as motivated by theoretical predictions such as BR scaling discussed in Sect. 3.2.1). It can be accommodated by appropriate mean-fields in the transport equations, together with replacing the free masses  $m_\rho$  by  $m_\rho^*$  in Eqs. (4.76) or (4.77), as has been done, *e.g.*, in Refs. [38, 37, 39, 232, 230, 233]. On the other

hand, medium modifications which go beyond the mean-field treatment of on-shell quasiparticles are not easily implemented. This is obvious for the case in which the in-medium widths of the propagated hadrons become so large that they lose their quasiparticle nature. Although there is no satisfactory solution to this problem yet (see Ref. [234, 235] for recent progress), some attempts have been made to account for the broadening effect of the  $\rho$  in a transport framework. In Ref. [36] the cross section approach based on Eq. (4.76) has been employed by simply multiplying  $\sigma_{\pi^+\pi^-\rightarrow e^+e^-}(M)$  with a temperature-dependent ‘in-medium correction factor’, which is determined as the ratio

$$R_{\text{med}}(M, T) \equiv \frac{[dR/dM^2 d^3q]_{q=0}^{\text{med}}}{[dR/dM^2 d^3q]_{q=0}^{\text{free}}} \quad (4.81)$$

of the (equilibrium) dilepton production rate for free  $\pi\pi$  annihilation over the in-medium one [113]. To assign a temperature for a given  $\pi\pi$  event necessary to evaluate  $R_{\text{med}}$ , the local (invariant) pion density in the transport has been used assuming local thermal equilibrium. A possible three-momentum dependence (at fixed invariant mass  $M$ ) as well as dispersion corrections to the explicit pion propagation in the transport have been neglected (the impact of a modified pion dispersion relation on the overall transport dynamics has been shown to be small in Ref. [236]). Along similar lines Refs. [48, 237] proceeded in taking the  $\pi\pi$  annihilation cross section as

$$\sigma_{\pi^+\pi^-\rightarrow e^+e^-}(M) = -\frac{16\pi^2\alpha^2}{g_{\rho\pi\pi}^2} \frac{1}{p_\pi^2 M^2} (m_\rho^{(0)})^4 \text{Im}D_\rho(q_0, \vec{q}) \quad (4.82)$$

with the full in-medium spectral function based on the many-body calculations of Refs. [47, 102, 126], including the non-trivial three-momentum dependence (for the vacuum spectral function Eq. (4.76) is recovered). Here the temperature has been deduced from the slope parameter associated with the pion-momentum distributions in the local rest frame (‘comoving’ frame). Both calculations are in principle plagued by a singularity towards the two-pion threshold  $M = 2m_\pi$ , caused by the inherent inconsistency of how the pions are treated in the transport and in the dilepton rate. However, in practice this failure does not seem to entail severe disturbances except for very close to threshold. In Refs. [48, 237] the additional decays of  $\rho$  mesons produced in meson-baryon and baryon-baryon interactions have been accounted for by using a medium modified mass distribution according to

$$\frac{dN_\rho}{dM} = -\frac{2M}{\pi} \text{Im}D_\rho(q_0, \vec{q}), \quad (4.83)$$

together with a constant branching ratio of  $\Gamma_{\rho\rightarrow ee}/\Gamma_\rho^{\text{tot}} = 4.5 \cdot 10^{-5}$  for the dilepton channel. This leads to a quite different spectral shape as compared to the  $\pi\pi$  component included via Eq. (4.76), and might not be realistic (see also the criticism in Ref. [235]). It has been improved in due course by introducing an additional phase space factor  $(M/m_\rho)^2$  into the electromagnetic branching ratio.

To avoid double counting when using medium-modified dilepton rates, it is important to omit explicit production channels that are included in the medium effects [48]; *e.g.*, if the  $\rho$  selfenergy in the in-medium propagator contains  $\pi\rho \rightarrow a_1$  contributions, the explicit  $a_1 \rightarrow \pi e^+e^-$  decays have to be switched off. This holds for any process that can be generated by cutting any selfenergy diagram of the many-body spectral function.

### 4.4.3 Thermal Fireball Expansion

A much simplified attempt to capture the basic features of a heavy-ion reaction relevant for dilepton production is represented by fireball models, some of which are reminiscent to the Bjorken hydrodynamical description. One class of approaches [47] is based on temperature evolutions parameterized in accordance with microscopic transport simulations [232], *e.g.*,

$$T(t) = (T^i - T^\infty) e^{-t/\tau} + T^\infty \quad (4.84)$$

with the initial temperature of the hadronic phase,  $T^i$ , a time constant  $\tau$  and an 'asymptotic' temperature  $T^\infty$ . The baryon density is determined by the number of participants supplemented with an (isotropic) volume expansion, which can be approximately described by an 'average' baryon chemical potential, *e.g.*,  $\mu_B \simeq 350 - 400$  MeV for lab-energies of 158–200 AGeV. The total dilepton yield from  $\pi\pi$  annihilation is then normalized to the transport results for the case when no-medium effects are included. The pertinent normalization factor turns out to be  $N_0 \simeq 2 - 3$  and can be understood as an overpopulation of the pion phase space due to a finite chemical potential. In fact, for typical SpS freezeout temperatures of  $T_{fo} \simeq 120$  MeV, the simplistic fireball model results in a total pion number which falls short by about 50% as compared to the experimentally observed pion-to-baryon ratio of 5:1 if no pion chemical potential is involved. This can be corrected for by introducing a finite value of  $\mu_\pi \simeq 50$  MeV, amounting to a pion fugacity (in Boltzmann approximation) of  $z_\pi = e^{\mu_\pi/T_{fo}} \simeq 1.5$ . On the level of dilepton production from  $\pi\pi$  annihilation [238, 239] this results in an enhancement factor of  $N_0 \simeq z_\rho = z_\pi^2 \simeq 2.3$ .

A more microscopic understanding of the emergence of finite (meson) chemical potentials can be gained by noticing that the strong interactions of, *e.g.*, pions –  $\pi\pi$  scattering or  $\pi N$  interactions dominated by baryonic resonances – are essentially elastic, *i.e.*, pion-number conserving. Maintaining the assumption of local thermal equilibrium pion-number and entropy conservation then enforces the build-up of a pion chemical potential in the expansion and cooling process within the hadronic phase of a heavy-ion collision, as has been first pointed out in Ref. [197]. Such a scenario fits in fact nicely into the picture of recent hadro-chemical analysis [5, 240, 3], where a large body of data for finally observed particle abundances at SpS energies (158 AGeV) could be accommodated by a universal temperature and baryon chemical potential of  $(T, \mu_N)_{ch} \simeq (175, 270)$  MeV, characterizing the *chemical* freezeout of the system (the same method successfully describes the AGS data as well, cf. Fig. 1.1). From here on the particle composition in terms of (*w.r.t.* to strong interactions) stable particles does no longer change, although the hadronic system still interacts via elastic collisions sustaining thermal equilibrium until the *thermal* freezeout is reached. The evolution proceeds along a trajectory in the  $T - \mu_N$  plane which can be determined by imposing entropy and baryon-number conservation within, *e.g.*, a hadronic resonance gas equation of state. The induced pion ( $\mu_\pi(T)$ ) and kaon ( $\mu_K(T) \simeq \mu_{\bar{K}}(T)$ ) chemical potentials along this trajectory increase approximately linearly, reaching typical values of  $\mu_\pi^{fo} \simeq 60 - 80$  MeV and  $\mu_{K, \bar{K}}^{fo} \simeq 100 - 130$  MeV at thermal freezeout, being located around  $(T, \mu_N)_{fo} \simeq (115 \pm 10, 430 \pm 30)$  MeV. Other chemical potentials associated with strong interactions are kept in relative chemical equilibrium, *e.g.*,  $\mu_\Delta = \mu_N + \mu_\pi$  or  $\mu_\rho = 2\mu_\pi$  according to elastic reactions  $\pi N \rightarrow \Delta \rightarrow \pi N$  or  $\pi\pi \rightarrow \rho \rightarrow \pi\pi$ .

Finally one needs to introduce a time scale to obtain the volume expansion. For SpS energies

the latter is realistically approximated by a cylindrical geometry as

$$V_{FC}^{(2)}(t) = 2 \left( z_0 + v_z t + \frac{1}{2} a_z t^2 \right) \pi \left( r_0 + \frac{1}{2} a_\perp t^2 \right)^2, \quad (4.85)$$

where two firecylinders expanding in the  $\pm z$  direction have been employed to allow for a sufficient spread in the particle rapidity distributions. Guided by hydrodynamical simulations [43] the primordial longitudinal motion for Pb(158 AGeV)+Au reactions is taken to be  $v_z = 0.5c$ , and the longitudinal and transverse acceleration are fixed to give final velocities  $v_z(t_{fo}) \simeq 0.75c$ ,  $v_\perp(t_{fo}) \simeq 0.55c$  as borne out from experiment [241] (this, in turn, requires fireball lifetimes of about  $t_{fo} = 10-12$  fm/c and implies transverse expansion by 3-4 fm, consistent with HBT analyses [242]). The parameter  $r_0$  denotes the initial nuclear overlap radius, *e.g.*,  $r_0 = 4.6$  fm for collisions with impact parameter  $b = 5$  fm and  $N_B \simeq 260$  participant baryons. The parameter  $z_0$  is equivalent to a formation time and fixes the starting point of the trajectory in the  $(T, \mu_N)$  plane. Estimates for the initial baryon densities can be taken, *e.g.*, from RQMD calculations which for CERN-SpS energies typically lie around  $\varrho_B^i \simeq 2 - 4\varrho_0$  [243], corresponding to, *e.g.*,  $(T, \varrho_B)_{ini} = (190 \text{ MeV}, 2.55\varrho_0)$  on the above specified trajectory.

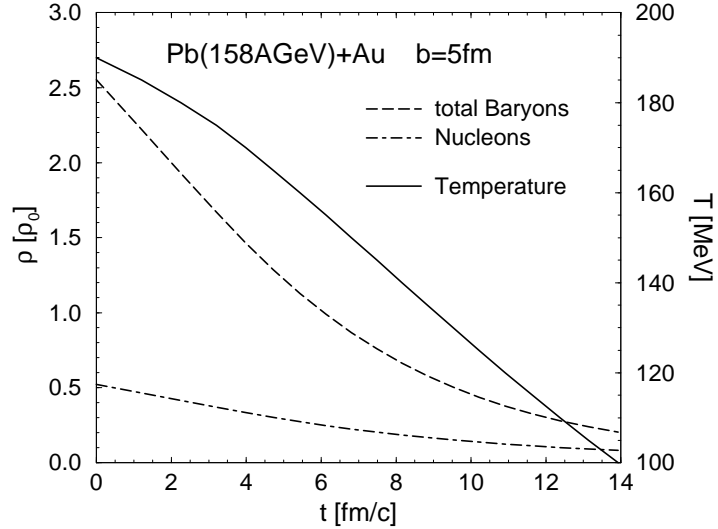


Figure 4.8: Time evolution of temperature (full line, right scale), total baryon density (long-dashed line, left scale) and nucleon density (dashed-dotted line, left scale) as typical for central Pb(158A GeV)+Au collisions at impact parameter  $b=5$  fm with fixed entropy per baryon and assuming effective pion- and kaon-number conservation.

Dilepton spectra from in-medium  $\pi\pi$  annihilation (or, equivalently,  $\rho$  decays) are now straight-

forwardly calculated by integrating the thermal rate, Eq. (4.34). Using  $q_0 dq_0 = M dM$ , one has

$$\begin{aligned}
\frac{dN_{\pi\pi\rightarrow ee}}{dM d\eta} &= \int_0^{t_{fo}} dt V_{FC}(t) \int d^3q \frac{M}{q_0} \frac{dR_{\pi\pi\rightarrow ee}}{d^4q}(q_0, \vec{q}; \mu_B, \mu_\pi, T) \text{Acc}(M, \vec{q}) \\
&= \frac{\alpha^2}{\pi^3 g_{\pi\pi\rho}^2 M} \int_0^{t_{fo}} dt V_{FC}(t) \int \frac{d^3q}{q_0} f^\rho(q_0; \mu_\rho, T) \mathcal{F}(M, \vec{q}; \mu_B, \mu_\pi, T) \text{Acc}(M, \vec{q}) ,
\end{aligned}
\tag{4.86}$$

where the function  $\text{Acc}(M, \vec{q})$  accounts for the experimental acceptance cuts specific to the detector characteristics (*e.g.*, in the CERES experiment each electron/positron track is required to have transverse momentum  $p_T > 0.2$  GeV, to fall in the (pseudo-) rapidity interval  $2.1 < \eta < 2.65$ , and to have a pair opening angle  $\Theta_{ee} > 35$  mrad). The meson chemical potentials have throughout been introduced in Boltzmann approximation, *i.e.*,  $f^\pi(\omega; \mu_\pi, T) \equiv f^\pi(\omega; T) e^{\mu_\pi/T}$ , etc..

The fireball models certainly oversimplify the dynamics present in more realistic descriptions of relativistic heavy-ion collisions. However, their relative simplicity enables more transparent comparisons between various underlying models for the microscopic rates [142, 47, 100, 205, 244, 50] at the level of experimentally observed data, potentially discriminating different temperature and density dependencies of bare rates once integrated over a common 'cooling-curve'.

## 4.5 Dilepton Spectra at BEVALAC/SIS Energies

The first measurements of dilepton invariant mass spectra in proton and heavy-ion induced reactions at bombarding energies in the 1-5 AGeV range have been performed by the DLS collaboration for p+Be collisions at 1, 2.1 and 4.9 AGeV, for Ca+Ca at 1 and 2 AGeV and for Nb+Nb at 1.05 AGeV [33]. Although the *cms* energy available in a primary nucleon-nucleon collision at 1 GeV laboratory energy only suffices to produce dilepton pairs of invariant masses up to  $M \simeq 0.45$  GeV, significant yields have been observed beyond this naive kinematical limit in the collisions involving heavy ions. Therefore, these first generation DLS data have been interpreted as the first evidence for the  $\pi\pi \rightarrow e^+e^-$  annihilation channel, predominantly populating the invariant mass region  $M_{ee} \geq 0.4$  GeV (up to about 1 GeV). Theoretical calculations based on BUU transport models [245, 246] have confirmed this conjecture. Also, for lower invariant masses,  $M \leq 0.4$  GeV, the major contributions to the dilepton spectra were identified as Dalitz decays of  $\Delta$ 's and  $\eta$ 's as well as proton-neutron Bremsstrahlung processes, resulting in a fair agreement with the first generation DLS data [245, 246]. The limited statistics of the latter did not allow for any further conclusions.

From more recent publications of the DLS collaboration [34] it turns out that new measurements of dilepton yields in  $p+p$ ,  $p+d$  as well as in 1 AGeV  $d+C$ ,  $\text{He}+C$ ,  $C+C$  and  $\text{Ca}+C$  collisions have been substantially revised in comparison to the previous data set [33] due to improvements of the DLS detector and of the data analysis, correcting for dead-time losses. The  $p+p$  data for 1–5 GeV incident energies are reasonably well described by standard Dalitz and vector meson decay sources (for recent transport calculations see Ref. [247] using the UrQMD and Ref. [248] using the HSD approach; both analyses essentially agree up to slight uncertainties in some meson

production channels; also the role of  $N(1520) \rightarrow Ne^+e^-$  decays, not included in Ref. [247], was found to be significant in Ref. [248] especially for the higher energies). This gives confidence in the elementary production channels when carrying the calculations to the more complicated systems. Nevertheless, significant discrepancies start to build up already for light projectiles such as in d+Ca and He+Ca systems [247]. In the 1 AGeV C+C and Ca+Ca reactions the experimental reanalysis [34] resulted in corrections of up to factors of 6–7 as compared to the first generation data. Consequently, the afore mentioned theoretical approaches now appreciably underestimate the dilepton yield in the invariant mass region  $0.15 \text{ GeV} \leq M_{ee} \leq 0.65 \text{ GeV}$ . This is apparent, *e.g.*, from the left panels of Fig. 4.9, where a rather complete calculation of the various dilepton sources including (free)  $\pi\pi$  annihilation employing the HSD model is displayed [237]. In particular, this calculation reproduces well the total yields and transverse momentum spectra of  $\pi$ 's and  $\eta$ 's as measured for the same collision systems and energies by the TAPS collaboration [249]. This imposes stringent constraints on the dilepton yields from  $\pi^0$  and  $\eta$  Dalitz decays. Note that the former result in a satisfactory description of the mass region  $M_{ee} \leq 0.15 \text{ GeV}$ . On the other hand, it was noted in Ref. [34] that, assuming an isotropic dilepton emission from a thermal source, the new DLS data could be accounted for by (arbitrarily) increasing the  $\eta$  contribution by a large factor close to 10. This observation could be reconciled with the TAPS data imposing a dramatic anisotropy in the  $\eta$  production, since the TAPS data are taken mainly at mid-rapidity, whereas the DLS data are at forward rapidities. Although the HSD calculations show some enhancement of the  $\eta$  distributions [237] at forward angles, this would at maximum allow for a 20% enhancement of the total  $\eta$  yields [249] which is nowhere close to providing an excess of the  $\eta$  signal as required to reproduce the DLS data.

The question thus arises whether in-medium effects can resolve the discrepancy. As an example of the conditions probed at BEVALAC energies, Fig. 4.10 shows a typical time dependence of the baryon density for inclusive Ca+Ca collisions at 1 AGeV bombarding energy as extracted from the transport model of Ref. [250]. The evolution roughly proceeds in 3 stages: in the first 5 fm/c the nuclei penetrate each other to form a high-density phase at about  $2\rho_0$  which then quite rapidly dilutes towards freezeout. The accompanying temperatures at the highest densities are around  $T \simeq 80 - 100 \text{ MeV}$  and therefore one should expect the system to stay in the hadronic phase throughout. Since the pion densities are rather small ( $n_\pi = 0.03 \text{ fm}^{-3}$  at  $T=100 \text{ MeV}$ ), the dominant medium effects should be driven by nucleons and baryonic resonances in the system (note that at  $T=100 \text{ MeV}$  already  $\sim 25\%$  of the baryons are thermally excited into  $\Delta$ 's).

In Ref. [237], the impact of many-body effects [47, 102] on the  $\rho$ -meson spectral function, generated through  $\pi N$  and  $\rho N$  interactions (also including finite-temperature effects, which are, however, much smaller), has been investigated. The results are shown in the two right panels of Fig. 4.9. Apparently, the full results still underestimate the second generation DLS data by a factor of 2–3. Very similar results are obtained [237] when employing the finite-density/zero-temperature  $\rho$ -meson spectral function of Ref. [101], which is based on a selfconsistent calculation of resonant  $\rho N$  interactions. Since present transport approaches cannot fully account for the off-shell dynamics of the pions (especially close to and below the two-pion threshold), additional calculations using the thermal fireball along the lines of Sect. 4.4.3 have been performed. Integrating the thermal dilepton emission rates over the density and temperature profile of Fig. 4.10 leads to very similar results as obtained in the HSD calculation.

Alternative theoretical attempts were made by including dropping vector meson masses in trans-

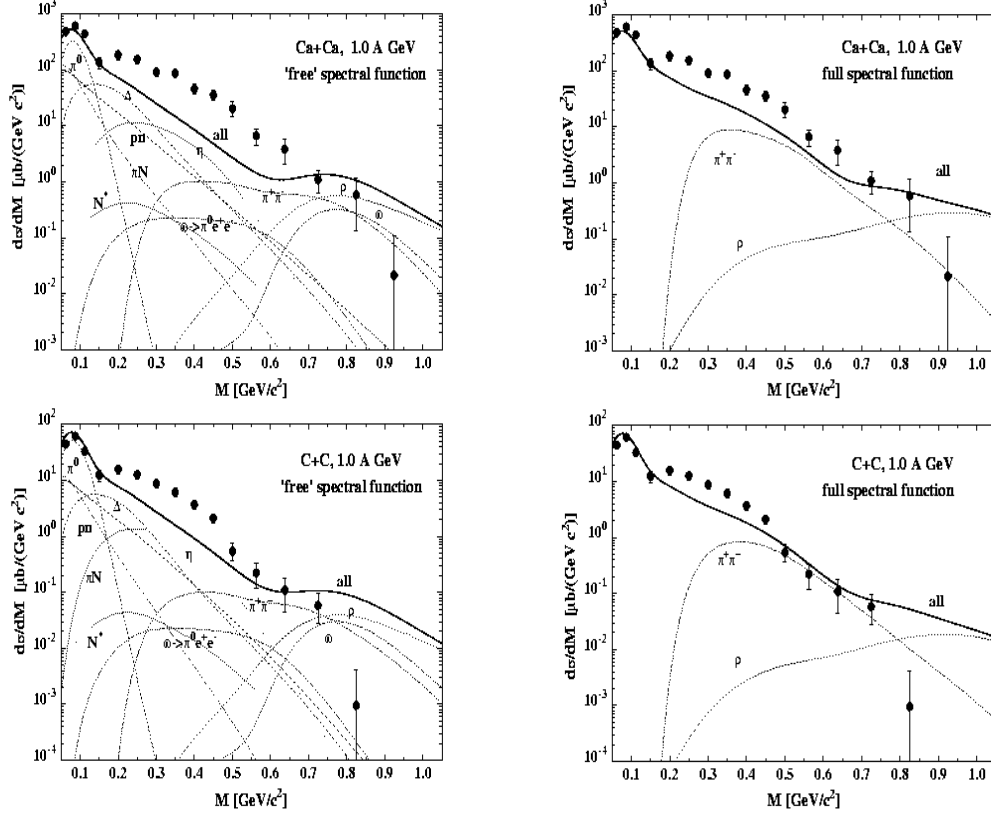


Figure 4.9: Dilepton spectra as measured in Ca+Ca (upper panels) and C+C (lower panels) reactions at 1.0 A GeV projectile energies. The experimental data from the DLS collaboration [34] are compared to HSD transport calculations, using either a 'free'  $\rho$  spectral function (left panels) or the in-medium one from Refs. [47, 102] (right panels) for both  $\pi\pi$  annihilation and direct decays of  $\rho$  mesons produced in baryonic collisions. The DLS acceptance filter (version 4.1) as well as a mass resolution of  $\Delta M/M = 10\%$  are included. The thick solid lines represent the total results. The thin lines in the left panels indicate the individual contributions from the different production channels, *i.e.*, starting from low  $M$ : Dalitz decays  $\pi^0 \rightarrow \gamma e^+e^-$  (dashed line),  $\eta \rightarrow \gamma e^+e^-$  (dotted line),  $\Delta \rightarrow N e^+e^-$  (dashed line),  $\omega \rightarrow \pi^0 e^+e^-$  (dot-dashed line),  $N^* \rightarrow N e^+e^-$  (dotted line), proton-neutron bremsstrahlung (dot-dashed line),  $\pi N$  bremsstrahlung (dot-dot-dashed line); for  $M \approx 0.8$  GeV:  $\omega \rightarrow e^+e^-$  (dot-dashed line),  $\rho^0 \rightarrow e^+e^-$  (dashed line),  $\pi^+\pi^- \rightarrow \rho \rightarrow e^+e^-$  (dot-dashed line). The plots are taken from Ref. [237].



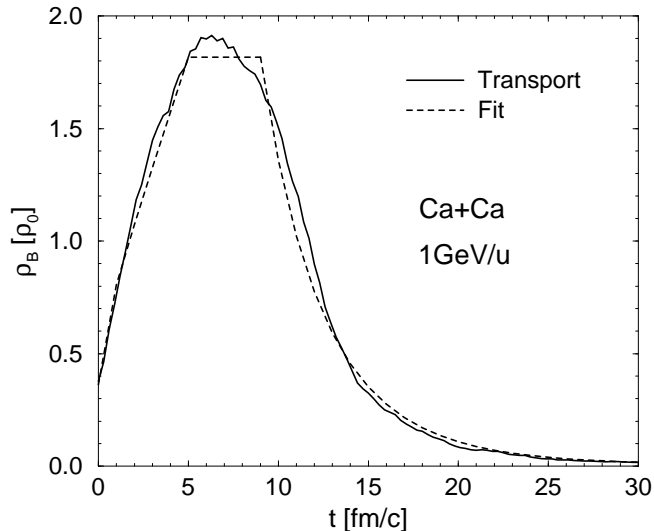


Figure 4.10: Evolution of average baryon density as a function of time in inclusive 1 AGeV Ca+Ca collisions as extracted from the transport model of Ref. [250] (solid curve); the dashed curve is a simple parameterization thereof with a maximal temperature of  $T_{max} = 100$  MeV in the high density phase and a time-independent baryon chemical potential of  $\mu_B = 0.76$  GeV.

port calculations. Ref. [233] focused on the role of the  $N(1520)$ -resonance, which exhibits a strong coupling to the  $\rho N/\gamma N$  channel, see Sects. 3.2.3 and 4.1.2. Rather than including it via the in-medium  $\rho$ -meson spectral function as was done in Ref. [237], the Dalitz decays  $N(1520) \rightarrow Ne^+e^-$  were evaluated explicitly, confirming its relative importance for the low-mass dilepton spectra. However, once an additional reduction of the  $\rho$  mass is introduced (using, *e.g.*, the QCD sum rule results,  $m_V^* = m_V(1 - C\varrho/\varrho_0)$  with  $C \simeq 0.18$ ), the hadronic decay width of the  $N(1520)$  strongly increases due to the opening of phase space in the  $\rho N$  decay, which results in a net reduction of the dilepton yield from  $N(1520)$  decays (note that the in-medium broadening is included in the many-body calculations of Refs. [102, 101]). Although the direct  $\rho$  decay contributions are enhanced by a factor of about 3 with a dropping  $\rho$  mass, the total spectra still underestimate the DLS data by a factor of 3–4 for invariant masses  $0.15 \text{ GeV} \leq M \leq 0.5 \text{ GeV}$ . Similar conclusions have been reached in Ref. [247] where the use of dropping vector meson masses has been found to give a small net increase of the spectra around  $M \simeq 0.4 \text{ GeV}$ , together with the reduction around the free  $\rho/\omega$  peak.

Concluding this Section we emphasize that there is currently no theoretical explanation of the second generation DLS data for dilepton production in 1–2 AGeV heavy-ion collisions, with the various model predictions falling short by large factors of 2–3 above the  $\pi^0$  Dalitz region and below  $M \simeq 0.5 \text{ GeV}$ . The upcoming high-precision dilepton measurements with the HADES detector at

GSI will be crucial to shed new light on this situation.

## 4.6 Dilepton Spectra at CERN-SpS Energies

The dilepton program at the CERN-SpS started in 1990–1992 with the  $^{32}\text{S}$  beam at 200 AGeV, followed by a 450 GeV proton run in 1993 and  $^{208}\text{Pb}$  nuclei accelerated to 158 AGeV in 1995, 1996 and 1998. Data have been taken by three collaborations: CERES/NA45 for  $e^+e^-$  pairs using  $^{197}\text{Au}$  targets (as well as  $^9\text{Be}$  in the proton run) [20, 23, 251], HELIOS-3 [24] for  $\mu^+\mu^-$  pairs using  $^{184}\text{W}$  targets, and NA38/NA50 [25, 26, 27] also for  $\mu^+\mu^-$  pairs using  $^{32}\text{S}$ , Cu and  $^{238}\text{U}$  as well as  $^{208}\text{Pb}$  targets for the lead runs. The major challenge in these experiments is the large background due to both charged hadrons and, more severely, combinatorial misidentification of pairs in the same event, *i.e.*, the pairing of  $l^+$  and  $l^-$  tracks which did not arise from the decay of the *same* virtual photon (or other *correlated* physical processes, as, *e.g.*, the so-called ‘open charm’ contributions, where a pairwise production of  $D\bar{D}$  mesons is followed by subsequent weak decays  $D \rightarrow l^+X$  and  $\bar{D} \rightarrow l^-X$ ). In the CERES experiment, *e.g.*, charged hadrons are suppressed with Cerenkov detectors, whereas the combinatorial background to the ‘physical’  $e^+e^-$  signal is typically determined through pairing of like-sign pairs, *i.e.*,  $e^+e^+$  and  $e^-e^-$ .

As a result of the different ways in handling these problems, the kinematical regions covered by the three experiments are quite distinct, see Fig. 4.11. Before one can identify non-trivial signals from the highly complicated measurements in nucleus-nucleus collisions, one has to have good control over the more simple systems first. The proton-induced reactions, supposedly governed by the mere free decays of the produced hadrons involving no significant rescattering, thus serve as an important aid in understanding the detector systematics. The free hadronic decay contributions have become known as the hadronic cocktail and will be discussed in the next Section. Since at full CERN-SpS energies the pion-to-baryon ratio observed in the final state of heavy-ion induced reactions is about 5:1 (with little dependence on the impact parameter  $b$ ), the dominant in-medium source is expected to stem from  $\pi\pi$  annihilation. The assessment of this contribution without any medium-modifications will be addressed in sect. 4.6.2. In Sects. 4.6.3 and 4.6.4 we proceed to the analysis of the experimental data in the available kinematic projections, *i.e.*, invariant mass and transverse pair-momentum, with emphasis on in-medium effects that have been proposed. In Sect. 4.6.5 we discuss how the various parts of the in-medium signals relate to the time of emission within different theoretical models. In particular, the issue of quark-gluon/hadron duality, raised in Sect. 4.2.3, will be reiterated for both the low- and intermediate-mass region.

### 4.6.1 Decays after Freezeout: Hadronic Cocktail versus Experiment

From the experimental side, a systematic study of the cocktail contributions has been performed by the CERES/NA45 collaboration. It has been shown [20] that the  $e^+e^-$  invariant mass spectra in  $p+\text{Be}$  and  $p+\text{Au}$ , normalized to the number of charged particles observed in the same rapidity window, can be well reproduced in terms of known hadron decays using particle production multiplicities from  $p+p$  data, cf. Fig. 1.3 in the Introduction. The low-mass end of the spectrum,  $M_{ee} \leq 0.15$  GeV, is completely saturated by  $\pi^0$  Dalitz decays, whereas for  $0.15 \text{ GeV} \leq M_{ee} \leq 0.6$  GeV  $\eta$  and  $\omega$  Dalitz decays are prevailing. Beyond  $M_{ee} = 0.6$  GeV up to about 1.5 GeV the direct decays

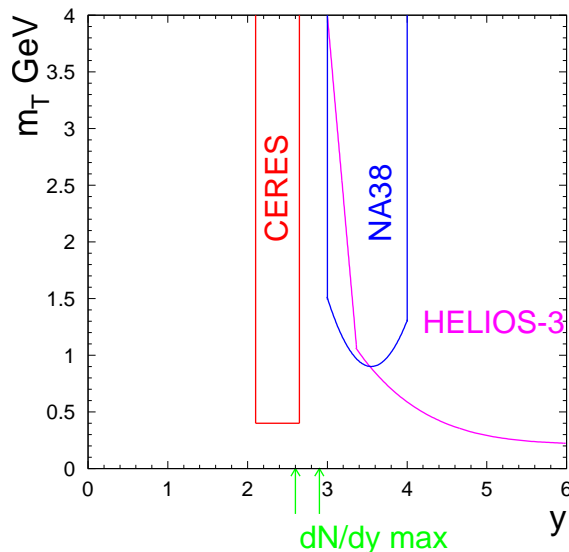


Figure 4.11: Kinematical regions covered by the three collaborations that have measured dilepton spectra at full CERN-SpS energies of 158–200 AGeV. The plot is taken from Ref. [22].

of the light vector mesons,  $\rho, \omega, \phi \rightarrow e^+e^-$ , are the dominant sources, substantially smeared due to the finite mass resolution of about 10% in the CERES detector (which, in fact, stems from the finite momentum resolution of the individual lepton tracks). Here one should note that, for an equal number of produced  $\rho^0$ 's and  $\omega$ 's, the dilepton yield from the latter is by almost a factor of 2 larger than the former, since in free space the probability  $P_{V \rightarrow ee}$  for decaying into the dilepton channel is determined by the relative branching ratio of electromagnetic over total decay width, *i.e.*,

$$P_{V \rightarrow ee} = \frac{\Gamma_{V \rightarrow ee}}{\Gamma_V^{tot}} = \begin{cases} 0.0045\% , & V = \rho \\ 0.0071\% , & V = \omega \\ 0.0311\% , & V = \phi \end{cases} . \quad (4.87)$$

This is a quite different characteristics as compared to the signal from an interacting (thermalized) system, cf. Eq. (4.77) and the subsequent remarks. The CERES assessment of the cocktail in proton-induced reactions has been confirmed by microscopic transport calculations [38, 232]. The latter give equivalent results for the dimuon data of HELIOS-3 [24] taken in  $p+W$  reactions. Thus the measured dilepton spectra in proton-induced reactions at CERN-SpS energies can be well understood by the final-state hadron decays in a consistent way.

The situation changes drastically when moving to heavy-ion projectiles. In the first measurements at the CERN-SpS, which were performed with a 200 AGeV  $^{32}\text{S}$  beam, the CERES collab-

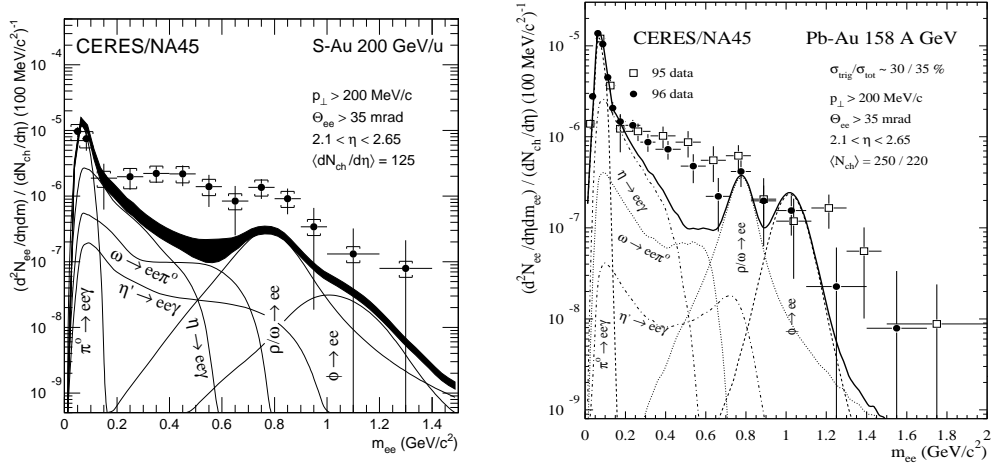


Figure 4.12: Dilepton spectra from heavy-ion collisions as measured by the CERES/NA45 collaboration. Left panel: central 200 AGeV S+Au collisions, contrasted with the hadronic cocktail contributions as extrapolated from hadron multiplicities in  $p+p$  data. The plot is taken from Ref. [20]. Right panel: 35% central 158 AGeV Pb+Au collisions (open squares: '95 data, full circles: '96 data), compared to a hadronic cocktail inferred from a thermal model with  $T = 175 \text{ MeV}$  and  $\mu_B = 270 \text{ MeV}$  [3], which reproduces the measured hadronic multiplicities in Pb+Pb collisions at identical projectile energy.

oration found a total enhancement factor of measured pairs over the expectation based on the cocktail of  $5.0 \pm 0.7(\text{stat}) \pm 2.0(\text{syst})$  (integrated over the invariant mass range 0.2–1.5 GeV) [20] in central collisions with  $^{197}\text{Au}$  targets. The enhancement is in fact most pronounced around  $M_{ee} \simeq 0.45 \text{ GeV}$ , reaching a factor of 10 (Fig. 4.12). Whereas the CERES data are taken close to midrapidity ( $2.1 \leq \eta \leq 2.65$ ), the HELIOS-3 experiment [24] covered more forward rapidities  $3.7 \leq \eta \leq 5.2$ . Here the enhancement, when comparing to transport calculations [39, 232], is less developed but still significant (although the HELIOS-3 collaboration did not quote any systematic errors).

The '95 and '96 runs with 158 AGeV  $^{208}\text{Pb}$  projectiles in essence confirmed the sulfur results, cf. right panel of Fig. 4.12. Here, the final state hadron decay contributions have been evaluated in an alternative way as recently developed by the CERES collaboration. It is based on hadron abundances from the thermal model of Ref. [3], where the (chemical) freezeout conditions for temperature and baryon chemical potential have been deduced from an optimal fit to a large body of hadronic observables at SpS and AGS energies (the such obtained cocktail agrees with sources scaled from  $p+p$  collisions within 20–30%, with the only exception of the  $\phi$  meson – related to

strangeness enhancement –, which we will not address here). The resulting enhancement of the '96 data over the 'thermal-model' cocktail in the 30% most central Pb+Au collisions then amounts to  $2.6 \pm 0.5(\text{stat.}) \pm 0.9(\text{syst.})$  [251] in the invariant mass range 0.25–0.7 GeV. In terms of the experimental analysis, the '96 data set is the best understood with the highest statistics (a factor of 5 larger than in '95). It is consistent with both the '95 sample and the '93 sulfur results within two standard deviations (note that the S+Au data are based on a higher centrality selection). Nevertheless, the net signal in the '96 data seems to lie systematically below the '95 data, this trend being more accentuated towards higher masses. In particular, at the free vector meson masses the '96 data are basically accounted for by the hadronic cocktail. If this feature will be confirmed in future measurements, it has severe consequences for the theoretical interpretation of the spectra. A rather precise determination of the  $\omega$  contribution, which is the dominant cocktail component at the  $\rho/\omega$  mass, will be most important to draw firm conclusions. Unfortunately, the  $\omega$  yield in heavy-ion reactions is not very well determined so far. In hydrodynamical calculations as, *e.g.*, presented in Ref. [252], the  $\omega$ -meson yield might be substantially smaller than in the CERES cocktail if its final abundance is determined by a simultaneous thermal *and* chemical freezeout temperature as low as  $T_{fo} = 120$  MeV. The most promising way to resolve this issue will be provided by an improved mass resolution in the dilepton measurements. If the latter can be reduced to about 2%, the  $\omega$  peak will clearly stick out, thus putting valuable constraints on other (in-medium) sources in its vicinity. An upgrade of the CERES experiment using an additional time projection chamber (TPC) is expected to achieve the required resolution. An accordingly small mass binning will critically depend on a sufficiently large data statistics.

Once the direct  $\omega \rightarrow e^+e^-$  decays are known, also the Dalitz-decay contributions  $\omega \rightarrow \pi^0 e^+e^-$  are fixed. The latter constitute an important part of the cocktail in the mass region where the experimental excess of dilepton pairs is the largest, *i.e.*,  $0.3 \text{ GeV} \leq M_{ee} \leq 0.6 \text{ GeV}$ . The other important hadronic decay in this region is  $\eta \rightarrow \gamma e^+e^-$  and, to a lesser extent,  $\eta' \rightarrow \gamma e^+e^-$ . Therefore, an enhanced production of  $\eta, \eta'$  mesons in heavy-ion as compared to proton-induced reactions could significantly alter the cocktail composition. Mechanisms for such a behavior have indeed been proposed in connection with the (partial) restoration of the  $U_A(1)$  symmetry (see also Sect. 2.1) in high density/temperature matter, reducing the  $\eta$  and  $\eta'$  masses and thus increasing their (final) abundances [253]. However, an enhanced  $\eta, \eta'$  production also entails an increase of the direct photon yield from the two-photon decay modes  $\eta, \eta' \rightarrow \gamma\gamma$ . In Ref. [254] upper limits on inclusive photon measurements in heavy-ion collisions at the SpS have been converted to a maximally allowed  $\eta$  production. Assuming that the upper limit of the photon signal is entirely saturated by extra  $\eta$  decays, it has been shown that the  $\eta$  yield in  $^{32}\text{S}$  induced reactions cannot be enhanced by more than a factor of 1.5 as compared to the  $p+p$  case. Similar arguments have been drawn to limit the  $\eta'$  enhancement to a factor of 2.5. As a result, using the upper bounds on  $\eta$  and  $\eta'$  numbers, the CERES cocktail in 200 AGeV S+Au collisions (displayed in the left panel of Fig. 4.12) is increased by at most 40% which is far from accounting for the observed excess in the 0.3–0.6 GeV region (this situation is reminiscent to BEVALAC/SIS energies, where an increased  $\eta$  yield as the source for the dilepton enhancement found by DLS in  $A$ - $A$  collisions has also been ruled out by means of the TAPS two-photon data, see Sect. 4.5). The failure of the hadronic cocktail to describe the low-mass dilepton spectra in nucleus-nucleus collisions at the SpS thus inevitably points towards radiation originating from processes occurring during the interaction phase of the collisions, which will be discussed in the following sections.

## 4.6.2 Free $\pi^+\pi^-$ Annihilation in the Hadronic Fireball

One of the strongest evidences for a 'non-trivial' source of dilepton pairs in heavy-ion reactions is illustrated in Fig. 4.13. The total  $e^+e^-$  pair yield, normalized to the number of charged particles in the final state, exhibits a clear increase with multiplicity, indicating two- (or more) body annihilations. Since the most abundant particles at SpS energies are pions, the obvious candidate for

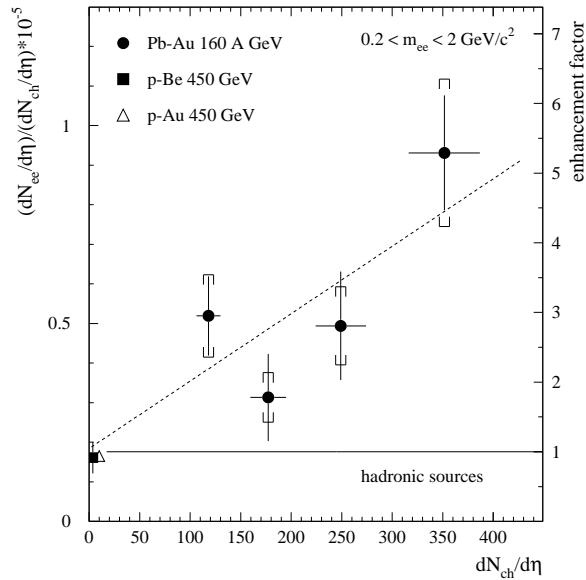


Figure 4.13: Total dilepton pair yield, normalized to the number of observed charged particles in the corresponding rapidity interval, and resulting enhancement factor over the hadronic cocktail (right vertical scale) as a function of charged particle multiplicity as found in different collision systems; the horizontal solid line indicates the expectation from final-state hadron decays whereas the dashed line is a linear interpolation of the data which implies a quadratic dependence on the number of charged particles as expected from an additional two-body annihilation source. The plot is taken from Ref. [23].

this behavior is the  $\pi^+\pi^- \rightarrow \rho^0 \rightarrow e^+e^-$  process. Many authors have calculated its contribution in various approaches to model the heavy-ion reaction dynamics, leading to rather good agreement with each other as we have already eluded to in the Introduction, see Fig. 1.4 for the case of  $^{32}\text{S}$ -induced reactions. All calculations share the common feature that, although the total yield is appreciably increased, the shape of the spectra strongly deviates from the data in that one finds too much yield around the free  $\rho$  mass and too little below, which is a trivial consequence of the free pion electromagnetic form factor peaking at the  $\rho$  resonance.

At this point it is useful to notice an important difference between transport and hydrodynamical approaches. In the latter the total yield is typically by a factor of at least 2 smaller than in the former ones if no chemical potentials for pions are involved as is the case, *e.g.*, for the (dotted) Hung-Shuryak curve [43] in the left panel of Fig. 1.4 (see also Ref. [214]). Although in both schemes the final hadronic spectra are usually equally well accounted for, hydrodynamic calculations involve smaller (average) pion densities  $n_\pi$  (due to the restriction to  $\mu_\pi = 0$ ) and hence larger fireball volumes  $V_{FB}$  to obtain an identical final number of pions. This means that, for a given total number of pions,  $N_\pi = n_\pi \times V$ , larger average densities in the transport simulations lead to a larger dilepton signal from  $\pi\pi$  annihilation, since the latter is basically proportional to the pion density *squared*,  $N_{\pi\pi \rightarrow ee} \propto n_\pi^2 \times V$ . On the other hand, in the Bjorken-type hydrodynamical calculations of Baier *et al.* [41] where a pion chemical potential of  $\mu_\pi = 100$  MeV has been employed, the dilepton yield is even slightly larger than in most of the transport results, cf. solid line in the left panel of Fig. 1.4. This is understandable, as the 'average' squared pion density in this calculation is increased over the  $\mu_\pi = 0$  case by roughly the squared fugacity  $(\exp[\mu_\pi/T])^2 \simeq \exp[2 \times 100/150] \simeq 4$ . Another quantity which governs the amount of dileptons radiated from the hadronic fireball is its total lifetime. For Pb+Au collisions at the full SpS energy (158 AGeV) the latter is around 10-15 fm/c. However, as pointed out by Shuryak and Hung [213], the upcoming low-energy run at 40 AGeV may lead to initial conditions that are close to the so-called 'softest' point in the EoS of the quark-hadron transition, associated with a very small initial pressure. In this case, the system expands very slowly entailing a much increased fireball lifetime which would have to leave its trace in the total dilepton yield.

The incompatibility of free  $\pi\pi$  annihilation persists in the Pb+Au data. Although the excess signal in the more recent CERES measurements is somewhat reduced as compared to the early sulfur runs the inclusion of free  $\pi\pi$  annihilation in theoretical models can still not resolve the discrepancy with the data. This statement is corroborated by the trend that in the Pb+Au system the cocktail is close to saturating the data in the  $\rho/\omega$  region, where the free  $\pi^+\pi^- \rightarrow \rho^0 \rightarrow e^+e^-$  process has its maximal contribution! Thus one is seemingly led to the following two alternatives:

- (i)  $\pi\pi$  annihilation is not an important ingredient in the dilepton spectra, but rather some very different processes with flat characteristics as a function of invariant mass, *e.g.*,  $q\bar{q}$  annihilation. However, this is not easy to imagine for the SpS conditions, where one expects the excited nuclear system to spend the major part of its space-time history in a hadronic phase with a large pion component;
- (ii)  $\pi\pi$  annihilation *is* the dominant process. In this case drastic medium modifications are inevitable to fill in the 0.3–0.6 GeV mass region without giving too much yield around the free  $\rho$ -meson mass.

Both possibilities will be considered in the forthcoming Sections.

### 4.6.3 Medium Effects I: Invariant Mass Spectra

Most of the in-medium effects proposed so far have drawn their attention to the pion-pion annihilation channel. They can be roughly divided into the following two categories:

- (I) a temperature- and density-dependent reduction ('dropping') of the  $\rho$  meson mass,  $m_\rho^*$ , according to BR scaling or the Hatsuda-Lee QCD sum rule calculations, usually applied without

invoking any changes in the pion propagation. This then entails a reduction of the  $\rho$ -meson width due to the shrinking pion phase space at smaller  $m_\rho^*$  as well as a sharp threshold – at twice the free pion mass  $2m_\pi$  – for the onset of the enhancement in the invariant mass dilepton spectra;

- (II) a modification of both  $\pi$  and  $\rho$  properties due to phenomenologically inferred interactions with the surrounding hadrons in the hot and dense gas which, depending on the language used, are encoded in the  $\rho$ -meson spectral function (*e.g.*, Refs. [47, 147, 101]), in vector current correlation functions (*e.g.*, in Refs. [100, 91]), in the pion electromagnetic form factor (Ref. [113]), etc.. Also the rate calculations for individual processes as, *e.g.*, performed in Refs. [119, 221], should be assigned to this category, as was discussed in Sect. 4.2.1.

## 200 AGeV Sulfur Beam Runs

For dilepton spectra in the 200 AGeV  $^{32}\text{S}$ -induced reactions the consequences of a dropping  $\rho$ -meson mass have been explored in Refs. [38, 37, 39, 232]. All these analyses find good agreement with the experimental data (Fig. 4.14). The mechanism is clear: in the early phase, characterized

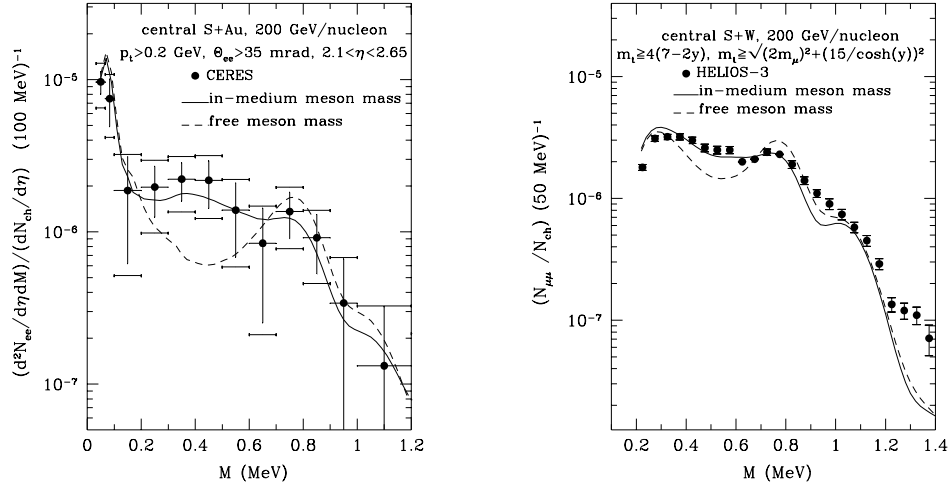


Figure 4.14: Comparison of dilepton data from central 200 AGeV sulfur-induced reactions on heavy nuclei with transport calculations employing a dropping  $\rho$  mass (full curves) as opposed to a free  $\rho$  mass (dashed curves) [232]; left panel: CERES dielectron spectra on Au targets; right panel: HELIOS-3 dimuon spectra on W targets.

by hadronic initial conditions of  $T^i \simeq 170$  MeV and  $\varrho_B^i \simeq 2.5\varrho_0$ , the in-medium mass  $m_\rho^*$  is close to



the two-pion threshold. As the hot fireball expands thereby diluting and cooling,  $m_\rho^*$  starts to rise and sweeps across the low-mass region thus filling the dilepton continuum between 0.3 and 0.6 GeV (at freezeout, the  $\rho$ -meson has regained about 80% of its vacuum mass). At the same time, the  $\rho$  (or  $\pi\pi$ ) contribution around the free  $\rho$  peak is strongly reduced, which is also in line with the experimental data. However, between the  $\omega$  and the  $\phi$  mass the situation is less clear, mainly due to limited experimental mass resolution and statistics (the former amounting to  $\sim 8$ -11% in this mass region for the '92-'95 CERES data). The medium modifications of the  $\omega$  meson itself have only little impact on the dilepton spectra, although in BR scaling the  $\omega$  mass is subjected to the same reduction as the  $\rho$  mass. The reason is simply that the  $\omega \rightarrow e^+e^-$  decays mostly occur after the hadronic freezeout where medium effects are absent. The final number of  $\omega$  mesons is roughly equal to the case where no dropping masses are assumed. This is so because in Refs. [37, 232] rather large pion chemical potentials  $\mu_\pi \simeq 100$  MeV are present in the initial conditions when using the free masses to correctly reproduce the observed number of final pions. On the other hand, when using in-medium masses, much smaller  $\mu_\pi$  are required to obtain about the same final number of pions and  $\rho/\omega$  mesons. Within the Walecka-type mean-field potentials employed in the transport equations of Refs. [37, 232] the scalar field has been assumed to act on the constituent  $u$ -/ $d$ - quark content of the hadrons only, thus leaving the mass of the  $\phi$  meson, which is an almost pure  $s\bar{s}$  state, unchanged. An important point to note is that the baryons (rather than pions which govern the finite-temperature effects) in the hadronic fireball are the key component in generating the large (attractive) scalar fields which are at the origin of the dilepton enhancement.

Dropping meson masses have also been implemented in hydrodynamical simulations [41, 43]. Although the total dilepton signal in the latter is typically smaller than in the transport frameworks (if  $\mu_\pi \equiv 0$ , see previous Section), they also give reasonable agreement with the S+Au data [41, 43]

As representatives for the analyses of the CERES S+Au data that are based on more 'conventional' scenarios we have chosen the calculations within the chiral reduction approach [100] and the many-body approach for the  $\rho$ -meson spectral function [47] in its recent version (including constraints from nuclear photoabsorption [102] and  $\pi N \rightarrow \rho N$  data [49], Rhosobar excitations on thermally excited baryon resonances as well as a more complete assessment of the mesonic contributions [123]). The results are confronted in Fig. 4.15 with experiment. To facilitate the direct comparison both spectra have been computed in the thermal fireball expansion of Ref. [47] (with  $T^i = 170$  MeV,  $T^\infty = 110$  MeV,  $\tau = 8$  fm/c,  $t_{fo} = 10$  fm/c in Eq. (4.84),  $N_B^{part} = 110$ , a constant isotropic expansion velocity  $v = 0.4c$  and  $\mu_B = 0.39$  GeV which translates into initial/freezeout baryon densities of  $\rho_B^i = 2.49\rho_0$  /  $\rho_B^{fo} = 0.32\rho_0$  and a freezeout temperature of  $T^{fo} = 127$  MeV; in addition an overall normalization factor  $N_0=3$  has been introduced in reminiscence to transport results [37], corresponding to an 'average' pion chemical potential of  $\sim 80$  MeV). Neither of the two 'conventional' approaches gives as good agreement with the S+Au data as the dropping  $\rho$  mass scenarios (this is even more pronounced for other attempts [40, 221, 36, 41]), although the experimental uncertainty is not small. In the chiral reduction formalism (left panel in Fig. 4.15) the incoherent summation of individual rate contributions in a low-density expansion (for both pions and nucleons) generates some enhancement over the results based on free  $\pi\pi$  annihilation (dotted curve in the right panel), but does not lead to any depletion of the free  $\rho$  peak. Consequently, the *shape* of the theoretical curves does not match the experimental data very well. This is qualitatively different in the many-body approach (right panel in Fig. 4.15). The strong broadening

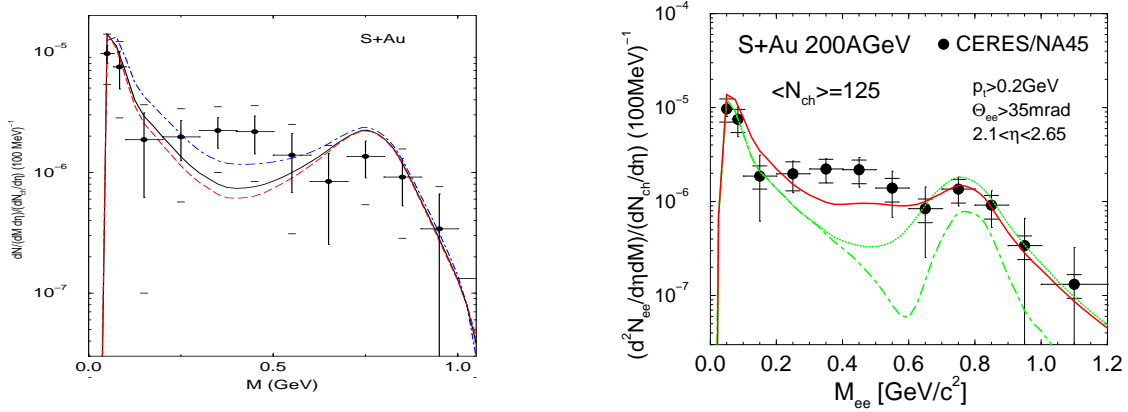


Figure 4.15: Comparison of CERES data from central 200 AGeV S+Au reactions with thermal fireball calculations including in-medium effects according to the chiral reduction formalism [100] (left panel; all curves include the hadronic cocktail as given by transport results [37]; in addition, in-medium radiation is accounted for in the following ways: pure pion gas (dashed curve), pion-nucleon gas using  $\varrho_N^i = 0.7\varrho_0$  corresponding to the realistic case of  $\mu_B = 0.39$  GeV (full curve), and pion-nucleon gas using the full baryon density  $\varrho_N^i \equiv \varrho_B^i = 2.5\varrho_0$  (dashed-dotted curve), and within the many-body approach for the  $\rho$  spectral function [47, 126, 49, 123] (right panel; dashed-dotted curve: hadronic cocktail; dotted curve: cocktail plus  $\pi\pi$  annihilation using the free  $\rho$  spectral function; full curve: cocktail plus  $\pi\pi$  annihilation using the in-medium  $\rho$  spectral function).

of the  $\rho$ -meson spectral function yields a factor of  $\sim 2$  more enhancement below  $M_{ee} \simeq 0.6$  GeV together with some reduction in the  $\rho/\omega$  region, which makes it somewhat more compatible with the data. A possible caveat might be given by the fact that the (experimental) systematic errors presumably have little (or at least a very smooth) dependence on invariant mass. This could mean that an agreement of the theoretical curves in the 0.3–0.5 GeV region entails a disagreement around  $M_{ee} \simeq 0.2$  GeV and vice versa. We will come back to this point further below. Another noteworthy feature is that, although the in-medium spectral function is larger than the free one at the high mass end for  $M_{ee} \geq 0.9$  GeV (cf. Fig. 3.19), this feature does not show up in the dilepton spectrum in the right panel of Fig. 4.15, which can be traced back to the mass resolution of the CERES detector in the '92 setup ( $\delta M/M \simeq 11\%$  around  $M \simeq 1$  GeV).

The spectral function approach has also been employed using a more realistic description of the heavy-ion reaction dynamics within the HSD transport simulations [48]. Fig. 4.16 shows the results for the HELIOS-3 data in 200 AGeV S+W collisions using the free (upper panel) and in-medium (lower panel)  $\rho$  spectral function, the latter based on the model of Refs. [102, 126]. Again, the broadening of the  $\rho$  spectral function significantly improves the agreement with experiment.

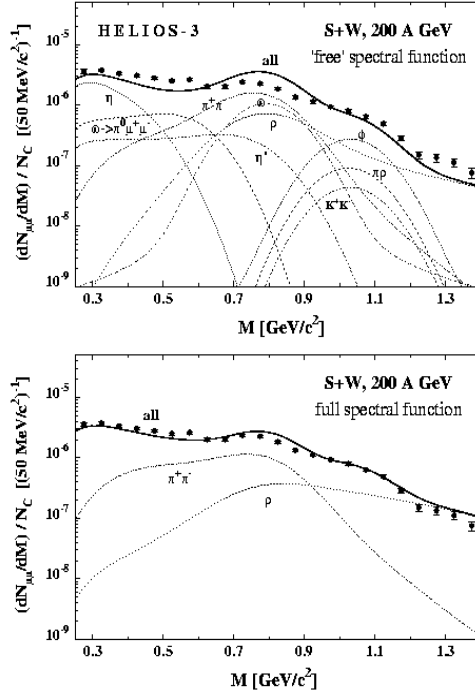


Figure 4.16: Comparison of HELIOS-3 data from central 200 AGeV S+W reactions with HSD transport calculations [48] employing free (upper panel) and in-medium (lower panel)  $\rho$  spectral functions from Refs. [47, 102]; note that the high-mass end of the contribution labeled by ' $\rho$ ' (which stem from meson-baryon and baryon-baryon collisions) is probably somewhat overestimated, cf. the remarks following Eq. (4.83).

### 158 AGeV Lead Beam Runs

Again, let us first address analyses that involve dropping meson masses. Fig. 4.17 shows results of the HSD transport approach [230], which once more demonstrate that a reduced  $\rho$ -meson mass is very well in line with the experimentally observed low-mass dilepton enhancement at full CERN-SpS energies, most notably around the 0.5 GeV region. Similar conclusions have been drawn in the transport calculations of Ref. [255] for the 8% most central sample of the '95 CERES data, as well as in the hydrodynamical description of Ref. [43].

Proceeding to category II ('conventional' medium modifications), we display in Fig. 4.18 a comparison of transport and fireball calculations. The left panel shows recent BUU transport calculations [257] along the lines of Ref. [36] where the in-medium effects entirely reside in finite temperature effects in the  $\pi\pi$  annihilation channel and  $\pi\rho$ -type contributions (dominated by the  $a_1(1260)$ ). Due to collisional broadening introduced in the (denominator of) the pion electromag-

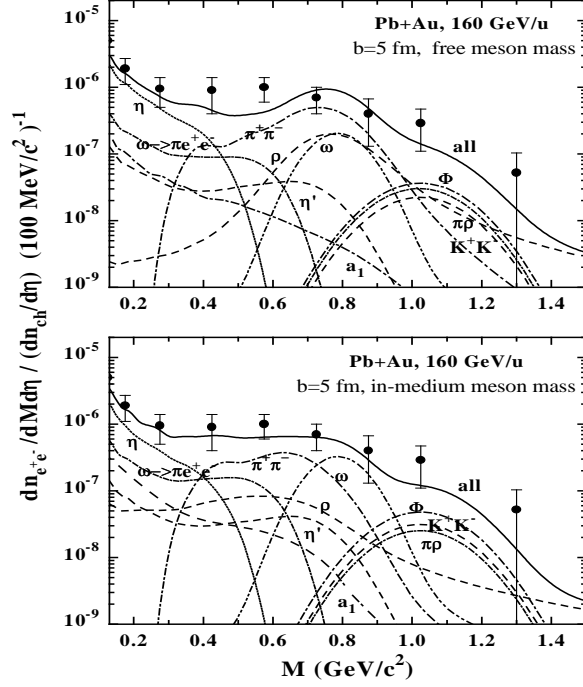


Figure 4.17: Comparison of the (preliminary) '95 CERES data [21] from 35% central 158 AGeV Pb+Au reactions with HSD transport calculations [230] employing free (upper panel) and dropping (lower panel) meson masses.

netic form factor the significance of the in-medium  $\pi\pi$  channel is rather moderate; the processes inducing the broadening (*i.e.*,  $\pi\rho$  collisions) are treated explicitly for dilepton production to approximately restore unitarity in the transport framework. Within 1.5 standard deviations, all data points for 30% central Pb+Au are reproduced; in the low-mass region,  $M_{ee} \simeq 0.3 - 0.6$  GeV, this is largely achieved through a strong contribution of the  $\omega \rightarrow \pi^0 e^+ e^-$  and  $\eta \rightarrow \gamma e^+ e^-$  Dalitz decays, each about a factor of 2 larger than in the CERES cocktail. As we have mentioned earlier, especially the  $\omega$  contribution is as of now not very well under control (and has been introduced through suitable initial conditions in the transport); on the other hand, one also realizes from the left panel of Fig. 4.18 that at the free  $\rho/\omega$  mass the direct decays  $\omega \rightarrow e^+ e^-$  tend to overestimate the experimental data, *i.e.*, the freezeout  $\omega$  abundance has been pushed to its limit. In contrast, the in-medium spectral function approach [142, 47, 147, 91, 101] assigns the major part of the low-mass enhancement to the (modified)  $\pi\pi$  channel including the effects of baryons. The right panel

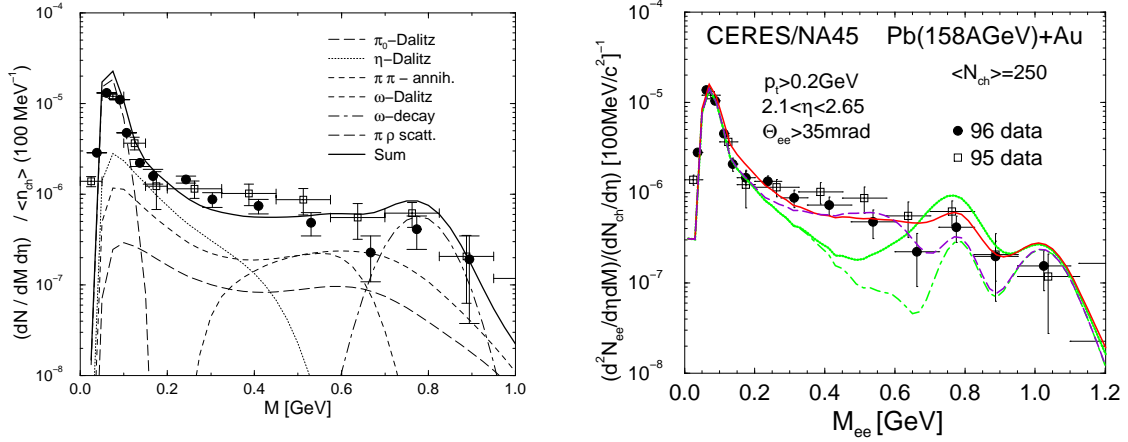


Figure 4.18: Comparison of the CERES data from 35%/30% central 158 AGeV Pb+Au collisions with BUU transport calculations [36, 257] including finite-temperature effects in the pion electromagnetic form factor and through explicit  $\pi\rho$  scattering (left panel). Right panel: fireball calculations [47] using thermal production rates from in-medium  $\pi\pi$  annihilation in three scenarios; dashed-dotted line: CERES cocktail (no in-medium contribution, no  $\rho$  decays); dotted line: cocktail plus free  $\pi\pi$  annihilation; solid line: cocktail plus  $\pi\pi$  annihilation employing the in-medium  $\rho$  spectral function [102, 123, 50]; long-dashed line: cocktail plus  $\pi\pi$  annihilation using a dropping  $\rho$  mass.

of Fig. 4.18 shows the pertinent results [123, 50] employing a thermal fireball model including the experimentally determined hadro-chemical freezeout as well as the subsequent build-up of finite pion chemical potentials (cf. Sect. 4.4.3) in 30% central Pb+Au (the time evolution is specified by initial/freezeout conditions  $(T, \varrho_B)_{ini} = (190 \text{ MeV}, 2.55 \varrho_0)$ ,  $(T, \varrho_B)_{fo} = (115 \text{ MeV}, 0.33 \varrho_0)$  with  $N_B^{part} = 260$ ). The hadronic cocktail part has been taken from the CERES collaboration [256] based on an identical chemical freezeout but with the  $\rho$ -meson contribution removed, since the latter is accounted for by the in-medium  $\pi\pi$  annihilation at the freezeout stage of the fireball. Also included in Fig. 4.18 is the result obtained with a dropping  $\rho$  mass based on the same fireball evolution. The density and temperature dependence of  $m_\rho^*$  has been assumed to resemble QCD sum rule estimates,

$$m_\rho^* = m_\rho (1 - C \varrho_B / \varrho_0) (1 - (T/T_c^X)^2)^\alpha \quad (4.88)$$

with  $C = 0.15$ ,  $T_c^X = 200 \text{ MeV}$  and  $\alpha = 0.3$ . Given the experimental uncertainties both the dropping  $\rho$  mass and the in-medium broadening give reasonable account for the dilepton enhancement in the 0.3–0.6 GeV region. Substantial differences set in beyond, where the down-shifted  $\rho$  mass does no longer contribute, as opposed to the broadening scenario. At the  $\rho/\omega$  peak, the more recent data seem to favor the former, but between the  $\omega$  and  $\phi$ , the in-medium spectral function might do better, providing sufficient yield. Once again we see that an improved mass resolution of the measurements, separating  $\omega$  and  $\phi$  cocktail ingredients more distinctly, is crucial to reach

definite conclusions on these issues.

Hydrodynamical calculations employing in-medium rates of category II have been performed recently in Ref. [252]. In particular, the differences between the many-body [47, 102] and the chiral reduction approach [100] and their consequences for dilepton production in central Pb+Au have been explored in some detail. On the level of the bare rates the two approaches agree reasonably well in the pion gas sector, but differ by factors of  $\sim 2$  already at finite (nucleon) densities as low as  $0.5\rho_0$ , cf. Sect. 4.2.1 and Fig. 4.4<sup>2</sup>. This directly translates into a similar discrepancy in the  $\pi\pi$  induced dilepton signal, with the many-body rates resulting in the larger yield (left panel of Fig. 4.19), once more demonstrating that baryons play an important role at full SpS energies of 158–200 AGeV. These findings are very reminiscent to the naive fireball calculations in central S+Au

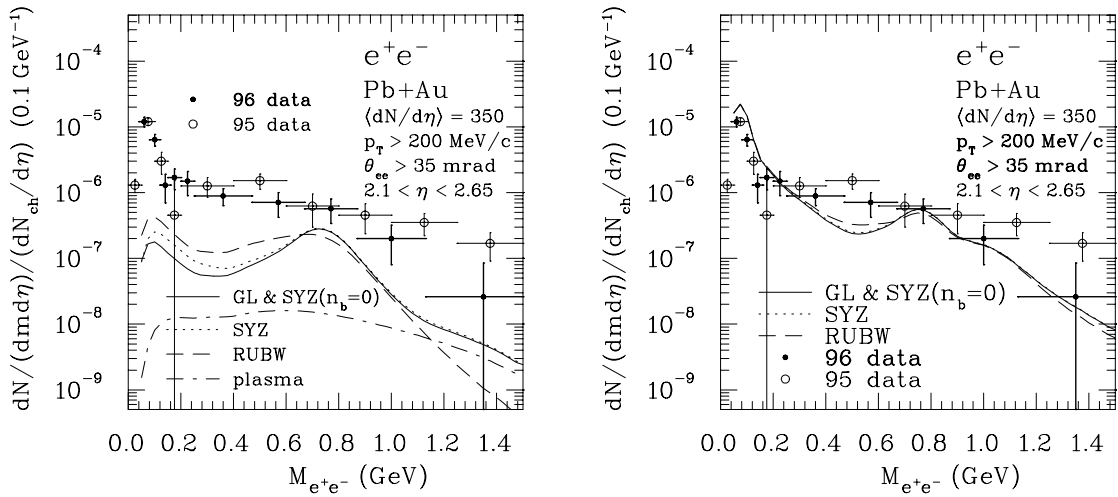


Figure 4.19: Comparison of the '95 and '96 CERES data from 8% central 158 AGeV Pb+Au with hydrodynamical calculations [252]; left panel: dielectron yields from the interaction phase using hadronic rates without baryonic effects [119, 99] (solid line) and including baryonic effects according to the chiral reduction [100] (dotted line) or the many-body framework [102] (long-dashed line), and from the QGP phase using perturbative  $q\bar{q}$  annihilation (dashed-dotted line); right panel: final spectra including hadron decays after freezeout (line identification as in left panel).

displayed in Fig. 4.15. Note that the absolute magnitude of the  $\pi\pi$ -induced signal in Fig. 4.19 is appreciably smaller than in transport calculations, owing to the vanishing pion chemical potential implicit in the hydrodynamical framework. The final results are therefore not quite able to account for the CERES data in the  $M_{ee} \simeq 0.5$  GeV region. At the same time, as a consequence of the rather small thermal  $\omega$  meson abundance at freezeout, the signal from direct  $\omega \rightarrow e^+e^-$  decays amounts

<sup>2</sup>One should note that the  $\rho$  spectral function on which the calculations in Ref. [252] are based, is not the most recent (more complete) one, although it includes constraints from photoabsorption spectra according to Ref. [102].

to only about 50% of the one in the CERES cocktail; thus, there is no issue of overpredicting the  $\rho/\omega$  region (right panel of Fig. 4.19).

One of the most attractive features of hydrodynamic simulations is their capability of incorporating phase transitions in the time evolution in a well-defined way via the equation of state. For SpS energies at 158–200 AGeV, however, the general findings are [40, 43, 214] that the dilepton signal from a possibly formed quark-gluon plasma, as estimated by employing perturbative  $q\bar{q} \rightarrow e\bar{e}$  annihilation rates, is down by about an order of magnitude as compared to the  $\pi\pi$  channel for invariant masses below 1 GeV (dashed-dotted curve in the left panel of Fig. 4.19). Recalling that the thermal  $q\bar{q}$  production rates are not very different from the in-medium hadronic ones (cf. Fig 4.6 in Sect. 4.2.3), one has to conclude that at SpS energies the space-time volume occupied by the QGP phase is rather small (this might not be the case for the mixed phase).

The CERES collaboration has also analyzed their data with respect to centrality dependence of the invariant mass spectra, *i.e.*, dividing them in four distinct event classes with average charged multiplicities  $\langle N_{ch} \rangle = 150, 210, 270$  and 350. Although one finds a clear increase of the enhancement with  $\langle N_{ch} \rangle$ , especially the low-multiplicity events do not allow for more quantitative statements. No systematic theoretical analyses are available yet.

#### 4.6.4 Medium Effects II: Transverse Momentum Dependencies

An additional observable to help discriminate different mechanisms that lead to a similar enhancement in the invariant mass spectra is the dilepton transverse momentum  $q_t$ , *i.e.*, the total momentum of the dilepton pair perpendicular to the beam axis of the colliding nuclei. From a theoretical point of view this possibility is provided by the fact that the specification of a preferred reference frame – that is, the thermal frame, in which the matter as a whole is at rest – breaks Lorentz invariance of space-time. It implies that the in-medium propagators of the vector mesons (or, equivalently, their spectral functions) separately depend on energy  $q_0$  and three-momentum modulus  $|\vec{q}|$  (or on invariant mass  $M = (q_0^2 - \vec{q}^2)^{1/2}$  and three-momentum). Moreover, their polarization states are no longer isotropic, but split up into two completely independent modes, most conveniently described in terms of longitudinal and transverse components, see Sect. 2.6, Eqs. (2.97), (2.98). A different behavior of the latter might induce anisotropies in the dilepton yield which are, however, extremely difficult to measure. No such attempt has been made to date. On the other hand, transverse momentum spectra in three (four) adjacent invariant mass bins have been extracted by the CERES collaboration in the '95 ('96) lead runs. Since in the CERES experiment the full kinematic information on the individual lepton tracks is recorded, their  $q_t$ -spectra are subject to the same statistical and systematic errors as the invariant mass spectra.

In the previous Section we have seen that both the dropping  $\rho$  mass and the in-medium spectral function scenarios can reproduce the invariant mass spectra at full CERN-SpS energies reasonably well. Both approaches have also been employed to calculate transverse momentum spectra [49, 103] (Figs. 4.20, 4.21). Naively one would expect that a mere reduction of the  $\rho$  mass does not entail any distinct traces in the  $q_t$ -dependence; this is, however, not true due to a subtle interplay with the thermal occupation factors  $f^\rho(q_0)$ , which depend on *energy*. Thus, for a small  $\rho$  mass  $m_\rho^*$ , the three-momentum dependence of  $q_0 = [(m_\rho^*)^2 + \vec{q}^2]^{1/2}$  is more pronounced, leading to a relative enhancement of  $\rho$  mesons of small three-momentum. This is nicely reflected by the left panel of Fig. 4.20, where the enhancement of the dropping  $\rho$  mass curve in the  $0.2 \text{ GeV} < M < 0.6 \text{ GeV}$

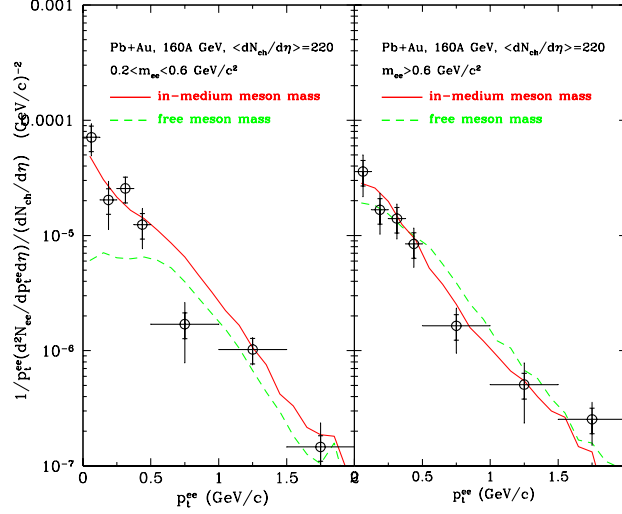


Figure 4.20: Comparison of the CERES transverse momentum spectra in two invariant mass bins from 30% central 158 AGeV Pb+Au [23] with dropping  $\rho$  mass calculations in a transport model [103]; dashed and full curves: using free and in-medium masses, respectively.

invariant mass bin is predominantly concentrated at transverse momenta  $q_t \lesssim 0.6$  GeV, in good agreement with the '95 CERES data. More complicated three-momentum dependencies may arise in the spectral function approach. This was first pointed out in Ref. [147], where substantial effects with increasing three-momentum were predicted on the basis of a strong  $\rho N$   $P$ -wave coupling to the  $N(1720)$  and  $\Delta(1905)$  resonances. The accompanying hadronic vertex form factors,

$$F_{\rho BN}(q) = \Lambda_{\rho BN}^2 / (\Lambda_{\rho BN}^2 + \vec{q}^2), \quad (4.89)$$

which govern the suppression of large three-momenta of the  $\rho$ , were used with rather hard cutoff parameters of  $\Lambda_{\rho BN} = 1.5$  GeV. However, in a subsequent analysis of photoabsorption spectra [102] it turned out that such values are not compatible with  $\gamma p$  and  $\gamma A$  data, requiring much softer  $\Lambda_{\rho BN} \simeq 0.6$  GeV. These constraints have been extracted before any data on dilepton  $q_t$ -spectra were available. A spectral function calculation of the latter [50], including these constraints, is shown in Fig. 4.21. Similar to the dropping  $\rho$  mass results, its basic features agree with the data.

In another projection of the data, the CERES collaboration generated invariant mass spectra for two distinct regions of transverse pair momentum, *i.e.*,  $q_t < 0.5$  GeV and  $q_t > 0.5$  GeV [251]. Again, one clearly observes that the major part of the low-mass enhancement is concentrated in the low-momentum bin, whereas the high-momentum bin is essentially consistent with the cocktail (Fig. 4.22). This is just opposite to the rate calculations based on  $P$ -wave  $\rho N$  scattering performed in Ref. [147], which confirms the necessity for rather soft form factors as predicted on the basis



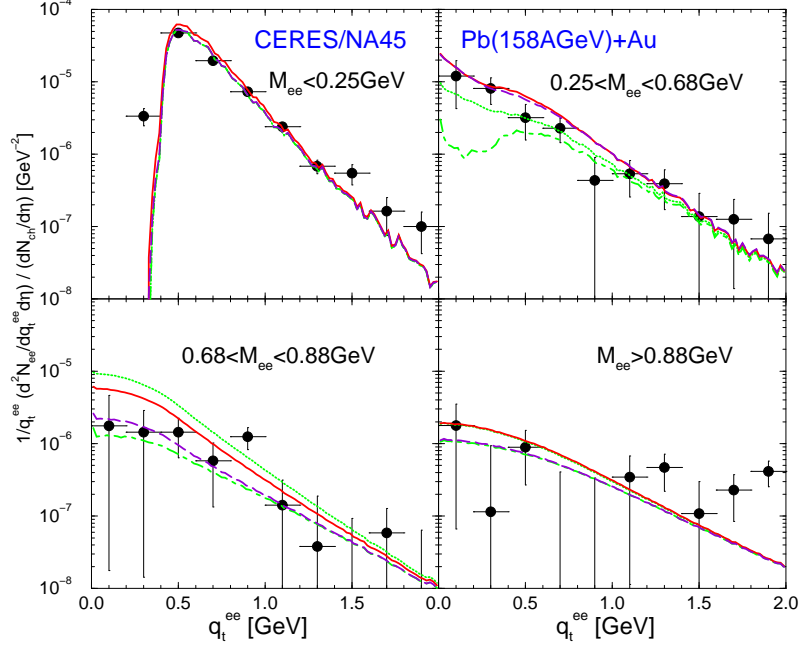


Figure 4.21: Comparison of the CERES transverse momentum spectra in four invariant mass bins from 30% central 158 AGeV Pb+Au [251] using a thermal fireball model including finite  $\mu_\pi$  [50]; dashed-dotted curves: CERES cocktail; dotted curves: cocktail + free  $\pi\pi$  annihilation, dashed curves: cocktail +  $\pi\pi$  annihilation with a dropping  $\rho$  mass, full curves: cocktail +  $\pi\pi$  annihilation using the in-medium  $\rho$  spectral function.

of photoabsorption data. The theoretical calculations shown in Fig. 4.22 contrast once more the results of a dropping  $\rho$  mass and the in-medium broadened spectral function. At the present status of the data, both explanations are viable.

#### 4.6.5 Time Dependence of In-Medium Signals

The great hope that has been associated with dilepton observables as penetrating probes is to learn about the innermost zones of high-density and high-temperature matter formed in the early stages of nuclear collisions. Thus, after our detailed study of various models in their application to experimental low-mass dilepton spectra we would like to address the question as to what extent signals from the highest excitation phases can be disentangled, *i.e.*, how certain features in the spectra might be related to the time (or temperature/density) of emission. Unfortunately, the answers are beset with strong model dependencies, even if the 'background' from the hadronic cocktail were accurately known (as we will for simplicity pretend in the following). The dropping  $\rho$  mass scenario implies an obvious correlation between invariant mass and emission time for the in-medium signal:

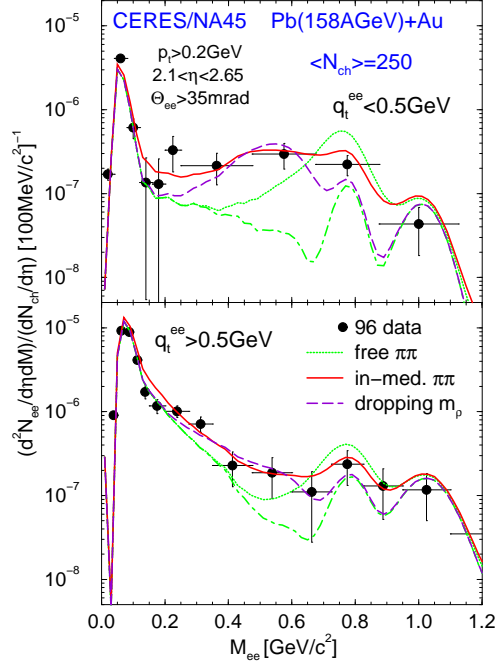


Figure 4.22: Comparison of 30% central 158 AGeV Pb+Au CERES invariant mass spectra in two transverse momentum bins [251],  $q_t < 0.5$  (upper panel) and  $q_t > 0.5$  (lower panel) with thermal fireball calculations [50] (including finite  $\mu_\pi$ ) employing a dropping  $\rho$  mass (dashed curves) and an in-medium spectral function (full curves); the dashed-dotted curve is the CERES cocktail (without the  $\rho \rightarrow e^+e^-$  contribution), added to the respective  $\pi\pi$  annihilation yields from the fireball.

using as a rough guideline the fireball evolution for 30% central Pb+Au collisions [50] (cf. Fig. 4.8) together with a temperature- and density-dependent mass given by the QCD sum rule-type relation (4.88), the time instances  $t=1, 6$  and  $11$  fm/c correspond to masses  $m_\rho^*(t)=275, 465$  and  $650$  MeV, respectively, which directly reflect the populated dilepton invariant mass regions. The situation is less straightforward when an in-medium spectral function is employed. The left panel of Fig. 4.23 shows a (partial) decomposition of the total in-medium signal in three equidistant time slabs. Within a few percent the integrated yield from each of the three time intervals is essentially equal which is due to a trade-off between increasing volume and decreasing temperature during the expansion. Although lower masses are preferably populated at earlier stages, the time dependence of the spectral shape is rather smooth especially when comparing to the dropping mass scenario. The most prominent feature associated with early emission times is a strong depletion of the free  $\rho$  peak around  $M \simeq 0.75$  GeV. The total final spectrum (solid line in Fig. 4.23) in fact closely

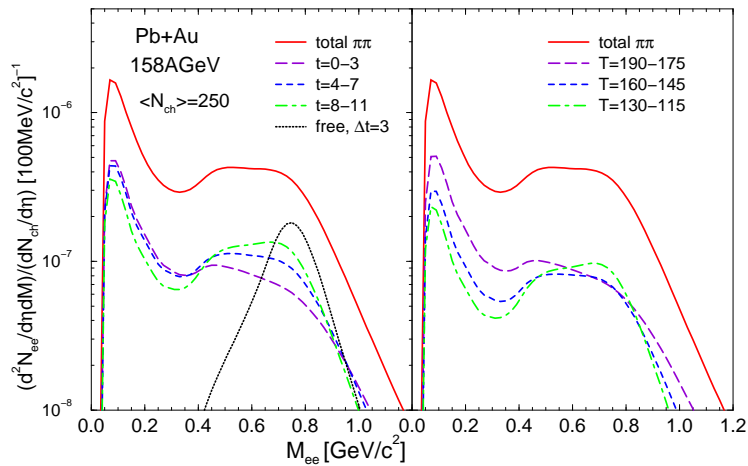


Figure 4.23: Decomposition of the  $\pi\pi \rightarrow ee$  signal employing the in-medium  $\rho$  spectral function from Refs. [102, 123, 50] in 30% central Pb+Au (including the acceptance of the CERES detector); the solid line is the total yield from a thermal fireball of lifetime  $t_{fo}=11.5$  fm/c. In the left panel, the long-dashed, short-dashed and dashed-dotted curves represent the contributions from the time intervals  $t=0-3$  fm/c,  $t=4-7$  fm/c and  $t=8-11$  fm/c, respectively, and the dotted curve arises for an emission via free  $\pi\pi$  annihilation over a duration of  $\Delta t = 3$  fm/c being almost independent on the evolution stage. In the right panel the yields arising during temperature intervals  $T=175-190$  MeV (long-dashed curve),  $T=145-160$  MeV (short-dashed curve) and  $T=115-140$  MeV (dashed-dotted curve) are displayed.

resembles the contribution from intermediate times (4–7 fm/c, short-dashed curve) multiplied by a factor of 4. This means that the time-integrated in-medium signal actually probes a hadronic resonance gas at an average temperature and density of about  $T \simeq 150 - 160$  MeV and  $\rho_B \simeq \rho_0$ , not very far from the expected phase boundary to the quark-gluon plasma. Also note that a typical emission spectrum from free  $\pi\pi$  annihilation is quite different from the in-medium pattern even close to freezeout.

At low masses a more pronounced differentiation emerges when one divides the emission contributions into temperature (density) slices, cf. right panel of Fig. 4.23. The strongest fingerprint of a high temperature/density phase seems to be around the free two-pion threshold,  $M_{ee} \simeq 0.3$  GeV. The difference to the time decomposition arises since the system spends somewhat longer time (3 fm/c) in the high temperature interval than in the two lower temperature bins (about 2fm/c). This effect originates from a (slight) softening of the equation of state as borne out of hydrodynamic simulations [213]. It is expected to be much more pronounced in the low-energy (40 AGeV) run at the SpS.

### 4.6.6 Intermediate-Mass Spectra

In this Section we would like to investigate in how far medium effects that have been invoked to explain the low-mass enhancement are relevant for/consistent with the intermediate-mass regime (IMR). In Sect. 4.2.3 it has already been eluded to the conjecture that in vacuum, starting from invariant masses of about  $M_{ee} \simeq 1.5$  GeV, one enters the 'dual' regime, *i.e.*, the thermal dilepton emission rate can be reasonably well accounted for without further medium effects by either

- (i) perturbative  $q\bar{q} \rightarrow e^+e^-$  annihilation, based on the observation that the reverse process accounts for the total inclusive cross section for  $e^+e^- \rightarrow \text{hadrons}$  within  $\sim 30\%$ , or
- (ii) binary hadronic collisions, once an appropriate set of meson states is included, being similarly constrained by  $e^+e^- \rightarrow \text{hadrons}$  cross sections in the corresponding (exclusive) channels.

Then the following questions have to be asked:

- (1) Are such 'dual' rates compatible with experimental spectra?
- (2) How do medium effects, which are crucial at low masses, influence the intermediate-mass region?

For the quark-gluon description it has been argued that medium effects should play a minor role as the small distance annihilation of (nearly) massless quarks and antiquarks inhibits large corrections from the surrounding heat bath. However, this is much less obvious within the hadronic picture since the interacting mesons (such as in the dominant  $\pi a_1$  channel) carry substantial rest masses which already make up a large fraction of the  $cm$  energy so that the annihilation reactions involve fairly small momentum transfers.

At the CERN-SpS, intermediate-mass dilepton spectra have been measured by the HELIOS-3 and NA38/NA50 experiments. In analogy to the low-mass case one can divide the spectra into a (physical) background part and an in-medium signal radiated from the interaction phase of the fireball. If one again defines the background as the contributions arising in  $p+p$  collisions, the higher masses probed necessitate a somewhat different composition that now mainly stems from hard processes occurring in the primordial stage of the collision. Most notably these are Drell-Yan annihilation as well as open-charm decays (*i.e.*, an  $l^+l^-$  pair originating from the separate decay of an associatedly produced pair of  $D$  and  $\bar{D}$  mesons) which are negligible in the low-mass region [258], but start to dominate over the final-state meson decays for  $M_{ll} \gtrsim 1.5$  GeV. Contrary to the final-state meson decays, the initial hard processes are assumed to scale with the number of primary nucleon-nucleon collisions to provide their contribution in  $p+A$  and  $A+A$  reactions (for the open charm, *e.g.*, this has been verified for  $p+A$  collisions in Ref. [258]). Fig. 4.24 shows a comparison of the the HELIOS-3  $\mu^+\mu^-$  data from  $p+W$  and  $S+W$  collisions with the various background sources [29, 204]. Whereas the total background reproduces the  $p+W$  spectra quite satisfactorily, the  $S+W$  data are underestimated by a factor of 2–3 throughout the entire mass range from 1–2.5 GeV (equivalent observations have been reported from the NA38/NA50 collaboration [27]).

Li and Gale have performed transport calculations including the radiation from the fireball using the mesonic production rates from binary collisions [204]. They find good agreement with the HELIOS-3 data in the intermediate-mass region if no further medium effects are included (dotted line in Fig 4.25). In particular, this implies that both perturbative  $q\bar{q}$  rates and the lowest-order in temperature mixing effect in the axial-/vector correlator are compatible with the data (as follows from the rate comparison discussed in Sect. 4.2.3). On the other hand, the low-mass end of the spectrum (below  $\sim 1$  GeV) cannot be explained in terms of binary collisions without invoking any further medium effects. Li and Gale therefore employed the dropping mass scenario extrapolated

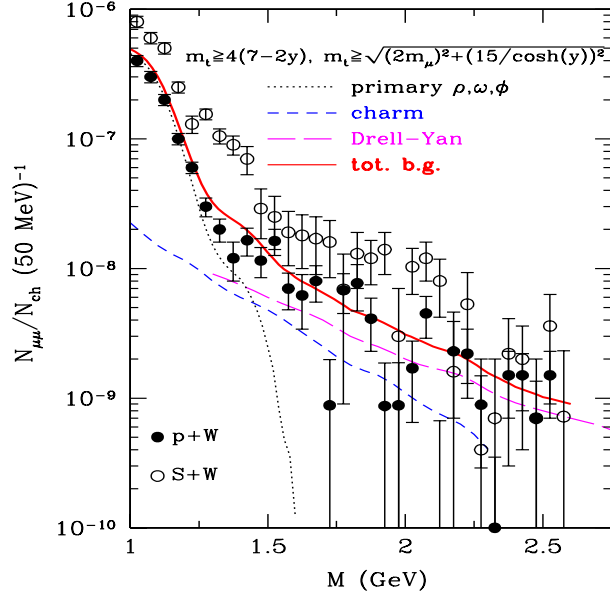


Figure 4.24: Dimuon invariant mass spectra from the HELIOS-3 collaboration [24] taken in 450 GeV proton-induced and 200 AGeV sulfur-induced reactions on tungsten targets (full and open circles, respectively), compared to the expected background yields from light vector mesons (dotted curve), Drell-Yan processes (long-dashed curve), open charm decays (short-dashed curve) and their sum (solid curve). The plot is taken from Ref. [204].

to include the higher mass (non-strange) vector resonances as well. The data are then nicely reproduced from the two-muon threshold up to about 1.2 GeV, but seem to be underestimated beyond (possibly also between the  $\omega$  and  $\phi$  mass).

Using the emission rates from the chiral reduction formalism, together with an expanding thermal fireball model [47], Lee *et al.* [205] have obtained similar results to the Li-Gale calculations with free meson masses.

As of now there are no intermediate-mass dilepton calculations available using in-medium many-body spectral functions. Here the question is whether a strong broadening of, *e.g.*, the  $\rho$  resonance could lead to an *over*-estimation of the data in the 1–1.5 GeV mass region. However, from a theoretical point of view, if the broadening scenario indeed approaches chiral restoration by merging into the perturbative plateau-value for the vector and axialvector correlators (as we have argued in Sects. 2.6, 4.2.3), the HELIOS-3 data will be reproduced, see the above remarks. Also note that the in-medium  $\rho$ -meson spectral function as used for the low-mass region actually exhibits only a rather moderate enhancement (factor of  $\sim 2$ ) over the vacuum one for invariant masses somewhat above the free  $\rho$  peak (Fig. 3.19). Above 1 GeV further contributions need to be included for a more complete description of the vector correlator, such as  $\pi a_1 \rightarrow \rho'$  selfenergies corresponding to four-pion like processes. This will closely resemble the kinetic theory treatment in terms of the various binary scattering processes, as performed in Ref. [204]. Since coherence effects in the many-

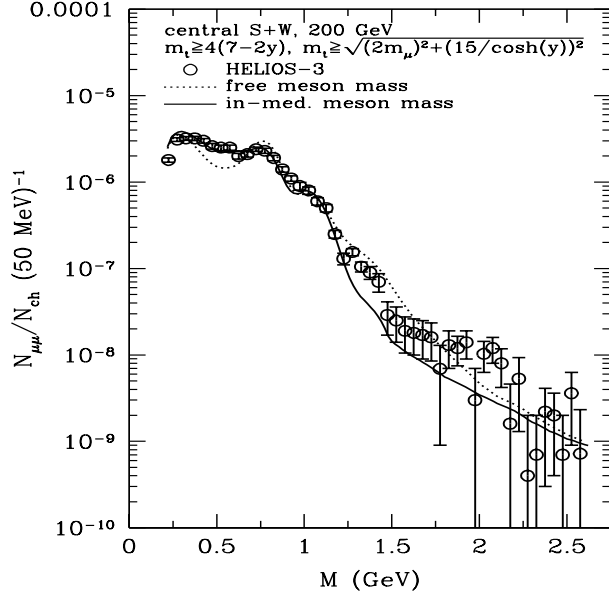


Figure 4.25: Dimuon invariant mass spectra as measured by the HELIOS-3 collaboration [24] in 200 AGeV S+W reactions, compared to transport calculations using a purely hadronic description for the dilepton radiation from the fireball; dotted line: employing free hadron masses; full line: dropping mass scenario. The plot is taken from Ref. [204].

body treatment are expected to be small especially towards higher energies (already in the low-mass region they were found to be quite moderate), there should be little discrepancies to the (incoherent) kinetic approach, even on a quantitative level. Beyond  $M = 1.5$  GeV the 'dual' (hadronic or partonic) production rates are characterized by an essentially flat spectral shape. Here the main issue therefore is whether the space-time description used for the calculations in the low-mass region will lead to a total yield that reproduces the experimentally observed enhancement. Another possible source of this excess has been pointed out by the NA50 collaboration: they showed [27] that the excess can be accounted for by introducing an anomalously increased production of open charm mesons by a factor of  $\sim 3$ . However, there are no theoretical indications for a suitable mechanism of this kind (the final answer will be provided by a direct measurement of produced  $D$  mesons at the CERN-SpS). Lin and Wang [259] have addressed the possibility of  $D$  meson rescattering to enrich the dilepton yield in the NA50 acceptance; however, this does not constitute more than a 20% effect. On the other hand, in the recent analysis of Ref. [244] it has been shown that the use of the dual lowest-order  $q\bar{q}$  annihilation rate throughout the entire mass range from 0–3 GeV folded over a schematic fireball evolution [47] leads to very similar yields in the IMR as obtained with a factor of 3 open charm enhancement; at the same time the (low-mass) CERES data are approximately accounted for (see also dashed curve in Fig. 4.29). Similar conclusions are reached in Ref. [260]: the NA50 enhancement between 1.5 and 3 GeV can be explained with the dual  $q\bar{q}$  rate employing the same fireball model [50] (being consistent with hadro-chemical analysis

of CERN-SpS data including finite pion chemical potentials towards thermal freezeout) that leads to a satisfactory description of the CERES data once medium effects in the  $\rho$  spectral function are incorporated.

## 4.7 Direct Photon Spectra

As we have stressed in Sect. 4.3, real photons and dileptons can be considered as two kinematical realizations of otherwise identical electromagnetic production mechanisms. For heavy-ion reactions it follows that any model which claims success in describing the observed dilepton spectra must also be consistent with direct photon spectra. The notion 'direct' has been introduced to refer to only those photons which are originating from the interaction phase of the fireball, *i.e.*, unlike the dilepton case, the contributions from hadron decays after freezeout are considered as a background that ought to be subtracted to obtain the final spectra. This, in fact, represents the main experimental difficulty, since around 90% or more of the photons produced in heavy-ion collisions at full SpS energies stem from the  $\pi^0 \rightarrow \gamma\gamma$  and  $\eta \rightarrow \gamma\gamma$  decays. As a consequence direct photon observables are about two orders of magnitude less sensitive to any in-medium signals than dileptons [261]. Also note that the observed single-photon energies pick up the laboratory three-momentum of the decaying hadron and hence are not restricted by the hadron rest mass – as opposed to the invariant masses of dileptons from the Dalitz decays, where  $M_{ll} \leq m_\pi$ , etc.. The major systematic error then arises from the uncertainty in the  $\pi^0$  and  $\eta$  abundances. The contributions from other mesons are usually estimated from the so-called ' $m_T$  scaling', *i.e.*, a  $\sim \exp(-\beta m_T)$  dependence of the transverse mass spectra with a universal slope parameter  $\beta$ . Photon measurements at the CERN-SpS have been performed by the HELIOS-2 [262], CERES [263] and WA80/WA98 [264, 265] collaborations. In central S+Au, WA80 found a photon excess of  $5\% \pm 5.8\%$ (syst)  $\pm 0.8\%$ (stat) consistent with CERES and HELIOS-2 results which carry somewhat larger errors. From these measurements they extracted an upper limit for direct photons at the 90% confidence level (see below), which has been used to test theoretical models. More recently, a preliminary direct photon spectrum for central Pb+Pb has been published [265].

In hydrodynamical simulations [266, 267] it has been claimed that the upper limits set by WA80 are not compatible with purely hadronic scenarios. However, these conclusions have been drawn using a very limited number of degrees of freedom in the hadronic gas phase ( $\pi, \eta, \omega, \rho$ ). For equal initial energy densities this leads to much larger initial temperatures in the hadronic phase than in a quark-gluon plasma, entailing much higher photon yields. Purely hadronic models with lower initial temperatures cannot be ruled out by this reasoning. In fact, the thermal production rates of photons from a QGP are presumably not very different from those of a hadron gas at the same temperature, as has been first noted in Ref. [206]. Hence, similar to what has been found for dileptons, one should expect that at CERN-SpS energies the rather small space-time volumes occupied by a possibly formed QGP do not generate substantial photon signals as compared to the hadronic phase. This has been explicitly demonstrated in the hydrodynamic calculations of Refs. [266, 214]. Thus one is led to focus on the multiple possibilities for hadronic photon production (Sect. 4.3).

Fig. 4.26 shows the photon transverse momentum spectra from various sources in central S+Au collisions at 200 AGeV, evaluated in the transport framework [268]. A kinematical cut in pseu-

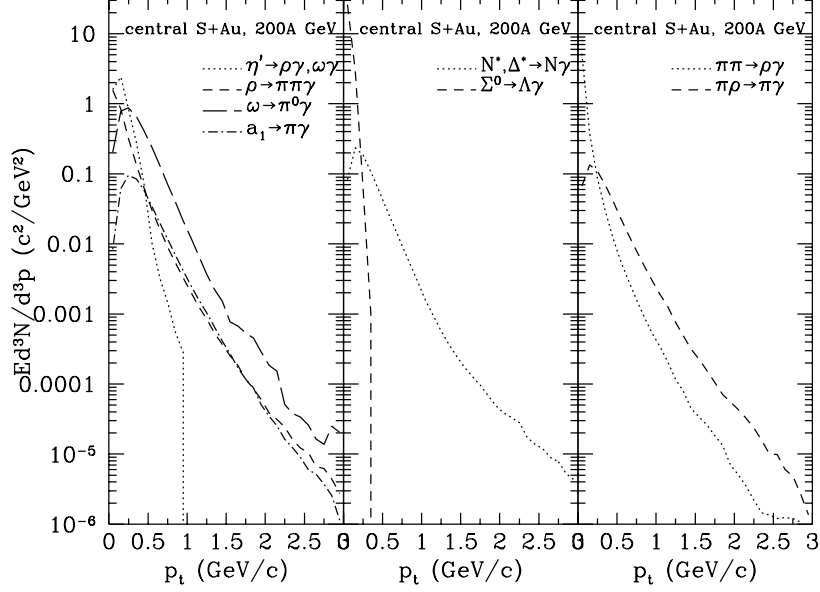


Figure 4.26: Thermal single-photon spectra from meson decays (left panel), baryon decays (middle panel) and two-body reactions (right panel) in transport calculations for central 200 AGeV S+Au collisions [268].

rapidity of  $2.1 < \eta < 2.9$  is applied to comply with the WA80 experiment. For transverse momenta  $q_t \geq 0.5$  GeV the dominant processes are radiative  $\omega$  and  $a_1$  decays, the latter significantly exceeding the nonresonant  $\pi\rho \rightarrow \pi\gamma$  reactions. Note that the baryonic decays seem to have little relevance here. Fig. 4.27 shows that the incoherent sum of all contributions (short-dashed curve) respects the experimental upper limits of WA80. Furthermore, applying the dropping-mass scenario within the same transport approach does not induce major changes in the final spectrum (full curve in Fig. 4.27), which can be traced back to compensating mechanisms: for the radiative decays of the vector mesons  $\rho$ ,  $\omega$  and  $a_1$ , their increased abundance (due to the smaller masses) is balanced by a reduced phase space for the decay products (see also Ref. [269], where similar observations have been made at the relevant temperatures of about  $T \simeq 160$  MeV). Analogous features have been found for other variants of the dropping  $\rho$ -meson mass scenario when implemented in the Hidden Local Symmetry approach for  $\pi$ - $\rho$ - $a_1$  dynamics [270]. Also shown in Fig. 4.27 are the hydrodynamical results of Ref. [266] (long-dashed curve) which, as mentioned above, strongly overshoot the WA80 bounds due to a high initial temperature in a purely hadronic description with rather few degrees of freedom. On the other hand, using a larger set of hadronic states (including



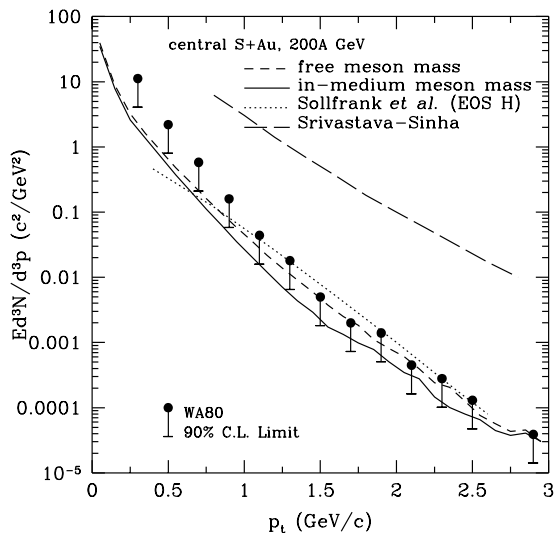


Figure 4.27: Total direct photon spectra in central 200 AGeV S+Au collisions compared to the upper limits of the WA80 collaboration [264]; full and short-dashed curves: transport calculations of Ref. [268] with and without dropping masses, respectively; long-dashed curve: Bjorken-type hydro-calculations with a purely hadronic equation of state including  $\pi, \eta, \rho$  and  $\omega$  mesons only [266]; dotted curve: 2+1 dimensional hydro-calculations employing a purely hadronic equation of state with a larger set of mesons as well as baryons [214]; both hydro-approaches have used the photon production rates of Ref. [206]. The compilation is taken from Ref. [268].

the lowest-lying pseudoscalar and vector meson nonet as well as baryon octet and decuplet), the hydrodynamical calculations of Ref. [214] are essentially compatible with the data and also not very different from the transport calculations.

Concerning the role of baryons, both the chiral reduction formalism [100] and the  $\rho$ -meson spectral function approach [47, 102, 49, 123] have reached conclusions which are at some variance with the relative assignments of the incoherent decomposition given in Fig. 4.26. Using the simple thermal fireball expansion for central S+Au collisions (where the baryon-density evolution is taken from the transport simulations) yields the photon  $q_t$ -spectra displayed in Fig. 4.28; for each of the two approaches, they are based on exactly the same ingredients as the corresponding dilepton spectra of Fig. 4.15. In the chiral reduction formalism the baryonic contributions are exclusively associated with the finite nucleon density in the fireball. According to the decomposition inferred from photoabsorption data (Fig. 4.1) the effects can be attributed to the  $\Delta(1232)$

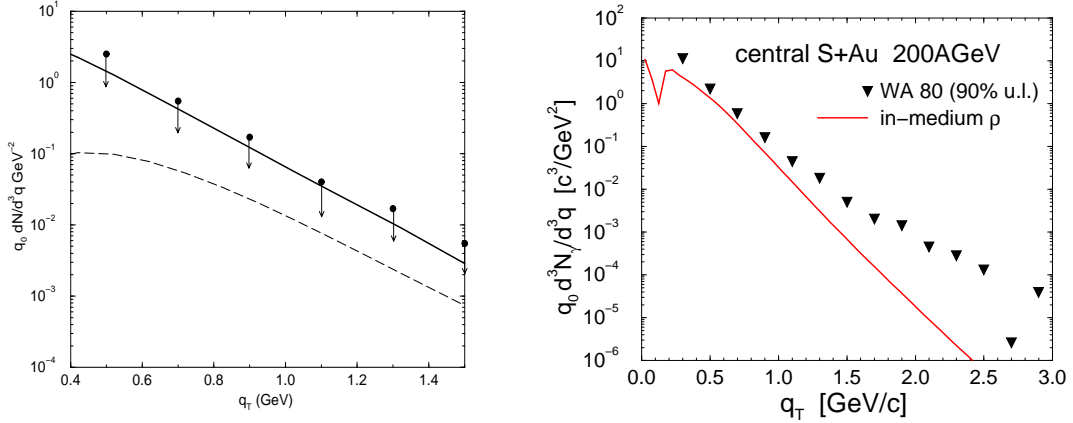


Figure 4.28: Direct photon spectra, compared to WA80 upper limits [264], in central 200 AGeV S+Au collisions using a simple fireball evolution with thermal rates from the chiral reduction formalism [100] (left panel; solid and dashed curve are obtained with and without the baryonic contributions, respectively) and the in-medium  $\rho$  spectral function [47, 102, 49, 123] (right panel).

for  $q_t \leq 0.4$  GeV and to the  $\pi N$ -'background' above. In the photon production spectra for central S+Au reactions they induce an enhancement over the mesonic contributions by a sizable factor (left panel of Fig. 4.28). Very similar results follow from the  $\rho$ -meson spectral function approach, which also reproduces well the nuclear photoabsorption spectra, albeit with a somewhat different decomposition, *i.e.*, a smaller  $\pi N$  'background' together with much larger contributions from direct  $\rho N$  resonances. This difference is not relevant for the direct photon spectra. On the other hand, recalling the comparison to the CERES dilepton spectra in central S+Au, it has been found that the  $\rho$ -meson spectral function approach *does* lead to a larger low-mass enhancement. This can be readily gleaned from the rate comparison exhibited in Fig. 4.4: compared to the Steele *et al.*-rates, the Rapp *et al.*-rates are by a factor 2–3 larger around  $M = 0.5$  GeV (but agree with the former towards the photon point).

## 4.8 Theoretical Implications

After the preceding rather detailed discussion of the various efforts made in exploring low-mass dilepton spectra in (ultra-) relativistic heavy-ion collisions (with additional impact from photon and intermediate-mass dilepton spectra), we have to face the question in which respects it has advanced our understanding of strongly interacting hot and dense matter. For that purpose let us try to critically review and compare the successes and failures as well as the interrelations of the different theoretical attempts that have been pursued to describe the various experiments.

Clearly, the BR scaling conjecture has been very successful in its application to low-mass

dilepton data at CERN-SpS energies of 158–200 AGeV. In its original form it predicts a very specific realization of chiral symmetry restoration, namely that all masses of the light (non-Goldstone) hadrons merge to zero. Most of the underlying arguments in its favor rely on mean-field type approximations, related to the decrease of the chiral quark condensate (via constituent quark masses) or to the presence of strong scalar fields in hot/dense hadronic matter. More recently connections have been drawn to link a reduction in the  $\rho$  and  $\omega$  masses in nuclear matter to strong collective excitations in  $\rho$ - $N$  and  $\omega$ - $N$  interactions, most notably through  $N(1520)N^{-1}$  states. The ramifications of this identification are still under debate.

On the other hand, the consequences of a strong in-medium broadening of the  $\rho$ -meson spectral function, as predicted on the basis of phenomenologically well-established hadronic interactions combined with standard many-body techniques, also seem to reproduce the SpS low-mass dilepton data fairly well. If this scenario holds true close to the phase transition, it implies that the chiral partner of the  $\rho$ , the  $a_1(1260)$ , becomes as broad and structureless: chiral symmetry restoration manifests itself through a merging of both vector and axialvector correlators into a flat continuum (such a behavior has been conjectured to signal deconfinement in Ref. [117]). If, in addition, the height of the continuum corresponds to the perturbative  $q\bar{q}$  plateau value characterized by the famous cross section ratio  $R = \sigma(e^+e^- \rightarrow \text{hadrons})/\sigma(e^+e^- \rightarrow \mu^+\mu^-) = 5/3$  ( $=2$ , when including strange quarks), nonperturbative effects would be marked as no longer relevant which, after all, constitutes the very essence of the quark-gluon plasma. This provokes the following theoretical exercise: we simply replace the in-medium hadronic rates in the expanding fireball model (4.86) by the perturbative  $q\bar{q}$  annihilation rates, (4.40), using the same time evolution of temperature and density. The result shown in Fig. 4.29 indicates that the global use of the pQCD rate looks quite reasonable but cannot fully account for the low-mass enhancement observed in the CERES data (unless one invokes nonperturbative effects, see, *e.g.*, Ref. [182]). More importantly, one should note that, whereas the hadronic medium effects are more sensitive to finite baryon densities, the lowest-order  $q\bar{q}$ -rates exhibit a negligible dependence on a finite quark chemical potential. This obvious 'duality-mismatch' clearly deserves further studies.

Nevertheless, let us return to the hadronic approaches and first address the question what the discriminating features for different fates of the  $\rho$  meson could be, *i.e.*, 'dropping mass' versus 'melting resonance'. Both lead to enhanced dilepton yields below the free  $\rho$  mass, but behave very differently above. Whereas the in-medium broadening implies an *enhancement* over free  $\pi\pi$  annihilation between, say, the  $\omega$  and the  $\phi$  mass, the dropping mass scenario predicts a *depletion* (the possible impact from higher states, such as the  $\rho'(1450)$ , entering this region should be small, since (a) it is not obvious that a large fraction of their mass is due to chiral symmetry breaking, and (b) they have little significance in the pion electromagnetic form factor). As stressed above, an improved mass resolution of the currently available dilepton measurements, together with sufficient statistics, should be able to settle this issue. The mass region just above the  $\rho/\omega$  resonances is also supposed to be accessible by the PHENIX experiment at RHIC, although plagued by a tremendous combinatorial background which may limit any sensitivity to resonance structures with sufficiently narrow widths. Also, both the broadening and the dropping mass are predominantly driven by finite baryon density effects, which are presumably small at RHIC. In this respect the upcoming low-energy run at 40 AGeV at the CERN-SpS will be ideally suited, probing even lower temperatures and higher baryon densities than with the 158 AGeV beams.

The lack of 'dramatic' effects in the  $\rho$  properties in a thermal gas of mesons, as found by many

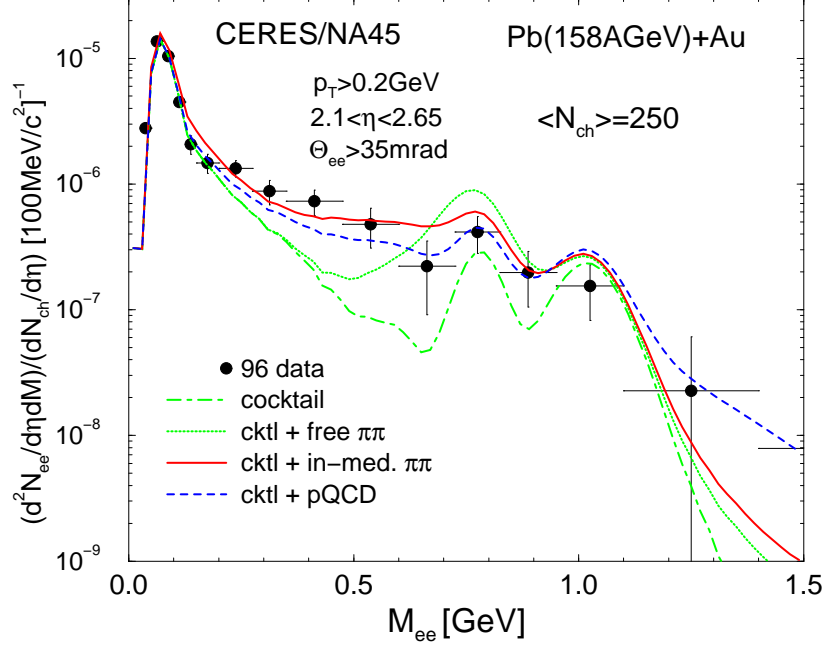


Figure 4.29: CERES dilepton spectra in 30% central Pb+Au collisions [251] compared to a thermal fireball calculation using lowest order  $q\bar{q} \rightarrow ee$  annihilation rates only (dashed line); also shown is the full in-medium  $\rho$  spectral function calculation (solid line). Both fireball yields are supplemented with the CERES cocktail.

authors [120, 47, 121, 122, 123], seems, however, somewhat puzzling. Phenomenologically this can be traced back to the weaker meson-meson interactions (especially with 'Goldstone-protected' pions), as compared to the meson-nucleon case. Thus, when carrying the calculations to higher densities it seems plausible that the  $\rho$  and the  $a_1$  could 'degenerate through broadening'. On the other hand, even at temperatures as high as  $T = 200$  MeV, quite moderate in-medium corrections to the  $\rho$  width have been deduced, reaching at most  $\Gamma_{med} \simeq 200$  MeV. Since this leaves a well-defined resonance structure, it appears unclear how the  $\rho$  and  $a_1$  spectral distributions merge at this point. These features might either point at some shortcomings in the phenomenological approaches or indicate that the lowest-order in temperature vector-axialvector mixing is the prevailing effect in pure *meson* matter. Also note that in most model calculations the chiral condensate exhibits a strong, linear decrease with nuclear density (leading to an appreciable reduction already at normal nuclear density), whereas its temperature dependence is much less pronounced until close to the critical temperature  $T_c^x$ . Again, dilepton measurements at RHIC will hopefully shed more light on the behavior of  $\rho$ ,  $\omega$  and  $\phi$  mesons in a high-temperature and low-baryon-density environment.

Next, we compare the hadronic many-body calculations to the chiral reduction formalism put

forward in its application to electromagnetic emission rates in Refs. [99, 100]. As far as low-mass dilepton production at the CERN-SpS is concerned, the latter seems to give a factor of 2–3 less enhancement in the relevant region around  $M_{ll} \simeq 0.4$  GeV than the results obtained with in-medium  $\rho$  spectral functions [47, 102, 49, 123, 50], see Figs. 4.15, 4.19. Although both approaches have been constrained by photoabsorption spectra on nucleons and nuclei the differences in the dilepton excess do mainly emerge from finite density effects. This is *not* due to a deviation at large densities (*i.e.*, through collective effects), but due to a different assignment of ‘background’ and resonance contributions in the photoabsorption data. When moving into the time-like dilepton regime (at small three-momentum), the resonance contributions (which are larger in the spectral function approach, most importantly the  $N(1520)$ ) are relatively much more enhanced than the structureless background (which is larger in the chiral reduction approach), being essentially a kinematic effect. This is further supported by the fact that in both approaches the direct photon spectra actually agree quite well when integrated over the temperature and density history of central S+Au collisions. Thus a careful separation of background and resonance contributions in the experimental photoabsorption data should provide the key for a more quantitative discrimination of the effects in the time-like regime.

From a theoretical point of view, the most distinctive feature between the many-body and the chiral reduction treatment lies in the fate of the  $\rho$  resonance peak: in the master formula framework in-medium corrections are obtained through additive terms in a temperature and density expansion, which have almost no impact on the free  $\rho$  peak, whereas the resummation of large imaginary parts in the many-body treatment of the  $\rho$  propagator induces a marked depletion. Model-independent results for the in-medium vector and axialvector correlators indeed require that, due to their mixing, strength should be removed from both the  $\rho$  and the  $a_1$  poles, at least to lowest order in temperature and in the chiral limit [88] (cf. Sect. 2.6). The phenomenological many-body calculations seem to comply with this feature, although their theoretical relation to chiral symmetry is not always obvious.

In finite-temperature calculations based on chiral  $\pi$ - $\rho$ - $a_1$  Lagrangians the mixing theorem has been shown to be satisfied [110], being mainly realized through a reduction of the  $\gamma$ - $\rho$  vector dominance coupling  $g_{\rho\gamma}(T)$  due to a finite-temperature pion tadpole loop. However, corresponding results for dilepton production rates cannot account for the low-mass enhancement observed at the CERN-SpS [36]. One may raise the question whether phenomenological calculations at finite temperature *and* density are still compatible with the data when including a suppression of the VDM coupling. Since  $[g_{\rho\gamma}(T)/g_{\rho\gamma}(0)]^2$  decreases to only about 80% at the relevant temperatures of  $T \simeq 150$  MeV (using the physical pion mass rather than the chiral limit), the answer is that it will only mildly affect the many-body results (in fact, a more complete calculation should also include a (moderate) finite-temperature softening of the single-pion dispersion relation, which re-generates a small enhancement below the free  $\rho$  mass).

Another, more practical, issue concerns the role of a finite pion chemical potential in the evolution of (ultra-) relativistic heavy-ion collisions. Although it should have only moderate influence on the *shape* of the dilepton spectra, it certainly has a severe impact on the *total yield* of dilepton pairs originating from  $\pi\pi$  annihilation in the interacting fireball (being proportional to the square of the pion density). Both microscopic transport and hydrodynamical calculations correctly reproduce the total number of pions at freezeout, but the former seem to imply a finite  $\mu_\pi$  (not present in current hydrodynamical analyses), resulting in a larger dilepton signal by a factor of 2–3. The

introduction of a  $\mu_\pi > 0$  in a thermal fireball calculation has been shown to essentially resolve this discrepancy [50]. This needs to be confirmed in a full hydrodynamic treatment.

Finally we repeat that there is currently no theoretical explanation available for the strong enhancement in the low-mass dilepton spectra measured by the DLS collaboration [34] in heavy-ion collisions at relativistic projectile energies (1–2 AGeV). Both the dropping-mass scenario [233] and the broadening of the in-medium  $\rho$  spectral function [237] fall short of the data by a factor of 2–3 at invariant masses around 0.4 GeV. Hopes to resolve this puzzle reside on the upcoming precision measurements to be performed with the HADES detector at SIS (GSI) at similar bombarding energies.

## Chapter 5

# Conclusions

The investigation of hadron properties in a hot and dense environment as produced in energetic collisions of heavy nuclei represents one of the main frontiers in modern nuclear physics. In particular, it is directly related to the approach towards the QCD phase transition, which constitutes the 'Holy Grail' of the ultrarelativistic heavy-ion initiative. In the present article we have tried to review a very active subfield of this research program, namely the major theoretical accomplishments that have been achieved in connection with low-mass dilepton production over the past five years or so. Of course, the strong interest in this rapidly developing field is largely fueled by the exciting data that our experimental colleagues have obtained despite the notorious difficulties in extracting these observables.

The nature of dilepton final states mediated by electromagnetic currents immediately attaches to the vector mesons as the key objects for gaining direct non-trivial information on in-medium effects. In the low-mass region which we have focused on, these are the  $\rho$ ,  $\omega$  and  $\phi$  mesons, with the  $\rho$  meson playing the dominant role since it has the shortest lifetime and the largest dilepton decay width. The now widely accepted viewpoint is that the main nonperturbative feature of low-energy strong interactions – the spontaneous breakdown of the global chiral symmetry in the fundamental QCD Lagrangian – is not only responsible for the build-up of the 'constituent' quark masses but governs the appearance of the low-energy hadron spectrum altogether. Hence the approach to chiral restoration in hot/dense matter is intimately related to changing in-medium properties of light hadrons. Here the only strict prediction from QCD is that the spectral distributions of 'chiral partners' have to become identical (or 'degenerate'). This is encoded in 'Weinberg sum rules' which (in the chiral limit) relate the energy-integrated difference of the vector and axialvector correlators to the weak pion-decay constant,  $f_\pi$ , one of the order parameters for chiral symmetry restoration. Medium effects of the  $\rho$  meson therefore necessarily have to be put into context with those of its chiral partner, the  $a_1$  meson, as well as the pion. *How* the 'degeneration' is realized in nature is far from obvious and marks the central question to be answered in our context. For the  $\omega$  meson the problem is further complicated by the fact that it couples to three-pion (or  $\pi$ - $\rho$ ) states through the Wess-Zumino term and hence the anomaly structure of QCD. Also the assessment of in-medium properties of the  $\phi$  meson is hampered by the fact that the current mass of the  $s$ -quark is quite large so that arguments based on the chiral limit are not as stringent as in the  $u$ - $d$  sector.

Based on general properties of QCD we have started our discussion with a focus on model-independent approaches. To lowest order in temperature (and in the chiral limit), soft pion theorems imply the leading temperature effect to be a mere mixing between vector and axialvector correlators with no medium effects in the correlators themselves. QCD sum rules relate physical vacuum correlators to the various condensates thus providing a direct link between physically observed hadrons and the underlying QCD vacuum structure. It has now become clear that, when applied within a hadronic medium, they have limited predictive power for in-medium spectral distributions since they only provide a band of allowed combinations of large/small masses with corresponding large/small widths of the light vector mesons.

More specific predictions can be obtained from hadronic model Lagrangians which have been applied at various levels of approximations. Mean-field treatments typically focus on the in-medium behavior of the masses, and here results from chiral Lagrangians including vector mesons as gauge bosons (when applied at finite temperature) seem to allow for both an increasing  $\rho$ -meson mass – becoming degenerate with the  $a_1$  – as well as a decreasing mass as conjectured in the famous Brown-Rho paper based on scale invariance arguments. On the other hand, several independent many-body calculations of in-medium vector meson spectral functions come to the consensus that multiple interactions in hadronic matter inevitably induce a broadening of the spectral distributions. Nevertheless, certain  $S$ -wave scattering processes – most importantly resonant  $\rho N \rightarrow N(1520)$  excitations – can be associated with a reduction of the  $\rho/\omega$  mass. Towards higher densities, however, the widths of the spectral functions (most prominently for the  $\rho$  meson) increase to such an extent that the entire resonance structures are ‘melted’ into an essentially structureless continuum. At the same time the real parts in the propagators also become very flat so that the concept of a single mass ceases to be meaningful.

We have argued that a scenario of melting resonances has in fact the very appealing feature to establish a continuous link (‘duality’) between hadron- and quark-gluon-based calculations of the vector correlator, in the following sense: in vacuum the ‘duality-threshold’, *i.e.*, the invariant mass where the total cross section  $\sigma(e^+e^- \rightarrow \text{hadrons})$  empirically starts to follow the perturbative QCD prediction for  $q\bar{q}$  production is located at about  $M \simeq 1.5$  GeV. Resonance formation at lower invariant masses is an inherently nonperturbative effect associated with spontaneous chiral symmetry breaking which is a ‘large distance phenomenon’. It should not play any role at the small space-time distances probed beyond 1.5 GeV. Consequently, above this mass also the axialvector correlator, being identical to the vector one, ought to be given by perturbative QCD (which is unfortunately not well-established experimentally). Medium modifications can be studied through dilepton production, the reverse process of  $e^+e^-$  annihilation. We have pointed out that the finite-temperature mixing of vector and axialvector channels, which to lowest order arises from the coupling to pions of the heat bath, suffices to equalize the hadronic and quark-antiquark description down to the  $\phi$  meson mass when extrapolated to temperatures where chiral symmetry is restored. This feature is corroborated by model-independent approaches, such as the chiral reduction formalism, as well as detailed model calculations in the region above the  $\phi$  meson peak. It can thus be stated that ‘duality’ of hadronic and quark descriptions for the in-medium rates down to 1 GeV is well established for the case of vanishing baryon density and is likely to also hold for the latter case. The appealing physical interpretation is that, as electromagnetic probes couple to charges, in the vicinity of the phase boundary it becomes immaterial whether they reside in free quarks or in a large number of strongly interacting hadrons.



The continuation of the 'duality' argument to even lower invariant masses is not rigorously established at present, although suggestive indications have emerged. It is clear that the lowest-order mixing does not affect dynamically generated (low-mass) resonance structures in the correlators. This is precisely where the many-body effects enter through a flattening of the resonance peaks, which now requires arbitrary orders in density introduced through resummations. Hadronic model calculations near the phase boundary show that the resulting dilepton rates in the  $\rho$  region and somewhat below continue to match rather well the perturbative quark-antiquark rates. Deviations set in for  $M \lesssim 0.5$  GeV. At such low invariant masses it is, however, conceivable that 'soft' processes could significantly alter the quark rates. From a more practical point of view, the melting of especially the  $\rho$  resonance directly entails an enhanced dilepton production *below* the free mass which has turned out to be compatible with current data from the SpS. At the same time, to verify the associated depletion of the in-medium signal in the free  $\rho/\omega$  mass region of the spectra, it will be crucial to discriminate free  $\omega$  decays, occurring after freezeout, which is anticipated to be feasible with improved mass resolution measurements at the CERN-SpS. Clearly, this applies equally to *both* the commissioned low-energy run at 40 AGeV *and* additional future ones at the full SpS energy.

There remain a number of further problems which have to be resolved. First, it will be important to establish a more profound theoretical connection between the processes that reshape the vector ( $\rho$ ) and axialvector ( $a_1$ ) spectral distributions. In particular one has to find reliable ways to perform a similarly advanced calculation for the in-medium properties of the  $a_1$  as has been achieved for the  $\rho$ . Also, since (at comparable densities) the medium effects from baryonic matter seem to be more pronounced than at finite temperature, the fate of the (light) vector mesons in purely mesonic matter near the phase boundary is not really settled. Here, the upcoming collider experiments at RHIC and LHC, where the meson-to-baryon ratios at midrapidity are expected to increase by another substantial factor ( $\sim 5$ – $10$  at RHIC) as compared to current SpS conditions, will provide answers.

## ACKNOWLEDGMENTS

Many of our experimental and theoretical colleagues have integrally contributed to the progress reported in this article. We especially thank our collaborators G.E. Brown, M. Buballa, M. Urban, G. Chanfray, W. Cassing, E.L. Bratkovskaya and C. Gale for the fruitful joined efforts. We are also grateful for many productive conversations with P. Braun-Munzinger, A. Drees, J.W. Durso, M. Ericson, J. Friese, B. Friman, F. Karsch, F. Klingl, C.M. Ko, V. Koch, G.Q. Li, C. Lourenço, V. Metag, U. Mosel, W. Nörenberg, M. Prakash, K. Redlich, M. Rho, A. Richter, P. Schuck, E.V. Shuryak, H. Sorge, H.J. Specht, J. Stachel, I. Tserruya, W. Weise, A. Wirzba and I. Zahed. We furthermore thank G.E. Brown, W. Cassing, C. Lourenço and B.J. Schaefer for useful comments and a careful reading of the manuscript. We apologize to our colleagues whose work we did not appropriately discuss. One of us (RR) acknowledges support from the Alexander-von-Humboldt foundation through a 3-year Feodor-Lynen fellowship at Stony Brook during which most of his work on the presented topics has been performed. This work is supported in part by the National Science Foundation under Grant No. NSF PHY98-00978, the U.S. Department of Energy under Grant No. DE-FG02-88ER40388, the BMBF and GSI Darmstadt.

# Bibliography

- [1] See, for example, the proceedings of the recent International Conferences on Ultrarelativistic Nucleus-Nucleus Collisions:  
Quark Matter '95, Nucl. Phys. **A590** (1995);  
Quark Matter '96, Nucl. Phys. **A610** (1996);  
Quark Matter '97, Nucl. Phys. **A638** (1998).
- [2] C.-Y. Wong, *Introduction to High-Energy Heavy-Ion Collisions*, World Scientific, Singapore 1994.
- [3] P. Braun-Munzinger and J. Stachel, Nucl. Phys. **A638** (1998) 3c.
- [4] J. Stachel, Proc. of the International Nuclear Physics Conference, Paris, Aug. 1998, Nucl. Phys. **A** in print, and nucl-ex/9903007.
- [5] P. Braun-Munzinger, J. Stachel, J. Wessels and N. Xu, Phys. Lett. **B365** (1996) 1.
- [6] W. Cassing and E.L. Bratkovskaya, Phys. Rep. **308** (1999) 65.
- [7] C.M. Ko, V. Koch and G.Q. Li, Annu. Rev. Nucl. Part. Sci. **47** (1997) 505.
- [8] E.L. Feinberg, Nuovo Cim. **A34** (1976) 391.
- [9] E.V. Shuryak, Phys. Lett. **B78** (1978) 150.
- [10] E.V. Shuryak, Phys. Rep. **61** (1980) 71.
- [11] K. Kajantie, J. Kapusta, L. McLerran, and A. Mekjian, Phys. Rev. **D34**, 2746 (1986).
- [12] I. Tserruya, Nucl. Phys. **A590** (1995) 127c.
- [13] R. Rueckel, Phys. Lett. **B64** (1976) 39.
- [14] J. Jalilian-Marian and V. Koch, Phys. Rev. **C58** (1998) 3763.
- [15] K. Geiger, Phys. Rep. **258** (1995) 237.
- [16] A. Drees, private communication.

- [17] T. Matsui and H. Satz, Phys. Lett. **B178** (1986) 416.
- [18] See, *e.g.*,  
 R. Vogt, Phys. Lett. **B430** (1998) 15;  
 D. Kharzeev, Nucl. Phys. **A638** (1998) 279c;  
 C.Y. Wong, Nucl. Phys. **A610** (1996) 434c.
- [19] L. McLerran and T. Toimela, Phys. Rev. **D31** (1985) 545.
- [20] G. Agakichiev *et al.*, CERES collaboration, Phys. Rev. Lett. **75** (1995) 1272;  
 P. Wurm for the CERES collaboration, Nucl. Phys. **A590** (1995) 103c;  
 A. Drees and T. Ullrich, CERES Memorandum (1995), unpublished.
- [21] Th. Ullrich for the CERES/NA45 collaboration, Nucl. Phys. **A610** (1996) 317c.
- [22] A. Drees, Nucl. Phys. **A610** (1996) 536c.
- [23] G. Agakichiev *et al.*, CERES collaboration, Phys. Lett. **B422** (1998) 405.
- [24] M. Masera for the HELIOS-3 collaboration, Nucl. Phys. **A590** (1995) 93c;  
 I. Kralik for the HELIOS-3 collaboration, Proc. of the International Workshop XXIII on 'Gross Properties of Nuclei and Nuclear Excitations', Hirschegg 1995, eds. H. Feldmeier and W. Nörenberg, (GSI-Darmstadt 1995), p.143;  
 A.L.S. Angelis *et al.* (HELIOS-3 Collaboration), Eur. Phys. J. **C5** (1998) 63.
- [25] M.C. Abreu *et al.* (NA38 collaboration), Phys. Lett. **B368** (1996) 230; *ibid.* 239.
- [26] M. Gonin *et al.* (NA50 collaboration), Nucl. Phys. **A610** (1996) 404c.
- [27] E. Scomparin *et al.* (NA50 collaboration), Nucl. Phys. **A610** (1996) 331c;  
 E. Scomparin *et al.* (NA50 collaboration), Proc. of the International Conference on 'Strangeness in Quark Matter '98' (Padova, Italy, 20.-24.07.98), J. Phys. **G25** (1999) 235;  
 P. Bordalo *et al.* (NA50 collaboration), Proc. of Quark Matter '99 (Torino, Italy, 10.-15.05.99), to be published in Nucl. Phys. **A**.
- [28] A. de Falco *et al.* (NA38/NA50 collaboration), Nucl. Phys. **A638** (1998) 487c;  
 M.C. Abreu *et al.* (NA38/NA50 collaboration), *Low mass dimuon production in proton and ion induced interactions at the SPS*, preprint CERN-EP/99-112, submitted to Eur. Phys. J. **C**.
- [29] A. Drees, Nucl. Phys. **A630** (1998) 449c.
- [30] I. Tserruya, Nucl. Phys. **A638** (1998) 365c.
- [31] P. Wurm, Proc. of APCTP Workshop on 'Hadron Properties in Medium' (World Scientific, Singapore, 1998).

- [32] T.J. Hallman and J. Thomas, Nucl. Phys. **A590** (1995) 399c;  
D.P. Morrison *et al.*, Nucl. Phys. **A638** (1998) 565c.
- [33] G. Roche *et al.* (DLS collaboration), Phys. Rev. Lett. **61** (1988) 1069;  
C. Naudet *et al.* (DLS collaboration), Phys. Rev. Lett. **62** (1989) 2652;  
G. Roche *et al.* (DLS collaboration), Phys. Lett. **B226** (1989) 228;  
S. Beedoe *et al.* (DLS collaboration), Phys. Rev. **C47** (1993) 2840.
- [34] R.J. Porter *et al.* (DLS collaboration), Phys. Rev. Lett. **79** (1997) 1229;  
W.K. Wilson *et al.* (DLS collaboration), Phys. Rev. **C57** (1997) 1865.
- [35] W. Koenig, Proc. of the Workshop on 'Dilepton Production in Relativistic Heavy-Ion Collisions', ed. H. Bokemeyer (GSI, Darmstadt, 1994).
- [36] V. Koch and C. Song, Phys. Rev. **C54** (1996) 1903.
- [37] G.Q. Li, C.M. Ko and G.E. Brown, Phys. Rev. Lett. **75** (1995) 4007; Nucl. Phys. **A606** (1996) 568.
- [38] W. Cassing, W. Ehehalt and C.M. Ko, Phys. Lett. **B363** (1995) 35.
- [39] W. Cassing, W. Ehehalt and I. Kralik, Phys. Lett. **B377** (1996) 5.
- [40] D.K. Srivastava, B. Sinha and C. Gale, Phys. Rev. **C53** (1996) R567.
- [41] R. Baier, M. Dirks and K. Redlich, Phys. Rev. **D55** (1997) 4344; Proc. of the 28th Int. Conf. on High Energy Physics, Warszawa, Poland (July 1996), hep-ph/9612448.
- [42] L.A. Winkelmann *et al.*, Nucl. Phys. **A610** (1996) 116c.
- [43] C.M. Hung and E.V. Shuryak, Phys. Rev. **C56** (1997) 453.
- [44] J. Murray, W. Bauer and K. Haglin, Phys. Rev. **C57** (1998) 882.
- [45] G.E. Brown and M. Rho, Phys. Rev. Lett. **66** (1991) 2720.
- [46] T. Hatsuda and S.H. Lee, Phys. Rev. **C46** (1992) R34.
- [47] R. Rapp, G. Chanfray and J. Wambach, Nucl. Phys. **A617** (1997) 472.
- [48] W. Cassing, E.L. Bratkovskaya, R. Rapp and J. Wambach, Phys. Rev. **C57** (1998) 916.
- [49] R. Rapp, Proc. of the 33rd Rencontres de Moriond on 'QCD and High Energy Hadronic Interactions', Les Arcs (France), March 21-28, 1998, published in Edition Frontiers, ed. J. Tran Thanh Van, and nucl-th/9804065.
- [50] R. Rapp and J. Wambach, hep-ph/9907502.

- [51] For theoretical introductions, see, *e.g.*,  
 F.J. Yndurain, *Quantum Chromodynamics: an Introduction to the Theory of Quarks and Gluons*, Springer, Heidelberg/New York (1983);  
 T.D. Lee, *Particle Physics and Introduction to Field Theory*, Harwood Academic, London (1981);  
 F.E. Close, *An Introduction to Quarks and Partons*, Academic Press, New York (1979).
- [52] M. Schmelling, Proc. of the XXVIII. International Conference on 'High Energy Physics', Warsaw, July 25-31, 1996, and hep-ex/9701002.
- [53] For overviews, see, *e.g.*,  
 B.W. Lee, *Chiral Dynamics*, Gordon & Breach, London (1972);  
 S. Weinberg, in 'Lectures on Elementary Particles and Quantum Field Theory', Vol. 1, E. Deser, M. Grisaru and H. Pendleton (Eds.), MIT Press, Cambridge (Massachusetts) (1970) 283;  
 V. de Alfaro, S. Fubini, G. Furlan and C. Rossetti, *Currents in Hadronic Physics*, North-Holland, Amsterdam (1973).
- [54] T. Schäfer and E.V. Shuryak, Rev. Mod. Phys. **70** (1998) 323.
- [55] M.C. Chu, J.M. Grandy, S. Huang and J.W. Negele, Phys. Rev. **D49** (1994) 6039;  
 J.W. Negele, Proc. of LATTICE 98, and hep-lat/9810053.
- [56] E.G. Drukarev and E.M. Levin, Prog. Part. Nucl. Phys. **27** (1991) 77.
- [57] Y. Nambu and G. Jona-Lasinio, Phys. Rev. **122** (1961) 345; *ibid.* **124** (1961) 246;  
 Y. Nambu and D. Lurie, Phys. Rev. **125** (1962) 1429.
- [58] M. Gell-Mann, R.J. Oakes and B. Renner, Phys. Rev. **175** (1968) 2195.
- [59] M.A. Shifman, A.I. Vainshtein and V.I. Zakharov, Nucl. Phys. **B147** (1979) 385.
- [60] G. Chanfray, private communication.
- [61] J. Gasser, H. Leutwyler and M.E. Saino, Phys. Lett. **B253** (1991) 252.
- [62] I. Jameson, A.W. Thomas and G. Chanfray, J. Phys. **G18** (1992) L159.
- [63] M. Birse and J. McGovern, Phys. Lett. **B292** (1992) 242.
- [64] J. Gasser and H. Leutwyler, Phys. Lett. **B184** (1987) 83.
- [65] P. Gerber and H. Leutwyler, Nucl. Phys. **B321** (1989) 327.
- [66] H. Leutwyler, *Deconfinement and Chiral Symmetry*, in 'QCD 20 years later', Vol. 2, P.M. Zervas and H.A. Kastrup (Eds.), World Scientific, Singapore, (1993) 693.
- [67] R. Brockmann and W. Weise, Phys. Lett. **B267** (1996) 40.
- [68] Z. Aouissat, G. Chanfray, P. Schuck and J. Wambach, Nucl. Phys. **A603** (1996) 458.

- [69] B.-J. Schaefer and H. Pirner, nucl-th/9903003.
- [70] J. Kapusta, *Finite Temperature Field Theory*, Cambridge University Press, 1989.
- [71] K.G. Wilson, Phys. Rev. **D10** (1974) 2445.
- [72] J. Kogut and L. Susskind, Phys. Rev. **D11** (1975) 395.
- [73] D. Kaplan, Phys. Lett. **B288** (1992) 342;  
Y. Shamir, Nucl. Phys. **B406** (1993) 90;  
for a recent review, see also T. Blum, Nucl. Phys. Proc. Suppl. **73** (1999) 167.
- [74] C. Bernard *et al.*, Phys. Rev. **D55** (1997) 6861.
- [75] G. Boyd and D.E. Miller, hep-ph/9608482.
- [76] H. Satz, private communication (1999).
- [77] F. Karsch, Nucl. Phys. **A590** (1995) 367c.
- [78] S. Gottlieb *et al.*, Phys. Rev. **D55** (1997) 6852.
- [79] Z. Huang, Phys. Lett. **B361** (1995) 131.
- [80] C. Bacci *et al.* ( $\gamma\gamma 2$  collaboration), Phys. Lett. **B86** (1979) 234.
- [81] B. Wiik and G. Wolf, *Electron-Positron Interactions* (Springer Verlag, Berlin 1979).
- [82] L.M. Barkov *et al.*, (OLYA collaboration), Nucl. Phys. **B256**, 365 (1985).
- [83] A. Cordier *et al.* (DM1 collaboration), Nucl. Phys. **B172** (1980) 13.
- [84] V. Siderov, Proc. of the International Symposium on 'Lepton and Photon Interactions' (1979) (Fermilab, Batavia 1980).
- [85] S. Weinberg, Phys. Rev. Lett. **18** (1967) 507.
- [86] K. Kawarabayashi and M. Suzuki, Phys. Rev. Lett. **16** (1966) 255;  
Riazuddin und Fayyazuddin, Phys. Rev. **147** (1966) 1071.
- [87] J. Kapusta and E.V. Shuryak, Phys. Rev. **D49** (1994) 4694.
- [88] M. Dey, V.L. Eletsky and B.L. Ioffe, Phys. Lett. **B252** (1990) 620;  
V.L. Eletsky, Phys. Lett. **B245** (1990) 229.
- [89] B. Krippa, Phys. Lett. **B427** (1998) 13.
- [90] M.C. Birse, Phys. Rev. **C53** (1996) R2048.
- [91] F. Klingl, N. Kaiser and W. Weise, Nucl. Phys. **A624** (1997) 527.
- [92] D.B. Leinweber, Ann. Phys. **254** (1997) 328.

- [93] M. Asakawa and C.M. Ko, Phys. Rev. **C48** (1993) R526; Nucl. Phys. **A560** (1993) 399.
- [94] S. Leupold, W. Peters and U. Mosel, Nucl. Phys. **A628** (1998) 311.
- [95] B. Borasoy and U.-G. Meißner, Phys. Lett. **B365** (1996) 285.
- [96] H. Yamagishi and I. Zahed, Ann. Phys. **247** (1996) 292.
- [97] M. Veltmann, Phys. Rev. Lett. **17** (1966) 553;  
J.S. Bell, Nuovo Cim. **50 A** (1967) 129.
- [98] R.E. Peierls, Proc. Roy. Soc. (London) **A214** (1952) 143.
- [99] J.V. Steele, H. Yamagishi and I. Zahed, Phys. Lett. **B384** (1996) 255.
- [100] J.V. Steele, H. Yamagishi and I. Zahed, Phys. Rev. **D56** (1997) 5605.
- [101] W. Peters, M. Post, H. Lenske, S. Leupold and U. Mosel, Nucl. Phys. **A632** (1998) 109.
- [102] R. Rapp, M. Urban, M. Buballa and J. Wambach, Phys. Lett. **B417** (1998) 1.
- [103] G.E. Brown, G.Q. Li, R. Rapp, M. Rho and J. Wambach, Acta Phys. Polon. **B29** (1998) 2309.
- [104] J.V. Steele and I. Zahed, hep-ph/9901385.
- [105] R.D. Pisarski, Phys. Rev. **D52** (1995) R3773; hep-ph/9503330 (unpublished);  
hep-ph/9505257 (unpublished).
- [106] T. Hatsuda and T. Kunihiro, Phys. Lett. **B185** (1987) 304.
- [107] J.J. Sakurai, *Currents and Mesons* (University of Chicago, Chicago 1969).
- [108] V.L. Eletsky and B.L. Ioffe, Phys. Rev. **D51** (1995) 2371.
- [109] U.-G. Meißner, Phys. Rep. **161** (1988) 213.
- [110] S.H. Lee, C. Song and H. Yabu, Phys. Lett. **B341** (1995) 407.
- [111] C. Song, Phys. Rev. **C47** (1993) 3338; Phys. Rev. **D48** (1993) 1375; Phys. Rev. **D53** (1996) 3962.
- [112] M. Bando, T. Kugo, S. Uehara, K. Yamawaki and T. Yanagida, Phys. Rev. Lett. **54** (1985) 1215;  
M. Bando, T. Kugo and K. Yamawaki, Phys. Rep. **164** (1988) 217.
- [113] C. Song and V. Koch, Phys. Rev. **C54** (1996) 3218.
- [114] G. Chanfray and P. Schuck, Nucl. Phys. **A545** (1992) 271c; Nucl. Phys. **A555** (1993) 329.
- [115] C.A. Dominguez and M. Loewe, Nucl. Phys. **B** (Proc. Suppl.) **16** (1990) 403; Zeit. Phys. **C49** (1991) 423.

- [116] V.L. Eletsky and B.L. Ioffe, Phys. Rev. **D47** (1993) 3083.
- [117] C.A. Dominguez and M. Loewe, Phys. Lett. **B233** (1989) 201.
- [118] C. Gale and J. Kapusta, Nucl. Phys. **B357** (1991) 65.
- [119] C. Gale and P. Lichard, Phys. Rev. **D49** (1994) 3338.
- [120] K. Haglin, Nucl. Phys. **A584** (1995) 719.
- [121] V.L. Eletsky, B.L. Ioffe and J.I. Kapusta, Eur. Phys. J. **A3** (1998) 381; V.L. Eletsky and J.I. Kapusta, nucl-th/9810052.
- [122] S. Gao, C. Gale, C. Ernst, H. Stöcker and W. Greiner, nucl-th/9812059.
- [123] R. Rapp and C. Gale, Phys. Rev. **C** (1999) in print, and hep-ph/9902268.
- [124] S. Gao and C. Gale, Phys. Rev. **C57** (1998) 254.
- [125] J.J. Sakurai, Ann. Phys. **11** (1960) 1.
- [126] M. Urban, M. Buballa, R. Rapp and J. Wambach, Nucl. Phys. **A641** (1998) 433.
- [127] E.V. Shuryak, Nucl. Phys. **A533** (1991) 761.
- [128] R. Rapp and J. Wambach, Phys. Lett. **B315** (1993) 220; *ibid.* **B351** (1995) 50.
- [129] R. Rapp, PhD thesis Bonn 1996, in *Berichte des Forschungszentrum Jülich* vol. 3195 (Jülich, 1996) p. 1-141.
- [130] R. Rapp, J.W. Durso and J. Wambach, Nucl. Phys. **A596** (1996) 436.
- [131] T. Hatsuda and T. Kunihiro, Prog. Theo. Phys. **91** (1987) 284.
- [132] N. Kaiser and U.-G. Meißner, Nucl. Phys. **A519** (1990) 671.
- [133] C. Itzykson and J.B. Zuber, *Quantum Field Theory* (McGraw Hill, New York, 1980).
- [134] T.E.O. Ericson and W. Weise, *Pions and Nuclei* (Clarendon, Oxford, 1988).
- [135] J. Ellis, Nucl. Phys. **B22** (1970) 478;  
B.A. Campbell, J. Ellis and K.A. Olive, Nucl. Phys. **B345** (1990) 57.
- [136] G.E. Brown and M. Rho, Phys. Rep. **269** (1996) 333.
- [137] A.B. Migdal, E.E. Saperstein, M.A. Troitsky and D.N. Voskresensky, Phys. Rep. **192** (1990) 179.
- [138] R. Rapp and J. Wambach, Nucl. Phys. **A573** (1994) 626.
- [139] J.C. Ward, Phys. Rev. **78** (1950) 182;  
Y. Takahasi, Nuovo Cim. **6** (1957) 371.



- [140] M. Herrmann, B. Friman and W. Nörenberg, Nucl. Phys. **A545** (1992) 267c; Nucl. Phys. **A560** (1993) 411.
- [141] M. Asakawa, C. M. Ko, P. Lévai and X. J. Qiu, Phys. Rev. **C46** (1992) R1159.
- [142] G. Chanfray, R. Rapp and J. Wambach, Phys. Rev. Lett. **76** (1996) 368.
- [143] R. Machleidt, K. Holinde and C. Elster, Phys. Rep. **149** (1987) 1.
- [144] G. Chanfray, J. Delorme, M. Ericson and M. Rosa-Clot, nucl-th/9809007.
- [145] N. Kaiser, P.B. Siegel and W. Weise, Nucl Phys. **A594** (1995) 325.
- [146] Particle Data Group, R.M. Barnett *et al.*, Phys. Rev. **D54** (1996) 1.
- [147] B. Friman, Nucl. Phys. **A610** (1996) 358c;  
B. Friman and H.J. Pirner, Nucl. Phys. **A617** (1997) 496.
- [148] B. Friman, M. Lutz and G. Wolf, Proc. of *BARYONS 98*, Bonn (Germany), Sept. 98, and nucl-th/9811040.
- [149] V.L. Eletsky and B.L. Ioffe, Phys. Rev. Lett. **78** (1997) 1010.
- [150] T.H. Bauer, R.D. Spital, D.R. Yennie and F.M. Pipkin, Rev. Mod. Phys. **50** (1978) 261.
- [151] L.A. Kondratyuk, A. Sibirtsev, W. Cassing, Ye.S. Golubeva and M. Effenberger, Phys. Rev. **C58** (1998) 1078.
- [152] F. Klingl, N. Kaiser and W. Weise, Zeit. Phys. **A356** (1996) 193.
- [153] B. Friman, Proc. of the ACTP Workshop on 'Hadron Properties in Medium', Seoul, Korea, Oct. 27-31, 1997, to be published, and nucl-th/9801053;  
Acta Phys. Polon. **B29** (1998) 3195, and nucl-th/9808071.
- [154] W.M. Layson, Nuovo Cim. **20** (1961) 1207.
- [155] J.H. Koch and E.J. Moniz, Phys. Rev. **C 27** (1983) 751.
- [156] F. Bonnutti *et al.*, Phys. Rev. Lett. **77** (1996) 603.
- [157] C. Gaarde *et al.*, SATURNE proposal (1996).
- [158] TAGX Collaboration, G.J. Lolos *et al.*, Phys. Rev. Lett. **80** (1998) 241;  
G.M. Huber, G.J. Lolos and Z. Papandreou, Phys. Rev. Lett. **80** (1998) 5285.
- [159] G. Freedom, International Workshop on 'Soft Dilepton Production', LBNL. August 20-22, 1997.
- [160] W. Schön, H. Bokemeyer, W. Koenig and W. Metag, Acta Phys. Polon. **B27** (1996) 2959.
- [161] R.S. Hayano *et al.*, GSI-SIS proposal #214 (1997).

- [162] F. Klingl and W. Weise, Nucl. Phys. **A606** (1996) 329.
- [163] M. Effenberger, A. Hombach, S. Teis and U. Mosel, Nucl. Phys. **A613** (1997) 353;  
M. Effenberger and U. Mosel, Proc. of the 'Conference on Perspectives in Hadronic Physics',  
Trieste, May 12-16, 1997, and nucl-th/9707010.
- [164] Particle Data Group, Phys. Rev. **D50** (1994) 1173.
- [165] A. Lepretre *et al.*, Phys. Lett. **79B** (1978) 43.
- [166] J. Ahrens, Nucl. Phys. **A446** (1985) 229c;  
J. Ahrens *et al.*, Phys. Lett. **146B** (1984) 303.
- [167] Th. Frommhold *et al.*, Phys. Lett. **B295** (1992) 28; Zeit. Phys. **A350** (1994) 249.
- [168] N. Bianchi *et al.*, Phys. Lett. **B299** (1993) 219; Phys. Rev. **C54** (1996) 1688.
- [169] R.L. Walker, Phys. Rev. **182** (1969) 1729.
- [170] B. Krusche *et al.*, Phys. Rev. Lett. **74** (1995) 3736.
- [171] A. Braghieri *et al.*, Phys. Lett. **B363** (1995) 46.
- [172] W.M. Alberico, G. Gervino, and A. Lavagno, Phys. Lett. **B321** (1994) 177.
- [173] L.A. Kondratyuk, M.I. Krivoruchenko, N. Bianchi, E. De Sanctis and V. Muccifora, Nucl.  
Phys. **A579** (1994) 453.
- [174] N.M. Kroll, T.D. Lee and B. Zumino, Phys. Rev. **157** (1967) 1376.
- [175] T.A. Armstrong *et al.*, Phys. Rev. **D5** (1972) 1640.
- [176] T.A. Armstrong *et al.*, Nucl. Phys. **B41** (1972) 445.
- [177] J. Cleymans, J. Fingberg and K. Redlich, Phys. Rev. **D35** (1987) 2153.
- [178] H.-J. Schulze and D. Blaschke, Phys. Lett. **B386** (1996) 429.
- [179] E. Braaten, R.D. Pisarski and T.C. Wang, Phys. Rev. Lett. **64** (1990) 2242.
- [180] L. Chatterjee and C.-Y. Wong, Phys. Rev. **C51** (1995) 2125.
- [181] M.G.-H. Mostafa, C.-Y. Wong, L. Chatterjee and Z.-Q. Wang, hep-ph/9503357.
- [182] C.H. Lee, J. Wirstam, I. Zahed and T.H. Hansson, Phys. Lett. **B448** (1999) 168.
- [183] T. Schäfer, E.V. Shuryak and J.J.M. Verbaarschot, Phys. Rev. **D51** (1995) 1267.
- [184] M. Velkovsky and E.V. Shuryak, Phys. Rev. **D56** (1997) 2766.
- [185] R. Rapp, T. Schäfer, E.V. Shuryak and M. Velkovsky, to appear in Ann. Phys. (1999), and  
hep-ph/9904353.

- [186] H.A. Weldon, hep-ph/9908204.
- [187] A. Peshier and M. Thoma, hep-ph/9907268.
- [188] S.M.H. Wong, Zeit. Phys. **C53** (1992) 465.
- [189] J. Cleymans, V.V. Goloviznin and K. Redlich, Phys. Rev. **D47** (1993) 989.
- [190] J.D. Bjorken, K.L. Kowalski and C.C. Taylor, Proc. of Les Rencontres de la Vallee D' Aoste, La Thuile, Italy, 1993, ed. by M. Greco (Edition Frontiers, Gif-sur-Yvette, 1993), p. 507.
- [191] K. Rajagopal and F. Wilczek, Nucl. Phys. **B404** (1993) 577.
- [192] Z. Huang and X.-N. Wang, Phys. Lett. **B383** (1996) 457.
- [193] Y. Kluger, V. Koch, J. Randrup and X.-N. Wang, Phys. Rev. **C57** (1998) 280.
- [194] S. Gavin, Nucl. Phys. **B351** (1991) 561.
- [195] W. Ehehalt and W. Cassing, Nucl. Phys. **A602** (1996) 449.
- [196] X.-N. Wang and M. Gyulassy, Phys. Rev. **D44** (1991) 3501.
- [197] H. Bebie, P. Gerber, J.L. Goity and H. Leutwyler, Nucl. Phys. **B378** (1992) 95.
- [198] B. Nilsson-Almquist and E. Stenlund, Comput. Phys. Commun. **43** (1987) 387.
- [199] R. Baier, M. Dirks and C. Redlich, Acta Phys. Polon. **B28** (1997) 2873.
- [200] R. Rapp, Proc. of Quark Matter '99 (Torino, Italy, 10.-15.05.99), to be published in Nucl. Phys. **A**, and hep-ph/9907342.
- [201] A.V. Leonidov and P.V. Ruuskanen, Heavy Ion Phys. **1** (1995) 61; Eur. Phys. J. **C4** (1998) 519.
- [202] C. Song, C.M. Ko, and C. Gale, Phys. Rev. **D50**, R1827 (1994).
- [203] J.K. Kim, P. Ko, K.Y. Lee, and S. Rudaz, Phys. Rev. **D53** (1996) 4787.
- [204] G.Q. Li and C. Gale, Phys. Rev. Lett. **81** (1998) 1572; Phys. Rev. **C58** (1998) 2914.
- [205] C.-H. Lee, H. Yamagishi and I. Zahed, Phys. Rev. **C58** (1998) 2899.
- [206] J. Kapusta, P. Lichard and D. Seibert, Phys. Rev. **D44** (1991) 2774; and *Erratum, ibid.* **D47** (1993) 4171.
- [207] L.D. Landau, Izv. Akad. Nauk. SSSR Ser. Fiz. **17** (1953) 51.
- [208] E.V. Shuryak, Yad. Fiz. **20** (1974) 549.
- [209] F. Cooper, G. Frye and E. Schonberg, Phys. Rev. **D11** (1975) 292.

- [210] H. von Gersdorff, L. McLerran, M. Kataja and P.V. Ruuskanen, Phys. Rev. **D34** (1986) 794.
- [211] E. Schnedermann and U. Heinz, Phys. Rev. Lett. **69** (1992) 2908.
- [212] U. Katscher, D.H. Rischke, J.A. Maruhn, W. Greiner, I.N. Mishustin and L.M. Saratov, Zeit. Phys. **A346** (1993) 209.
- [213] C.M. Hung and E.V. Shuryak, Phys. Rev. Lett. **75** (1995) 4003.
- [214] J. Sollfrank, P. Huovinen, M. Kataja, P.V. Ruuskanen, M. Prakash and R. Venugopalan, Phys. Rev. **C55** (1997) 392.
- [215] D.H. Rischke, Y. Pürsün and J.A. Maruhn, Nucl. Phys. **A595** (1995) 383; and *Erratum*, *ibid.* **A596** (1996) 717.
- [216] B.R. Schlei, Heavy Ion Phys. **5** (1997) 403.
- [217] D.K. Srivastava, J. Pan, V. Emel'yanov and C. Gale, Phys. Lett. **B329** (1994) 157.
- [218] J.D. Bjorken, Phys. Rev. **D27** (1983) 140.
- [219] R. Hwa and K. Kajantie, Phys. Rev. **D32** (1985) 1109.
- [220] B. Kämpfer, O.P. Pavlenko, A. Peshier and G. Soff, Phys. Rev. **C52** (1995) 2704.
- [221] K. Haglin, Phys. Rev. **C53** (1996) R2606.
- [222] G.F. Bertsch and S. Das Gupta, Phys. Rep. **160** (1988) 189.
- [223] C.M. Ko and Q. Li, Phys. Rev. **C37** (1988) R2270.
- [224] B. Blättel, V. Koch, W. Cassing and U. Mosel, Phys. Rev. **C38** (1988) 1767;  
for a review, see *e.g.*, B. Blättel, V. Koch and U. Mosel, Rep. Prog. Phys. **56** (1993) 1.
- [225] J. Aichelin, Phys. Rep. **202** (1991) 233.
- [226] H. Sorge, H. Stöcker and W. Greiner, Ann. Phys. **192** (1989) 266.
- [227] S.A. Bass *et al.*, Prog. Part. Nucl. Phys. **41** (1998) 225.
- [228] K. Weber, B. Blättel, W. Cassing, H.-C. Dönges, V. Koch, A. Lang and U. Mosel, Nucl. Phys. **A539** (1992) 713.
- [229] B.D. Serot and J.D. Walecka, Adv. Nucl. Phys. **16** (1986) 1.
- [230] E.L. Bratkovskaya and W. Cassing, Nucl. Phys. **A619** (1997) 413.
- [231] G.Q. Li and C.M. Ko, Nucl. Phys. **A582** (1995) 731.
- [232] G.Q. Li, C.M. Ko, G.E. Brown and H. Sorge, Nucl. Phys. **A611** (1996) 539.
- [233] E.L. Bratkovskaya and C.M. Ko, Phys. Lett. **B445** (1999) 265.

- [234] W. Cassing and S. Juchem, nucl-th/9903070.
- [235] J. Knoll, nucl-th/9811099.
- [236] V. Koch and G.F. Bertsch, Nucl. Phys. **A552** (1993) 591.
- [237] E.L. Bratkovskaya, W. Cassing, R. Rapp and J. Wambach, Nucl. Phys. **A634** (1998) 168.
- [238] P. Koch, Zeit. Phys. **C57** (1993) 283.
- [239] B. Kämpfer, P. Koch and O.P. Pavlenko, Phys. Rev. **C49** (1994) 1132.
- [240] P. Braun-Munzinger and J. Stachel, Nucl. Phys. **A606** (1996) 320.
- [241] J. Stachel, Nucl. Phys. **A610** (1996) 509c.
- [242] U.A. Wiedemann, Proc. of Quark Matter '99, Torino (Italy), May 10-15, 1999, and nucl-th/9907048.
- [243] H. Sorge, Phys. Lett. **B373** (1996) 16.
- [244] K. Gallmeister, B. Kämpfer and O.P. Pavlenko, hep-ph/9908269.
- [245] L. Xiong, Z.G. Wu, C.M. Ko and J.Q. Wu, Nucl. Phys. **A512** (1990) 772.
- [246] Gy. Wolf, G. Batko, W. Cassing, U. Mosel, K. Niita and M. Schäfer, Nucl. Phys. **A517** (1990) 615;  
Gy. Wolf, W. Cassing and U. Mosel, Nucl. Phys. **A552** (1993) 549.
- [247] C. Ernst, S.A. Bass, M. Belkacem, H. Stöcker and W. Greiner, Phys. Rev. **C58** (1998) 447.
- [248] E.L. Bratkovskaya, W. Cassing, M. Effenberger and U. Mosel, Nucl. Phys. **A653** (1999) 301.
- [249] R. Auerbeck *et al.* (TAPS collaboration), Zeit. Phys. **A359** (1997) 65.
- [250] J. Zhang and C. Gale, Phys. Rev. **C50** (1994) 1617.
- [251] B. Lenkeit, Doctoral Thesis, University of Heidelberg, 1998.
- [252] P. Huovinen and M. Prakash, Phys. Lett. **B450** (1999) 15.
- [253] J. Kapusta, D. Kharzeev and L. McLerran, Phys. Rev. **D53** (1996) 5028;  
Z. Huang and X.-N. Wang, *ibid.* 5034.
- [254] A. Drees, Phys. Lett. **B388** (1996) 380.
- [255] G.Q. Li, G.E. Brown and C.M. Ko, Nucl. Phys. **A630** (1998) 563.
- [256] D. Irmscher, Doctoral Dissertation, Univ. Heidelberg 1993; T. Ullrich, Doctoral Dissertation, Univ. Heidelberg 1994; G. Agakichiev et al., CERES collaboration, Eur. Phys. J. **C4** (1998) 231; and A. Drees, private communication.

- [257] V. Koch, Proc. of the XXXVII. International 'Winter Meeting on Nuclear Physics', Bormio (Italy) Jan. 1999, and nucl-th/9903008.
- [258] P. Braun-Munzinger, D. Miskowiec, A. Drees and C. Lourenço, Eur. Phys. J. **C1** (1998) 123.
- [259] Z. Lin and X.N. Wang, Phys. Lett. **B444** (1998) 245.
- [260] R. Rapp and E.V. Shuryak, in preparation.
- [261] I. Tserruya, Prog. Theor. Phys. Suppl. **129** (1997) 145.
- [262] T. Akesson *et al.*, HELIOS-2 collaboration, Zeit. Phys. **C46** (1990) 369.
- [263] R. Baur *et al.*, CERES collaboration, Zeit. Phys. **C71** (1996) 571.
- [264] R. Albrecht *et al.*, WA80 collaboration, Phys. Rev. Lett. **76** (1996) 3506.
- [265] B. Wyslouch for the WA98 collaboration, Nucl. Phys. **A638** (1998) 147c.
- [266] D.K. Srivastava and B. Sinha, Phys. Rev. Lett. **73** (1994) 2421
- [267] A. Dumitru *et al.*, Phys. Rev. **C51** (1995) 2166.
- [268] G.Q. Li and G.E. Brown, Nucl. Phys. **A632** (1998) 153.
- [269] S. Sarkar *et al.*, Nucl. Phys. **A634** (1998) 206.
- [270] M.-A. Halasz, J.V. Steele, G.Q. Li and G.E. Brown, Phys. Rev. **C58** (1998) 365.